JUSTUS-LIEBIG- UNIVERSITÄT GIEßEN
I. Physikalisches Institut

Optochemical sensor systems for aerospace applications

Sumit Paul

Vollständiger Abdruck der von der Fakultät für
Physik der Justus Liebig Universität, Gießen
zur Erlangung des akademischen Grades eines

Doktor der Naturwissenschaften (Dr. rer. nat.)

Vorsitzender:	Prof. Dr. Peter J. Klar
Prüfer der Dissertation:	1. Prof. Dr. Martin Eickhoff 2. Prof. Dr. Claus-Dieter Kohl 3. Prof. Dr. Bernd Smarsly

Tag der Disputation: 18.07.2014

Abstract

In safety-critical applications opto-chemical sensors are preferred over conventional electrochemical ones due to several key advantages: built in media separation, harsh environment capability and electromagnetic immunity. In this thesis opto-chemical sensors whose functionality is based on the infrared absorption of fluids and/or the photoluminescence of nanostructure immersed in gaseous or fluid media are investigated. Application domains assessed relate to the fields of aeronautic safety and the smart maintenance of commercial aircrafts.

Chapter 1 focuses on chemical contamination monitoring in phosphate ester based hydraulic fluids. By implementing such sensors in an aircraft, key contamination parameters can be assessed without taking fluid samples from the pressurized hydraulic system. By performing repeated measurements on the hydraulic fluid, degradation trends can be established and maintenance actions can be scheduled before any irreversible damage on the fluid or on the hydraulic system occurred. By performing the necessary maintenance actions at a pre-determined time in a pre-determined place, expensive ground time of commercial aircrafts can be minimized and significant costs due to unscheduled maintenance can be avoided. The chemical properties of aviation hydraulic fluids and their degradation mechanisms are described in the first part of this chapter. This is followed by a presentation of results gained from Fourier Transform Infra-Red (FTIR) measurements on hydraulic fluids in different states of contamination and degradation. These results show that the free water content and the Total Acid Number (TAN) can be inferred from changes in the O-H stretching vibration bands in 3200 cm^{-1} - 3800 cm^{-1} range. With this knowledge in mind, a miniaturized mid-infrared (MIR) sensor system has been realized, which allows these contamination parameters to be determined online inside a functional hydraulic system. In order to avoid flow restrictions in the hydraulic system, an extension of this MIR sensor principle into the near infrared (NIR) range of overtone vibrations is presented. The functionality of this chemical sensor system is complemented by a particle contamination sensor whose function is based on a light barrier principle. Both sensors in combination allow all practically relevant contamination parameters to be monitored online, inside an aircraft or in a ground support car directly on the airfield.

Chapter 2 presents an all-optical sensor system that employs InGaN/GaN nanowire heterostructures (NWH) as optochemical transducers for gas detecti-

on. This transducer principle is best suited for safety-critical applications where reliable media separation is required, e.g. leaks in fuel and hydraulic lines. The photoluminescence intensity of the nanostructure has been found to be enhanced upon exposure to hydrogen and hydrocarbon gases and to be quenched upon exposure to oxidizing gases, such as O_2, NO_2 and O_3. The chapter begins with the description of potential gas sensing applications in an aircraft. Afterwards the theory relating to the gas sensing mechanism using nanowires is discussed. Thereafter, the growth of group III-nitride based nanowires is presented, followed by a description of an optical fiber based sensor system that uses these nanowires as opto-chemical transducers. This experimental section also describes the gas test rig that had been used to assess the sensor performance. The presentation of the experimental results is divided in two parts: The first part focuses on the results obtained with hydrogen and hydrocarbon gases, while the second part describes the sensor response to different oxidizing gases. Minimum detectable H_2 concentrations as low as 200 ppb at 50^oC, and O_3 concentrations as low as 10 ppb at room temperature, are demonstrated. The effects of temperature and humidity variations on the gas sensitivity are also reported in detail.

Chapter 3 begins with a brief presentation of pH-monitoring needs inside an aircraft. A particularly interesting application is the monitoring of the pH value of onboard-generated drinking water, coming from a fuel cell. Thereafter GaN/InGaN quantum dots (QDs) are described with their possible use as opto-chemical transducers for measuring pH changes in fluids. The related sensing mechanism is briefly described, followed by a description of the test setup. The results section proves the variation of photoluminescence intensity with applied electrical bias and with pH changes inside a fluid medium. The accessible pH range extends from pH = 7 to pH = 2. Resolutions of less than 0.1 pH units and response times in the order of seconds have been achieved.

Zusammenfassung

In sicherheitskritischen Anwendungen werden opto-chemische Sensoren gegenüber den herkömmlichen elektrochemischen Sensoren aufgrund einiger besonderer Vorteile bevorzugt: ihre intrinsische Medientrennung, ihre Eignung für raue Umgebungen und ihre elektromagnetische Störunanfälligkeit. Diese Doktorarbeit beschäftigt sich mit opto-chemischen Sensoren deren Funktion auf den Absorptionseigenschaften von Flüssigkeiten im infraroten Bereich und / oder auf Photolumineszenz von Nanostrukturen in flüssigen oder gasförmigen Medien beruhen. Ihre Anwendung liegen hierbei im Bereich der Flugsicherung und der intelligenten Wartung ziviler Verkehrsflugzeuge.

Kapitel 1 konzentriert sich auf die Überwachung chemischer Verunreinigungen in Phosphatester basierten Hydraulikflüssigkeiten. Durch das Einbringen der Sensoren im Flugzeug, können hierbei wichtige Verschmutzungsparameter erfasst werden ohne Flüssigkeitsproben aus dem unter Druck stehenden Hydrauliksystem entnehmen zu müssen. Durch wiederholte Messung der Hydraulikflüssigkeit, können Abnutzungstrends der Flüssigkeit erfasst und Wartungsaktionen anberaumt werden, bevor irreversibler Schaden an der Flüssigkeit oder am Hydrauliksystem auftritt. Durch die Durchführung der Wartungsarbeit zu einer geplanten Zeit, an einem geplanten Ort, können teure Stillstandszeiten minimiert und erhebliche Kosten, wie sie durch außerplanmäßige Reparaturen entstehen, vermieden werden. Die chemischen Eigenschaften der im Flugbetrieb eingesetzten Hydraulikflüssigkeiten und ihre Abnutzungsmechanismen werden im ersten Teil des Kapitels beschrieben. Im Anschluss werden Ergebnisse einer Fourier Transform Infrarotmessung von Hydraulikflüssigkeiten mit unterschiedlichen Verschmutzungs- und Degenerationsgraden präsentiert. Die Ergebnisse zeigen, dass der freie Wasseranteil und die Total Acid Number (TAN) von Veränderungen des O-H Gruppen Streckresonanzbandes im Bereich von 3200 cm^{-1} - 3800 cm^{-1} abgeleitet werden kann. Auf Basis dieser Erkenntnis wurde ein Mit-infrarot Sensorsystem (MIR) entwickelt, welches es ermöglich diese Parameter online, innerhalb eines betriebsfähigen Hydrauliksystems zu überwachen. Um Durchflusseinschränkungen im Hydrauliksystem zu vermeiden, wird auf Basis von Oberwellenschwingungen eine Erweiterung des MIR Sensorprinzips auf den Nahinfrarotbereich (NIR) vorgestellt. Die Wirkungsweise dieses Sensorsystems wird durch einen Partikelsensor ergänzt, der nach dem Prinzip einer Lichtschranke funktioniert. In Kombination ermöglichen es beide Sensoren alle praktisch relevanten Verschmutzungsparameter im Flugzeug oder in einem versorgungsfahrzeug auf dem Rollfeld direkt online zu überwachen.

Kapitel 2 stellt ein voll-optisches Sensorsystem unter Verwendung von InGaN/GaN Nanowire Heterostructuren (NWH) als opto-chemische Wandler zur Gasdetektion vor. Dieses Wandlerprinzip ist für sicherheitskritische Anwendungen wie z.B. Lecks in Kraftstoff- oder Hydraulikleitungen, die eine zuverlässige Medientrennung benötigen, am besten geeignet. Die Intensität der Photolumineszenz der Nanostruktur wird hierbei durch die Anwesenheit von Wasserstoff und kohlenwasserstoffhaltigen Gasen verstärkt bzw. in Anwesenheit oxidierender Gase wir Sauerstoff, Stickstoffdioxid oder Ozon reduziert. Das Kapitel beginnt mit einer Beschreibung möglich Gassensoranwendungen im Flugzeug. Im Anschluss wird die Theorie bezüglich der Gassensormechanismen von Nanowires erläutert. Danach wird das Verfahren zum Wachstum von III-Nitrid-basierten Nanowires vorgestellt und ein Lichtwellenleiter basiertes Sensorsystem vorgestellt, das Nanowires als opto-chemische Wandler einsetzt. Dieser experimentelle Abschnitt beschreibt zudem den Testaufbau, der zur Bestimmung der Sensorperformance verwendet wurde. Die Vorstellung der experimentellen Ergebnis gliedert sich in 2 Teile: Der erste Teil konzentriert sich auf die Ergebnisse, die mit Wasserstoff und kohlenwasserstoffhaltigen Gasen erzielt wurden, während der zweite Teil das Sensorverhalten bezüglich verschiedener Oxidationsgase behandelt. Hierbei werden Nachweisgrenzen von 200 ppb bei 50°C für Wasserstoff und von 10 ppb bei Raumtemperatur für Ozon aufgezeigt. Zudem wird im Detail über die Einflüsse von Temperatur- und Feuchtevariationen berichtet.

Kapitel 3 beginnt mit einer kurzen Vorstellung der Anforderungen der pH-Wert Überwachung im Flugzeug. Eine besonderes interessante Anwendung ist hierbei die Überwachung des pH-Wert von Trinkwasser, welches On-board aus einer Brennstoffzelle generiert wird. Danach werden GaN/InGaN Quantum Dots (QDs) und ihre mögliche Anwendung zur Bestimmung von ph-Wert Änderungen in Flüssigkeiten beschrieben. Der entsprechende Sensormechanismus wird kurz vorgestellt und im Anschluss wird der Versuchsaufbau beschrieben. Im Ergebnisteil wird die Veränderung der Photolumineszenzintensität bei elektrischer Vorspannung und bei variablen pH-Werten in einem flüssigen Medium nachgewiesen. Der Messbereich erstreckt sich hierbei von pH=7 bis pH=2. Hierbei werden Auflösungen von unter 0.1 pH und Antwortzeiten in der Größenordnung von Sekunden erreicht.

Declaration

I herewith declare that I have produced this paper without the prohibited assistance of third parties and without making use of aids other than those specified; notions taken over directly or indirectly from other sources have been identified as such. This paper has not previously been presented in identical or similar form to any other German or foreign examination board.

The thesis work was conducted from 05/2008 to 04/2012 under the supervision of Prof. Martin Eickhoff at Justus Liebig Universität, Gießen and Dr. Gerhard Müller at EADS Deutschland GmbH, Ottobrunn.

Gießen,

Contents

Introduction

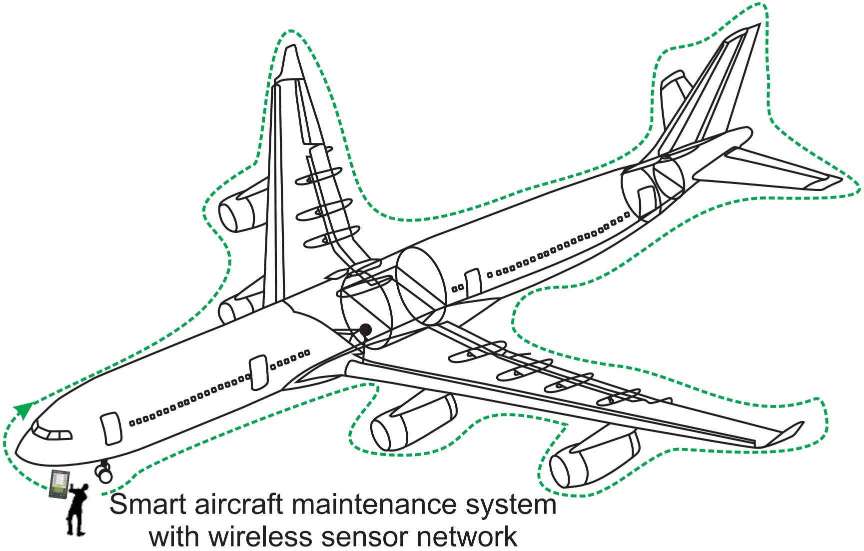

Innovation has long been a hallmark of the aerospace and defense industry in achieving unprecedented technical advances for the fields of science and engineering. To cope up with challenging demands such as, soaring number of passengers, improving fuel efficiency, reducing environmental impacts etc. the ever-growing aerospace industry remained the the epitome of several innovations. Over the years safety, security, reliability, comfort and maintenance costs are key areas where quality is crucial in the judgment of an aircraft. Different sensors play the role of key components to address these essential issues. The industry is always pursuing its quest for novel sensing materials and technologies to ensure that air travel continues to be one of the safest and greenest means of transportation. The principle aim of this thesis is to explore the potential of optochemical sensors which can address these issues like safety, security, passenger comfort, smart maintenance and environment friendliness. The application areas and the solution possibilities which have been assessed in this thesis are briefly described in the following sections.

Potentials in aerospace applications

1. **Hydraulic fluid monitoring**
   Key aspects: ***smart maintenance and increased safety***
   Most of the mechanical systems in large commercial aircrafts, such as flight controls, brakes, landing gears, etc, are driven by hydraulic actuators. For instance, a short haul carrier like Airbus A320 has three continuously operating hydraulic systems,

each containing 60 liters of hydraulic fluid. At present, assessing the condition of the hydraulic fluid in an aircraft is laborious, time-consuming and expensive. Therefore, the fluid is typically tested less than once a year with the risk of unscheduled maintenance if the fluid has exceeded its limits of usage. Consequential interruption of the airline service bears a huge economic cost. In current aircraft maintenance procedure hydraulic fluid is to be tapped using a dedicated sampling valve, fluid samples to be taken and sent to dedicated laboratories for off-site analysis. Time to get analysis results is typically a few days. Maintenance actions therefore can only be taken after several days of delay. This current situation of fluid monitoring can be ameliorated in case on-line measurements become possible. "On-line" in this case means that the hydraulic system needs not to be tapped and that the results of a measurement are available on-site immediately.

In this thesis an integrated sensor system is presented which can evaluate the state of the fluid on-line. This sensor can be implemented in the high pressure hydraulic system for performing measurements of relevant fluid properties on board. Repeating such measurements on a daily or weekly basis, as for instance before take-off or after landing, a degradation trend can be established and a time limit may be estimated after which maintenance actions need to be taken. With this knowledge of the fluid health evolution, and useful fluid lifetime, maintenance actions on the hydraulic fluid can be strategically scheduled, i.e. made to coincide with other necessary maintenance actions. In this way unscheduled maintenance is avoided and a higher level of aircraft availability is ensured.

2. **Gas monitoring**
   Key aspects: *increased safety and security*
   Leak monitoring is required whenever hydrogen and hydrocarbon carrying installations are operated inside confined spaces. In an aircraft leak-monitoring is essential in fuel and hydraulic lines or fuel cells. In order to be useful as leak-monitoring devices, hydrogen and/or hydrocarbon sensors require high sensitivity, good selectivity and reasonably short response times. In addition, leak monitoring sensors should not form ignition sources by themselves when leaks have actually occurred and when potentially combustible atmospheres have already built up.

   A novel semiconductor nanosensor is presented in this thesis, which can be applied as a potential leak detection sensor.

3. **On - board water monitoring**
   Key aspects: *safety, economy, environment friendly*
   Implementing fuel cells inside aircrafts for power generation is widely addressed by all major aircraft manufacturers. Besides electricity, such fuel cells also produce water and oxygen-depleted air as by-products. Whereas the oxygen-depleted air can be used to prevent the build-up of potentially explosive air-fuel mixtures inside the fuel tanks, the by-product water can be used for drinking, cooking and washing onboard. Due to strict regulation in aviation industry, the pH of the water has to be monitored

> continuously. Therefore, aircraft manufacturers are interested in pH sensors which can operate in harsh environments like fuel cells and which can be operated without tiresome periodic regular calibration routines.

To summarize, the hydraulic fluid monitoring sensor can contribute to increasing the aircraft system integrity and to reduce maintenance costs. The gas sensors can help to improve flight safety and security. Last but not least, pH sensors can serve to make the aircrafts greener.

Chapter
1

Hydraulic fluid monitoring

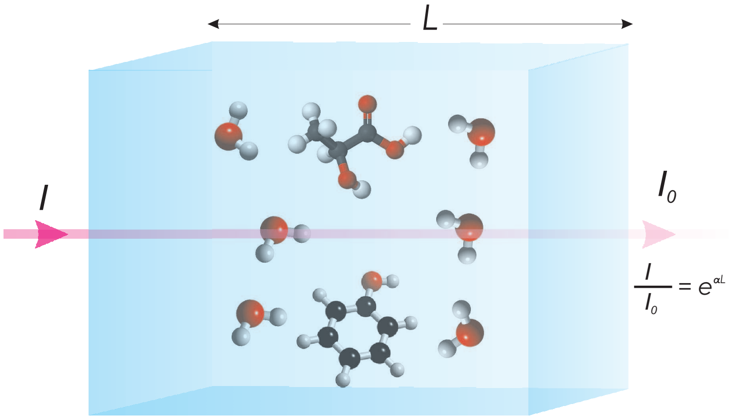

In an aircraft the hydraulic system is the power delivering mechanism for various safety-critical consumers ranging from landing gear to the elevator. Typical hydraulic system driven components of an aircraft are illustrated in Fig. 1.1. The operation of commercial aircrafts relies on the smooth and reliable functioning of this large number of hydraulic actuators. The hydraulic system therefore forms an important and safety-critical subsystem of a commercial aircraft.

In the early days of aviation, hydraulics was limited to simple brake systems using castor oil and natural rubber seals. Such simple systems lasted for a number of years until higher demands on actuator systems emerged. In particular, the demand for higher hydraulic system pressures soon exceeded the capability of simple castor oil. This caused manufacturers to change to petroleum-based fluids and neoprene seals, a technology which was widely used in World War-II aircrafts. Fires and explosions in aircrafts with petroleum-based hydraulic fluids, soon generated a general quest for innovative, fire-resistant hydraulic fluids. By the beginning of the 1950's the first commercial phosphate ester based hydraulic fluid became available. By the end of the 1950's almost all civilian jet aircraft were operating with phosphate-ester-based fluids, a situation which still persists up to the present day.

Hydraulic fluids based on phosphate-esters are hygroscopic [1] and their chemical properties are highly dependent on operation conditions. As a result, their lifetime is highly

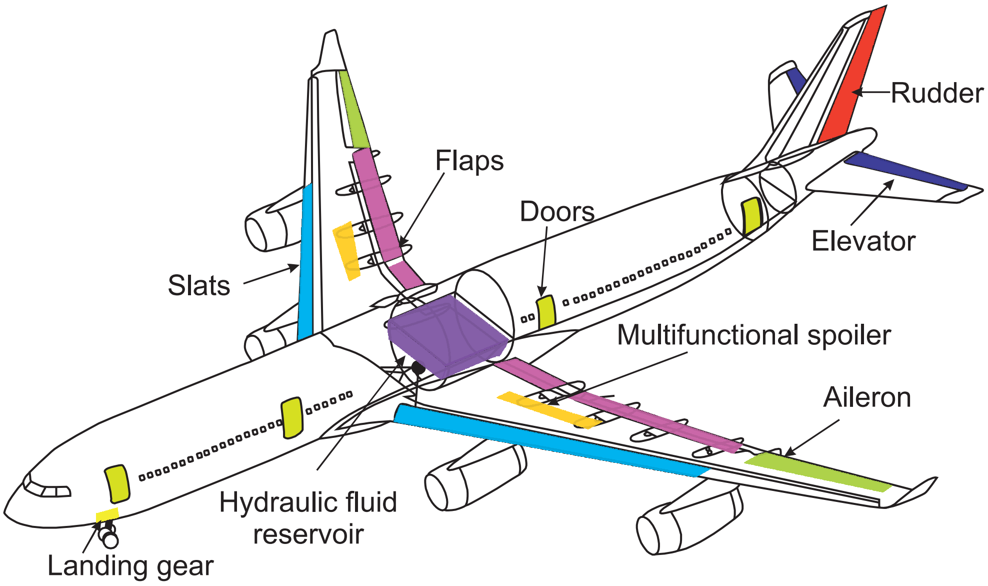

Figure 1.1: *Typical hydraulic system driven components of a civil aircraft is shown in this figure. Different colors of actuators indicate different functional units. Frequent hydraulic fluid health monitoring can ensure better system reliability.*

unpredictable. The performance of the entire aircraft hydraulic system is affected by the condition of the hydraulic fluid and if chemical degradation goes undetected, it may cause downstream mechanical damage to the hydraulic system itself and to its consumers such as flight controls or the landing gears. The damage may be economic at best or catastrophic at worst.

1.1 Properties of aviation hydraulic fluids

Phosphate-ester-based fluids have found wide-spread applications not only in aeronautics but also in a much wider range of industries wherever fire hazards exist and where safe working environment needs to be assured. Aviation hydraulic fluids must be extremely reliable and able to withstand high specific loadings and extreme environmental conditions. The chemical composition of such fluids is largely determined by the requirements of fire resistance, low-mass density, and good low-temperature performance.

1.1.1 Chemistry of aviation hydraulic fluid

Esters, in general, are produced by the reaction of acids and alcohols [2]. Phosphate-esters are esters formed from alcohols and phosphoric acid. General structure of phosphate-ester is illustrated in Fig. 1.2.

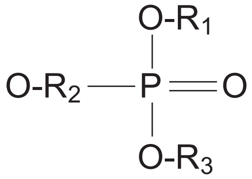

Figure 1.2: *Chemical structure of phosphate-ester; R represents the hydrocarbon substituents.*

Common reaction routes proceed through the reaction of phosphoryl chloride ($POCl_3$) with phenol (ArOH) or alcohol (ROH), or, less commonly, sodium phenoxides/alkoxides (RONa), as indicated in the following reaction paths:

$$3ROH + POCl_3 \rightarrow (RO)_3PO + 3HCl \tag{1.1}$$

$$3ArOH + POCl_3 \rightarrow (ArO)_3PO + 3HCl \tag{1.2}$$

$$3RONa + POCl_3 \rightarrow (RO)_3PO + 3NaCl \tag{1.3}$$

where, R is an alkyl group and Ar is an aryl group.

Fire-resistant hydraulic fluids mainly consist of neutral tri-alkyl-phosphates, tri-aryl-phosphates and mixtures of alkyl-aryl-phosphates [3]. Alkyl groups are mainly formed with a chain length of C_4-C_{10} (e.g. tri-butyl phosphate). In alkyl-aryl-phosphates alkyl-groups are partially substituted by phenyl-groups until eventually purely aromatic aryl-phosphates are obtained. Chemical structures of commonly used alkyl-aryl-phosphates are illustrated in Fig. 1.3.

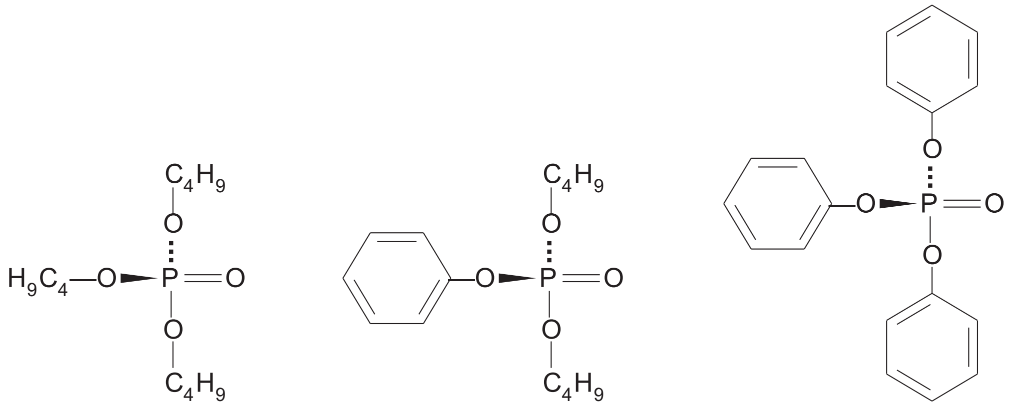

(a) (b) (c)

Figure 1.3: *Chemical formula of constituents of aircraft certified hydraulic fluids; a.)Tributyl phosphate b.)di-butyl phenyl phosphate c.)Triphenyl phosphate.*

Whereas the phosphate nucleus largely determines the fire resistance of the fluid, the other physico-chemical properties are mainly determined by the hydrocarbon side-groups. The weight ratio of the alkyl- and aryl-groups, in particular, determines the average molecular weight, the specific gravity and the viscosity of the base fluid. Mixed aryl-alkyl phosphates are used in the aviation industry as they improve both the low temperature properties of the base fluid as well as their high-temperature stability [4]. Commercial aviation hydraulic fluid base stocks mainly consist of mixtures of tributyl phosphate, di-butyl phenyl phosphate and triphenyl phosphate [5,6], with the mixing ratio depending on the specific kind of application. The above constituents make up roughly 99% of the fluid. Aviation hydraulic fluids, in addition, contain around 1% additives [7]. These additives include antioxidants, antiwear- and viscosity index improvers, and also minor amounts of metal deactivators and dyes [8].

One of the most widely-used aviation hydraulic fluids is Skydrol LD4, produced by Solutia Inc. The main constituents of the fluids according to material safety data sheet are presented in the following table.

Substance	**w/w (%)**
Tributyl phosphate	58.2%
Dibutyl phenyl phosphate	20 - 30%
Butyl diphenyl phosphate	5-10%
2,6-di-tert-butyl-p-cresol	1-5%
Cyclic Epoxy Ester	≤10%

Table 1.1: *Chemical composition of a widely used hydraulic fluid Skydrol LD4 [6].*

1.1.2 Degradation mechanism

The degradation of phosphate-esters can be explained by three different reaction pathways: pyrolysis, oxidation and hydrolysis. The environmental condition to which the fluid is exposed in the aircraft determines which degradation mechanism dominates. All these degradation mechanisms produce acid as the main degradation product. Thermal degradation or pyrolysis occurs only temperatures above 150°C, which is normally not encountered in aviation hydraulic system. During this process, the alkyl groups break up from the parent molecules and form unsaturated hydrocarbons (e.g. butane). In general, phosphate-esters exhibit a high resistance to oxidation. Moreover, the availability of free oxygen in hermetically designed aviation hydraulic system is very low. Oxidation, therefore, does not play a major role as a degradation process.

Phosphate-ester fluids are polar and they tend to absorb water. Such dissolved water can cause disintegration of the phosphate-ester molecules through hydrolysis.

$$Ester + H_2O \overset{Heat}{\longrightarrow} Alcohol + Organic\ acid \tag{1.4}$$

The above reaction leads to the formation of weak organic acids. The phosphate-esters themselves can also form strong acids through the reaction:

$$Phosphate - Ester + H_2O \overset{Heat}{\longrightarrow} Alcohol + H_3PO_4 \tag{1.5}$$

The generation of alcohols can ultimately lead to gas bubbles that compromise the force-transmitting properties of the fluid. Phosphorus acid molecules, on the other hand, can interact with dissolved water to form H_3O^+ ions, which may induce corrosion.

$$3H_2O + H_3PO_4 \leftrightarrow 3H_3O^+ + PO_4^{-3} \tag{1.6}$$

The hydrolysis of a phosphate-ester-based fluid is schematically illustrated in Fig. 1.4. It indicates that, in addition to water, acid formation also requires a significant amount of thermal agitation.

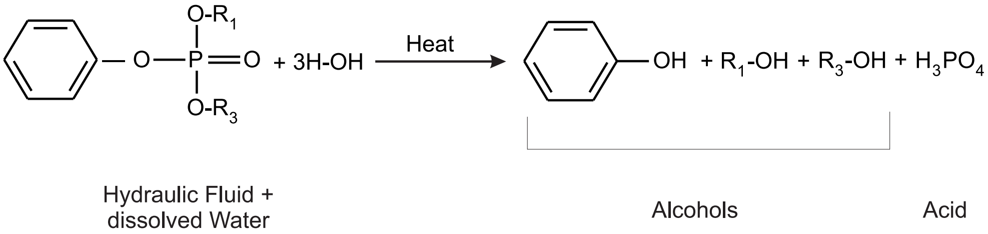

Figure 1.4: *Chemical reactions following the take-up of water into a phosphate-ester based hydraulic fluid. During hydrolysis the phosphate-ester molecule is disintegrated into alcohols and acid.*

1.1.3 Contamination parameters

Contamination in the hydraulic system can affect the performance of both the hydraulic fluid and the system components.The contamination parameters of interest to be monitored are:

A. Water content

Due to their hygroscopicity, water vapor can become dissolved in all kinds of phosphate-ester based hydraulic fluids. Such "free water" can freeze and produce blockages and thus cause mechanical damage inside pumps and actuators [9]. In normal operation, free water is removed by means of a water separation unit and it is discarded once the engines and the Auxiliary Power Unit (APU) have been switched off. In tropical and subtropical countries with high humidity climate, control units are normally not switched off overnight, even so water absorption cannot be discarded. In such cases the amount of dissolved water may easily rise to and beyond a critical level ($\approx 0.8\%$ by weight).

B. Acidity

Under conditions of thermal agitation, "free water" can react with phosphate-ester-based fluids by means of hydrolysis. Upon disintegration of the base fluid, various kinds of alcohols are formed alongside with phosphorus acid molecules [10]. The phosphorus acid molecules, in turn, may dissociate in the remaining dissolved water and form phosphoric acid, which is corrosive and likely to inflict damage on all kinds of metallic components inside the hydraulic system. Especially, such corrosion damage can have adverse consequences if it occurs on the sharp edges of tightly fitting parts inside hydraulic actuators. The dissolved alcohols, on the other hand, can form gas bubbles and thus compromise the functioning of some equipments. For these reasons, acidity is the key parameter that defines fluid life.

The Total Acid Number (TAN) is the measure of acidic species present in the fluid. The unit is mg KOH/g, which indicates the amount of KOH (in mg) required to neutralize 1 g of fluid. Aircraft manufacturers typically recommend a maximum TAN of 1.5 mg KOH/g.

C. Dissolved air

In case of system pressure drop, dissolved gases can form bubbles, causing cavitation and compromising the force transmitting properties of the fluid. Air in the system will also result in oxidation of the fluid.

D. Chlorine

Although progressively being phased out for environmental and toxicological reasons, chlorinated solvents - inadvertently introduced during cleaning procedures can interact with the free water contamination in the fluid and release chlorine ions. Sodium chloride aerosols are often formed on warm coastal cities and the ions may dissolve in moist fluid. The resulting chlorinated aqueous solutions are highly corrosive and may cause corrosion damage on all kinds of mechanical components of the hydraulic system. The 'In service' limit of chlorine contamination is $\leq$ 200 ppm.

E. Particulate matter contamination

Once the fluid has become corrosive by chemical degradation, it may attack all kinds of metallic parts inside the hydraulic system. Corrosive attack tends to generate particle contamination in the fluid and the freed particles in turn may cause downstream mechanical damage as they are transported through the many narrow constrictions inside hydraulic actuators. In this sense particle contamination monitoring complements the monitoring of the chemical parameters A) - D).

In the following, evidence is presented that it is possible to assess the take-up of water (parameter A) and the subsequent hydrolysis of the base fluid and the concomitant generation of acidity (parameter B) as the fluid becomes additionally exposed to Joule heating. It is further shown that both parameters can be assessed with the help of a non-dispersive infrared (NDIR) sensor system through optical windows, i.e. without tapping fluid from a pressurized hydraulic system.

1.1.4 State of the art for hydraulic fluid monitoring

At present, assessing the condition of the hydraulic fluid in an aircraft is laborious, time-consuming and expensive. Therefore the fluid is typically tested less than once a year with the risk of unscheduled maintenance if the fluid has exceeded its limits of usage. Consequential interruption of the airline service bears a huge economic cost. The current state of the art in aircraft maintenance is that hydraulic fuel testing is carried out off-line. "Off-line" meaning that the hydraulic system needs to be tapped using a dedicated sampling valve, fluid samples to be taken and sent to dedicated laboratories for off-site analysis. Time to get analysis results is typically a few days and therefore, maintenance actions can only be taken after several days of delay.

1.1.5 Scopes for improvements

The current situation of fluid monitoring can be ameliorated in case on-line measurements become possible. "On-line" in this case means that the hydraulic system does not need to be tapped and that the results of a measurement are available on-site immediately. Performing measurements of relevant fluid properties on board and repeating such measurements on a daily or weekly basis, as for instance before take-off or after landing, a degradation trend can be established and a time-limit may be estimated after which maintenance actions need to be taken. With this knowledge of the fluid health evolution, and useful fluid lifetime, maintenance actions on the hydraulic fluid can be strategically scheduled i.e., made to coincide with other necessary maintenance actions. In this way unscheduled maintenance is avoided and a higher level of aircraft availability is ensured.

1.1.6 Motivation for using infrared absorption monitoring

In organic chemistry, infrared (IR) absorption is regarded as an invaluable tool for structure determination and verification. One of the most distinctive and easily recognizable peaks in IR-absorption is the O-H structure due to stretching and bending vibrations. This absorption band has a wide range of applications in sensor systems.
The preferance of IR-absorption monitoring for chemical detection can be justified by the following reasons:

- **Non destructive:** IR absorption does not cause damage or chemical change to the sensing medium.
- **Media separation:** The sensing elements and electronics never come in direct contact with hazardous sensing medium.
- **High sensitivity:** IR spectroscopy is preferred for its capability of detecting contamination in sub ppm to percentage region.
- **High selectivity:** Molecules consisting of two or more dissimilar atoms absorb infrared radiation in a unique manner and are detectable using infrared techniques.
- **Simplicity in sample preparation:** Samples being viewed do not require any sort of special preparation.
- **Ease of instrumentation:** IR based sensor system can be implemented with very simple mechanical setups and the low cost IR elements are widely commercially available.

As a result, there is virtually an unlimited number of applications for which the IR-absorption technology can be used.

1.1.7 Previous applications of IR technology in oil condition monitoring

In recent years there have been a number of reports on oil condition monitoring sensors using infrared (IR) absorption as a working principle. The work reported so far has focused on transformer, lubrication and engine oils, which are in wide-spread commercial use. Other reports have focused on mineral oil based hydraulic fluids, which are widely applied in ground-bound heavy machinery and in the tooling industry.

All of the below-mentioned work makes use of the fact that there are several IR absorption lines available which are indicative of water, oxidization, sulfation and alcohol contaminations in the base fluid. Kudlaty et al. (2003), for instance, have reported on an IR absorption sensor for industrial lubrication oils based on the principle of Attenuated Total Reflection (ATR) monitoring [11]. Adams (2007) reported on the Fourier Transform Infrared (FTIR) analysis of lubrication oils for antioxidant and acidity detection [12]. Agoston et al. (2008) used an online sensor assembly consisting of an incandescent IR emitter, an IR detector and a narrowband IR filter for evaluating the oxidation number of oils by monitoring the absorption within a selected IR band and a reference band [13]. Kasberger and Jakoby (2007) introduced a new design for an integrated, online lubrication oil sensor system based on a mono-mode IR waveguide, which can be fabricated in thin film technology [14].

Dedicated research on aviation hydraulic fluids, which is the subject matter of this thesis has not yet been reported.

1.2 Mid infrared based chemical contamination monitoring

Infrared spectroscopy provides a fast and effective way to identify functional group present in a molecule by observing the related absorption bands. The infrared spectrum is divided into different regions, which is depicted in Fig. 1.5.

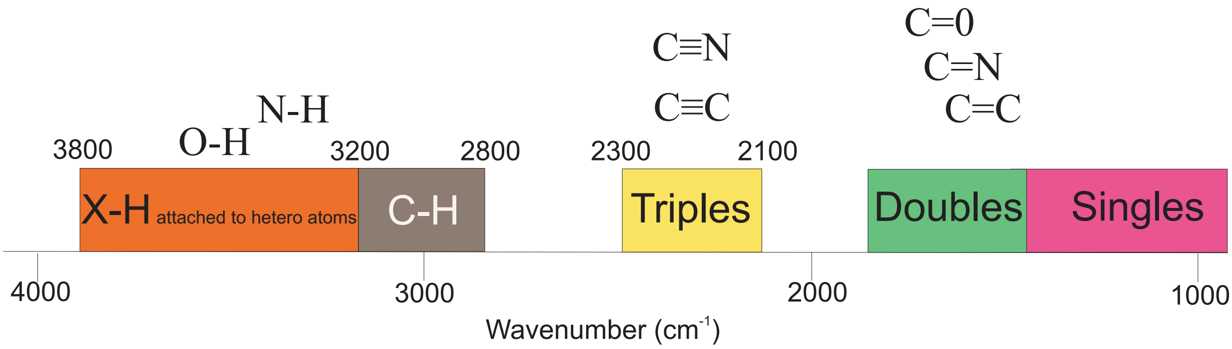

Figure 1.5: *Mid infrared molecular absorption bands. O-H vibration bands lie in the range of 3200 cm^{-1} to 3600 cm^{-1} [15].*

The highest energy region from 3800 cm^{-1} to 2800 cm^{-1} is also known as the hydrogen region. Absorption due to O-H, N-H and C-H bond stretches occur here. These absorption bands are very high in energy because hydrogen is a very light atom. The polar bonds are generally stronger than the non-polar bonds and thus absorb at higher frequencies (C-H<N-H<O-H). The C-H bond strength varies slightly due to the hybridization of the carbon atom increasing in the orders (sp^3 $\approx$ 3000 cm^{-1}, sp^2 $\approx$ 3080 cm^{-1}, sp $\approx$ 3300 cm^{-1}). The bonds involving heavier atoms absorb at lower energies [16].

In the triple bond region from 2300 to 2100 cm^{-1}, absorption due to C≡N and C≡C triple bond stretches occur. The weaker double and single bond stretches occur at lower wavenumber. In the single bond region from 1500 to 500 cm^{-1} absorption due to single bond stretching and bending occurs. Due to the high number of bands in this region, they are difficult to be assigned to specific vibrations. However, the large number of bands makes this region useful for comparing spectra and so this is known as fingerprint region.

Fig. 1.6 illustrates the Fourier Transform Infrared (FTIR) absorption spectra of a thin film of Skydrol LD4 - a special kind of phosphate-ester fluid. The spectra were recorded in transmission mode, using a Thermo Scientific Nicolet iS10 FTIR spectrometer. The custom made cuvette for the fluid samples consisted of KBr pressed discs with a 200 μm spacer between them. The instrument was suitably purged with nitrogen gas and 50 'scans' were acquired for each spectrum, at a resolution of 2 cm^{-1}. Careful consideration of Fig. 1.4 reveals that in the degradation interaction with water, the number of O-H bonds is conserved. A second point to note is that the O-H groups are initially associated with water and after hydrolysis with various kinds of alcohols. A further interesting point to note is that such different kinds of O-H groups can be distinguished on account of their different infrared absorption properties [11,12,17–19]. Alcohols exhibit O-H absorption features that are low-frequency-shifted towards smaller wavenumbers than for the polar water molecules.

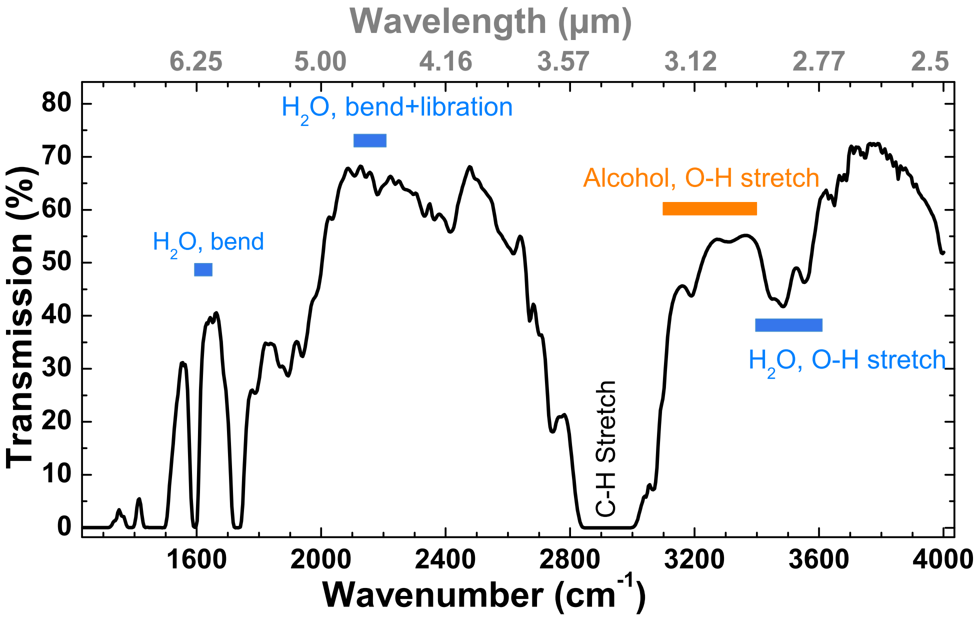

Figure 1.6: *FTIR spectrum of Skydrol LD4 - a widely used aviation hydraulic fluid; absorption path length: 200 µm, prominent O-H and C-H vibration bands can be observed.*

This is the case for butanol and phenol, i.e. disintegration products of typical hydraulic fluids. From the above discussion, we can summarize that the presence of dissolved water and the trend of disintegration products of phosphate-ester based hydraulic fluids may be detected by monitoring the intensity and the spectral distribution of the O-H absorption feature in the wavenumber range between 3200 cm^{-1} and 3700 cm^{-1}.

1.2.1 Optical monitoring of chemical changes in water-contaminated and thermally treated Skydrol LD4

Following the above ideas a series of experiments was performed to assess the infrared absorption characteristics of Skydrol LD4 samples in its pure state, after the addition of various amounts of water and after performing additional heat treatments. In this way it was attempted to arrive at a set of optical features that allow the state of contamination and degradation to be assessed by purely optical means. As a first result we present in Fig. 1.7 FTIR spectra of water-contaminated samples of Skydrol LD4. Whereas very low O-H absorption feature is present in pure Skydrol, a broad O-H feature, centered around 3500 cm^{-1}, is observed in water-contaminated samples. This figure shows that water addition is associated with a strong and continuous increase in the O-H absorption band centered around 3500 cm^{-1}. Smaller, but similar changes can also be observed around 1600 cm^{-1} and 2100 cm^{-1}. These latter two absorptions result from rocking and bending vibrations of the H_2O molecules. As the changes in optical transmission at around 3500 cm^{-1} clearly scale with the amount of added water, the dissolved water content in Skydrol LD4 can easily be determined by means of IR absorption. The optical path length in this case was 0.2 mm, i.e. a narrow gap. Titration of these water-contaminated samples

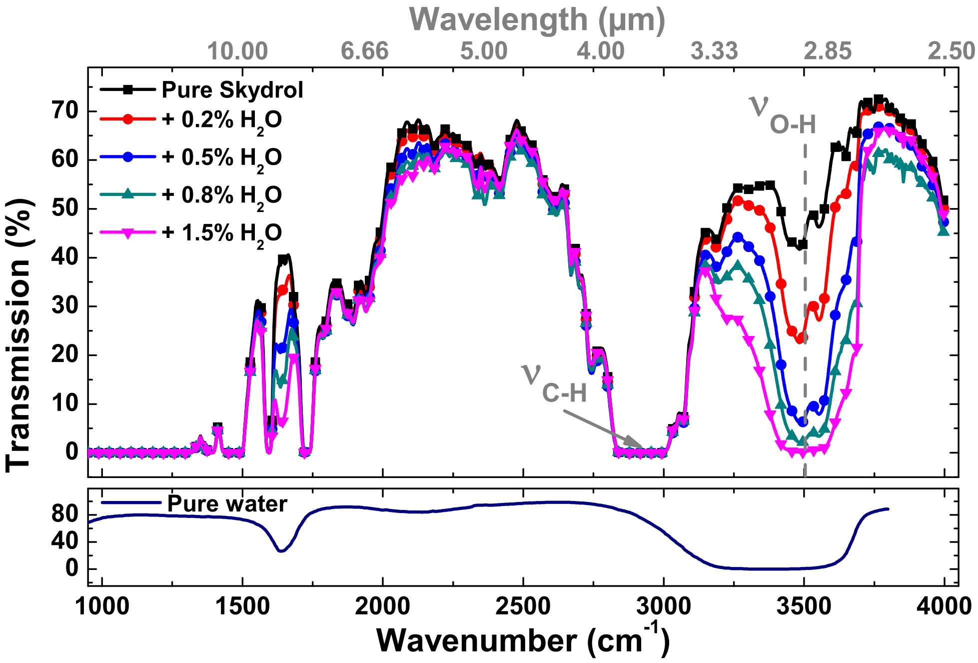

Figure 1.7: *IR transmission spectra of pure and water-contaminated samples of Skydrol LD4; optical path length: 0.2 mm; increasing water contamination causes increased absorption around 3500 cm^{-1} center line. As a comparison, the spectrum of pure water measured using a capillary film is shown below [20].*

further revealed that such fluids are not acidic. Neutralization in each case was obtained with less than 0.1 mg KOH/g Skydrol LD4.

In a hydraulic system Joule heat is generated when the fluid is pressed through the many narrow constrictions inside hydraulic actuators. In order to simulate this situation, boiling temperatures beyond the normal operation range had been used to accelerate acidity generation in our laboratory tests [21]. To this end the above fluid samples were boiled at 200°C for 8 h in glass flasks with tightly fitting glass seals. After heat treatment the same set of measurements, i.e. IR absorption and titration for the TAN values were repeated.

The effect of heat treatment on the water absorption line at around 3500 cm^{-1} is shown in Fig. 1.8. Spectrum a and b represent the state before heat treatment. Whereas c,d and e show the effect of an additional heat treatment. TAN values in this latter case have been raised into the range between 1 and 2 mg KOH/g. For the sake of comparison we have also introduced three columns that delineate narrow spectral regions that embrace the water O-H absorption feature. In the first case of dissolved water (a and b) the O-H absorption feature is more or less symmetric with respect to the center line independent of the water content. In the second case (c, d and e), when there was an additional input of heat, the O-H absorption feature is clearly red-shifted towards lower photon energies. Additionally, the symmetry around 3500 cm^{-1} disappears in this case.

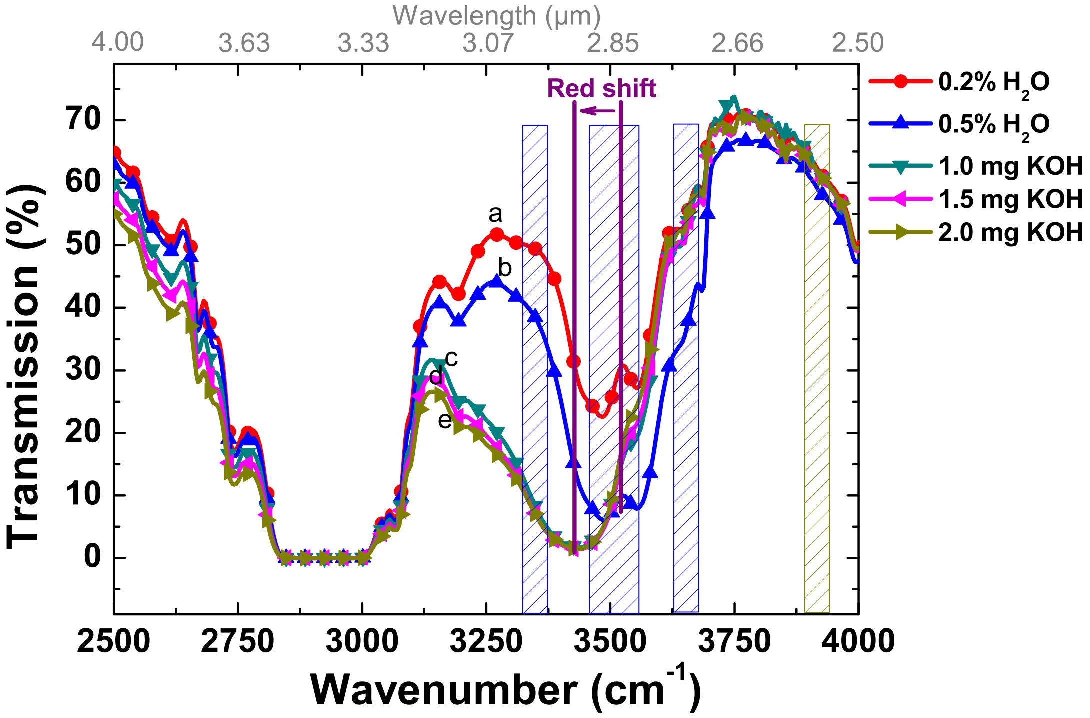

Figure 1.8: *IR transmission of water-contaminated and heat-treated Skydrol LD4; a, b after addition of increasing amounts of water; c, d, e after additional heat treatment leading to acidification. The O-H absorption lines of the heat treated samples get shifted to lower wavenumber region.*

The three bars in the middle of Fig. 1.8 represent the three measurement windows from which we want to determine the fluid quality and the fourth, the rightmost bar represents a reference window. Extensive tests have shown that in this latter spectral window the optical properties of the fluids are not influenced by any of the chemical changes in the fluid. This latter window can therefore be used to monitor the transparency of the sapphire windows and the brightness of the IR source.

1.2.2 Influence of additional phenol on FTIR spectrum

In order to reveal the reason for the red-shift of the O-H absorption feature, FTIR measurements were performed on pure samples of Skydrol LD4 to which additions of butanol and phenol had been added. These two kinds of alcohols are known to be main decomposition products of Skydrol hydrolysis. For comparison, additional fluid samples were prepared to which both alcohol and water were added. A result that was obtained on these latter kinds of fluid is shown in Fig. 1.9. These data clearly show that increasing phenol additions produce an increasing O-H absorption at around 3250 cm^{-1}. In comparison, additions of both water and phenol produce a double-peak structure with a first absorption peak at around 3500 cm^{-1} and a second one at around 3250 cm^{-1}. As the additional water dilution does reduce the TAN as revealed from titration but leave the phenol O-H absorption feature intact, it is clear that IR absorption measures the presence of hydrolysis products that have been formed in the course of an acidification process but not the acid itself.

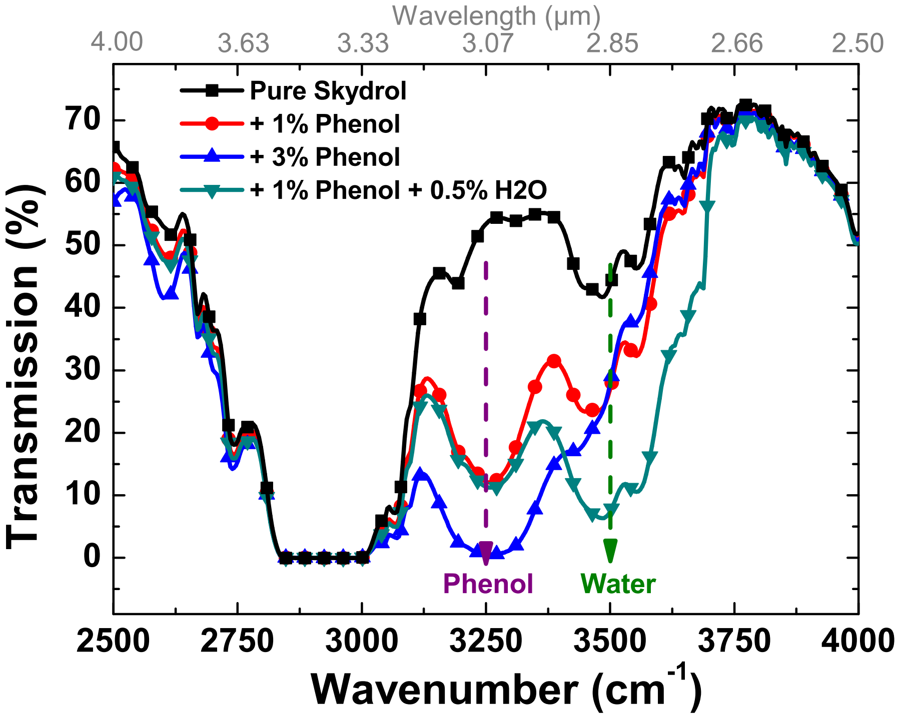

Figure 1.9: *IR transmission of Skydrol LD4 with different additions of phenol and a mixture of phenol and water. Phenol addition resulted in a red shift of the O-H vibration line.*

This same conclusion is further emphasized by an experiment in which fresh water had been added to an acid fluid sample (not shown in the figure). Deliberate additions of new water left the low wavenumber part of the O-H absorption feature largely unaffected, but added significant spectral weight on the high wavenumber side. This un-reacted water had a clear impact on the TAN of the fluid as the dissolved acid was diluted by the fresh water, not, however, on the presence or absence of hydrolysis products that had been generated in the preceding heat treatment. The spectroscopic data, therefore, do provide clues to the actual amount of free water that can still be removed by filtration and to the total amount of hydrolysis products that had been generated up to the point of measurement.

1.2.3 Optical absorption mapping of other hydraulic fluids

In the experiments reported above, low-density Skydrol LD-4 had exclusively been used. In addition to that, a whole number of other phosphate-ester based fluids are qualified for aircraft use. In aircraft operation also mixtures of those fluids may be used. A relevant question therefore is whether the method of optical transmission mapping, which had been developed for Skydrol LD-4, can also be applied to this larger group of fluids and possibly to mixtures thereof. Attempting to answer this question, the same range of measurements was repeated on samples of HyJet IV, HyJet A+ and Skydrol 500B. Table 1.2 shows the chemical composition of these fluids. In the following section, we will briefly show that these fluids exhibit strikingly similar IR spectra.

In Fig. 1.10 we present the IR spectra of a range of different phosphate-ester fluids both in

Content/property	Low Density			High density
	Skydrol LD4	**HyJet IV A+**	**HyJet V**	**Skydrol 500B**
Tributyl phosphate	58.2%	70-80%	70-80%	19.8%
di/-butyl phenyl phosphate	25-30%	-	-	50-70%
Triphenyl phosphate	-	<2.5%	<2.5%	-
ρ at 25^{o}C[g/cm^3]	1.009	0.996	0.997	1.057

Table 1.2: *Main constituents of aircraft certified hydraulic fluids [5, 6].*

their nominally pure and in their water-contaminated states. It shows that both data sets are remarkably similar. The two outstanding features in all kinds of fluids are a very strong C-H vibration line at around 2900 cm^{-1} and an O-H vibration line at around 3500 cm^{-1}. Whereas the first line is intrinsic to the fluids, the strength of the second line depends on the amount of water that had been added. The strength of this second line depends only very little on the kind of the base fluid that had been used for soaking up the water. The differences between the four base fluids, are very marginal at around 3500 cm^{-1} and moderate in their respective high- and low-energy wings. Similar data have been observed on the same range of fluid samples contaminated with other water concentrations.

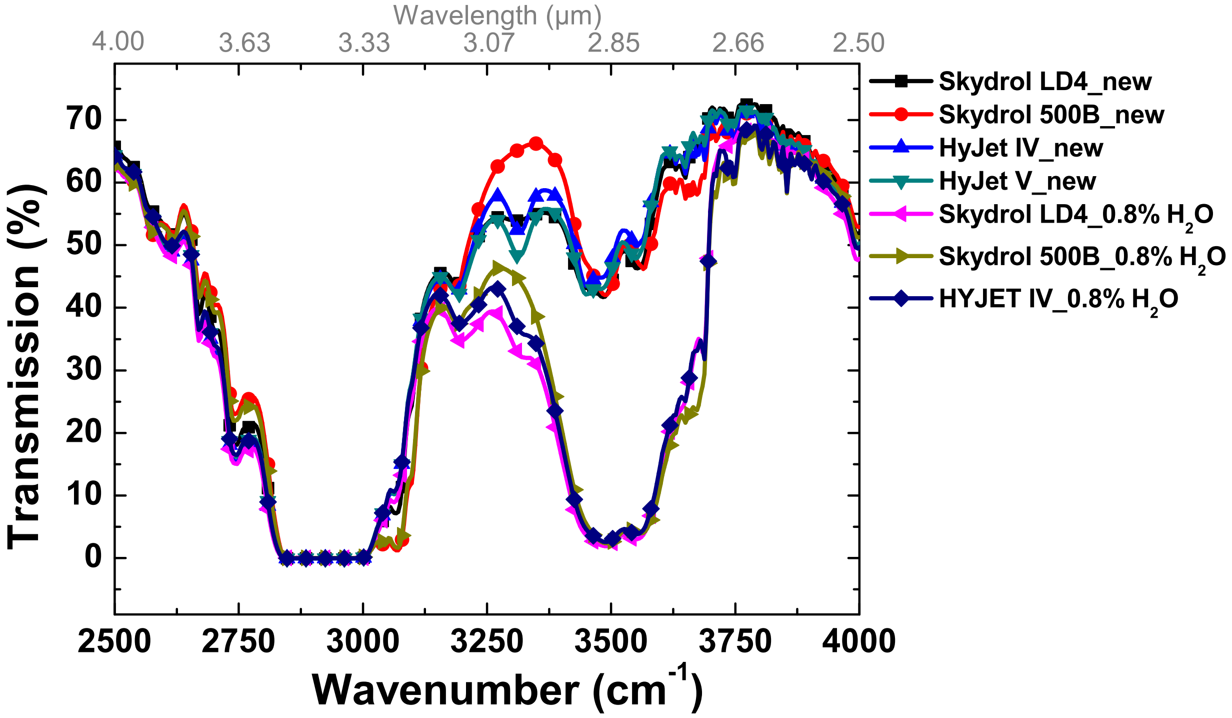

Figure 1.10: *IR spectra of different hydraulic fluids in their nominally pure state and after addition of 0.8% water. The absorption around 3500 cm^{-1} is determined by the amount of water present in the fluid. There is hardly any influence of the base fluid in this band.*

Transmission spectra of Hyjet V with different levels of acid and phenol contamination are presented in Fig. 1.11. Comparing these results with Figs. 1.8 and 1.9, it becomes evident that both fluids exhibit closely similar transmission spectra and that both behave in a very similar manner when they are heat-treated or when alcohols are added. Again hydrolysis induces the same kind of low-frequency shift of the O-H absorption feature. Phenol additions confirmed that the O-H shift is related to the same cause as in Skydrol LD4 (Fig. 1.9), i.e. formation of free alcohols.

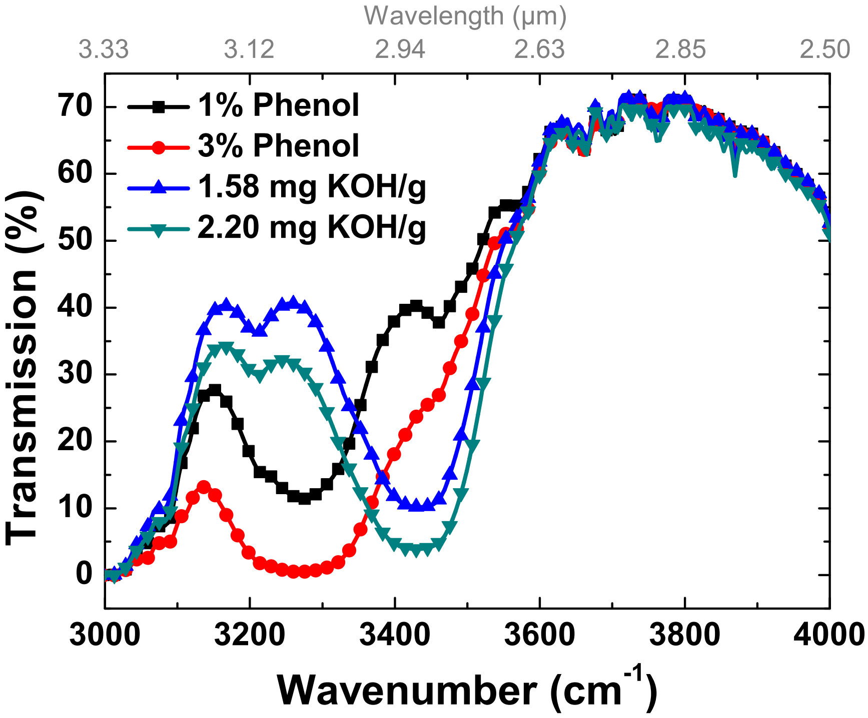

Figure 1.11: *IR spectra of hydraulic fluid "HyJet V" with different TAN or different levels of Phenol contamination. The absorption features are very similar to the data shown for Skydrol LD 4 in earlier sections.*

1.2.4 Neutralization test

In the previous sections it was shown that there is a clear correlation between the TAN value on the one hand and optical absorption features deriving from increasing alcohol contents on the other hand. Attempting to further test this correlation, neutralization tests were performed. In these tests samples were taken from a volume of acidic Skydrol with an initial TAN of 5.72 mg KOH/g and increasing amounts of either pure, distilled water or of 0.1 M KOH/H_2O solutions were added, until complete neutralization was obtained. The data in Fig. 1.12 show that additions of distilled water and diluted KOH produced similar spectral changes whereas, the TAN values of the mixed fluids, as derived from standard chemical titration, were quite different. The example below shows that an addition of 0.5% and 2.0% of 0.1 M KOH/H_2O decreased the TAN from 5.8 mg KOH/g to 5.3 and 2.70 mg KOH/g, respectively, while the addition of water left the TAN largely unaffected. Table 1.3 lists the TAN value of the examined samples.

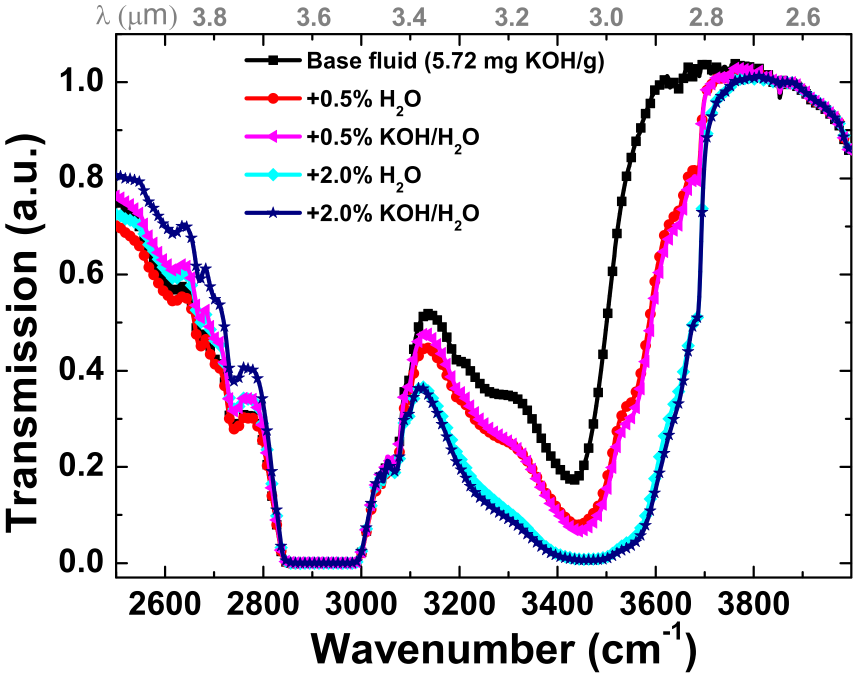

Figure 1.12: *Spectral analysis of the acid contaminated fluid samples diluted with distilled water and 0.1 M KOH/H_2O solution. Although addition of KOH/H_2O changed the TAN value of the fluids significantly, there was no remarkable change in the desired spectral area.*

As shown in Fig. 1.12, water peak around 3500 cm^{-1} show added spectral weight with additional water or KOH solution. The spectrum with same amount of added water or KOH solution are almost identical, although they had different TAN values. Addition of KOH resulted in the neutralization of phosphoric acid formed during the heat treatment of the water contaminated fluids according to the following equation:

$$3KOH + H_3PO_4 \rightarrow 3H_2O + K_3PO_4 \tag{1.7}$$

The alcohol formed during the hydrolysis process remains unchanged due to the addition of KOH or H_2O. Therefore, addition of same amount of H_2O or KOH resulted in almost

Fluid	TAN value [mg KOH/g]
Base fluid	5.72
+0.5% H_2O	6.2
+0.5% 0.1M KOH/H_2O	5.3
+2.0% H_2O	6.2
+2.0% 0.1M KOH/H_2O	2.7

Table 1.3: *TAN value of the base fluid and the neutralized fluids. Deionized water does not have big impact on the TAN value. Whereas, KOH/H_2O neutralizes the acidity significantly.*

identical spectrum, although the TAN value differed in the two solutions significantly. This kind of neutralization of hydraulic fluid is not a realistic case in a closed system.

1.2.5 TAN evolution: Heat treatment of the hydraulic fluids

In order to assess the effects of heat treatment and thermal degradation, three base samples with different TAN values were prepared. Sample 0 is fresh Skydrol with TAN = 0.12 mg KOH/g. Samples 1 and 2 were prepared by diluting a higher TAN solution (20 mg KOH/g) with different amounts of fresh Skydrol. Initially, all samples had water concentrations of less than 0.2%. To facilitate hydrolysis, distilled water was added to reach a concentration of 0.5%. As water is not readily soluble in Skydrol, the samples were treated in an ultrasonic bath to obtain reasonably homogenous mixtures. Thereafter the samples were heated at 180°C for 6 hours in two steps and FTIR spectra were recorded after each step. Fig. 1.13(a) presents the sample preparation steps schematically and Fig. 1.13(b) illustrates the color evolution of one sample after heat treatment. All fluid samples had the same initial clear purple color in the beginning. In the course of prolonged heat treatments these became increasingly darker. This increase in darkness indicates ongoing oxidation of the fluid. Fig. 1.13(b) shows that the purple color of Skydrol did not change after the first 6 hours of heating at 180°C. However, after repeating this process for a second time, the fluid turned significantly darker.

The evolution of TAN value for the three samples in all measurement steps is listed in Table 1.4. The FTIR spectra of the three fluid samples are illustrated in Fig. 1.14. The values are normalized with regard to the transmission at reference wavenumber 3900 cm^{-1}. At step M1, the samples are not intentionally water contaminated and therefore have almost identical absorption at 3500 cm^{-1}. The asymmetry in transmission of the two neighboring lines ΔTr (ΔTr= $Tr_{3650\ cm^{-1}}$ - $Tr_{3350\ cm^{-1}}$) increased as the TAN value of the samples raised. The change in spectrum due to water addition can be seen in Fig. 1.14(b). The increased absorption at 3500 cm^{-1} is caused by the added water. ΔTr is slightly reduced in this case. The Hydroxyl (-OH) groups in alcohol and water molecules are polar. A hydrogen bond is formed between the hydrogen of the -OH group of alcohol and oxygen of the water molecule. This reduces the polarity of the -OH group and thereby the transmission around 3350 cm^{-1}. This causes slightly less asymmetry between the two TAN sensing lines after addition of water. After heating the samples at 180°C for 6 hours, the TAN value of the samples increases significantly. As shown in Fig. 1.14(c), the center line of symmetry at

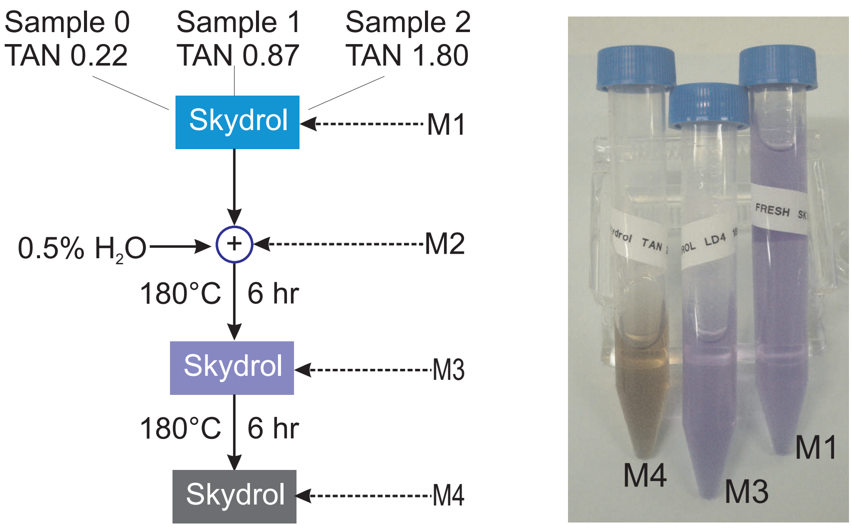

(a) (b)

Figure 1.13: *(a) Preparation and measurement steps performed to assess degradation processes in Skydrol LD4. Three initial samples with different TAN values were mixed with water and heated in two temperature steps: (b) Photograph of "Sample 0" taken after at prolonged heat treatment and degradation. Initially purple hydraulic fluids become dark when oxidized in the course of heating. The numbers M1-M4 refer to different steps of preparation indicated in Fig. 1.13(a).*

3500 cm^{-1} is red shifted for ca. 80 cm^{-1} due to higher degradation or additional alcohol formation.

Measurement Step/Sample	Sample 0	Sample 1	Sample 2
M1	0.22	0.87	1.80
M2	0.24	0.98	1.90
M3	2.40	6.50	4.40
M4	24.22	-	-

Table 1.4: *Evolution of TAN value for the three samples in different measurement steps.*

The TAN value rose to 2.44, 6.5 and 4.4 mg KOH/g for sample 0, 1 and 2 respectively. ΔTr for all three samples grew notably. The TAN value and ΔTr for samples with such a high TAN value do not follow a consistent relationship. The effect of second heat treatment of the sample is illustrated in Fig. 1.14(d). The TAN value of sample 0 rose by almost a factor of 10. The color of the fluid changed from purple to dark brown. Huge spectral weight was added to the region < 3000 cm^{-1}, which indicates the generation of additional C-H stretch bands. The O-H absorption is also further red shifted by about 250 cm^{-1}.

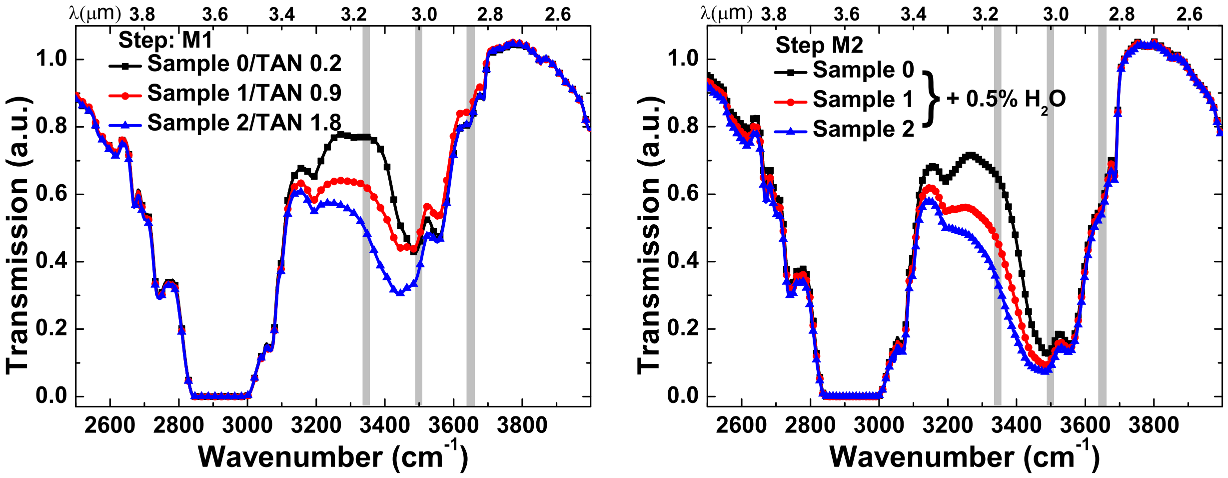

(a) Spectra at M1

(b) Spectra at M2

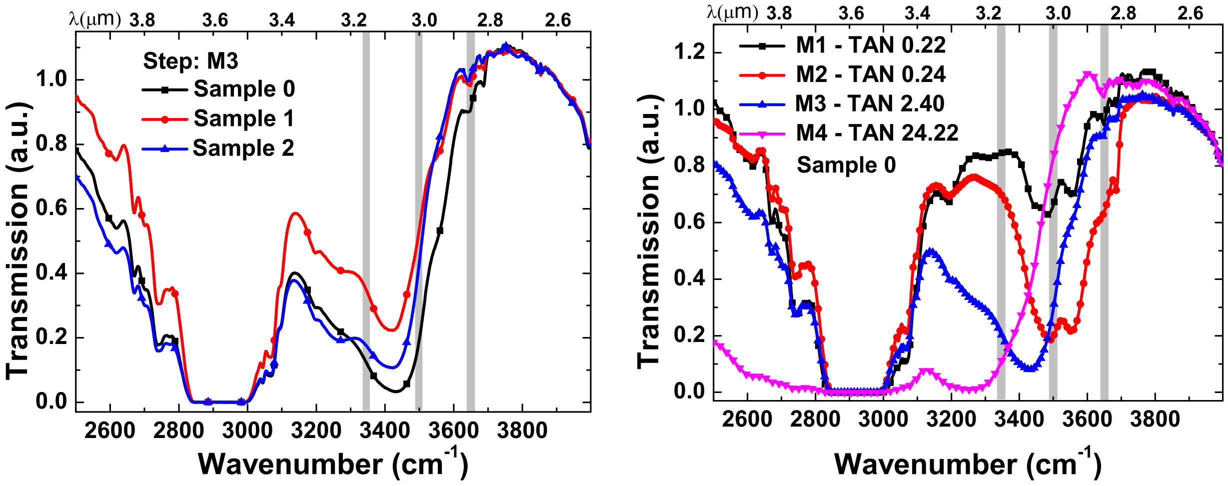

(c) Spectra at M3

(d) Spectra of Sample 0 at M1-M4

Figure 1.14: *FTIR spectra obtained on test samples with different initial acidities ("Sample 0" 0.12 mg KOH/g, "Sample 1" 0.78 mg KOH/g; "Sample 2" 1.80 mg KOH/g). The three grey bars indicate the spectral positions of the measurement channels described in section 1.2.1: a) initial spectra featuring different TAN values; b) effect of added water; c) effect of first heat treatment at 180° C; d) Spectra of Sample 0 at all four measurement steps (M1-M4).*

The sudden surge in TAN value can be explained by the activities of the additives in the fluid. In the course of fluid degradation, weak acids (e.g. carboxylic acids) are formed alongside with strong phosphoric acid. These organic acids are formed by the degradation of the acidity scavenger molecules which are important additives inside the fluid. One commonly used acid scavenger is cyclic epoxy ester. The take up of water by these acid scavenger molecules is illustrated in Fig. 1.15(a). Acidity levels below 1.5 mg KOH/g are due to weak acids. These build up gradually and are not neutralized by the acid scavenger. While the strong acids are neutralized by the scavenger, the weak acids continue to accumulate. Weak acids are therefore an indication of the extent of fluid degradation. Up to 90% depletion of acid scavenger, the TAN increases gradually. Between 90-96% scavenger depletion, the acid concentration starts to increase exponentially. Beyond this level there is a huge surge in the acid level, which requires immediate replacement of the fluid. The evolution of TAN value over the aircraft's operating time is illustrated in Fig. 1.15(b) [22].

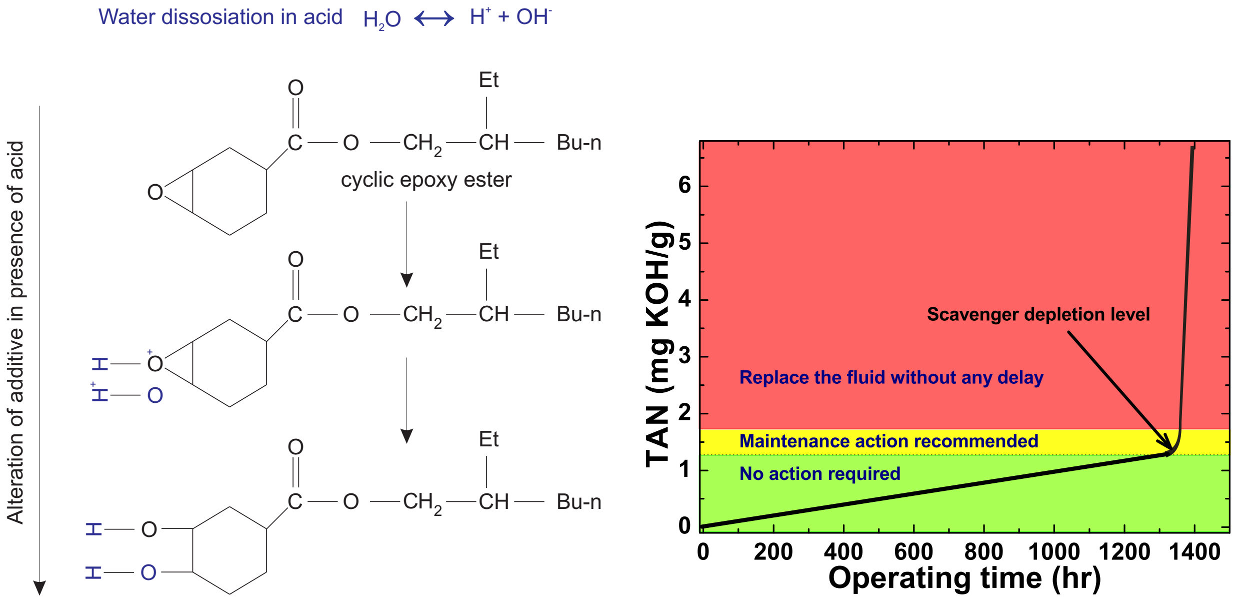

(a) (b)

Figure 1.15: *a) Activity of acid scavenger molecules in hydraulic fluid. 2-ethylhexyl 7-oxabicyclo[4.1.0] heptane-3-carboxylate is a commonly used epoxy ester used as acid scavenger. These epoxy ester molecules react with the hydroxyl ion formed by water in presence of acid. Thus the reaction product is weak carboxylic acid. b) development of TAN value of hydraulic fluid in operation. Operating condition: 0.5%* H_2O*, 125°C. TAN value surges beyond 1.5 mg KOH/g due to the complete depletion of acid scavenger [22].*

1.2.6 Modeling of the fluid degradation behavior

As explained above, the C-H and O-H stretch vibration lines are the two most prominent features in the FTIR spectra of Skydrol. With the knowledge about the fluid degradation mechanisms at hand, one can now build a model with three Gaussian absorption peaks that allows experimental spectra to be fitted and more precise degradation parameters to be determined. Example fits obtained with this model are shown in Fig. 1.16. The three Gaussian absorption peaks (dashed lines) are chosen to fit the spectral positions of the hydrocarbon, alcohol and water absorption lines around 2950 cm^{-1}, 3350 cm^{-1} and 3500 cm^{-1} respectively. The peak amplitudes and the FWHM values of these Gaussians can then be adjusted to fit the measured spectra and to retrieve the most appropriate values of the degradation parameters.

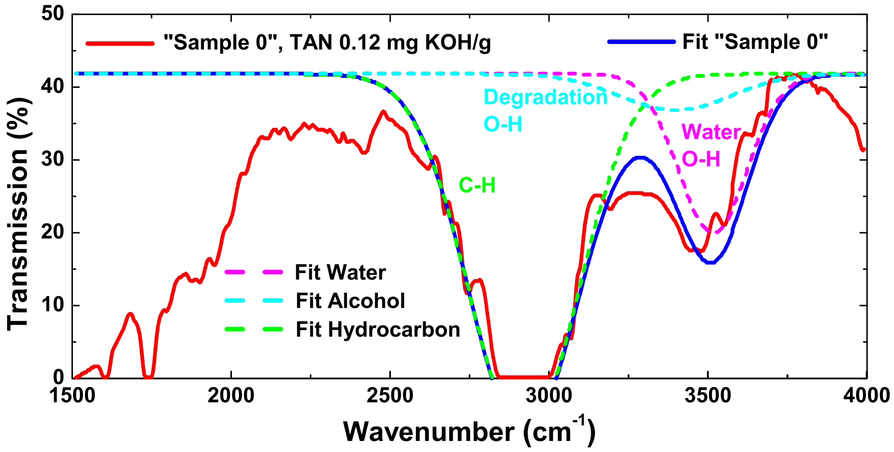

(a) "Sample 0" - TAN 0.12 mg KOH/g

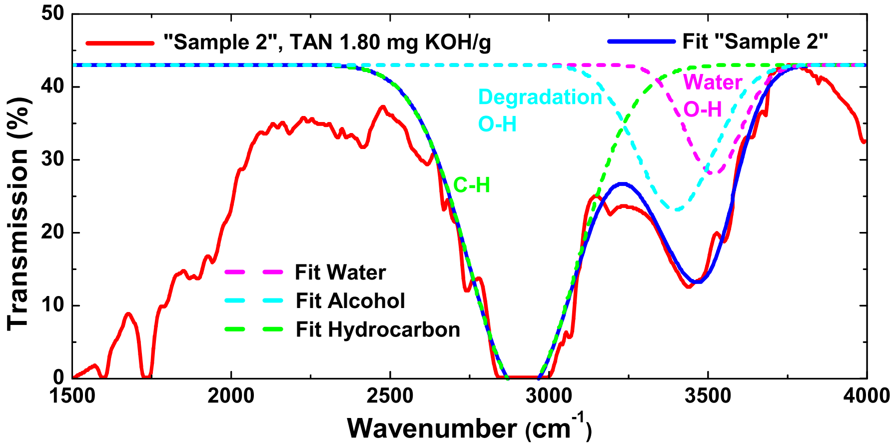

(b) "Sample 2" - TAN 1.80 mg KOH/g

Figure 1.16: *Gauss fittings of FTIR spectra for two samples with different degradation states. Three Gauss-shaped curves can be derived with C-H, Alcohol and* H_2O *absorption lines. (a) "Sample 0" with TAN value of 0.12 mg KOH/g, (b) "Sample 2" with TAN value 1.80 mg KOH/g.*

Fig. 1.16(a) shows the spectrum of fresh Skydrol with a very small TAN value and without any intentional water contamination. The amplitude of the water O-H Gauss curve is several times bigger than that of the degradations O-H or alcohols. Fig. 1.16(b) represents a fluid sample with high TAN value of 1.8 mg KOH/g. The red shift of the O-H absorption peak is seen to arise from a change in the relative amplitudes of the water and degradation Gauss curves.

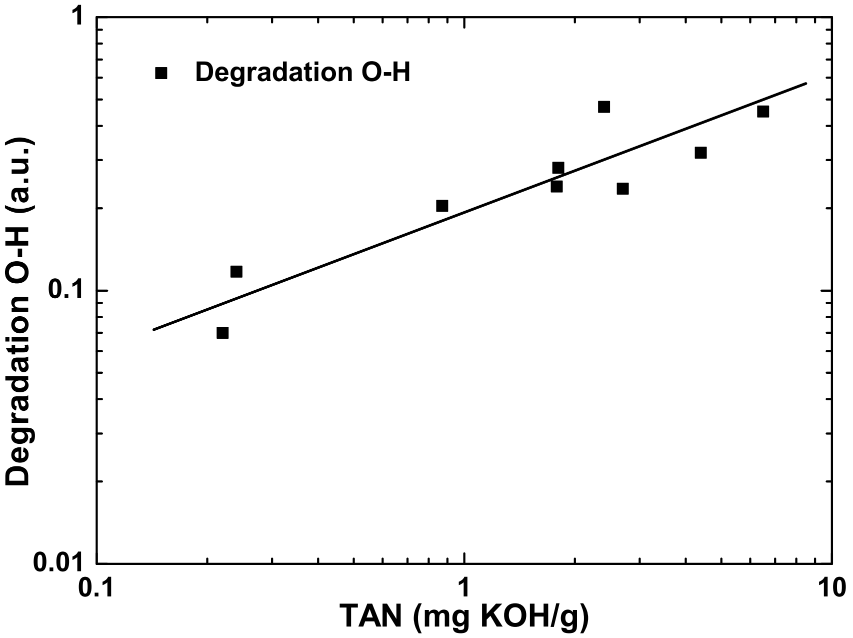

Figure 1.17: *Variation of the amplitude of degradation O-H Gauss curves as obtained from spectrum similar to Fig. 1.16.*

Fig. 1.17 shows the change of the O-H degradation peak amplitude with the TAN value of Skydrol samples. The individual data points have been obtained from fitting the peak amplitudes of the degradation O-H peaks in samples with different TAN values. In order to obtain a relative measure for the acidity, the degradation peak amplitudes have been normalized to the relative strengths of the C-H absorption peaks in these same samples. The fitted straight line shows that the degradation peak amplitude scales with the square root of the titrated TAN value.

1.2.7 Demonstrator sensor system

In order to demonstrate the usefulness of the above-described IR transmission mapping procedures a demonstrator sensor system for practical application was built up. The principle architecture of this sensor system is displayed in Fig. 1.18.

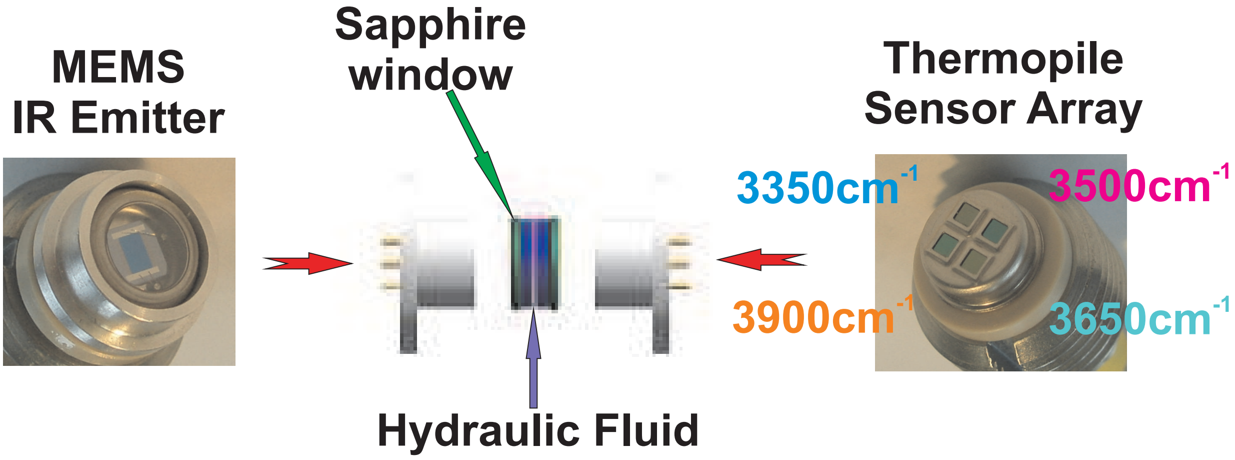

Figure 1.18: *Schematics of IR detection system consisting of a MEMS-based IR emitter (left), an optical path (middle) and a 4-thermopile IR sensor array (right).*

On the left-hand side of Fig. 1.18, pulsed IR radiation is produced by a broadband (1-10 μm) MEMS thermal IR emitter from Intex Inc. Thermal emitters are low cost, robust and simple IR sources [23]. The fluid to be tested is passed through an optical absorption path that is limited on both sides by IR-transparent sapphire windows. The IR radiation is passed through the liquid and detected on the other side by a thermopile detector array produced by Micro Hybrid Electronic GmbH. The Bi-Sb thermopiles are well known as high-sensitivity wide-band IR detectors [24]. Thermopiles exhibit good linearity, require no optical chopper, no electrical bias and can operate over a broad temperature range [25]. The four detectors in this array are fitted with narrow-band-pass IR filters with center wavenumber as indicated in Fig. 1.8. Following the ideas explained earlier, three of these spectral windows embrace the OH-absorption features in the fluid and the fourth is a reference window. The center wavenumber of the optical filters, supplied by Jenoptik AG, deviated slightly from the wavenumbers indicated in Fig. 1.18 i.e. 3875 cm^{-1}, 3663 cm^{-1}, 3480 cm^{-1} and 3322 cm^{-1}. Special care was taken in the assembly of the thermopile arrays to avoid cross talk between the individual channels. The cross talk ratio of each channel to its three neighbor channels was less than 2%. The characteristic curves of the IR emitter, the bandpass filters and the thermopile detector are presented in Fig. 1.19.

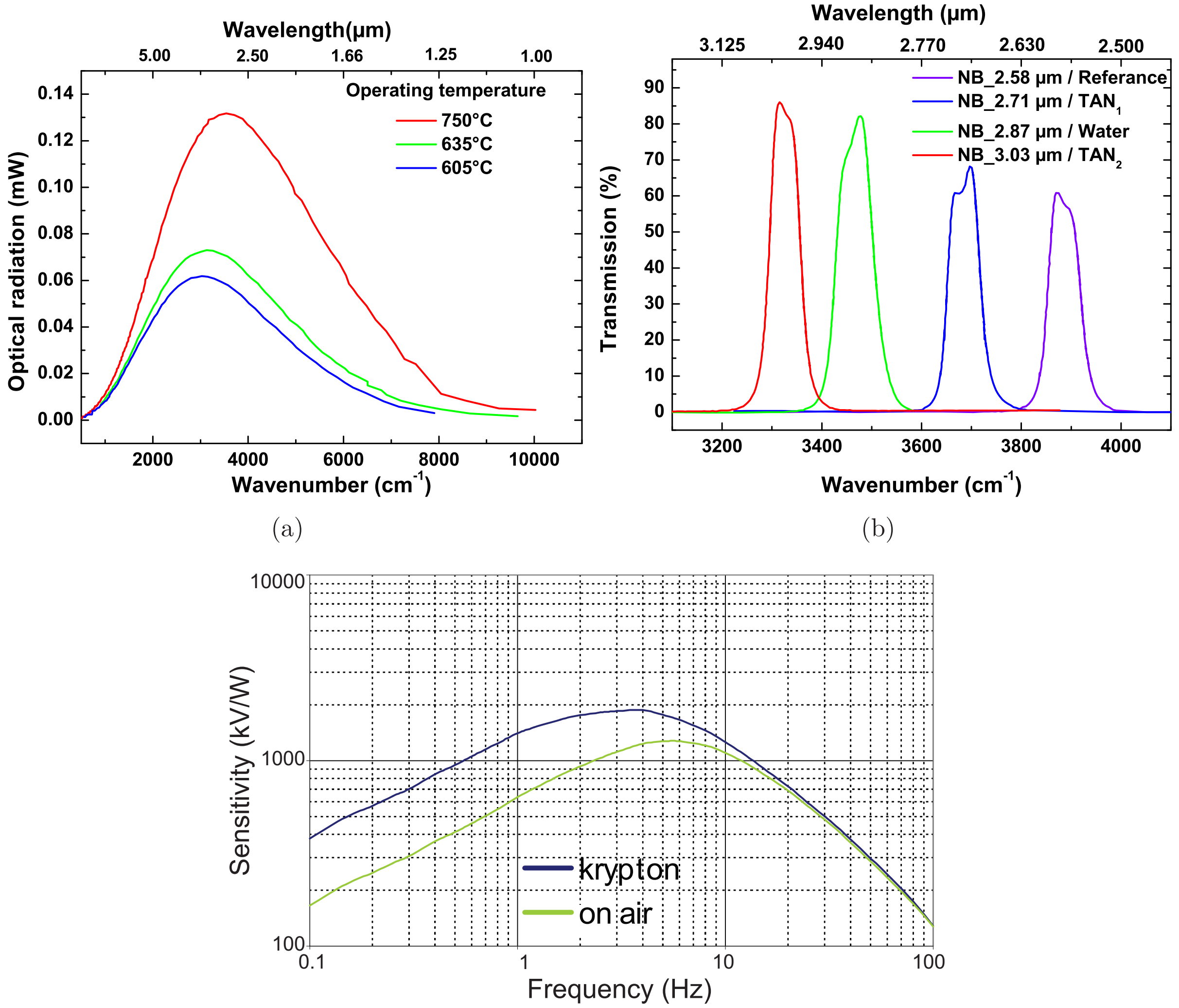

(a) (b)

(c)

Figure 1.19: *(a) Optical radiation of the broadband thermal infrared emitter at different operating temperatures. The peak emission at 750°C was found to be at 3520 cm^{-1} or 2.84 µm. (b) Transmission characteristics of the four optical filters. The center wavenumber of the optical filters are 3875 cm^{-1} or 2.58 µm, 3663 cm^{-1} or 2.73 µm, 3480 cm^{-1} or 2.87 µm, and 3322 cm^{-1} or 3.01 µm. (c) Frequency response of the thermopile. Hermetically sealed detector was filled with inert gas krypton to enhance the sensitivity. In the sensor system, the IR emitter was modulated at 5 Hz to achieve the maximum thermopile response. All the characteristic curves are collected from the corresponding data sheets.*

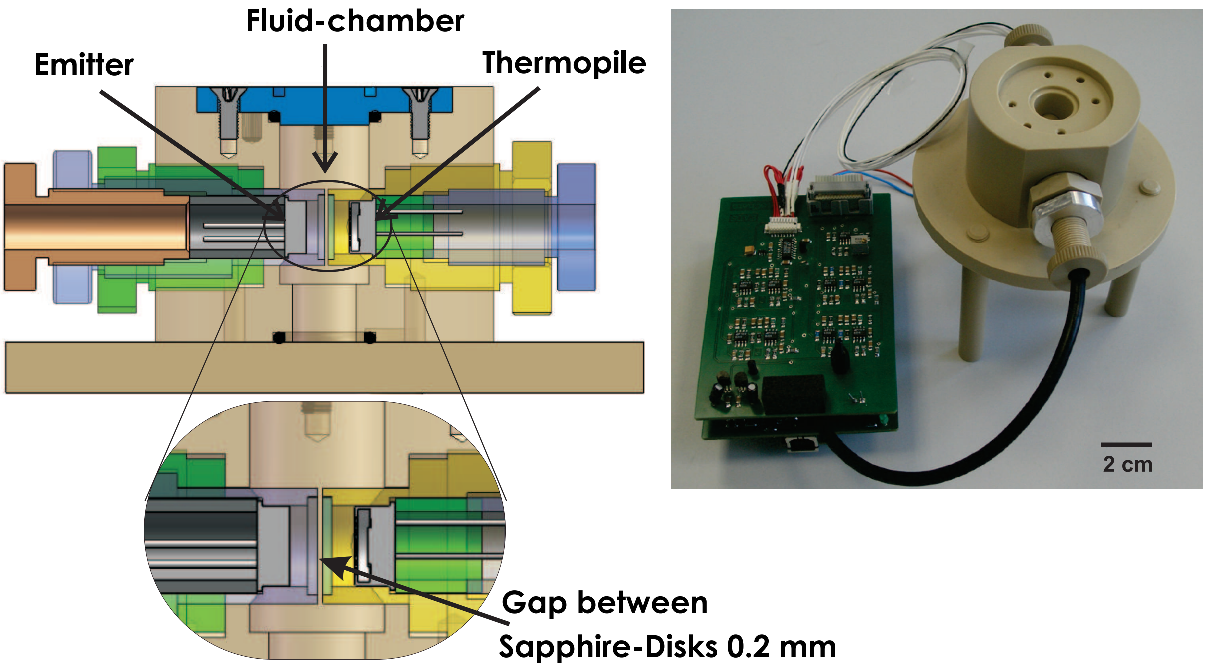

Figure 1.20: *IR sensor system as integrated:(left) Schematics, (right) realized sensor system.*

The mechanical setup of this sensor system is shown in Fig. 1.20. This small sensor vessel consists of high-performance thermoplastic Polyaryl-Ether-Ether-Ketone (PEEK). It can be filled with a few ml of fluid and its transparency can be tested by monitoring the transmission of the IR light across a 0.2 mm fluid channel, accessible via two adjacent sapphire windows. The sensor electronics is realized on two printed circuit boards (PCB) which contain the emitter driver and the detector electronics. A commercial USB data acquisition board was used to interface the sensor system to a PC with a dedicated application built with LabView software.

1.2.8 Data acquisition electronics

The emitter is driven by a power operational amplifier (OP). The OP drives a 2 kHz AC current through the platinum heater meander of the MEMS IR emitter. AC powering is used to avoid electro-migration-induced heater degradation. The AC drive current in turn is modulated with a low frequency ramp signal to produce low-frequency modulated IR light (5 Hz). The current through the emitter and the voltage across the emitter were sensed to monitor the output power. The sensor electronics consists of four identical blocks for the four optical channels. Each channel contains a voltage follower or unity gain buffer to provide current gain, followed by a high-impedance amplifier and a low pass filter (f_c = 20 Hz) on the output side. The filter embraces the modulation frequency of the MEMS IR emitter. A temperature sensor was embedded in the thermopile array package. All signals were acquired through a USB data acquisition module from National Instruments. A LabVIEW program was developed for data acquisition and signal processing.

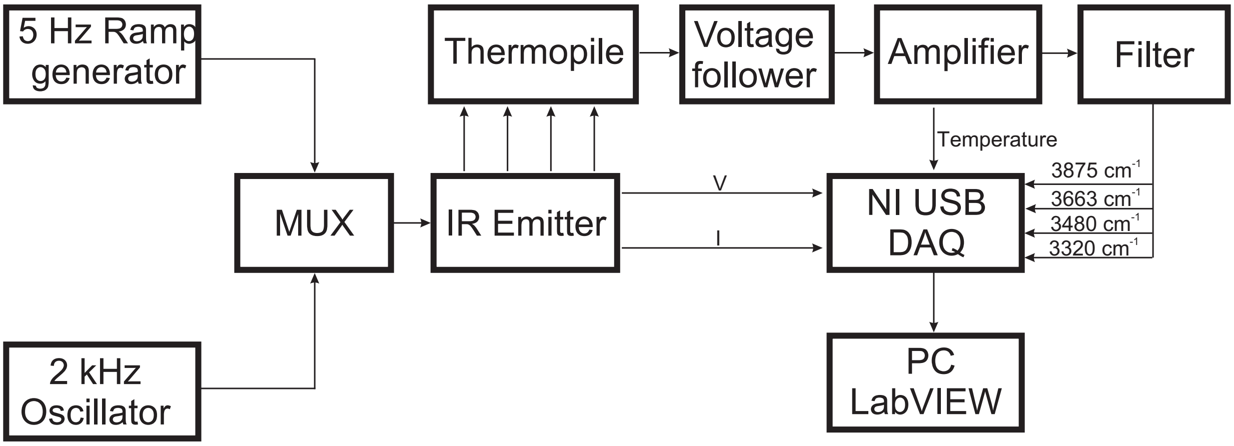

Figure 1.21: *Block diagram of the sensor electronics.*

The block diagram of the sensor electronics is presented in Fig. 1.21. The thermal IR emitter in this detector system is modulated with a frequency of 5 Hz. The four thermopile receivers on the opposite side will therefore produce four approximately sinusoidal output voltages $V_{3875\ cm^{-1}}$, $V_{3660\ cm^{-1}}$, $V_{3480\ cm^{-1}}$, and $V_{3320\ cm^{-1}}$, respectively. These output voltages in turn will depend on the amount of IR radiation that is emitted by the thermal IR source on the left and the transparency of the fluid gap. For ensuring a good lifetime of the thermal IR emitter, the sources should not be operated at temperatures above 750°C. On the other hand, the amplification on the receiver side should be adjusted in such a way that the AC amplitude at the output of the analogue electronics should not exceed the acceptance range of the follow-on AD converter (5 V) under conditions of full transparency ($\approx$ 88% for an empty, i.e. air-filled sensor) or about 65% for a fluid-filled sensor i.e. $V_{peak} = 5\ V \times 0.64 = 3.2\ V$.

1.2.9 Fluid property measurement with sensor system

With this demonstrator system a number of tests were performed. Fluids with different water and acid contents were filled into the sensor vessel and the IR transparency of the fluid in the four different spectral windows was measured.

Water sensitivity of the sensor

Fig. 1.22 shows, how the transparency in the three channels varies as the water content of the hydraulic fluids is increased. The optical absorption in solids and liquids follows the Lambert Beer law [26]. This expectation is confirmed by the data of Fig. 1.22: whereas the transparency of the 3480 cm^{-1} channel rapidly decreases as the water concentration is increased, a slower and closely identical decrease is observed in the two neighbor channels which trace the transparency in the high- and low-energy wings of the 3480 cm^{-1} absorption feature. The exponential decay of sensor signal with increasing water concentration can be interpreted by equations 1.8 - 1.10.

$$V_{3320}(C_{H_2O}) = 0.689 \times exp^{(-0.99 \times C_{H_2O}(\%))} \tag{1.8}$$

$$V_{3480}(C_{H_2O}) = 0.587 \times exp^{(-2.10 \times C_{H_2O}(\%))} \tag{1.9}$$

$$V_{3660}(C_{H_2O}) = 0.764 \times exp^{(-0.98 \times C_{H_2O}(\%))} \tag{1.10}$$

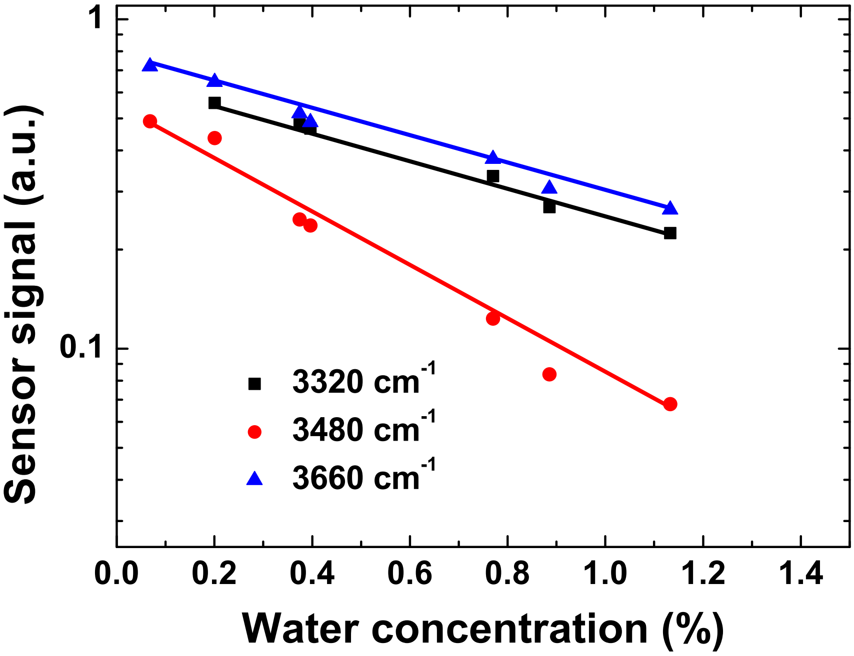

Figure 1.22: *Variation of the thermopile detector output with the water content of Skydrol LD-4. The curve with the steep slope refers to the 3480 cm^{-1} center absorption band and the shallower ones to the high- and low-energy absorption bands around 3660 cm^{-1} and 3320 cm^{-1}, respectively. The output signals were normalized to the 3875 cm^{-1} reference channel.*

TAN sensitivity of the sensor

In a second set of experiments the response of the four thermopile channels to artificially degraded (acid contaminated) Skydrol LD-4 samples were tested. In order to test the sensor system, several solutions were prepared with TAN values in the range of 0 to 1 mg KOH/g by diluting a base fluid of higher TAN value with fresh Skydrol. As revealed from Fig. 1.23, the difference in the transparency of the 3320 cm^{-1} and 3660 cm^{-1} channels scales logarithmically as the TAN value is increased. This logarithmic relationship is elaborated in equation 1.11, where $\Delta V = V_{3660\ cm^{-1}} - V_{3320\ cm^{-1}}$, normalized to the 3875 cm^{-1} reference channel. For larger TAN values, a saturation of the sensor signal is observed. A quantitative determination of TAN values larger than 1 mg KOH/g, therefore, is not possible with this sensor principle.

$$TAN_{mgKOH/g} = \frac{1}{4.772} ln \frac{\Delta V}{64.7 \times 10^{-3}} \tag{1.11}$$

$$for, 0 < TAN \leq 1 \; mg \; KOH/g$$

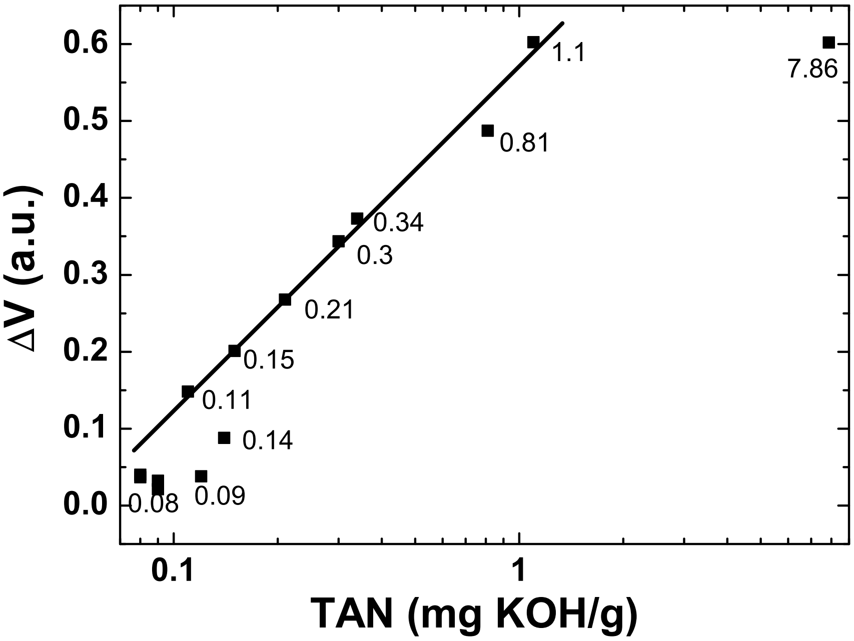

Figure 1.23: *Acid sensitivity of the sensor system. The difference in output signals of the 3660 cm^{-1} and 3320 cm^{-1} channels shows a logarithmic dependence on TAN in the range of 0 to 1 mg KOH/g, shown in equation 1.11.*

"Health Plot" of hydraulic fluids

The dissolved water in hydraulic fluid can be removed by polymeric filters, vacuum distillation or by headspace dehumidification [27]. Keeping in mind that dissolved water can be removed from hydraulic fluids, but that hydrolyzed and acidified fluid needs to be replaced to prevent damage to the hydraulic system, maintenance-relevant information can be retrieved considering the IR transmission in the three spectral windows. In order to retrieve this information, we calculated the difference in transmissions as measured by the thermopiles in the 3320 cm^{-1} and 3660 cm^{-1} spectral windows, i.e.: ΔV and plotted them as a function of the transmission $V_{3480\ cm^{-1}}$ in the center 3480 cm^{-1} window. This is depicted in Fig. 1.24 using the data of Figs. 1.22 and 1.23.

The data points in Fig. 1.24 can be regarded as two-dimensional state vectors that indicate the "health" of the hydraulic fluid. The fluid is "healthy", i.e. uncontaminated in case the state vector signifies a high transparency at around 3480 cm^{-1} and a small asymmetry ΔV. Addition of water will shift back the state vector towards lower values of $V_{3480cm^{-1}}$ with the asymmetry ΔV lying close to zero. Fluid degradation, i.e. hydrolysis and acidification shifts the state vector to large positive values of ΔV with $V_{3480\ cm^{-1}}$ staying at fairly high values. This health plot therefore can be interpreted as a straight-forward way to arrive at

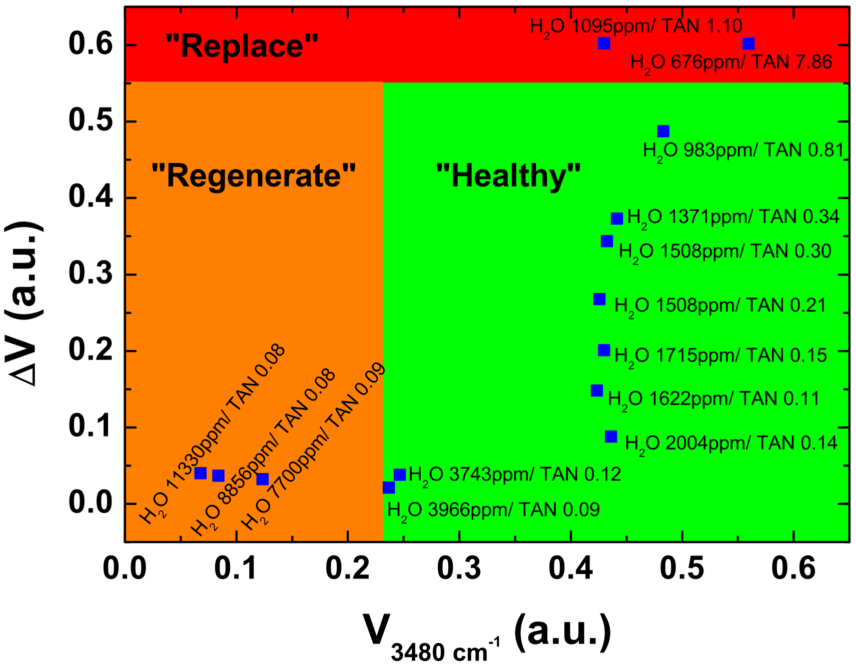

Figure 1.24: *"Health plot" of pure and degraded hydraulic fluids as determined by the NDIR sensor system demonstrator. This is based on the authorized in-service limits by Airbus for water and TAN.*

relevant maintenance decisions.

1.2.10 Synopsis of mid infrared hydraulic fluid monitoring

What has been achieved?

- Two important chemical contamination properties, i.e. water and acid formation in phosphate-ester hydraulic fluid can be monitored by NDIR absorption.
- Since NDIR senses localized vibrations of O-H groups associated with water and hydrolysis products (alcohols), the sensor principle is independent of the composition of the aryl/alkyl phosphate-ester base fluids.
- A sensor system is demonstrated for "online" health monitoring of the fluids in aircraft hydraulic systems. The system comprises a broad-band thermal IR emitter, a 4-channel thermopile and a tiny fluid channel between the two elements. Commercially available MEMS components were used for the construction.
- The accessible water detection range (0-1.5%) complies with the range of water contaminations that can appear in the practical aircraft operation.
- The accessible TAN detection range (0-1 mg KOH/g), however, is somewhat smaller than the maximum allowed TAN value of 1.5 mg KOH/g (for Airbus aircraft). The detection limit is dependent on the length of the optical absorption path. This limit can be slightly increased by narrowing the optical path.

What can be improved?

- To install the sensor system in an aircraft hydraulic line, construction of a mechanical manifold with sapphire optical windows that is sufficiently strong to sustain the pressures of ≈ 200-400 bar is required. This will be demonstrated in the later part of this chapter.
- Extension of TAN measurement range up to 2 mg KOH/g
- The narrow 200 μm absorption path is a severe obstacle for the fluid flow in any hydraulic line. Sensors with such narrow optical absorption paths can only be operated in a by-pass system with shut-off valves. Such mechanical complexity can be avoided in case sensors with optical absorption paths in the order of several mm can be built.
- To address the later point, in the following part, the potential of a sensor system based on near infrared overtone is investigated.

1.3 Near infrared - overtone based monitoring

Absorption features due to molecular overtone and combination vibration can be observed in the near infrared (NIR) region. As NIR transitions arise from the inharmonicity of molecular vibrations and as these are first-order forbidden by the laws of quantum mechanics, their absorption strengths are quite small [28]. NIR radiation therefore can penetrate much deeper into a fluid sample than MIR radiation. With regard to the fluid monitoring application addressed here, NIR systems therefore offer the advantage of sensor systems with much wider optical paths in the order of the open diameters of hydraulic fluid lines. NIR systems therefore can be directly inserted into hydraulic systems without causing excessive flow constrictions.

The chart in Fig. 1.25 shows the spectral positions of overtone vibrations and combinations of fundamental absorption bands in the NIR range. According to this table, the take-up of water can be detected in a whole number of spectral windows, i.e. at 0.95 μm, 1.40 μm, and 1.9 μm (OH overtones). Alcohols (R-OH) can also be detected in the nearby spectral windows. Besides hydraulic fluids, this principle is also applicable for monitoring other fluids like lubricants, engine oils, etc..

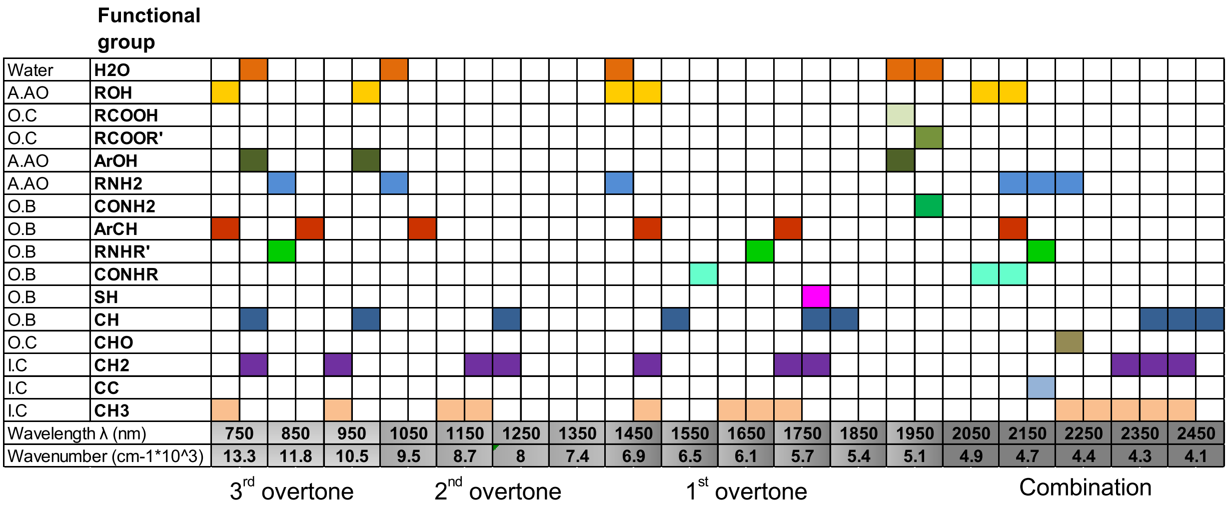

	Functional group																																				
Water	H2O		■					■								■										■	■										
A.AO	ROH	■					■									■	■												■	■							
O.C	RCOOH																									■											
O.C	RCOOR'																										■										
A.AO	ArOH		■				■																			■											
A.AO	RNH2			■				■								■														■	■	■					
O.B	CONH2																										■										
O.B	ArCH	■			■				■								■					■								■							
O.B	RNHR'			■																	■										■						
O.B	CONHR																		■										■	■							
O.B	SH																						■														
O.B	CH		■				■					■						■					■	■											■	■	■
O.C	CHO																															■					
I.C	CH2		■			■					■	■					■					■	■											■	■	■	
I.C	CC																														■						
I.C	CH3	■				■				■	■						■			■	■	■										■	■	■	■	■	
Wavelength λ (nm)		750		850		950		1050		1150		1250		1350		1450		1550		1650		1750		1850		1950		2050		2150		2250		2350		2450	
Wavenumber (cm-1*10^3)		13.3		11.8		10.5		9.5		8.7		8		7.4		6.9		6.5		6.1		5.7		5.4		5.1		4.9		4.7		4.4		4.3		4.1	
				3rd overtone								2nd overtone									1st overtone												Combination				

Figure 1.25: *NIR absorption bands of important functional groups in lubrication fluids. I.C. Oil Initial Composition, O.C. Oxidation Compound, A.AO Additive Antioxidant, O.B. other oil bands depending of the fluid [29].*

Another advantage of NIR over the MIR detector systems relates to the optical components. The MIR system described above employed a broadband thermal IR source as a light emitter and broadband thermal IR detectors as light receivers. Thermal light sources exhibit poor directionality and low output light powers inside the narrow spectral absorption lines of interest. Sufficient optical radiation power needs to be attained by high temperature operation of the thermal IR emitters, which, in turn, compromises source stability and results in high electrical power consumption. In the NIR spectral region, semiconductor diodes can be used for the light generation and detection. The advantages of LED light sources, in particular, are higher optical power, longer life time and lower cost.

1.3.1 Spectral analysis

Fig. 1.26 shows the NIR spectra of the hydraulic fluid Skydrol LD4 with different water contamination levels. The data clearly reveal that, dominant water absorption peaks are visible at 1.42 μm and 1.94 μm. The intensity of the first overtone is normally about one-tenth that of the corresponding fundamental vibration [30]. The first overtone at 1.42 μm is therefore less sensitive than that of the fundamental vibration at 1.94 μm. The titration of these water contaminated samples further revealed that such fluids are not acid. Neutralization in each case was obtained with less than 0.1 mg KOH/g.

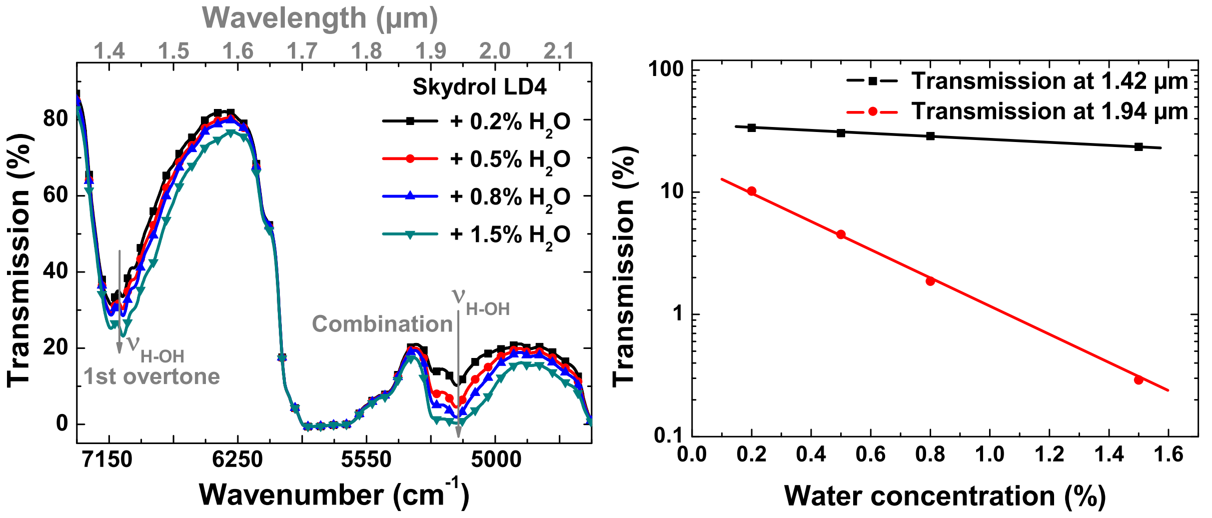

(a) (b)

Figure 1.26: *(a) IR transmission spectra of water-contaminated samples of Skydrol LD4; optical path length: 10 mm; (b) variation of the IR transmission of phosphate-ester hydraulic fluids (Skydrol LD4) with increasing water content at two prominent absorption lines, i.e. 1.42 µm & 1.94 µm. The strong decay refers to the 1.94 µm and the weaker decay to the 1.42 µm.*

Fig. 1.27 compares FTIR spectra of water-contaminated Skydrol LD4 samples with others that have been additionally heat treated to induce acid contamination. Unlike in the MIR case, the water absorption peak at 1.94 μm is not low frequency shifted as acid is formed. In these acid-contaminated samples spectral weight is added in the range extending from 2.04 μm to 2.12 μm. This spectral weight is due to the formation of alcohols like butanol and phenol during the hydrolysis. As shown in Fig. 1.27, three optical windows are selected for realizing a sensor system. The window centered at 1.94 μm determines the state of water concentration, whereas the window at 2.08 μm detects the state of acid contamination. The window at 1.83 μm is supposed to serve as a reference window to monitor the transparency of the fluid and the intensity of the LED. This reference band is barely affected by any chemical contamination.

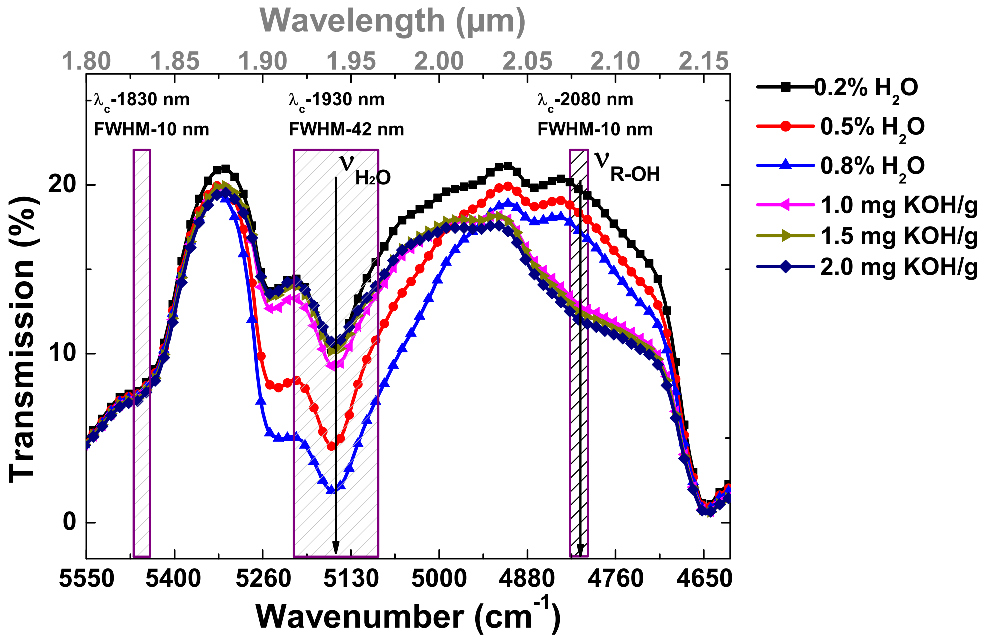

Figure 1.27: *Filter selection for chemical contamination monitoring. Filters at 1.93 µm and 2.07 µm detect water and acid concentrations respectively; the filter at 1.83 µm serves as a reference filter.*

1.3.2 Sensor system

The NIR sensor system was built using semiconductor opto-electronic devices. Two LEDs with peak emissions at 1.9 µm and 1.4 µm were selected as IR emitters. The 1.4 µm LED was composed of heterostructures grown on an InGaAsP substrate. The 1.95 µm LED was based on heterostructures (GaInAsSb/AlGaAsSb) grown on GaSb substrates. The cw (continuous wave) optical power of the LEDs were 2 mW and 1 mW for 1.4 µm and 1.9 µm at rated current. The FWHM of the LEDs varied from 100 nm to 150 nm. The emission spectrum of the LED and the spectral response of the photodiode are illustrated in Fig. 1.28.

Narrow bandpass optical filters shown in Fig. 1.27 could be mounted on the detector side of the sensor system. InGaAs and Ge photodiodes were used as detectors for absorption around 1.4 µm and 1.94 µm respectively. A transimpedance amplifier with adjustable gain converted the photocurrent signal from the photodiodes.

The fluid measurements were performed with the same measurement chamber as in the MIR sensor presented in Fig. 1.20. Suitable adapters were constructed to fit the LED and photodiode in this setup. The absorption path length of this measurement chamber could be varied from few µm to more than 1cm.

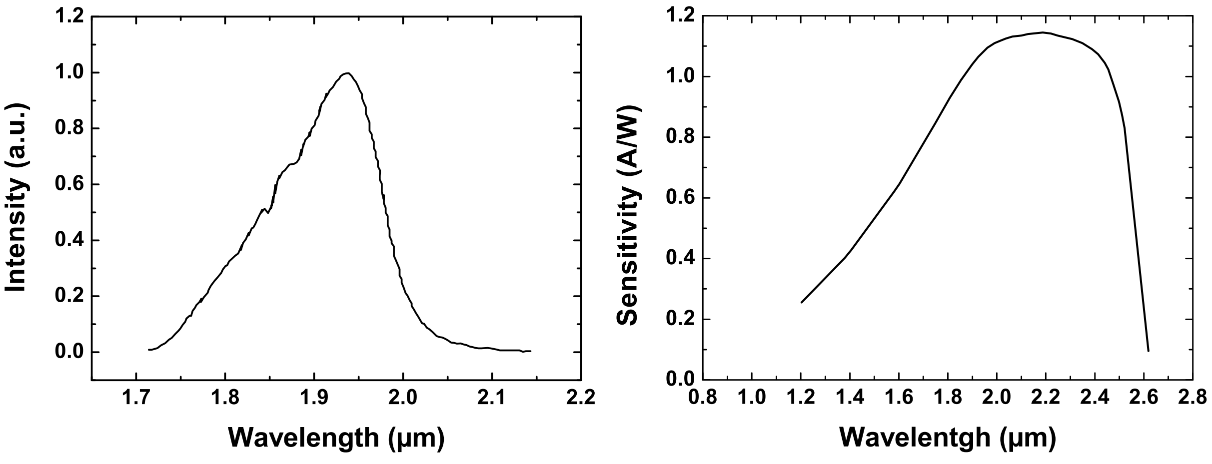

(a) (b)

Figure 1.28: *(a) Optical radiation spectrum of the mid infrared LED operated at quasi CW mode at rated current of 300 mA. (b) Spectral response of the InGaAs-photodiode. The characteristic curves are collected from the corresponding data sheets.*

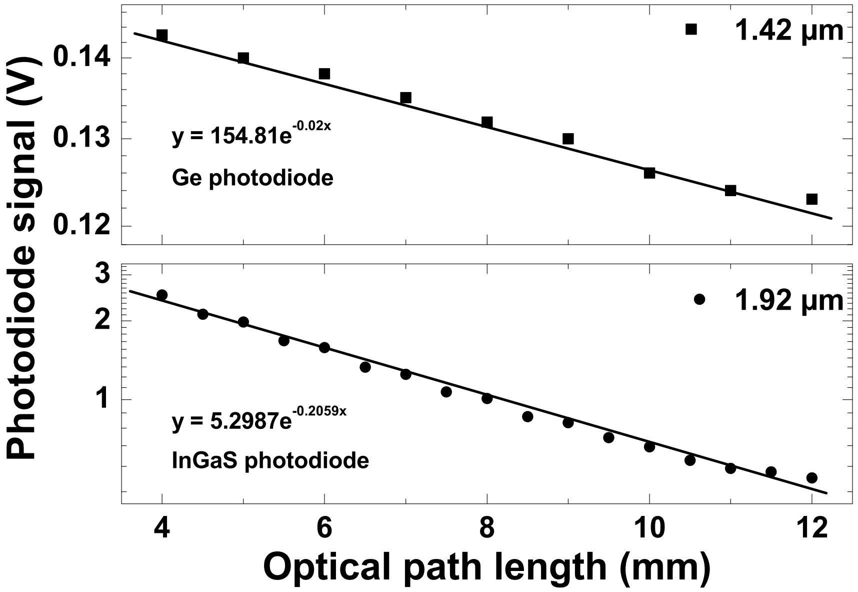

Figure 1.29: *Variation of NIR transmission of Skydrol LD4 with absorption path length at 1.42 µm and 1.94 µm. The optical excitation powers were 2 mW and 1 mW respectively. The absorption follows the Lambert-Beer law.*

1.3.3 Test results

To determine an optimum optical path length for measurement, the measurement chamber was filled with fresh Skydrol and then the absorption length was varied. The optical absorption in solids and liquids follows the Lambert-Beer law. Fig. 1.29 certifies this for the two experimented wavelengths. The intensity of light coming to the photodiode decreases exponentially with increasing optical path length. The attenuation coefficient(α) for 1.42 μm and 1.94 μm are 0.02 mm^{-1} and 0.2 mm^{-1} respectively.

Fig. 1.30 shows how the optical absorption scales with the water concentration of the tested fluid. Three different optical absorption paths were investigated during this experiment. Water contamination of the samples was increased up to 2%. The absorption of excitation light increased monotonously with increasing water concentration for all three cases. Smaller absorption paths gave rise to higher detector output signals. But the relative deviation in signal (δ=($V_{fresh\ fluid} - V_{contaminated\ fluid}$) $*$ 100/$V_{fresh\ fluid}$) increased in case of longer optical path length. With 2% water contamination δ was calculated to be 30%, 26% and 18% for 10 mm, 7 mm and 4 mm optical path respectively. Therefore, for better accuracy a wider fluid channel can be chosen.

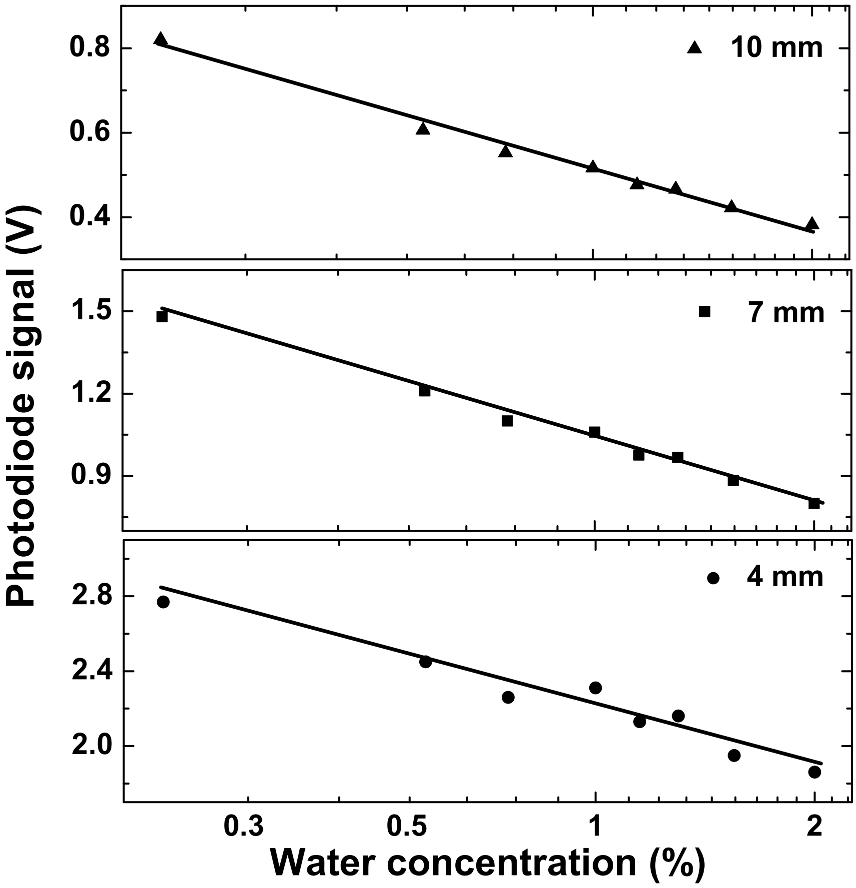

Figure 1.30: *Variation of the NIR transmission of Skydrol LD4 with increasing water content as measured at different absorption path lengths and 1.94 μm LED. Photodiode's output voltage is plotted in y axis*

$$V_{1.9\ \mu m}(C_{H_2O}) = 2.8\ \times\ exp^{(-0.219\ \times\ C_{H_2O}(\%))} \tag{1.12}$$

for 4 mm optical path length

All three plots in Fig. 1.30 can be expressed with exponential fit equation. The equation 1.12 is derived from the fit curve of 4 mm optical path length. The attenuation constant (α_{NIR}) in this case is 0.21/% H_2O, which is one tenth of that for the next harmonics at 3500 cm^{-1} ($\alpha_{MIR} = 2.11$/% H_2O, in equation 1.9).

A number of experiments were carried out with this NIR sensor system to characterize acid contaminated fluid samples. The changes in the spectral absorption at around $\lambda \approx 2.08\ \mu$m, however, could not uniquely be related to the TAN value of the fluid samples.

1.3.4 Synopsis of near infrared hydraulic fluid monitoring

- In the near infrared region aviation hydraulic fluids feature water-related absorption lines at around 1.4 μm and 1.9 μm.
- Making use of these water-related absorption lines a sensor system with excellent water sensitivity and a much wider optical path ($\approx$ 1 cm) could be demonstrated.
- A strong, contamination-related absorption also exists at around 2.08 μm. This latter line, however, could neither be related to the water content, nor to the TAN of the hydraulic fluid. Conclusive results for the TAN value therefore could not be obtained with this NIR detector system.

1.4 Acidity detection based on fluorescence

In the previous sections mid and near IR absorption sensors for hydraulic fluid have been described. In order to eliminate the limitations in the TAN detection that exist in the NIR range, another intrinsic property of the fluid, namely fluorescence, was investigated.

1.4.1 Phenol in hydraulic fluid

As discussed in section 1.1.2 Phosphate-ester hydraulic fluids are produced by making various kinds of alcohols react with phosphoric acid. In this reaction phosphate-ester molecules are formed along with water molecules:

$$Alcohols + phosphoric\ acid \xrightarrow{Heat} phosphate - ester + water \qquad (1.13)$$

The phosphate-ester fluid is obtained by removing the reaction water.

Hydraulic fluid degradation is basically the reversal of the above reaction. The initial step is the take up of humidity into the water-free phosphate-ester fluid. After this initial contamination step, water molecules remain chemically unchanged and are simply dissolved within the phosphate-ester fluid. When there is an additional heat input, the dissolved water may chemically react with the base fluid, causing it to disintegrate via hydrolysis. In the course of such hydrolysis events, alcoholic side groups become separated from their parent phosphate groups, forming free alcohols. This process continues until all side groups have been removed and the center phosphate group has been re-converted into a phosphoric acid molecule again. These disintegration steps are visualized in Fig. 1.31.

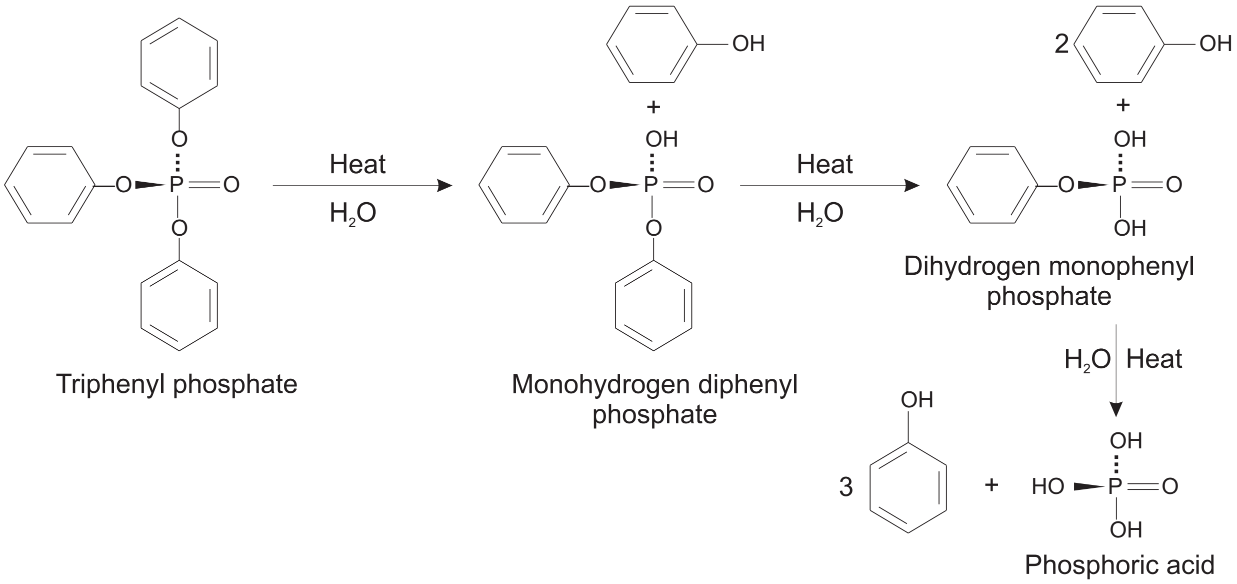

Figure 1.31: Chemical reactions following the take-up of water into a phosphate-ester based hydraulic fluid. Triphenyl phosphate molecules are disintegrated to phosphoric acid and phenol during the degradation process in presence of water and heat.

One of the hydrocarbon side groups in the Skydrol base fluid is a phenyl group, which turns into free phenol upon hydrolysis. Fig. 1.32(a) shows the emission spectrum and excitation coefficient of liquid phenol. As we can see here, phenol has a strong absorption in the range from 250 to 280 nm. It shows the luminescence in wavelength from 270 nm to 350 nm. The absorption spectrum of Skydrol LD4 showed in Fig. 1.32(b), also exhibits a strong absorption feature around 260 nm. In case this feature is due to free phenol in the hydraulic fluid, the phenol luminescence should be detectable in Skydrol and its strength should correlate with the strength of the 260 nm absorption feature.

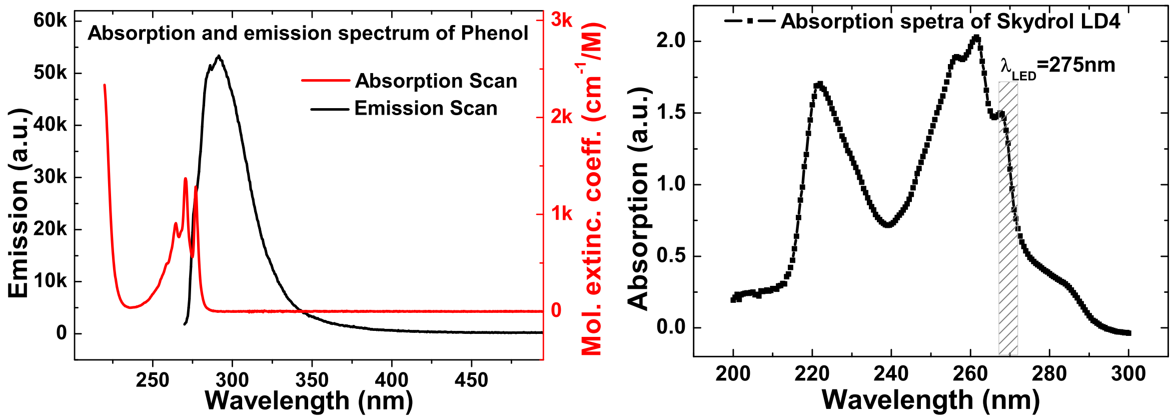

(a) (b)

Figure 1.32: *(a) Fluorescence and absorption spectra of liquid phenol (λ_{ex}=260 nm). Data collected from ref. [31]. (b) Absorption spectrum of Skydrol LD4 in deep UV region.*

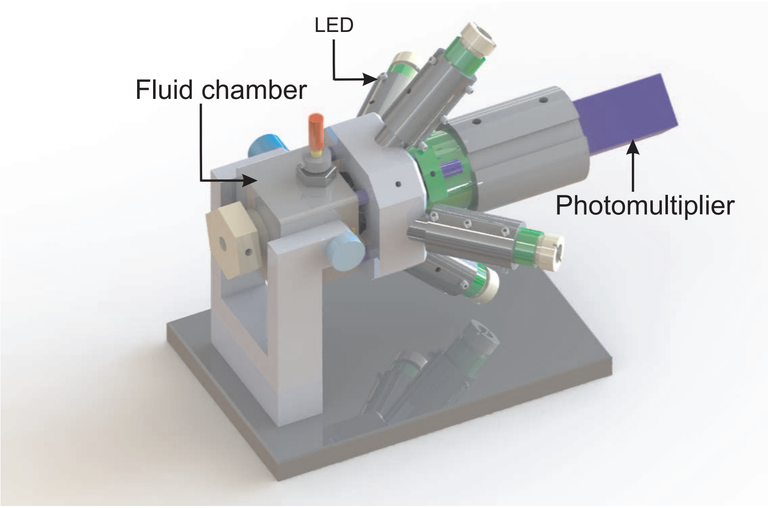

Figure 1.33: *Rendered view of the measurement chamber for the detection of fluorescence from hydraulic fluids. The fluid is illuminated with four LEDs through a sapphire window. Either a spectrometer or a photomultiplier can be used as a fluorescence detector.*

1.4.2 Measurement setup

For the luminescence measurements, hydraulic fluid samples were filled into a small measurement cell with sapphire optical windows. The measurement chamber is shown in Fig. 1.33. Through the transparent sapphire window the Skydrol samples were illuminated with short-wavelength UV light coming from a commercial UV LED supplied by Roithner Lasertechnik GmbH. The AlGaN based LED had a typical peak wavelength of 275 nm and optical output power of 480-800 μW. The fluorescence response was observed using a spectrometer. A stand alone photomultiplier with a suitable long pass optical filter was also used as a detector. The detection plane was positioned at right angles to the sapphire window.

1.4.3 Experimental results

Fig. 1.34(a) shows the fluorescence spectra of hydraulic fluids with different acid contamination levels. The fluorescence intensity increases monotonously with increasing acid contamination. The results here reveal that the intrinsic fluorescence of the phenyl group is strongly quenched as long as it is connected to its parent phosphate-ester molecule (i.e. fresh Skydrol). The quenching likely arises from the coupling to the phenyl group to a strongly electron-attracting phosphate group in the Skydrol molecule. Consistent with this explanation the optical quenching effect is reduced as more and more phenyl groups in the fluid become detached from their parent phosphate-ester molecules as hydrolysis goes on. As, according to the above explanations, increasing numbers of free phenol molecules are associated with increasing numbers of free phosphoric acid groups, the fluorescence intensity scales with the degradation level of the fluid or indirectly with the TAN value. Fig. 1.34(b) presents the results obtained with a photomultiplier as photo detector for fluorescence intensity. This correlation of chemical relevance to an optically observable parameter, in principle, enables a sensor to be built, which allows sensing the degradation of hydraulic fluids to be determined without tapping fluid from the hydraulic system.

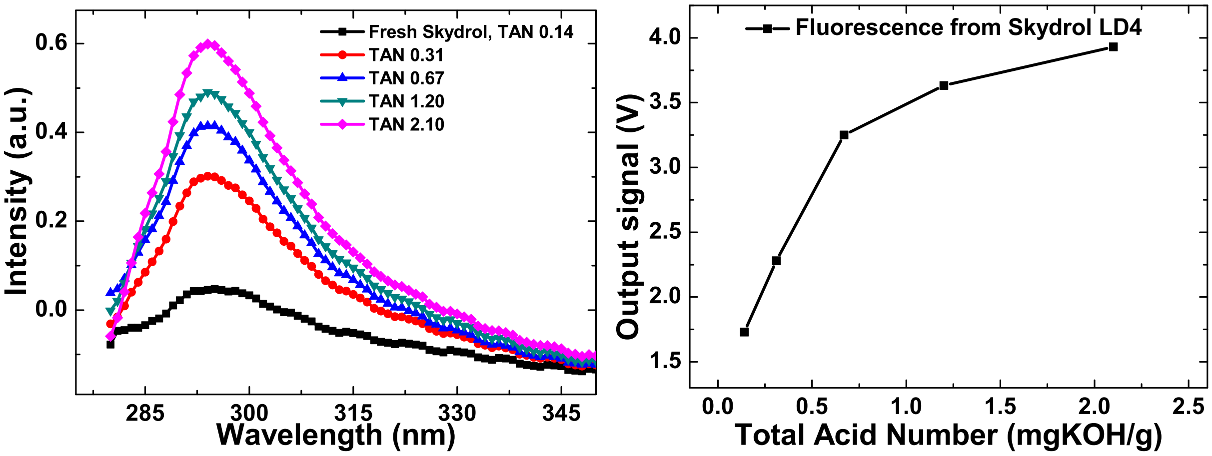

(a) (b)

Figure 1.34: *(a) Fluorescence spectra of hydraulic fluids with different acid contamination levels. (b) fluorescence of hydraulic fluids with different acid contaminations as observed with a photomultiplier.*

As we have discussed in section 1.2.3, a wide range of fluids are certified for use in civil aviation industry and the ratio of aryl/alkyl group varies between the manufacturers. Therefore, we have performed the fluorescence experiments with fluids from different manufacturers to determine their intrinsic fluorescence level. Fig. 1.35 shows the results for three different fluids. Here we can see that the fluorescence level of the fresh fluid varies enormously with different fluids due to different phenol content in base stocks. Consequently, the TAN value of a fluid mixture will not uniquely map onto its fluorescence level.

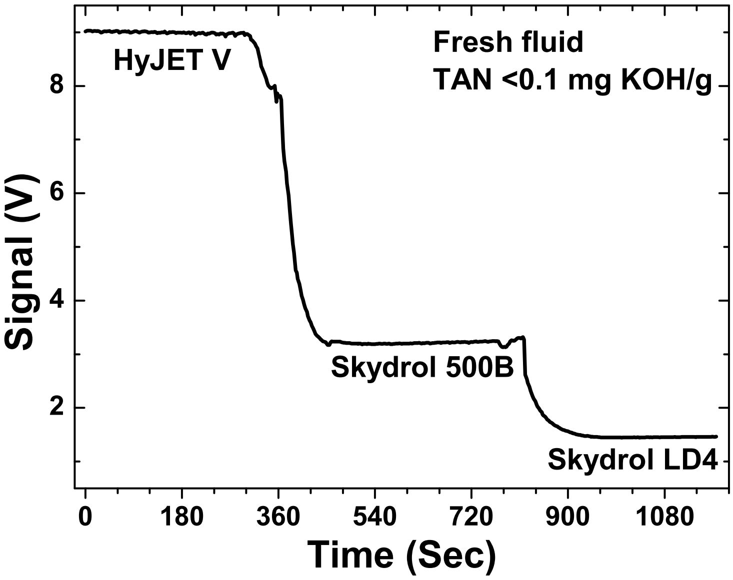

Figure 1.35: *Fluorescence intensity detected by the photomultiplier obtained with different brands of hydraulic fluids. This transient response was recorder with flowing the hydraulic fluids in the measurement chamber with a pump. Different amount of phenyl groups lead to different fluorescence intensity of fresh fluid.*

Although this fluorescence principle is not applicable to predict the TAN value directly, we can use this to determine the relative degradation or relative change in TAN of the fluid. There are also some military applications where mixtures of different fluids are not allowed. In this particular application, fluorescence can be used to obtain precise measurements of the TAN value.

1.4.4 Synopsis of TAN determination by fluorescence

- Within a given hydraulic fluid there is a one-to-one correlation between the TAN value and the fluorescence from phenol molecules.
- In mixtures of different hydraulic fluids there is no unique correlation between the TAN value and the fluorescence level.
- For a given mixture ratio, changes in the phenol fluorescence level are good indicators for fluid degradation.
- A fluorescence based measurement of TAN values is possible in certain military applications where mixtures of different fluids are not allowed.

1.5 Particulate matter monitoring

Chemical contaminations like acids and water determine the degree of corrosiveness that the phosphate-ester fluid may develop. Once it has become corrosive, the fluid may attack all kinds of metallic parts inside the hydraulic system. Corrosive attack tends to generate particle contamination in the fluid and the free particles in turn may cause downstream mechanical damage as they are transported through many narrow constrictions inside hydraulic actuators. Particle contamination therefore is considered to be most destructive one to the hydraulic system. Thus, pollution limits are defined to avoid any negative impact on the hydraulic system as well as to its consumer systems. Therefore, those limits need to be monitored on a regular basis to secure safe system operation.

There are several standards of quantifying the level of particulate matter contamination in hydraulic fluids. One of these measures is Aerospace Standard AS4059 with cumulative counting. Particle Contamination Count Number (PCCN) is determined by the number of particles present in 100 ml of fluid [32].

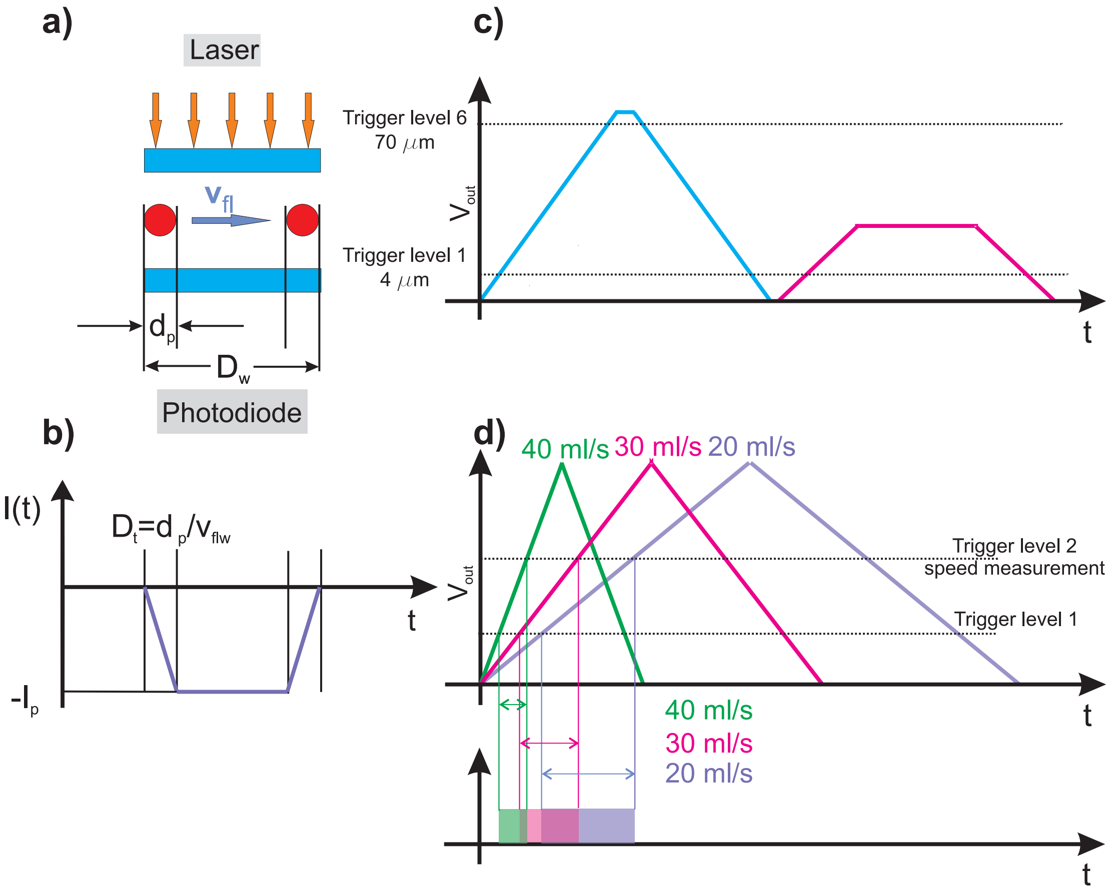

Figure 1.36: *Light barrier sensing principle, (a) particle drifting with a speed v_{fl} through a light barrier; (b) variation of the photocurrent during the particle transit; (c) output signals due to a leading small and a trailing large particle, both moving at a constant flow speed; (d) output signals due to a single large particle moving at different flow speeds.*

1.5.1 Sensing principle - Light barrier particle sensing

The task of detecting particle contamination is accomplished by detecting the shadowing effect in a light barrier system where the fluid is passed through a narrow constriction inside a fluid line. The measurement principle is illustrated in Fig. 1.36. A beam of light from a miniature laser and a photodiode are placed in the same axis with the narrow fluid flow between them. As shown in Fig. 1.36, the particle passing by the light path creates a shadow signal on the photodiode. By interpreting this photodiode signal we can determine the size of the particle and the flow speed as well.

For determining the PCCN along with the number of particles, the volume of the fluid passed during the measurement time τ_M has to be determined. To avoid the integration of a flow sensor in the system, we have used the light barrier sensor signal to perform the dual role of a particle counter and a flow sensor. As shown in Fig. 1.36c and d, the amplitude of the shadow sensed by the photodiode determines the particle size and the transition time determines the particle velocity (v_{fl}). Assuming that the particle velocity equals the flow velocity, for a given measurement time τ_M, the volume of the fluid (V_M) can be calculated from the following equation:

$$V_M = \frac{\pi}{4} \,.\, d_{min}^2 \,. v_{fl} \,.\, \tau_M \tag{1.14}$$

where, d_{min} is the diameter of flow channel.

1.5.2 Sensor system

A 3 mW laser lasing at 785 nm is used as the light source in the sensor system. Transmission spectra of different hydraulic fluids revealed that the fluids have more than 80% transmission at this wavelength, independent of the degree of chemical contamination. A silicon-photodiode with a response time of 10 ns is used to detect the particle shadows. For detecting particles in the 4-6 μm size range some fine tuning of the optical system was required. As the dark current-to-noise ratio of a photodiode depends on the size of the sensitive area, a photodiode with a small active area of 150 μm diameter was used. A collimating diaphragm of 80 μm was mounted in front of the laser to reduce the spot size of the light beam. 1 mm collimator lens mounted in front of the photodiode helped to align the 80 μm laser spot to the small active area of the photodiode.

The electronic circuit of the particle sensor is schematically shown in Fig. 1.37. The Si photodiode is followed by a transimpedance amplifier, which converts the photocurrent into a voltage output. In order to minimize the effects of electrical pick-up, the photodiode was co-integrated with a transimpedance amplifier on a small PCB. As particle diameters are expected to range from 4 μm to 70 μm, i.e. over a factor of $\approx$ 20, a variation of the particle shadow size over a factor of $\approx$ 400 needs to be dealt with. In the interest of resolving smaller particles with regard to larger ones, the second stage was configured as a logarithmic amplifier. This second stage is AC-coupled to the input stage to ensure that only transient signals due to particle shadowing are detected. The next stage is a low pass filter and a buffer amplifier to feed the follow-on circuits. The comparator switches at predefined voltage levels corresponding to the different particle size classes to generate a TTL signal for the counter circuit. A USB counter module was used for the data acquisition and a LabVIEW application was built for the signal processing.

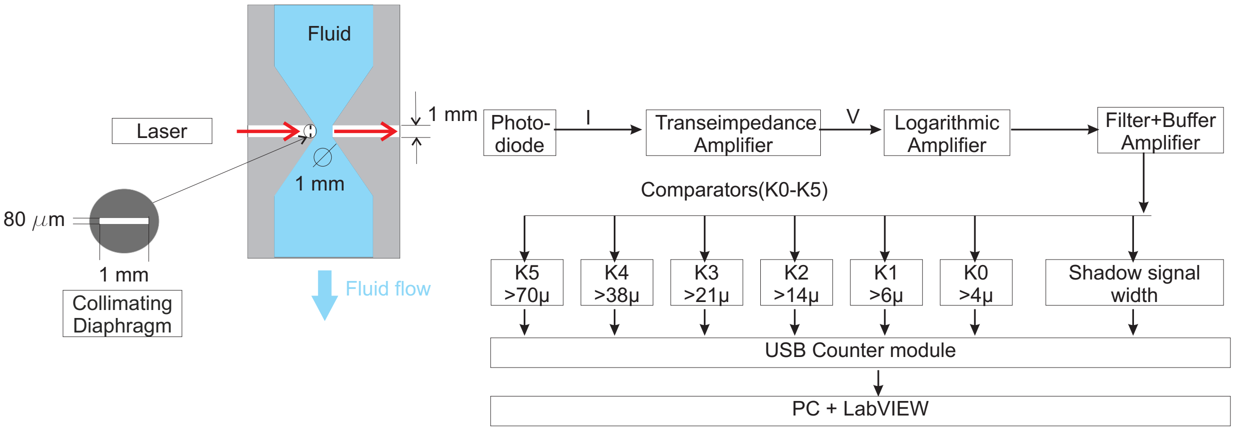

Figure 1.37: *Schematic of the light barrier system (left) and electronic circuit for data acquisition.*

1.5.3 Results

Rotating calibration wheel

Precise calibration of the particle sensor is essential for ensuring a reliable measurement. Experiments with circulating hazardous hydraulic fluids require considerable experimental effort. The sedimentation of particles in the system hampers the calibration process as well. In addition, obtaining test particles with narrow size distributions proved to be very complex. For the purpose of calibration we therefore performed experiments with "synthetic" particles. These particles consisted of photo-lithographically defined shadows formed on a transparent rotating disc. This disc, which is indicated in the left-hand part of Fig. 1.38, contains several rows of particle shadows with sizes corresponding to the particle size classes defined in the AS4059 standard.

The results obtained with the rotating disc are presented in Fig. 1.39. The inner track which consisted all the 6 different particle sizes was traced in this result. The signal at the logarithmic amplifier output clearly reveals that 4 μm particles can clearly be detected. The noise level for the two smallest particle sizes i.e. 4 μm and 6 μm is reduced significantly after the logarithmic amplifier.

Fig. 1.40 shows how the signal amplitude and pulse width changes when the speed of the rotating disc is changed. Whereas the speed of the rotating disc has hardly any influence on the particle signal amplitude. The pulse width is inversely proportional to the flow velocity. Obviously, an exact determination of v_{fl} requires both parameters to be determined independently and exactly.

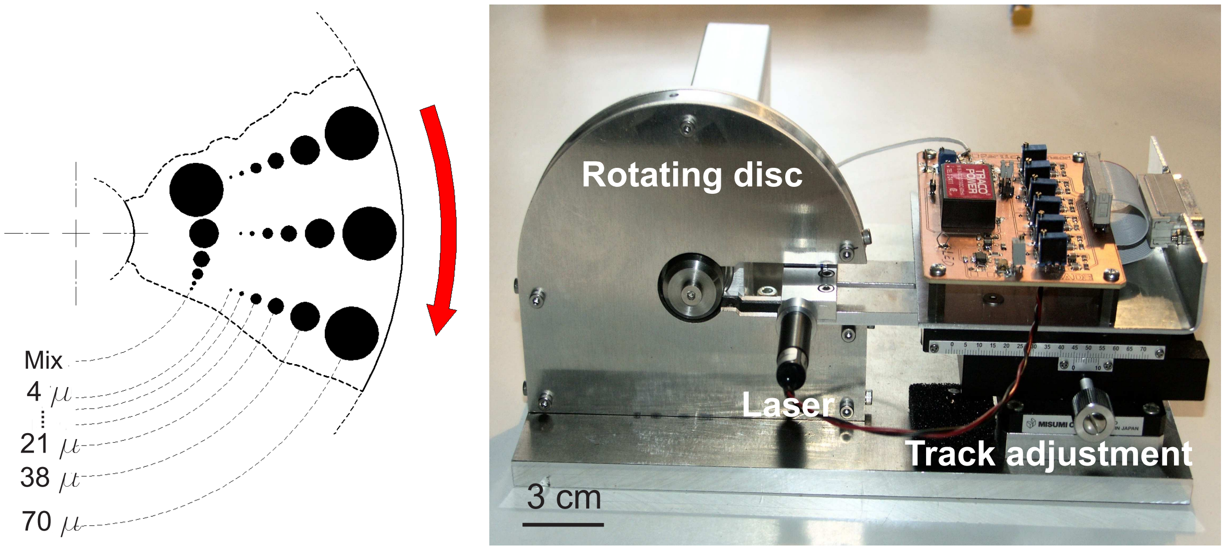

Figure 1.38: *(left) Rotating wheel with traces of photo-lithographically defined particle shadows; (right) wheel mounted on the shaft of an electrical motor. The light barrier (laser and Si-photodiode) can be positioned on the individual particle traces.*

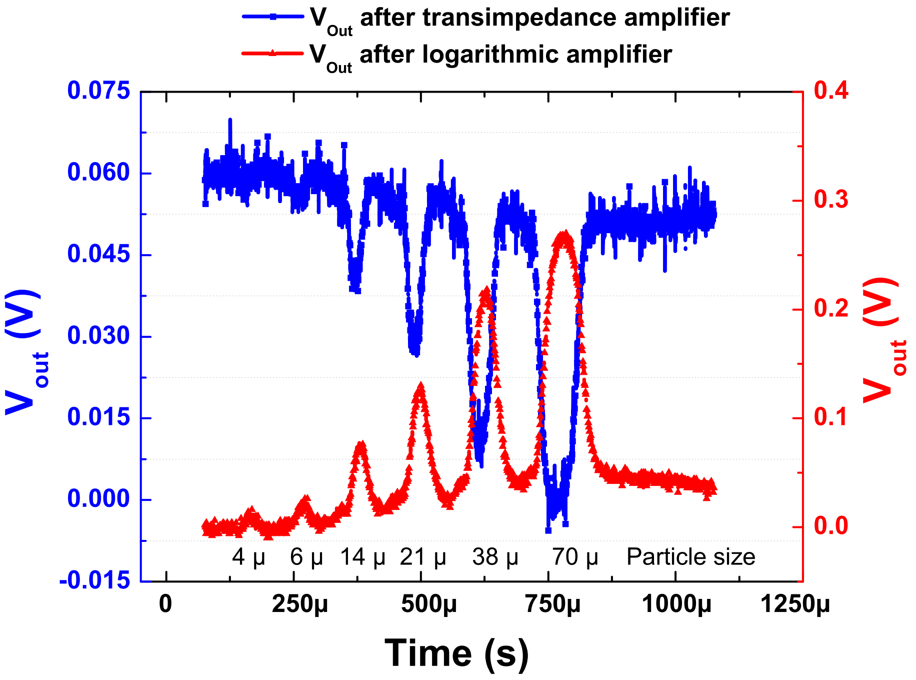

Figure 1.39: *Output signal of the photodiode in response to the series of particle shadows on the inner trace of the rotating wheel. The upper trace represents the output voltage of the transimpedance amplifier and the lower one the output voltage of the logarithmic amplifier.*

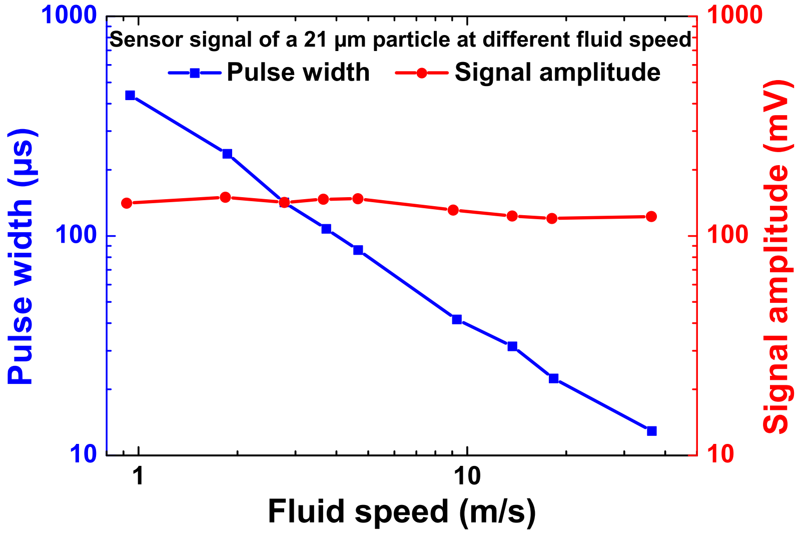

Figure 1.40: *Amplitude and pulse width of the photodiode signal in response to synthetic 21 µm particles as observed at different rotating disc speeds.*

Measurements with hydraulic fluid

For performing measurements with hydraulic fluid, a measurement setup with fluid in a circulated loop was built. The most important features of this set up are: (i) tiny dead volume to minimize the deposit of the standard particles, (ii) laminar flow to avoid disturbing effects due to turbulence and (iii) metallic pipes to avoid electrostatic loading. This setup is shown in Fig. 1.41(a).

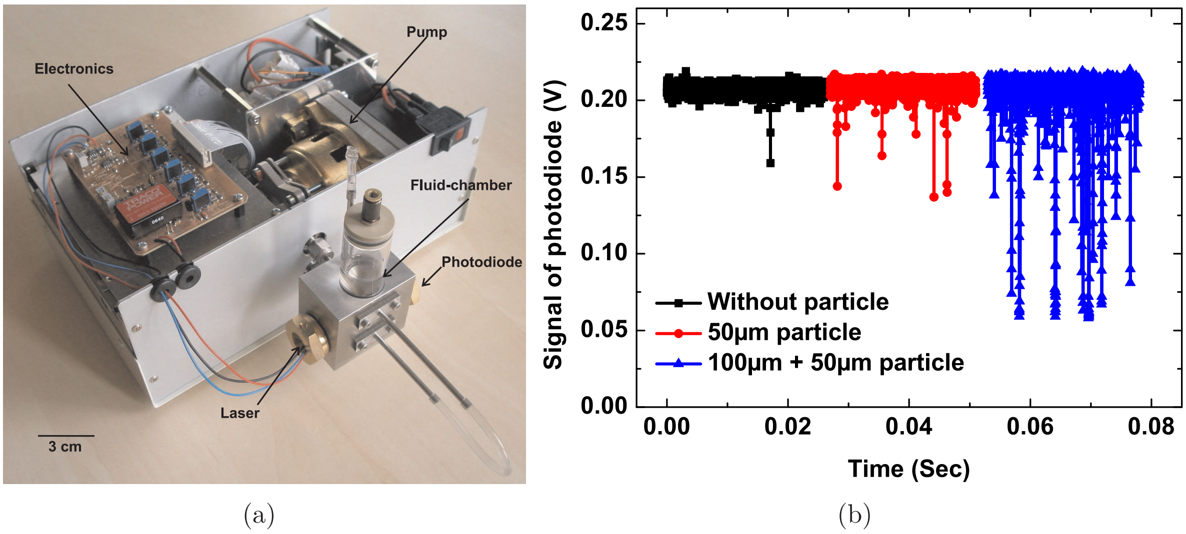

(a) (b)

Figure 1.41: *(a) Realized system for the determination of particle contaminations in hydraulic fluids; (b) measurement results obtained on fluids with addition of two different sizes of artificial particles.*

The measurement cell with the optoelectronic components is mounted on a side wall of the control box as shown in Fig. 1.41(a). On top of the measurement cell a small reservoir was mounted which could be filled with fluids containing well-controlled particle contaminations. The fluid was circulated through the measurement cell by a pump mounted inside the control box. With this pump the fluid flow speed could be varied between 2 and 10 m/s. Fig 1.41(b) shows the results of a measurement cycle performed with fluids contaminated with various test particles. The output signal of the photodiode clearly shows a correlation with the size and number of introduced particles in the fluid. The amplitude of the signal peaks increased with introduction of larger particles and the frequency of peaks rose with addition of particles.

1.6 Integrated sensor system

A possible combination of the particle counter discussed above with the infrared-based chemical contamination sensor for application in aircraft is schematically shown in Fig. 1.42. This multi-parameter sensor is to be inserted into a bypass line connecting the high- and the low-pressure sides of a hydraulic fluid reservoir. The particle counter is mounted on the high-pressure side and the cone-shaped restriction of the flow channel at the light-barrier position serves as a restrictor that reduces the pressure inside the chemical contamination sensor. The resulting low pressure in the chemical sensor part reduces the mechanical load on the relatively large sapphire windows and thus facilitates the mechanical dimensioning of this sensor section.

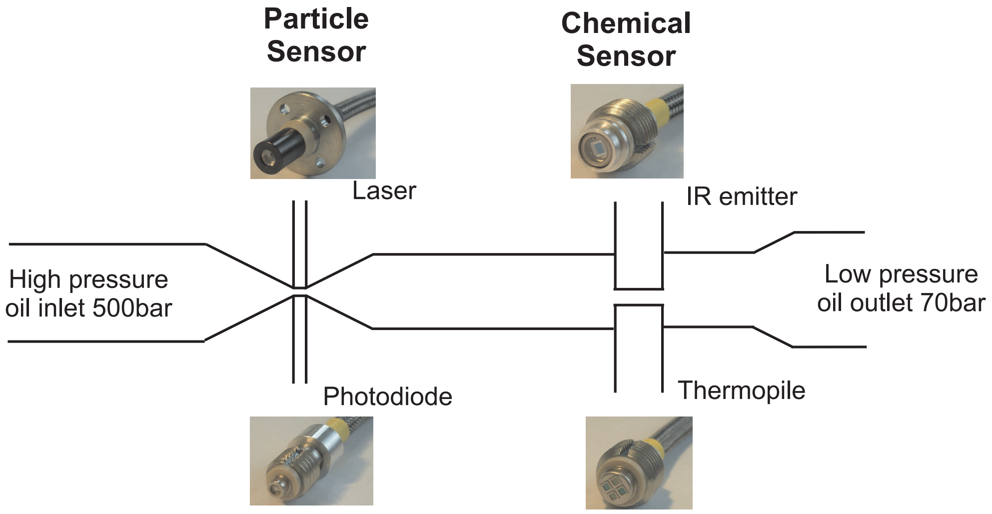

Figure 1.42: *Integration concept involving a particle counter and an infrared-based chemical contamination sensor.*

1.6.1 Test in Airbus hydraulic test bench

An integrated sensor system was built for testing in an Airbus hydraulic test bench in Toulouse, France. The AIRBUS ESTHER 3000 PSI hydraulic test bench mimics from a hydraulic system point of view the entire operation of an aircraft in a condensed way. During simulated flight envelopes, the hydraulic system is powered and actuators are moved as in realistic flight situations. Within this test bench, the sensor manifold was fitted between high and low pressure lines. Fig. 1.43(a) shows the manifold containing both the IR chemical sensor and the particle sensor.

Prior to the integration into the test bench, the manifold was tested to withstand pressures up to 300 bars. All components also had to pass a critical vibration test. After the sensor had been mounted into the test rig, a predefined amount of water was added to the reservoir in several steps. Water sensor results during these tests shown in Fig. 1.43(b), were coherent with the laboratory analysis of the water contamination. The acidity sensor also indicated a very low acidity consistent with the results of the laboratory analysis. No intentional particle contamination was added during these tests. The particle sensor could not reproduce the particle contamination number of the fluid that had previously been determined by laboratory tests. Particle sensors rather seemed to be able to detect instant changes in the particle contamination number caused by the triggering of actuators. Powering of the actuators seemed to create vortices which mobilize previously sedimented particles and which thus makes them visible for the particle detector.

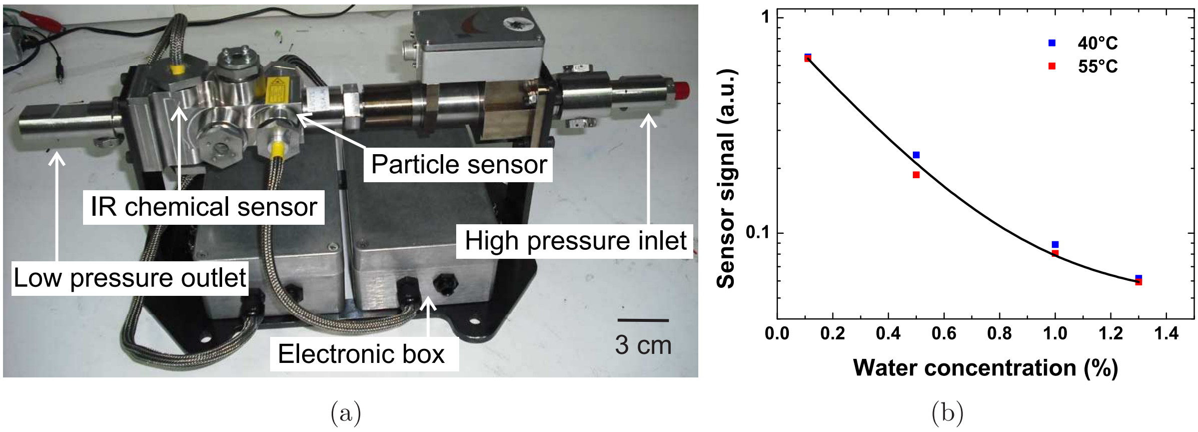

(a) (b)

Figure 1.43: *(a) Integrated sensor system for test in Airbus Esther hydraulic test bench. (b) Sensor response obtained with addition of water at two different temperatures.*

Chapter

2

Gas monitoring

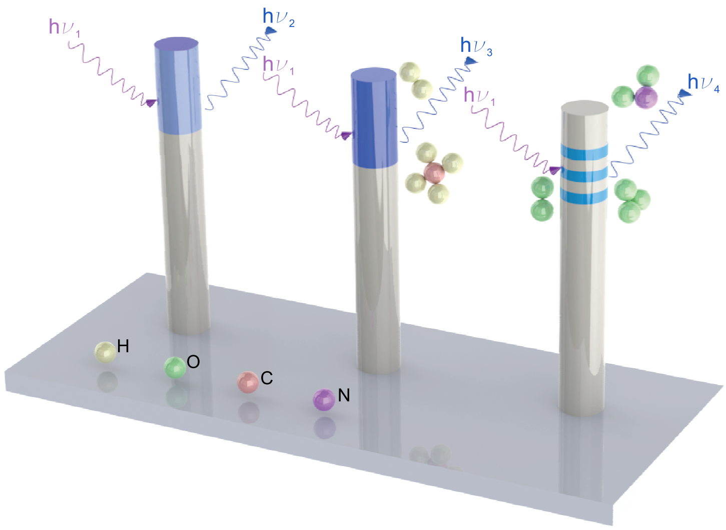

GaN/InGaN nanowires are introduced as optochemical transducers for gas detection. The chapter begins with the potential gas sensing applications in an aircraft. Then the current state of understanding the optical gas sensing mechanism of nanowires and nanowire heterostructures is summarized. Thereafter, experimental details are presented related to the growth of the nanowire transducers and their implementation into an optical fiber based sensor system. The experimental results are divided in to two parts: the first part focuses on the results obtained with hydrogen and hydrocarbon gases; the second part deals with the sensor response to different oxidizing gases.

2.1 Gas monitoring applications in aircraft

Increased passenger comfort, in-flight safety and security as well as smart maintenance are innovation drivers which are leading the aviation industry to investigate novel sensor-based monitoring and control applications and to assess novel sensor concepts and sensor technologies.

Typical applications of gas sensors inside aircraft are:

- Cabin air monitoring
- Fire alarm
- Exhaust gas monitoring
- Leak detection in fuel tank
- Leak detection in hydraulic fluid tank.

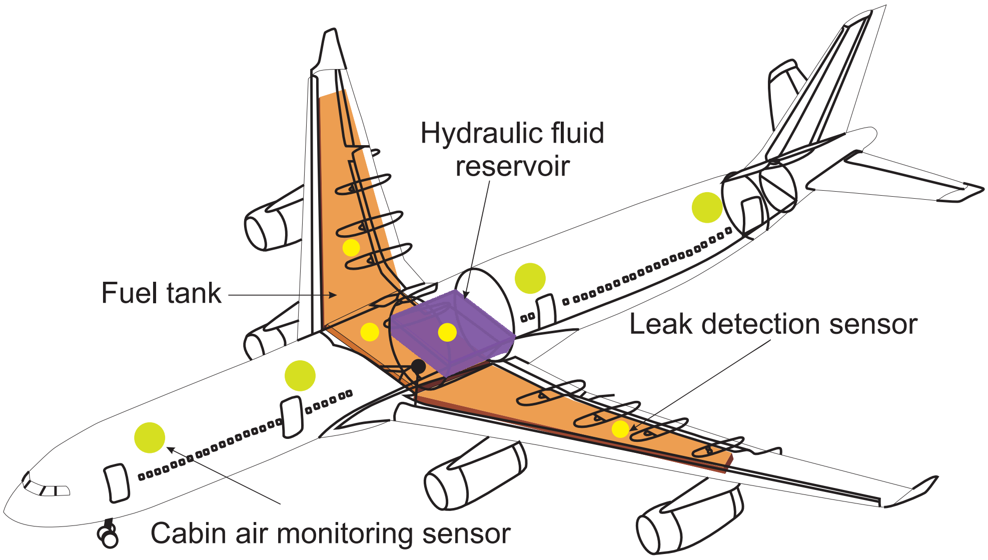

Figure 2.1: *Gas sensing applications in an aircraft is illustrated here. Different colors indicate different functional units.*

2.1.1 Cabin air monitoring

Next to seating, passengers rank air quality as a key comfort criterion in a commercial aircraft [33]. Local air quality is ensured by circulating air inside the passenger cabin while continuously replacing a portion of the used air with fresh from outside. Within the current technology outside air is taken onboard through the engines, circulated within the aircraft, and discarded through the toilets. Measurements of the air quality are currently not performed. Air quality is simply ensured by replacing the entire cabin air volume within less than three minutes. Collecting bleed air through the engines produces considerable friction which must be compensated by additional thrust. Present environmental control systems (ECS) contribute approximately 5% to the total fuel consumption of an aircraft [34]. Driving towards better fuel economy, non-bleed-air ECS architectures are being seriously considered. In such non-bleed air ECS, air monitoring and ventilation-on-demand schemes become increasingly important. Even in today's ECS, air monitoring can perform multiple functions. These are revealed as one moves along the air flow inside the aircraft. During cruise flight cold outside air becomes compressed inside the engines and is adiabatically heated to temperatures far beyond cabin temperature requirements. In order to become useful, the compressed bleed air must be cooled and stratospheric ozone must be catalytically converted into O_2. Like all pieces of technical equipment, the bleed air and the air pre-treatment systems can fail. Possible failures are leaks in the bleed air system and saturation of the catalytic converter. Routine monitoring for traces of lubrication oil and for stratospheric ozone can provide evidence for leaks in the bleed air system and insufficient catalyzer performance. Both pieces of information are important for establishing innovative maintenance-on-demand procedures. Local monitoring of H_2O, CO_2, and volatile hydrocarbons, on the other hand, can establish a measure of the local air quality and air circulation can be adjusted accordingly. Therefore, sensor signals here can contribute to passenger comfort and energy efficiency.

2.1.2 Security application

In the final stage the air is discarded through the toilets. In this final stage air monitoring can contribute to in-flight security. This latter opportunity of security monitoring reveals from the fact that toilets can be misused as chemical laboratories in which easily available liquids can be mixed and converted into improvised high explosives. Alleged terrorist plots of this kind have been discovered and prevented [35]. Precursor vapors to be detected are H_2SO_4, HNO_3, H_2O_2 and acetone - in variable background air.

2.1.3 Fire/smoke detection

Several aircraft areas are equipped with fire detection instruments. These are located in the cargo compartments, the electronic compartments and the lavatories [36]. The discarded air from the passenger cabin is passed through the cargo compartments, the avionic racks, and the in-flight entertainment equipment. All these compartments are inaccessible during flight and therefore need to be routinely monitored for fire hazards. In the event of a fire, many types of gases can evolve. In order to comply with the requested low false alarm rates of 1 per 10^7 flight hours [37], new kinds of fire detectors like multisensor/multicriteria (gas, smoke, heat etc.)- or gas sensor based fire detectors are being intensively investigated [38, 39].

2.1.4 Fuel/hydraulic leak detection

Hydrocarbon detection is an important asset to introduce into commercial airplanes, as such airplanes contain a multitude of fuel and hydraulic lines that cross many areas of the airplane not readily accessible to service personal. Due to intense vibrations, large temperature changes and high fluid pressures such lines bear a relatively high risk of leakage. Leakages in hydraulics lines cause fluid losses, compromise the hydraulic system performance, and spilled fluid causes corrosion on the fuselage and on the built-in instrumentation. Spilled fuel, on the other hand, can evaporate and form explosive fuel-air mixtures. In a rocket engine, when the hydrazine is leaked into air, it immediately dissociates into NO_2 [40]. As a result, NO_2 gas is detected in the trace amount to determine the fuel leakage. Leak detection by "smelling" evaporating fluid therefore can contribute to increases the safety of flying quite considerably.

2.2 State of the art gas sensing technologies

The field of gas sensors is a very diverse area of technology. This has partly to do with the multitude of gases which need to be detected in specific application domains and partly with the boundary conditions which are imposed on the use of gas sensors within these application domains. As a consequence, there is no single technological approach which is able to serve all practical needs. As there are many good text books and reviews in this field [41–43], only a brief overview in tabular form is given here. Table 2.1 presents an overview over the diverse kinds of sensor technologies that presently exist. Table 2.2 provides more detail on the sub-field of hydrogen gas sensors. Operating principle of most of the hydrocarbon sensors is the proton conduction of the sensing element, which is the sensing principle of hydrogen gas sensors as well and therefore not discussed here in details.

Sensor principle	***Operating principle/ device***	***Physical change/ measured***	***Characteristics***	
			Advantage	***Disadvantage***
Catalytic	Pellistor [44]	Temperature/ Resistance	Robust, stable, long lifetime, wide operating temperature range, low cost proven technology	Susceptible to poisoning, high power, requires oxygen for operation, positioning critical, long response time
	Thermoelectric [45]	Thermoelectric /Voltage		
Thermal conductivity	Calorimetric [46]	Temperature/ Voltage, Resistance	Fast, robust, stable wide measuring range, does not require O_2 , resistant to poisoning, low cost	High concentration only, limited range of gases, cannot measure gases with conductivity close to air, high maintenance
Electrochemical	Amperometric [47]	Electrical current	Can measure low concentration, wide range of gases can be detected, low power, high temperature operation possible	Restricted lifetime, regular calibration needed, positioning critical, aging, high cost
	Potentiometric	Voltage		
Optical	Optrode [48]	Transmission, Reflectance, λ-polarization, ϕ-shift	Can measure very low concentration, no source of ignition in explosive atmospheres, wide area, low calibration error	Drift by aging, high cost, positioning critical
	Infrared absorption	Transmission, Reflectance		
Acoustic	Surface acoustic wave [49]	Time	High sensitivity, fast, low power, wide detection range, long life	Sensitive to environment change, high cost, only low temperature operation
	Ultrasonic	Wave velocity		
Semiconductor [42]	Resistive	Resistance	Low cost, wide range of gases can be detected, long life, high sensitivity	poor selectivity, sensitive to environment change, drift, hysteresis
	Schottky diode	Current		
	MOS FET	Voltage		
	MIS capacitor	Capacitance		

Table 2.1: *Summary of basic gas sensing method. [50, 51]*

Like for other gases, several hydrogen sensors are available on the market. The performance and characteristics of these commercially available sensors are summarized in the following Table 2.2.

Sensor type	Principle/ Device	Measuring range/vol%	Response time(t_{90})/s	Gas environment	T_{life}/ years
Catalytic	Pellistor	Up to 4	<30	-20 to 70°C, 5-95% RH, 70-130 kPa	5
Thermal conductivity	Calorimetric	1 - 100	<10	0 to 50°C, 5-95% RH, 80-120 kPa	5
Electrochemical	Amperometric	up to 4	<90	-20 to 55°C, 5-95% RH, 80-110 kPa	2
Resistance based	Semiconducting metal–oxide [52]	up to 2	<20	-20 to 70°C, 10-95% RH, 80-120 kPa	>2
	Metallic resistor [53]	0.1-100	<15	0 to 45°C, 0-95% RH, up to 700 kPa	<10
Work function based	Capacitor [54]	up to 5	<60	-20 to 40°C, 0-95% RH, 80-120 kPa	10
	MOSFET [55]	up to 4.4	<2	-40 to 110°C, 5-95% RH, 70-130 kPa	10
Optical	Optrode [56, 57]	0.1-100	<60	-15 to 50°C, 0-95% RH, 75-175 kPa	5

Table 2.2: *Performance characteristics of commercially available hydrogen sensors. Data have been collected from datasheets provided by sensor suppliers. [50, 58]*

Usually, the technology involved is adapted to the specific application and to the available in-house technology.

2.2.1 Examples of nanowires as transducers

In 1962 it has been shown that the absorption or desorption of reactive gases at the surface of metal oxide semiconductors can lead to considerable electrical conductivity changes. This phenomenon was first demonstrated on thin films of zinc oxide [59]. More recently, advances in the field of nanotechnology have led to a surge in interest in the application of nano structures for gas detection. Various kinds of nanosensors (nanowires, -belts, -ribbons, -rods, -tubes) have been reported to be sensitive to different kinds of analyte gases [60]. Materials used in these sensors are mainly ZnO, SnO_2, TiO_2, WO_3, In_2O_3 etc [42, 61]. The small sizes and high surface-to-volume ratios of one-dimensional nano structures endow them with a variety of interesting and useful sensing properties such as high sensitivity and enhanced stability. Few examples of such nanosensors for gas detection are presented in the following sections.

Hydrogen sensors
MOX nanostructures have been proposed as highly sensitive hydrogen sensors. Examples are ZnO nanowires [62, 63], TiO_2 nanotubes [64, 65], SnO_2 nanowires [66, 67] and VO_2 nanowires [68]. Metalic nanodevices with tungsten [69] or palladium nanowires, synthesized by template manufacturing techniques have also been studied for hydrogen gas-sensing applications [70]. Pd-coated GaN nanowire sensors have been reported to exhibit room temperature sensitivity [71]. Nanofibers of a conductive polymer (polyaniline) [72], carbon nanotubes [73], single-walled carbon nanotubes and palladium nanoparticles on a flexible plastic substrate have been suggested for H_2 gas sensors in various applications [74].

Oxygen sensors
Work on SnO_2 single nanowire based FET structures showed that the conductance of the device decreased upon exposure to oxygen [75]. The photoluminescence intensity of SnO_2 nanoribbons have been reported to be sensitive to oxygen [76]. The intensity of the blue band PL declined with increasing oxygen concentration. Ultrafast resistive oxygen sensor elements of CeO_2 nanograins operated at 1073 K with response time of 9 ms have been investigated with the focus of application in automotive combustion engines [77]. Resistive sensors based on In_2O_3 nanopowder have been shown to be responsive to O_2 at RT. [78]. Ultra low concentrations (PPM level) of O_2 could be detected using ZnO nanobelts aided by UV exposure [79].

Nitrogen dioxide sensors
Most of the nanowire based sensors reported to date have been sensitive to NO_2. Hundreds of publications report on NO_2 sensing behavior of 1D nanostructure [60, 70, 80–85]. Ultrasensitive chemoresistors based on TiO_2 nanofibers showed sensitivity to single ppb gas concentration [86]. The resistance of the nanowires at moderate temperature to high temperature increased when these were exposed to NO_2. The sensitivity of the of Nanocrystalline WO_3 was increasing with decreasing grain size [87]. Exposure to UV radiation also enhances the sensitivity due to increased photoconductivity [88]. Carbon nanotube based devices also have reported to have profound response to NO_2 [89, 90]. Optical detection of NO_2 based on NW devices has been shown to be feasible by the group of G. Sberveglieri. Exposure to a few ppm concentrations of NO_2 significantly quenched the visible PL emission of SnO_2 and ZnO nanowires – a change which was not affected by variations in the relative humidity and in the presence of other trace gases [91–93].

Ozone sensors
Unlike other oxidizing gases ozone sensors based on nanowire devices have not been examined intensely. The resistivity of ZnO nanorods is reported to increase with increasing O_3 concentration [94–96]. In_2O_3 nanocrystals operating at 200°C are used for detecting O_3 concentrations at ppb levels [97]. Rapid response and recovery times in the range of a few seconds have been demonstrated by Chien et al. [98, 99]. Carbon nanotube based devices with very low detection limits and response times have been demonstrated by Park et al. [100].

Other chemical compounds which were reported to be detectable by nanowires are CO [101], NH_3 [102], ethanol [103], methanol [104], H_2S [105], He [106].

2.2.2 General sensing mechanism of conductive nanowire sensors

After intense research in the previous decade the sensing mechanisms in NW gas sensors have been established. In MOX NWs the sensing mechanism is mainly governed by oxygen vacancies at the NW surfaces which are electrically and chemically active. Two kinds of sensing responses dominate [107]: upon adsorption of oxidizing gases, such as O_2, O_3 and NO_2, at vacancy sites, electrons are withdrawn from the conduction band and immobilized at the adsorbed molecules that act as electron acceptors, forming various surface oxygen ion species. Upon adsorption, reducing gases such as CO and H_2 interact with the co-adsorbed oxygen ion species forming neutral reaction products such as H_2O and CO_2. In this way, surface-trapped electrons are released back to the conduction band. As revealed by Fig. 2.2 and the reactions below, both kinds of sensing interactions rely on the presence of oxygen at the sensor surface:

Reducing response:

$$CO + O^- \rightarrow CO_2 + e^- \tag{2.1}$$

Oxidizing response:

$$NO_2 + e^- \rightarrow NO_2^- \tag{2.2}$$

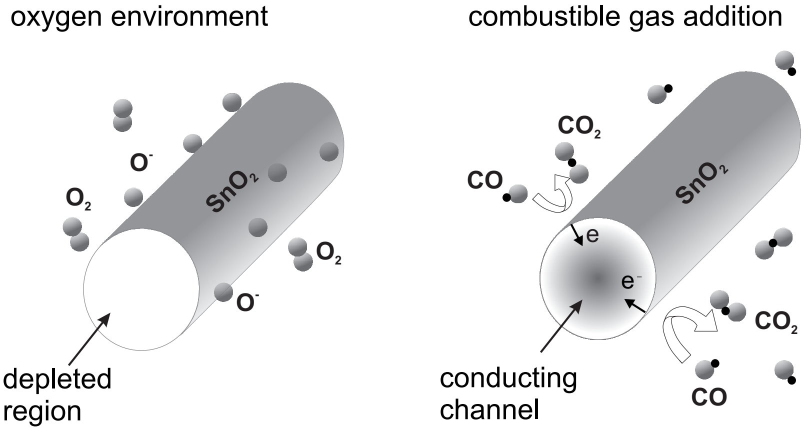

Figure 2.2: *Gas sensing interactions at SnO_2 NW surfaces: (left) exposure to oxidizing gases causes electrons from the NW bulk to become surface-trapped at adsorbed oxygen ion species, thus reducing the NW bulk conductivity; (right) adsorption of reducing gases and interaction with co-adsorbed oxygen ion species causes surface-trapped electrons to be transferred back into the NW bulk thus causing an enhanced conductivity [75].*

2.3 Optochemical nanowire gas sensors

In this work optochemical transducers based on group III-nitride nanostructures are investigated. The results presented in this thesis reveal the capability of such sensors to address several of those gas sensing applications that have been discussed in the previous section.

2.3.1 Advantages of optochemical sensors

The detection of chemical components by optical sensors offers particular advantages with respect to other electrochemical sensors.

- Optochemical transducers allow for the realization of sensor systems with built-in media separation and hence capable of operating in harsh environments. This concept is illistrated in Fig. 2.3.
- Significantly lower operating temperatures than field-effect (FE) and metal oxide (MOX) gas sensors.
- No electricity and complex wiring in safety critical areas are required.
- Optical excitation and interrogation exclusively through optical fibers.
- Immune to electromagnetic interference.
- No chemical changes in the medium to be sensed.

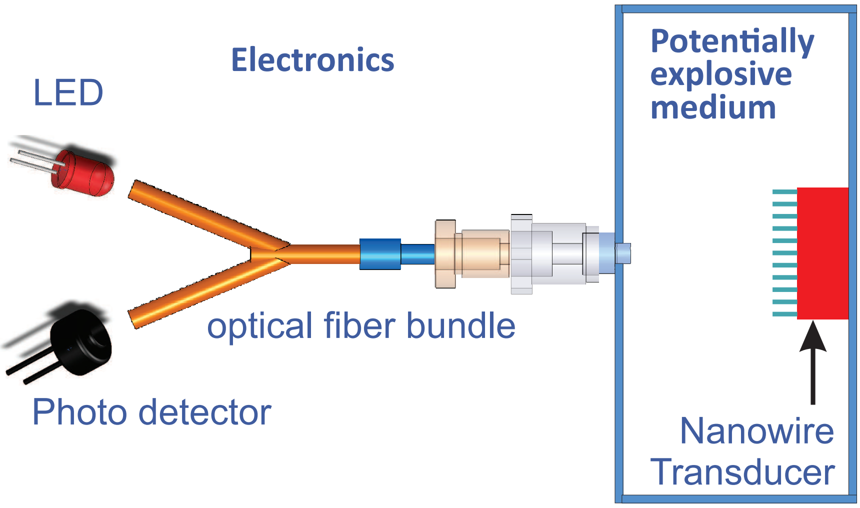

Figure 2.3: *Meadia seperation can be obtained by utilizing optochemical transducers.*

2.3.2 Group III-nitride as optochemical transducers

During the past two decades, group III-N compound semiconductors and their alloys have become a reliable technology base for the realization of innovative semiconductor devices [108, 109]. Photodetectors, light emitting diodes, lasers, HEMT (High Electron Mobility Transistors) and electro–optic modulators are just a few examples worth mentioning [110–

112]. Owing to their wide bandgap, these materials are excellent candidates for devices operating at high temperatures and in chemically aggressive environments. A wide range of physical, chemical and biological sensors has been realized using III-N materials. The electrical properties of devices realized with these materials have been intensely investigated for gas sensing applications during the previous decade [113–116].

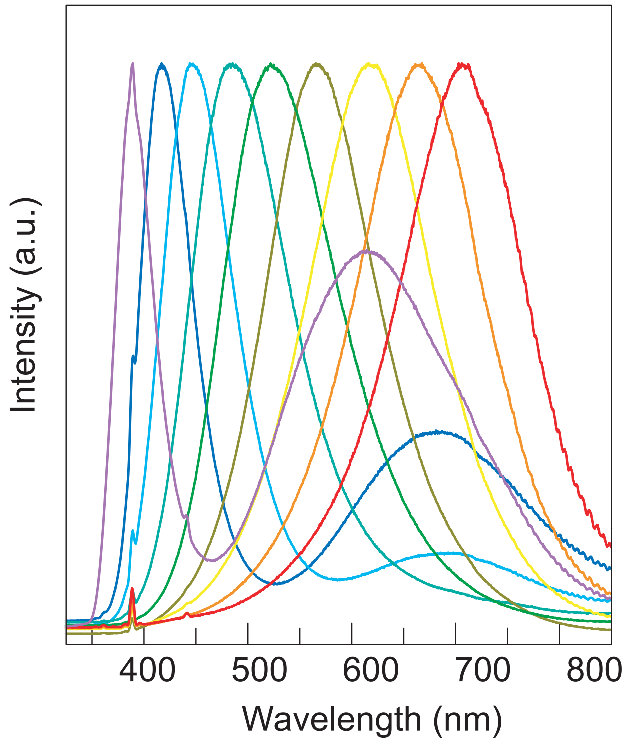

Figure 2.4: *PL emission of* $In_xGa_{1-x}N$ *nanowires (*$x = 0$ *to 0.6). The energy band gap of* $In_xGa_{1-x}N$ *can be engineered to cover from near ultraviolet to near infrared parts of the electromagnetic spectrum [117]. Copyright 2001 Nature Publishing Group.*

Wide-band-gap III-N binary and ternary alloys, with energy gaps ranging from the deep-ultraviolet to the mid infrared parts of the electromagnetic spectrum, belong to the group of dominant materials for optoelectronic devices [118]. Fig. 2.4 shows the tunability of the direct bandgap of $In_xGa_{1-x}N$ nanowires photoluminescence in the wavelength range from 325 to 850 nm. The high brightness and longer lifetimes of the nitride semiconductors make them optimum choices for optoelectronic devices [119].

2.3.3 Photoluminescence spectrum of GaN

Typical photoluminescence spectra of high quality unintentionally doped GaN grown by HVPE (hydride vapor phase epitaxy) and measured at room temperature and at 6 K are shown in Fig. 2.5 [120]. The PL spectrum changes significantly when going from 300 to 6 K with most apparent differences in the temperature dependence of the peak emission energy and the thermal broadening. At 6 K well resolved PL is visible near the intrinsic optical bandgap energy at 3.47 eV. This strongest peak is attributed to bound exciton recombination. Unintentionally doped GaN is invariably n-type in nature. Therefore this exciton recombination is associated with a neutral donor (D^0X). The bound excitons are found typically up to 100 K, where they thermally dissociate and the free exciton recombination dominates the spectrum. They are commonly denoted as A, B, and C valence bands, beginning from the top. Therefore, the main PL peak observed at room temperature at 3.40 eV is attributed to free A-exciton recombination.

In Fig. 2.5, at 6 K the D^0X is accompanied by a longitudinal-optical (L_0) phonon replica located at 3.38 eV nearly 92 meV lower in energy. Excitons are able to couple to the polar L_0 phonon modes of the crystal lattice due to the Fröhlich interaction [121]. This results in phonon replicas of the zero-phonon emission which are spaced at integers of the phonon energy, that is

$$h\nu = E_0 - nE_{ph} \tag{2.3}$$

where E_0 is the zero-phonon emission energy, n is an integer, and E_{ph} is the phonon energy. The origin of the PL peak at 3.33 eV in Fig. 2.5 is attributed to Mg-impurities in Ref. [120].

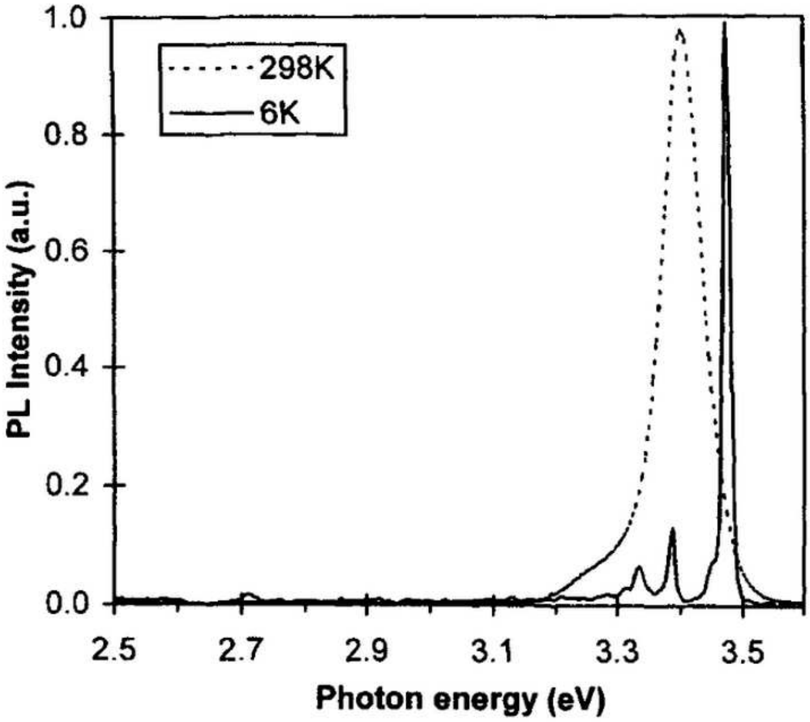

Figure 2.5: *Photoluminescence spectra of unintentionally doped GaN measured at room temperature and at 6 K [120, 122].*

At low temperature several near-bandgap PL peaks are noticeable in high quality GaN samples. The donor acceptor pair recombination (DAP) can be observed at 3.28 eV is due to the zero-phonon recombination of electrons bound to donors and holes bound to acceptors. The DAP transition energy is given by:

$$h\nu = E_g - E_D - E_A + \frac{q^2}{\epsilon R} \tag{2.4}$$

Where, E_g is the band gap energy, E_A and E_D are the ionization levels of the donor and the acceptor, respectively. The last term on the right hand side represents the Coulombic interaction between the ionized donors and acceptors. R is the distance between the charges and it is much larger than the lattice constant.

The most frequently observed PL bands related to defects in GaN is located at 2.2-2.3 eV. This band is referred to as "Yellow band" due to its spectral location. The origin of this PL peak is debated over the years till to date. Transition of free or weakly bound electrons from the CB edge to a deep acceptor level located around 860 meV above the valance band edge is mainly attributed to the origin of this luminescence. The ratio of the magnitude of near band edge PL peak and yellow PL peak is often referred to reflect the quality of GaN samples.

Band profile in nanowire

The presence of surface states in bulk semiconductors causes the Fermi level pinning which causes a band bending [123]. Because of this Fermi-level pinning at the surface, the electronic bands, conduction (E_C) and valence (E_V), are bent upward at the surface of a nanowire with n-type doping. This situation is schematically shown in Fig. 2.6. Electrons prefer the inner part of the column, whereas holes tend to move to the surface. Due to their spatial separation, surface recombination of carriers is almost impossible. As also shown in Fig. 2.6, a decrease of the column diameter leads to complete depletion at a critical diameter d_{crit} with unchanged surface barrier height. Down to this critical diameter, the recombination rate does not change significantly. Further reducing the dimensions, however, causes less band curvature and therefore a reduction of the barrier for surface electron hole pair recombination. With decreasing thickness now the recombination process is strongly enhanced.

Calarco et al. determined d_{crit} to be around 80 to 100 nm with his photoconductivity experiment utilizing GaN NW [124]. It was shown that the dark and photocurrents in GaN NW are governed by depletion space charge layers. With UV illumination the photocurrent through the NW remains on a relatively high level as long as the column diameters exceed the critical value around 80 to 100 nm, where the column is completely depleted. Below this critical diameter surface barriers are diminished and the photocurrent drops steadily due to enhanced surface recombination.

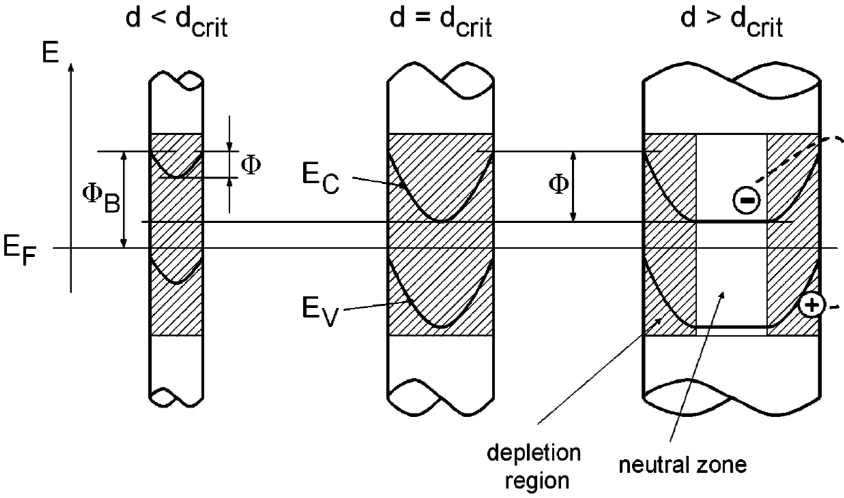

Figure 2.6: *Shape of conduction (E_C) and valence band edges (E_V) and depletion zones (shaded areas) in nanowires with different thicknesses d. The band bending causes electrons and holes to spatially separate and thus to avoid recombination. The detail on the right shows the surface recombination mechanism of photo-excited excess carriers [124].*

Nanowire heterostructures (NWH)

Nanowire heterostructures are formed by growth of dissimilar materials within nanowires. The optical properties of such heterostructures are determined by carrier confinement due to reduced lateral and axial dimensions and by the presence of polarization-induced internal electric fields [125].

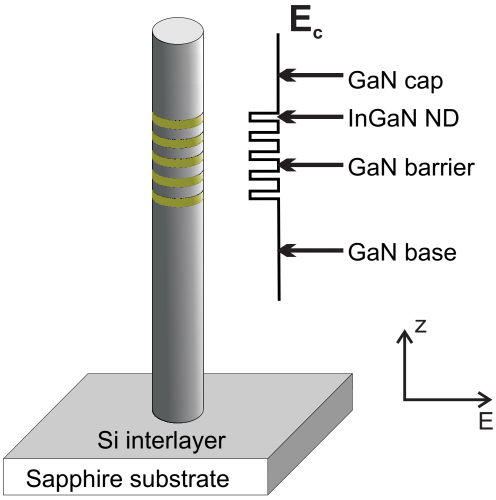

Figure 2.7: *Schematic illustration of an InGaN/GaN NWH grown on a sapphire substrate. The full line at the right shows the variation of the conduction band edge with the growth direction of NWH.*

The band discontinuities resulting from the difference in band gap energies cause the carrier confinement. For type-I heterostructure such as GaN/InGaN, both the conduction and valence band edges of InGaN is located within the band of GaN as shown in Fig. 2.7, which is advantageous for electrons and holes to simultaneously accumulate in the InGaN nanodiscs, and thus enhance the carrier recombination. The polarization discontinuity between GaN and InGaN results in a fixed charge density at the heterostructure interfaces. This charge density will thus generate an internal electric field and also induce a band bending along the axial direction in the nanodisc region. The presence of band bending influences the extraction of photogenerated carriers from the nanodiscs.

The nanowire axial heterostructures have been researched intensely for optical emission and detection applications, where the ability to embed the active material within transparent leads is of great advantage. In addition to this, tunable optical emission from quantum discs in nanowires has been demonstrated in several systems [126–131].

2.3.4 Advantages of nanowires and nanowire heterostructures as optoelectronic devices

III-V semiconductors in the form of NWs offer several advantages for opto-electronic applications [132–134].

- The geometry of free-standing NWs grown on a substrate is characterized by a small interface area and the nearby free sidewalls. Thus, strain induced by lattice mismatch can elastically relax for a wider range of mismatches and thicknesses than in conventional planar layers. Also, dislocations are discontinued at the interface or are likely to bend towards the sidewalls and they are much less likely to be formed due to the release of strain.
- The coupling of light into and out of NWs is expected to differ substantially from the planar case, which may lead to higher external quantum efficiencies of optoelectronic devices.
- A particularly promising use of these advantages can be made in the growth of III-V semiconductor NWs in high crystal quality on Si substrates. Progress in this field is likely to enable the fabrication of highly efficient light-emitting diodes on cost-effective substrates and the monolithic integration of light emitters with complementary metal oxide semiconductor (CMOS) technology [135].

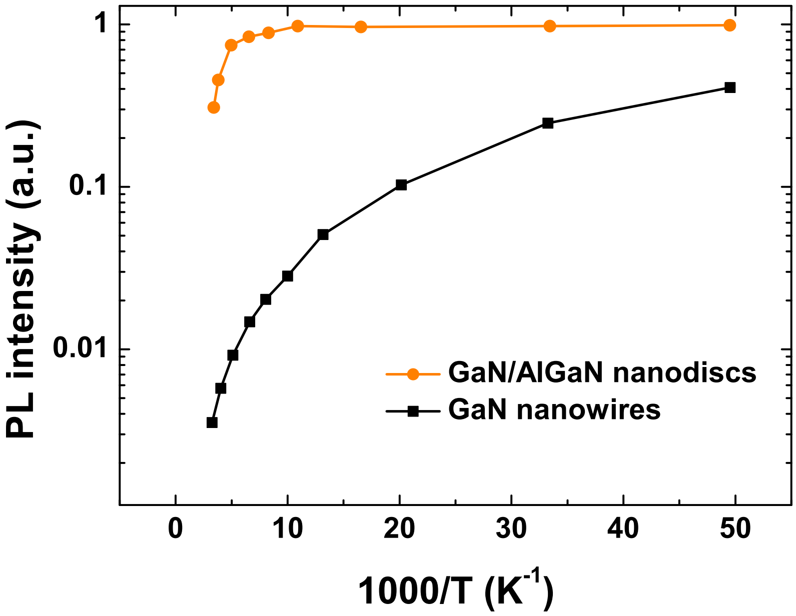

Figure 2.8: *Temperature dependence of the PL intensity of GaN nanowire ensemble (black) and GaN nanodiscs with embedded in GaN/AlGaN nanowires (amber). The PL intensity of nanowires with embedded nanodiscs shows significantly improved thermal stability in comparison to those without heterostructures [136].*

Nanowire heterostructures (NWHs) with the combination of two or more materials within the same nanowire structure offer the two important advantages over their homogeneous counterparts.

- Well controlled structure and PL emission energy
- High temperature stability of PL-emission

Fig. 2.8 compares the thermal stability of a GaN/Al$_x$Ga$_{1-x}$N heterostructures and the GaN homogeneous nanowires. At room temperature the PL intensity of the nanowires with heterostructures enhanced at least two orders of magnitude. This facilitates the operation of these structures as optochemical transducer at room temperature and above.

2.3.5 Growth process

A schematic of the nanowire heterostructures that make up the optochemical transducers is presented in Fig. 2.9. The hetereostructures were grown by plasma-assisted molecular beam epitaxy (PAMBE) at the Walter Schottky Institute in the Technical University of Munich. The GaN/InGaN NWHs consist of a GaN nanowire base part with a length of approximately 400 nm, followed directly by a number of GaN/InGaN heterostructures. The multi-quantum well structures consist of a series of InGaN nanodisks separated by 7 nm thick GaN barriers and a 20 nm GaN cap layer at the top surface. In our experiments the thickness d of the nanodisks was varied within the range 1.3 nm $< d <$ 4 nm. Typical NW diameters ranged between 25 nm up to 50 nm. In order to achieve light emission in the desired wavelength range, appropriate choices of the In molar fraction x were made as the In$_x$Ga$_{1-x}$N nanodisks were deposited.

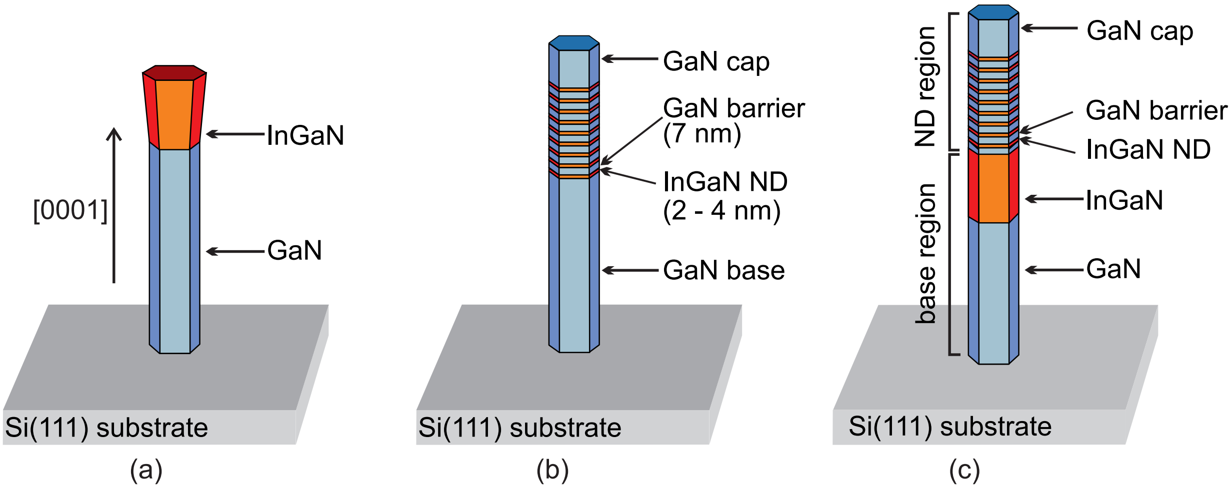

Figure 2.9: *Sketch of the nanowires with various kinds of heterostructures. The height of the nanowire is approximately 400 nm. The thickness of the nanodisks ranges between 1.3 nm to 4 nm.*

At low temperature the photoluminescence signal stemming from the GaN and InGaN base is much more intense than the signal stemming from the heterostructures. The relative contribution of the insertions rises with increasing temperature. We performed our sensing experiments at room temperature and above. Therefore we expected that the InGaN insertions should be less sensitive to temperature than the GaN and InGaN base.

The main challenge in the growth of these heterostructures is the large difference in growth temperatures of the GaN and InGaN material systems. This difference arises from the fact that In desorbs much more rapidly from the growth surface than Ga. In order to avoid InGaN decomposition, the GaN base region was grown at the optimum GaN growth temperature of T_{GaN} = 770°C. Thereafter, the deposition was stopped and the growth temperature was lowered to T_{InGaN} = 565°C to deposit the InGaN nanodisk regions. The lower growth temperature helped to avoid the problem of InGaN decomposition but also leads to a widening of the NW diameters at the outer surface of the NW array [137]. The In concentration in the InGaN part was adjusted from 20 to 35%, which resulted in PL peak emission energy of 2.70 to 2.25 eV and the band parameters reported in ref. [138].

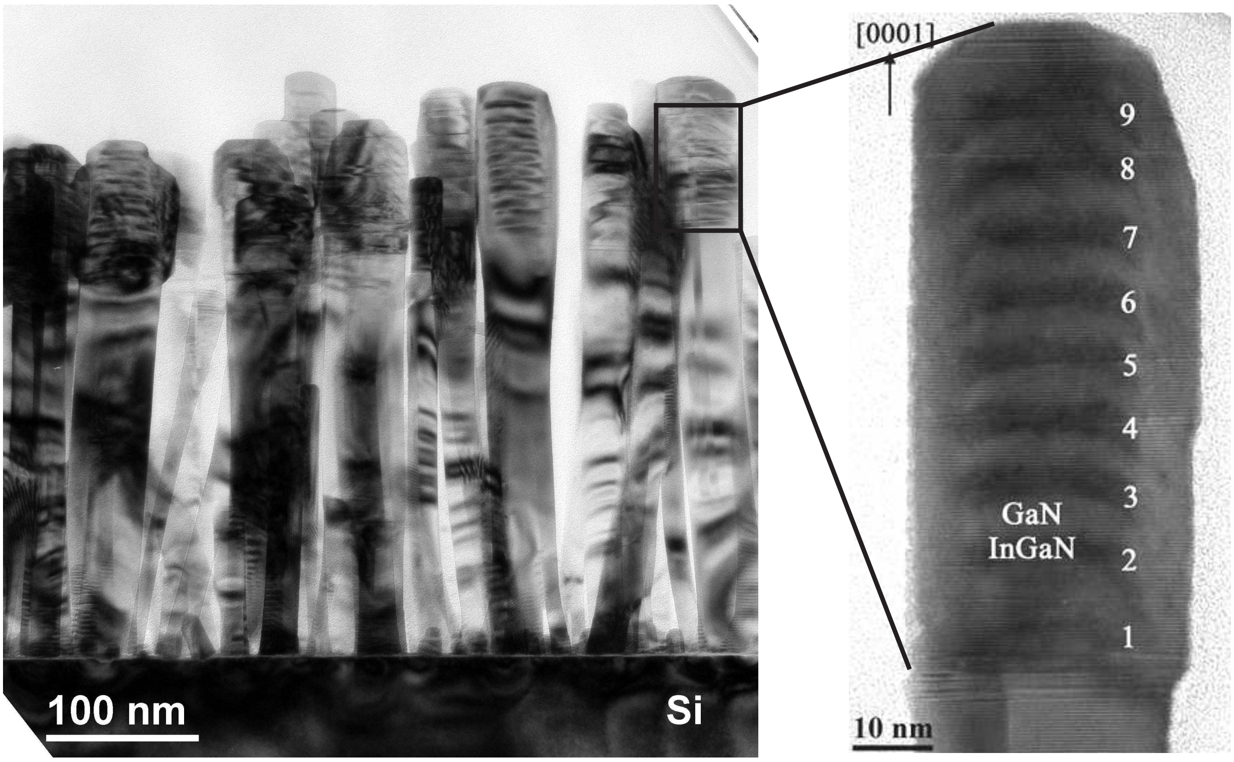

Figure 2.10: *Cross sectional TEM image along [11-20] GaN z.a. (zone axis), showing the overall nanowire structure (left) and 9 periods of GaN/InGaN QD-like nanodiscs (right) [137].*

Initially the NWHs were grown on Si substrates. Details on their growth on Si substrates have already been reported by Furtmayer et al. [139, 140]. Additionally, transparent sapphire substrates were chosen to illuminate directly through the substrate and achieve the desired media separation.

2.3.6 PL emission properties

The GaN- and InGaN-parts of the NWH exhibited an efficient PL emission when excited with UV light at wavelengths shorter than 354 nm. Low-temperature PL emission spectra obtained under such conditions are shown in Fig. 2.11. The spectra exhibit three distinct emission bands. The highest energy band centered around 3.45 eV is assigned to emission from the GaN NW base. A second, broader emission band centered at 3.15 eV is observed in both the low- and high-temperature grown superlattices. The emission band is assigned to recombination in cubic inclusion of InGaN alloys, formed due to the presence of BSFs (basal stacking faults) and In diffusion in the GaN/InGaN interface region or to localization at BSFs [137]. The emission band around 2.4 eV is assigned to emission from the InGaN NDs.

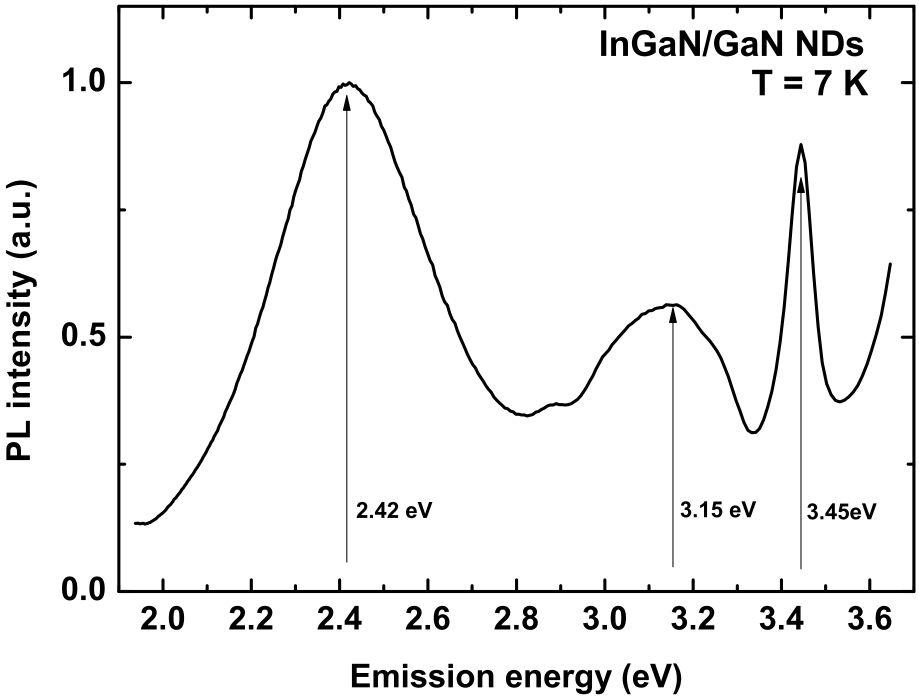

Figure 2.11: *Low temperature PL spectrum of GaN/InGaN NWH ensemble with series of embedded 4 nm InGaN nanodisks. Three different emission bands from the GaN base (high energies), the InGaN/GaN interfacial area (medium energies) and the InGaN NDs (low energies) can be distinguished [137].*

The most intense emission peak of the PL spectrum shown in Fig. 2.11 occurred at around 2.45 eV. The temperature dependance of this emission is illustrated in Fig. 2.12. Higher transducer temperatures caused the emission intensity to decrease. At room temperature the remaining emission intensity amounted to roughly 7.5% of its 10 K value. In general, the bandgap of semiconductors tends to decrease as the temperature is increased. Therefore a redshift is expected in the PL peak positions as the temperature is raised. Fig. 2.12 also shows the shift of peak emission energy towards slightly higher photon energies at higher temperatures. Instead of a steady red shift of the bandgap energy, the PL peak of InGaN related devices shows a "S-shaped" (red-blue-red shift) dependence of PL peak with rising temperature. Thermal activation of the localized carriers from deeper localization centers to shallower localization center is the reason behind the blue shift [141]. The carrier localization effect is caused by the inhomogeneous alloy composition [142]. The temperature dependence of the emission peak position is illustrated in Fig. 2.13. The peak emission here is blue shifted by about 20 meV in the temperature range of 7-30 K and is red-shifted by about 100 meV in the range of 60-300 K.

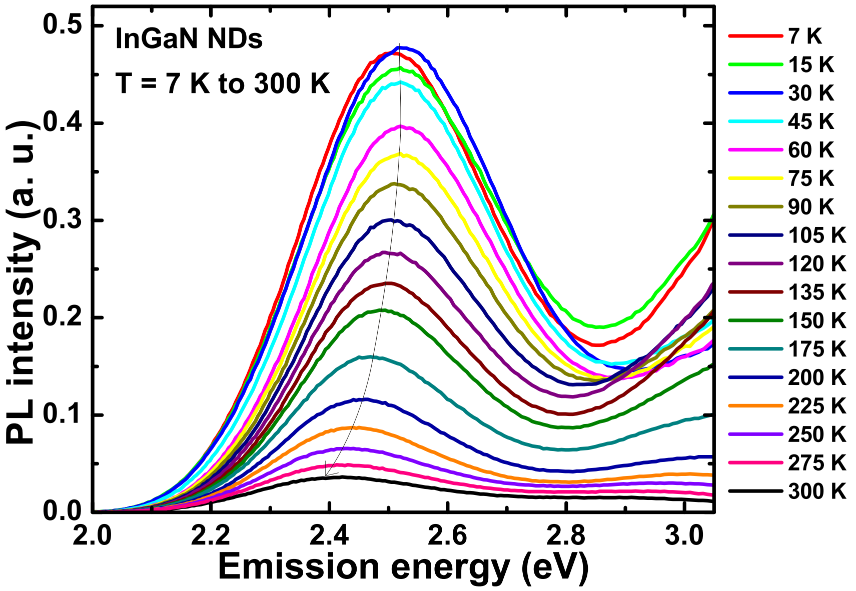

Figure 2.12: *PL emission spectra as measured from a sample with series of embedded 4 nm nanodisks at different temperatures. At room temperature 7.5% of the 10 K emission intensity is conserved.*

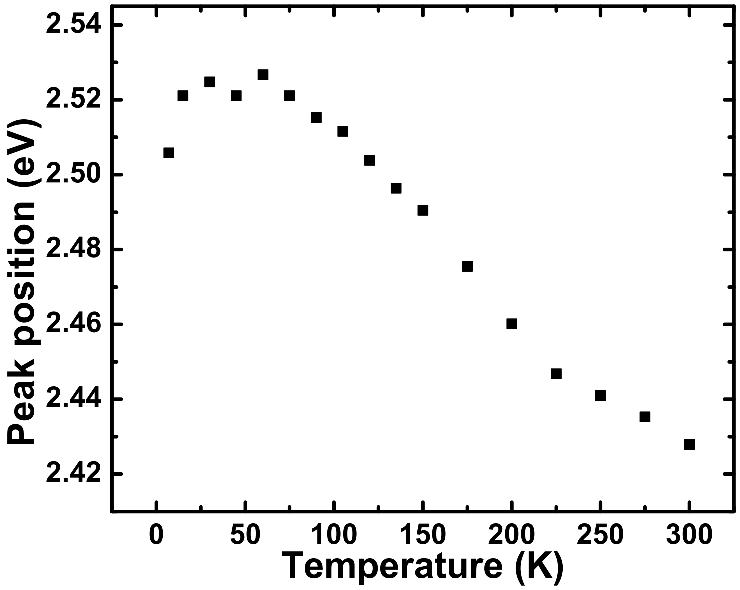

Figure 2.13: *Temperature dependence of the peak position of PL emission intensity. The main emission peak shows an S-shaped shift with increasing temperature [143].*

The temperature dependence of the bound exciton PL intensity is given by

$$I(T) = \frac{A}{B + C * e^{\frac{E_a}{k_b T}}} \tag{2.5}$$

with A and B being constants; C is the transition probability of nonradiative process, and E_a, is the activation energy. The activation energy is the energy difference between the radiative potential minimum and the intersection of the radiative and nonradiative potentials. Thermal fluctuations usually induce transitions to the non-radiative states and consequently a reduction in the PL intensity. Using the equation 2.5 and the data from Fig. 2.14, the activation energy is determined to be 44.7 meV. The temperature range covered here is from 7 K to 403 K.

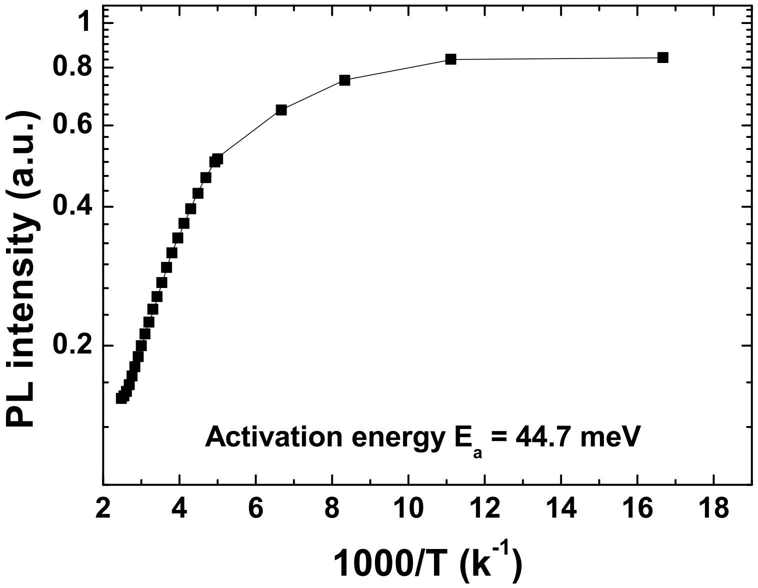

Figure 2.14: *Pl intensity as a function of 1000/T for the InGaN/GaN NWs with embeded NDs. Activation energy of -44 meV is obtained from the Arrhenius plot.*

Catalytic Pt deposition

In order to achieve sensitivity of the photoluminescence emission from the optochemical transducer to hydrogen and hydrocarbon gases in the ambient air, a semi transparent layer of catalytic metal has to be deposited onto the surface of the NWs. Hydrogen alters the electrical properties of a metal in which it is dissolved. Platinum metals (Ru, Os, Rh, Ir, Pd, Pt) show a significant tendency of dissolving hydrogen gas [144]. Among these metals Pd and Pt are mostly explored for sensing hydrogen in various devices. Pd has a higher permeability than Pt but the solubility of H_2 is larger in the former [145]. The 5 nm thick semitransparent layer of Pt was evaporated by a Pfeiffer PLS 570 electron beam evaporation system. The deposition rate was kept constant at 3 $\dot{A}$/s with the substrate holder rotating during the entire evaporation process. Due to the small layer thickness evaporated and the shadowing effects occurring at the vertical NW walls, the Pt film consisted of small patches of noble metal on the NW walls. The SEM (Scanning Electron Microscope) image of such Pt coated NW ensemble is presented in Fig 2.15.

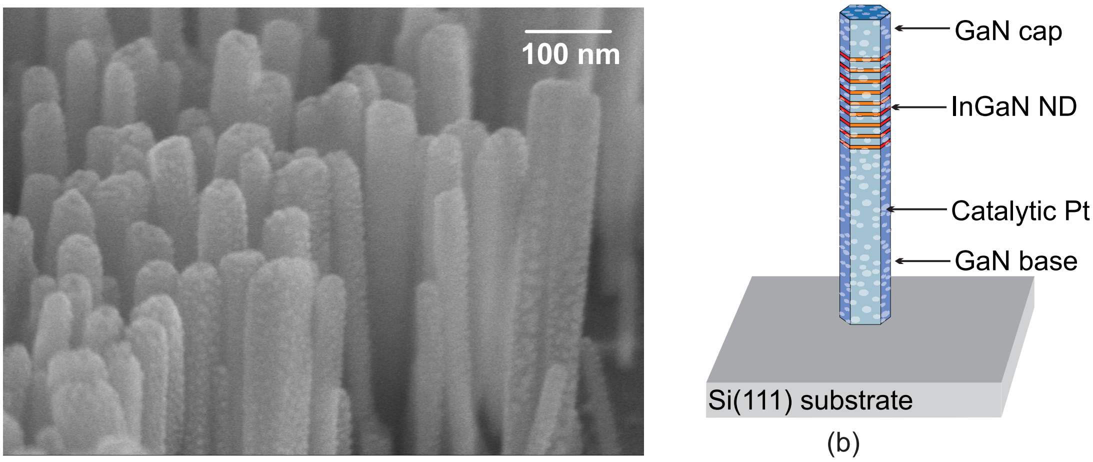

(a) (b)

Figure 2.15: *Semitransparent layer of catalytic Pt deposited on the NWH. a) partial coverage by the Pt catalytic layer was observed by SEM investigation. b) schematic of a NWH with Pt deposition.*

2.4 Sensor system

The overall architecture of the optochemical sensor system is shown in Fig. 2.16. The InGaN/GaN transducer element is mounted inside a small gas-tight aluminium chamber (3 cm^3) with inlet and outlet ports and with the transducer layers facing the interior of the gas cell. The inner walls of the gas cell were black eloxadized to reduce optical reflection. In order to allow experiments at different transducer temperatures, the optochemical transducers were mounted on ceramic heater substrates which carried screen-printed Pt heater meanders on their backsides [146].

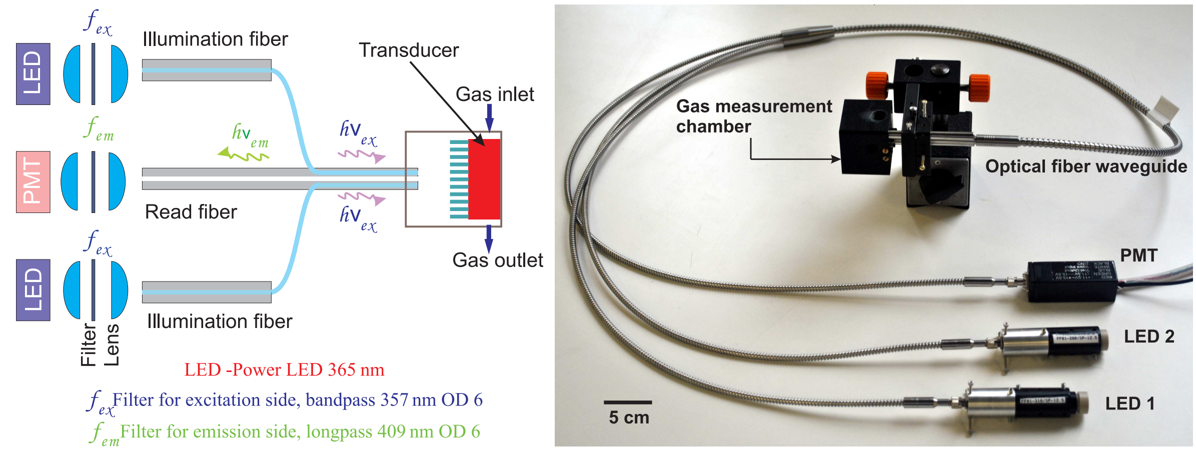

(a) (b)

Figure 2.16: *a) Schematics of the optical setup featuring three light fibers and an optochemical GaN/InGaN transducer; b) experimental setup containing optical fiber, LEDs, photomultiplier and gas measurement chamber.*

An optically transparent sapphire window opposite to the transducer chip allows optical excitation and PL detection. A common fiber bundle consisting of 200 fused silica fibers each with a diameter of 400 μm was used as a waveguide for both the PL excitation and the PL emission light. In order to enable this double function, the fiber bundle was separated into three branches with two of them being connected to UV power LEDs and the third to a photomultiplier detector.

Excitation of the NW-PL was performed by commercial UV power LEDs (Seoul Optodevice) with an optical power of 75 mW, a peak emission wavelength λ_p of 365 nm and a FWHM of 18 nm. A photomultiplier tube (H5784, Hamamatsu Photonics) was used for the PL detection. Both optical devices were implemented into the light-fiber system and optical filters were used to increase the fidelity of the optical output signal. On the excitation side band pass filters with $\lambda_c = 357$ nm and a FWHM of 44 nm were employed; on the detection side a long pass filter with $\lambda_c = 409$ nm was used. Both filters possessed an optical density (OD) greater than 5. LEDs, LED driver electronics and photomultiplier detector were all mounted outside the measurement chamber.

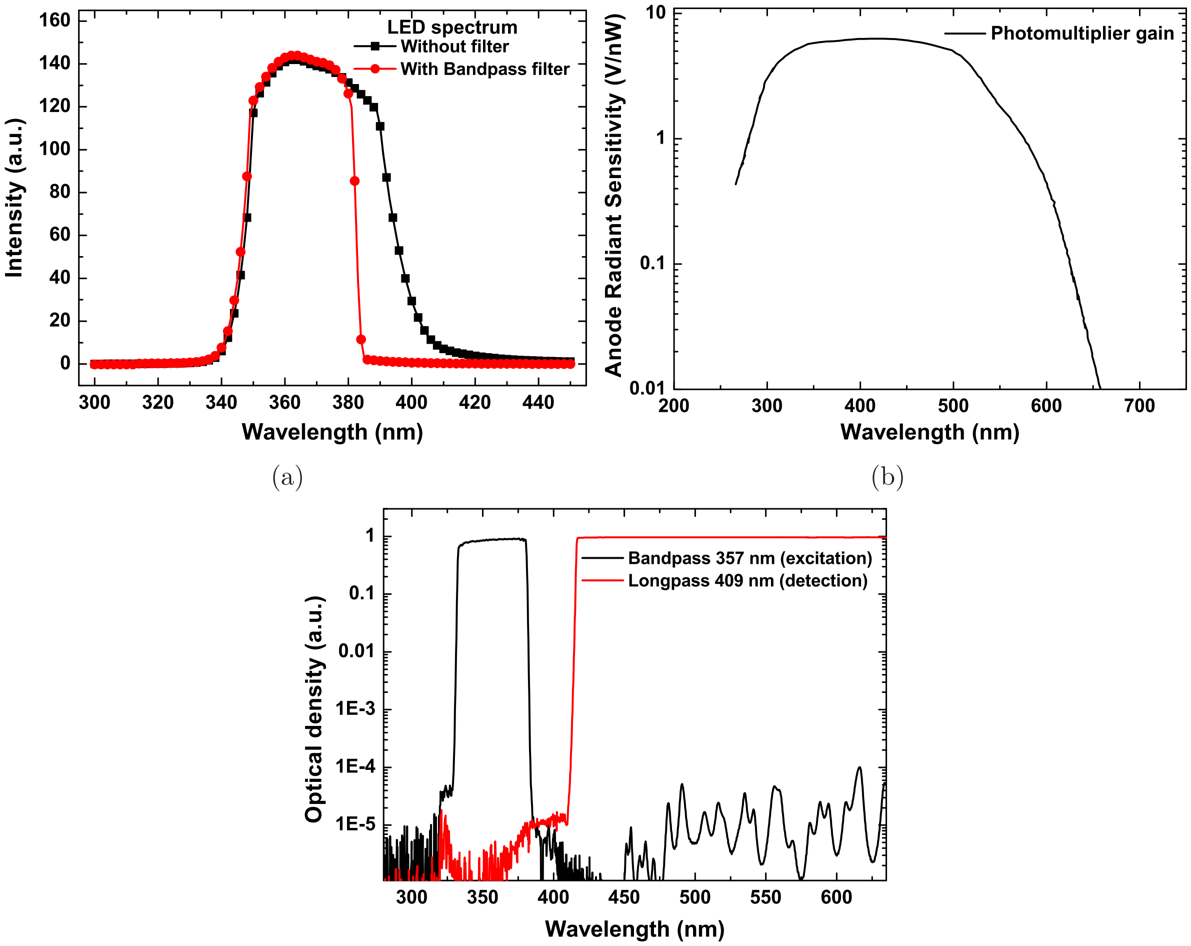

(a) (b)

(c)

Figure 2.17: *Characteristics of the optical components used for the sensor system: (a) optical radiation of the UV LED emitting at peak wavelength of 365 nm with and without the band pass filter. (b) response curve of the photomultiplier and (c) transmission characteristics of the band pass filter used for the emission side and long pass filter used for the detection side. The response curves of the photomultiplier and the optical filters are collected from the corresponding data sheets.*

Gas sensing tests were carried out in a gas mixing system that allows preparation of controlled mixtures of up to six gases or vapors. The schematics of the test setup is shown in Fig. 2.18. The flow rate of each gas was controlled by MFCs (Mass Flow Controller). Each MFC was regulated by a multi-gas controller module which connected to a PC via a GPIB interface. All analyte gases investigated were diluted in synthetic air (80% N_2 + 20% O_2). In addition, controlled relative humidity levels ranging from 10% to 90% were generated by vaporizing de-ionized H_2O into the synthetic background air. A total flow rate of 1000 standard cubic cm (sccm) was maintained during all measurements.

The PL intensity of the Pt:InGaN/GaN NW transducer exhibited changes in the percent range when exposed to small concentrations of analyte gas. The change in PL intensity was detected by the photomultiplier tube and evidenced by a change in its output voltage.

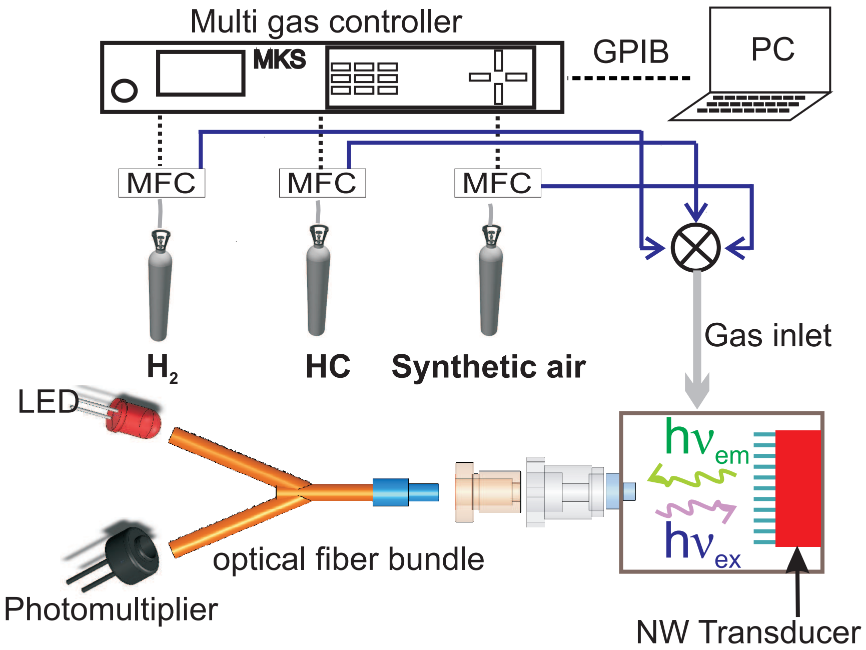

Figure 2.18: *Schematic of the experimental setup illustrating the optical transducer system and the gas mixing facility*

A block circuit diagram of the sensor system is presented in Fig. 2.19. Recent advancement in LED lighting technology has brought a wide range of electronic drivers for every possible application field. The LED driver used for this experiment worked as a constant current source in the range of 0-1.2 A and can be dimmed by an analog DC voltage. An USB DAQ module 6211 from National Instruments is used for controlling the LED driver IC. The current flown through the LED was monitored by the DAQ module via a transimpedance amplifier. The signal acquisition from the photomultiplier was also performed by DAQ module. A LabVIEW application was developed for controlling the electronic devices and for data acquisition, as well as for signal processing.

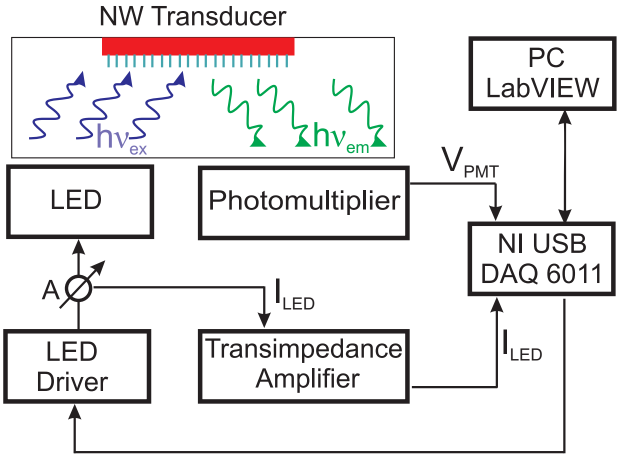

Figure 2.19: *Electronics controlling the photo-excitation of the optochemical transducers and the detection of the PL emission. The data acquisition was performed via an USB module (NI DAQ 6011) and LabView software*

2.5 H_2 and hydrocarbon detection

2.5.1 optochemical transducer principle

Normally undoped self-assembled GaN-NWs, grown by molecular beam epitaxy have been shown to be depleted of free charge carriers, provided that their thickness does not exceed several tens of nanometers [124] [147]. Depletion arises due to carrier trapping at localized surface states within the energy gap. Due to the moderate doping, the spatial extent of the surface band bending (SBB) exceeds the NW diameter, which results in fully depleted NWs and essentially flat band edges as shown in Fig. 2.20. Secondly, the photoluminescence properties are sensitive to the presence of gases in the ambient atmosphere. Uncoated GaN/AlGaN NW were shown to be sensitive to oxygen, and Pt-coated ones to hydrogen [136]. The gas response of the GaN/AlGaN NWs at room temperature and above was interpreted to be due to an increased (O_2) or a decreased (H_2) non-radiative surface recombination of photoexcited carriers. The reduced recombination at the surface of Pt coated NWs was attributed to the improved electron confinement caused by the potential drop arising from the O-H dipole layers that form at the Pt/III-N interface when H_2 molecules dissociate at the Pt surface and as H atoms diffuse to the interface [148] (Fig. 2.20c).

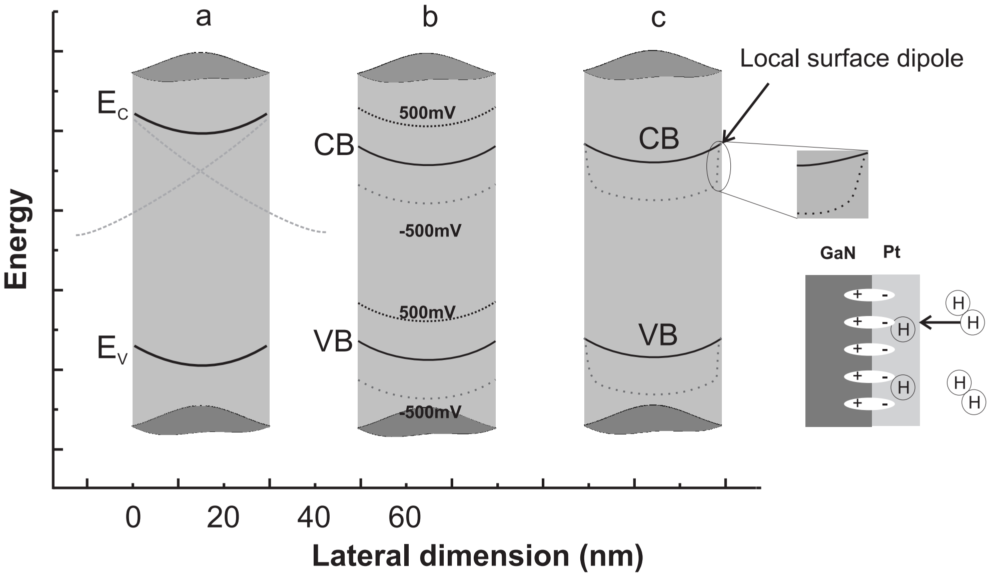

Figure 2.20: *Position of valence and conduction band edges across a NW: a) NW depleted from free charge carriers by overlapping space charge regions. The result is a significantly reduced surface band bending (SBB) across the NW [149, 150]. The solid lines show the conduction and valance band edges inside a fully depleted NW with a diameter of 30 nm. The dashed lines show how the band bending arises from the overlapping of surface depletion layers originating from opposite sides; b) Effect of variations in the surface potentials on the band profile inside a NW; c) Diffusion of atomic hydrogen through the Pt-layer and improved carrier confinement due to the formation of dipoles at the Pt/III-N interface. The better confinement leads to a reduced non-radiative recombination at the NW surface.*

2.5.2 Hydrogen detection

Fig. 2.21 presents the response of a NW transducer to different H_2 concentrations as measured at a temperature of 30°C. This transducer had InGaN NDs with GaN barrier on top of GaN+InGaN double base part, as illustrated in Fig 2.9c. The supplied gas pulses were produced by diluting the H_2 source gas (200 ppm H_2 in synthetic air) in a second flow of synthetic air. The sensor signal, i.e. the photomultiplier (PMT) output voltage, was found to scale with the H_2 concentration. Response and recovery time constants were in the order of 10 minutes. A much faster response could be observed at elevated transducer temperatures. Response and recovery times decreased to about 2-3 min at 40°C and to about 1 min at 80°C. Shorter response and recovery time constants by further temperature increase could not sensibly be realized as the PL intensity sharply dropped upon increasing the transducer temperature beyond 80°C. At 150°C a H_2 response could no longer be detected. Similar experiments performed with NWs without Pt coating resulted in no significant change in the PL intensity.

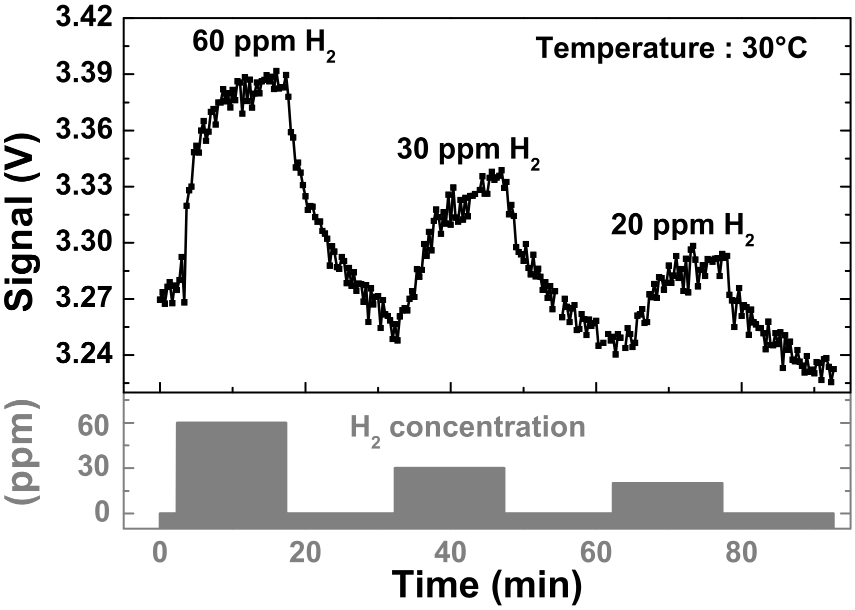

Figure 2.21: *PMT output signal in response to decreasing H_2 concentrations as observed at a transducer temperature of 30°C.*

The data of Fig. 2.21 and 2.22 represent raw data that had been directly observed at the output of the PMT amplifier. In order to make a connection to the usual convention of displaying gas response data, we will use in the following the quantity $R = (V_{gas} - V_0)/V_0$ as a measure of the gas response. R is the relative change of the PMT output voltage as the NW transducers are exposed to target gases.

The results in Fig. 2.23 demonstrate that dissociation of H_2 molecules and release of atomic hydrogen that can diffuse through the Pt layer is enhanced at elevated temperatures. This latter fact is further illustrated in Fig. 2.24, which summarizes the results of two detection experiments which had been performed at transducer temperatures of 50°C and 80°C and at considerably smaller H_2 concentrations. Under these latter conditions H_2 concentrations

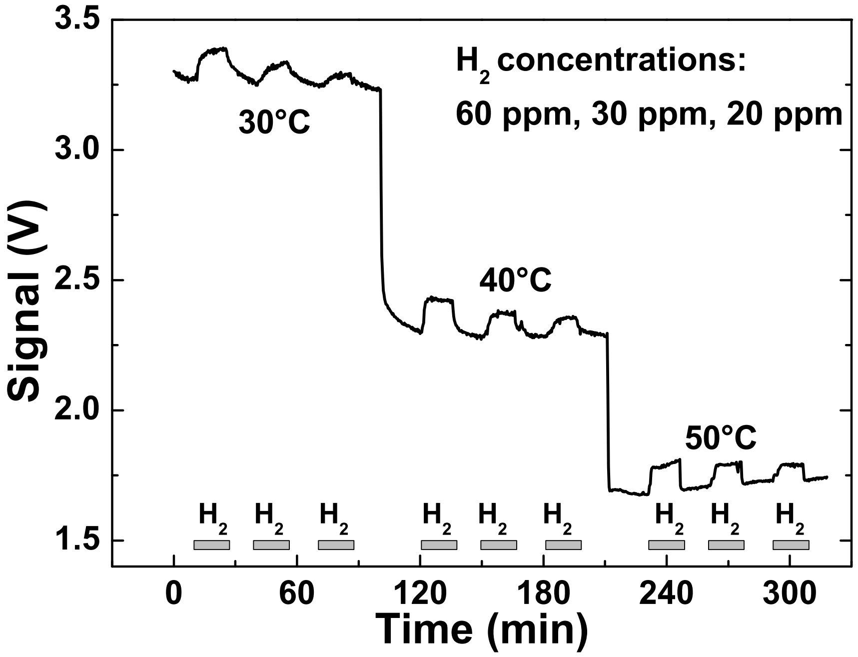

Figure 2.22: *PMT signal in response to H_2 pulses as observed at increasingly higher transducer temperatures. Higher operation temperature causes on one side reduced PL intensity, on other side improves response characteristic.*

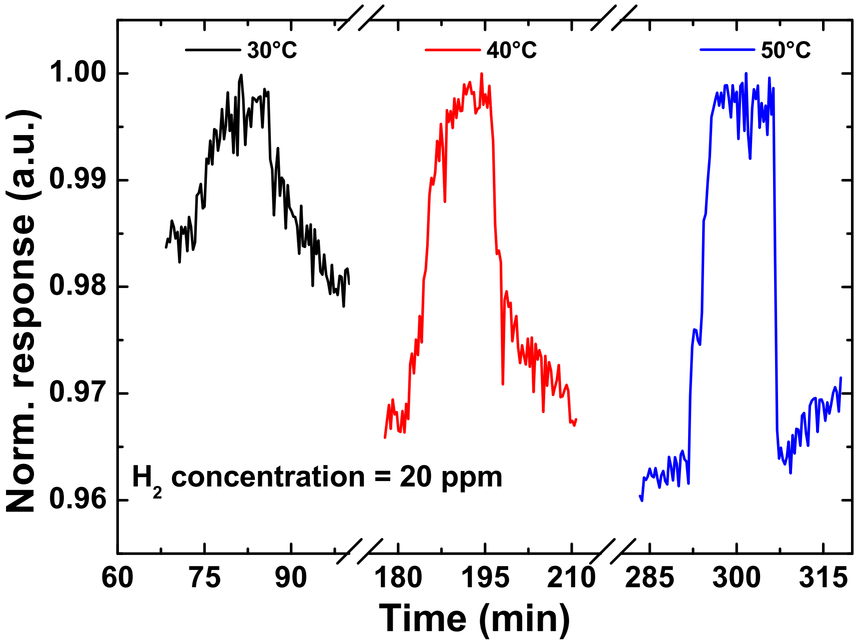

Figure 2.23: *Normalized response to 200 ppm H_2 as observed at increasingly higher transducer temperatures. Higher operation temperatures cause increased relative changes and faster response times.*

as low as 200 ppb could be clearly detected. For preparing a H_2 concentration of 200 ppb a first flow of 1 sccm of synthetic air (SA) with and a mixture of 200 ppm H_2 was mixed with a second flow of 999 sccm of pure synthetic air. The 1 sccm H_2/SA flow was controlled by a 10 sccm MFC, which allows for an accuracy of 1% of full scale. Adding up all error margins, we can arrive at a total error of ±21.2 ppb for a concentration of 200 ppb. The resulting response for 200 ppb H_2 was 0.2% at 50°C and 0.4% at 80°C. The rms noise voltage amounted to 0.05%. The drift of the PL baseline signal is of a purely thermal origin and arose due to an insufficient thermal stabilization of the sensor setup prior to the gas measurement.

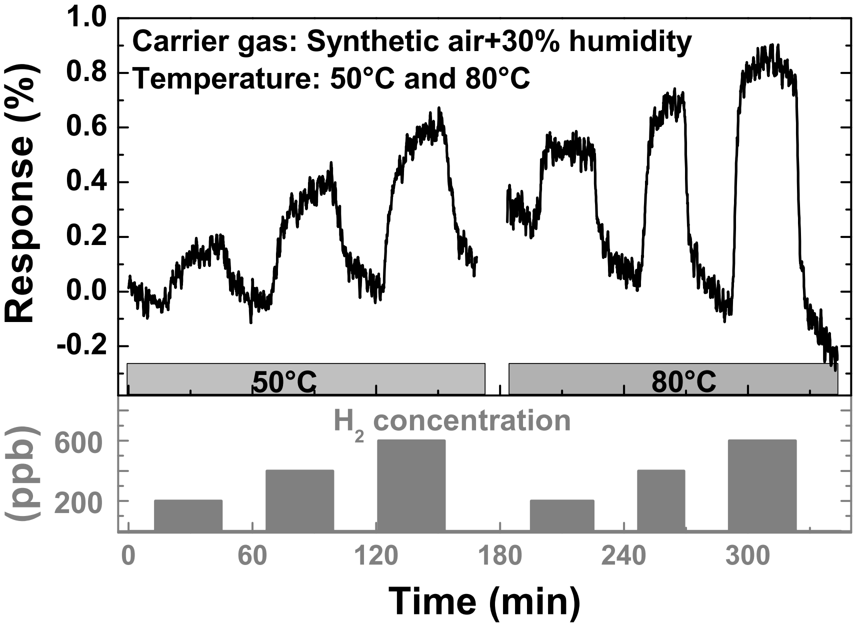

Figure 2.24: *Response to low H_2-concentrations at two different temperatures (50°C and 80°C). The background carrier gas in these experiments was humidified (30%) synthetic air. 200 ppb could be clearly resolved at both temperatures.*

Fig. 2.25 shows calibration curves derived from similar gas sensing tests as shown in Figs .2.22 and 2.24. In this latter graph the response R is plotted as a function of the H_2 concentration in the gas phase. These latter data reveal that R increases logarithmically with the H_2 concentration and that, for a given H_2 concentration, R increases with the transducer temperature ($T_{max} \approx 80°C$). The resulting behavior can be described by the following equation:

$$R_{H_2} = a_1 - b_1 * ln(C_{H_2} + c_1) \tag{2.6}$$

With the following parameters:
C_{H_2}: H_2 concentration in ppm, a_1 = -7.86, b_1 = -4.68, c_1 = 5.
a,b, and c are constants derived from data fitting. Temperature = 80°C

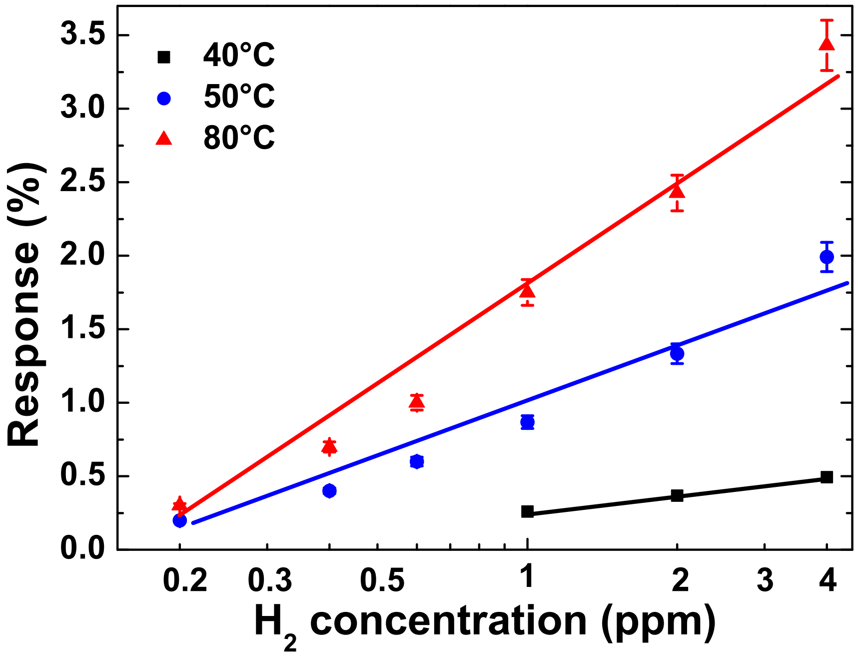

Figure 2.25: *Response to very small H_2 concentrations measured at different sensor operation temperatures. For a given temperature, the response increases logarithmically with increasing H_2 concentration.*

Effect of humidity

A further significant observation was that the H_2 response is humidity-dependent. In order to reveal this effect, a transducer was exposed to high concentrations of H_2 at different levels of background humidity and at increasingly higher transducer temperatures. It can be seen from Fig. 2.26 that the humidity affects the sensor baseline signal as well as the magnitude and the speed of the gas response. Similar effects could also be observed at 50°C. Humidity effects, however, disappeared when the transducer temperature was raised towards 100°C and beyond.

The faster response and the lower baseline signal both suggest that the adsorption of water vapor leads to an enhanced surface recombination rate. The microscopic origin of the H_2O-induced recombination centers cannot be revealed from the sensor response measurements. A realistic possibility, however, could be surface hydroxyl (OH) groups formed by the adsorption of water vapor. Such groups are known to form on the surface of metal oxide semiconductors in the presence of water vapor [151, 152] and such groups have also been invoked to explain the pH-response of GaN-based high-electron-mobility transistors (HEMT) [153] and of hydrogenated diamonds [154]. These OH groups can easily convert between positive, neutral and negative charge states. In order to form efficient recombination centers the OH groups need to reside on the uncovered parts of GaN surface and these groups need to be able to exchange H atoms with neighboring patches of Pt by means of catalytic spill-over. The schematic of this fact is illustrated in Fig. 2.27.

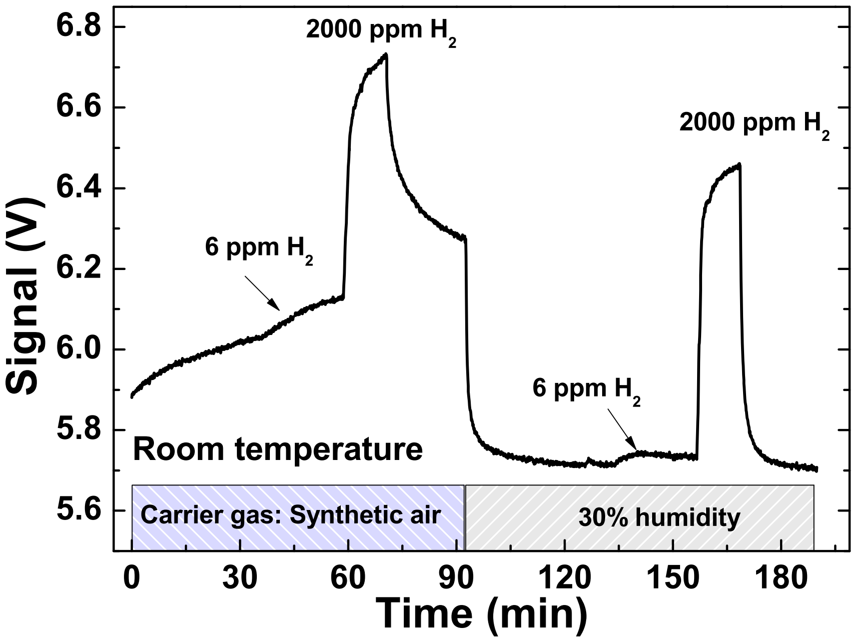

Figure 2.26: *Effect of humidity on H_2 detection. Background humidity decreases the baseline signal and improves the time response of the H_2 sensor signal.*

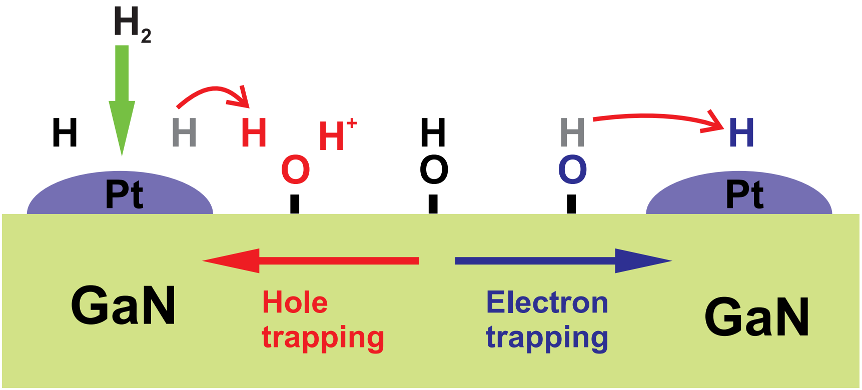

Figure 2.27: *Neutral OH surface groups are formed in the presence of humidity (middle). Such surface groups can form efficient recombination centers by trapping photo-generated electrons (right) or holes (left) from the NW bulk. For basic reasons of chemistry such charge changes need to be accompanied by compensating changes in the H coordination number.*

2.5.3 Hydrocarbon detection

In addition to a high sensitivity to H_2, Pt-coated InGaN/GaN optochemical transducers also exhibited a pronounced sensitivity to hydrocarbons. This hydrocarbon sensitivity is likely related to the primary sensitivity to H_2 as H atoms tend to split off from hydrocarbon molecules on heated and catalytically active noble metal surfaces. In general, it was observed that the magnitude and the speed of the gas-induced changes in the PL intensity scale with the stability of the chemical bonds in the different hydrocarbon molecules. As it is easier to eliminate hydrogen atoms from unsaturated hydrocarbons than from saturated ones, higher sensitivities and shorter response times were observed upon detection of unsaturated hydrocarbons. The transducers showed improved response with small amount of humidity in the background air as described in the previous section. Therefore, most of the measurements presented in the following sections were performed under the condition of 30% humidity.

Unsaturated hydrocarbons

In Fig. 2.28 the gas response to acetylene (C_2H_2) is shown. Due to the triple C-C bond (H-C≡C-H) it is easier to extract atomic hydrogen from C_2H_2 than from most other hydrocarbon species. Similar to the detection of H_2 the relative change in the PL intensity increases with increasing gas concentration and transducer temperature, whereas response and recovery times decrease. Minimum detectable concentrations were in the order of 5 ppm when the transducers were operated at 80°C.

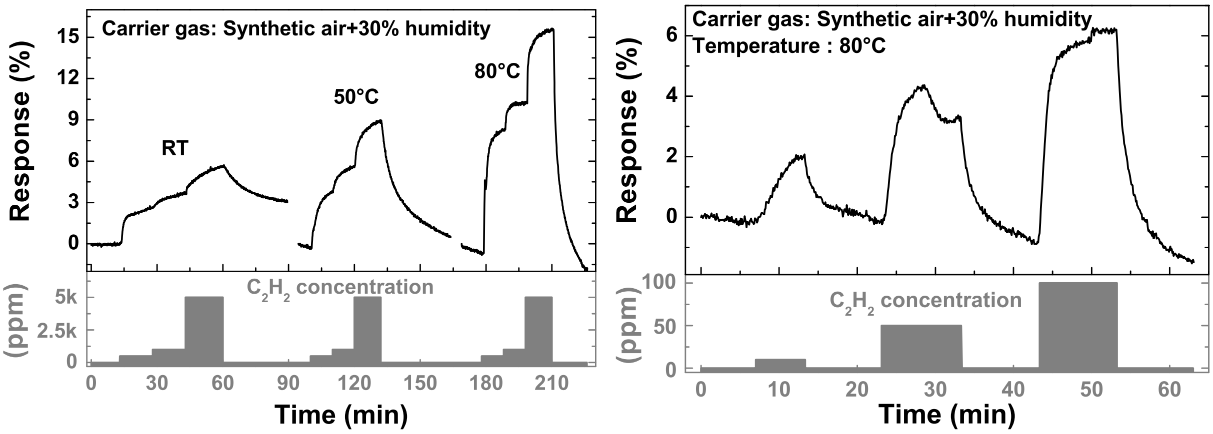

(a)

(b)

Figure 2.28: *a) Response to three C_2H_2 concentration steps (500, 1000 and 5000 ppm) applied at increasingly higher transducer temperatures; b) measurements at low C_2H_2 concentrations (10, 50 and 100 ppm) at a transducer temperature of 80°C.*

In the calibration graph of Fig. 2.29(a) the response is plotted as a function of the C_2H_2 concentration in the gas phase. As already observed in the case of H_2, the response increases logarithmically with the C_2H_2 concentration at a given temperature. As well as, for a given concentration at certain temperature range the response increases linearly with increasing temperature.

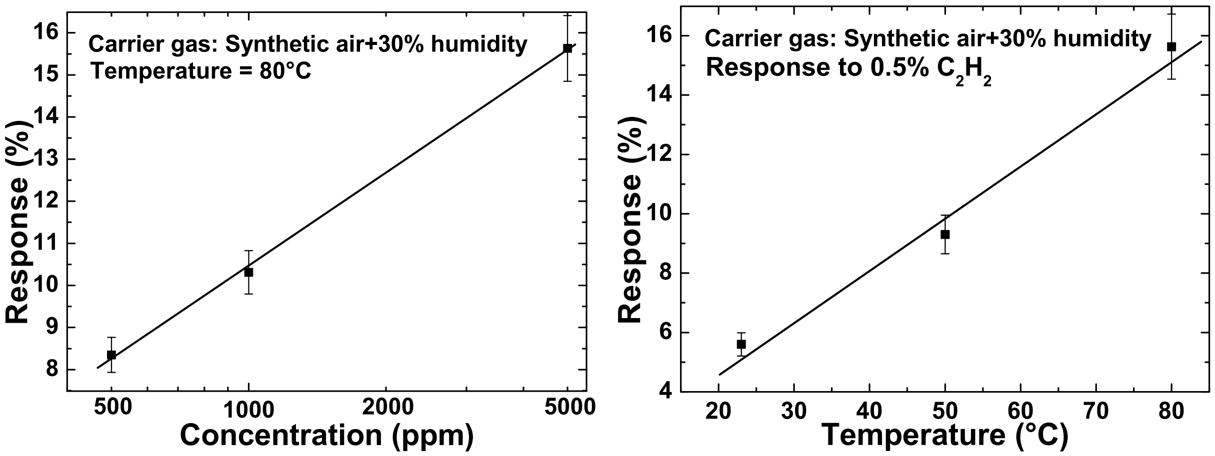

(a) (b)

Figure 2.29: *a) Calibration curve for C_2H_2 at 80°C. The response increases logarithmically with increasing C_2H_2 concentration. b) Temperature dependence of the response to 0.5% C_2H_2 is illustrated here. The response increases linearly with increasing temperature.*

In this case the logarithmic dependency of response to C_2H_2 concentration can be expressed by the following equation:

$$R_{C_2H_2} = a_2 - b_2 * ln(C_{C_2H_2} + c_2) \tag{2.7}$$

$C_{C_2H_2}$: C_2H_2 concentration in ppm, a_2 = -16.35, b_2 = -3.73, c_2 = 250.
Temperature = 80°C.

The linear dependence of the response to sensor temperature for a definite analyte concentration can be represented by the following equation:

$$R_{C_2H_2} = A_2 - B_2 * T \tag{2.8}$$

A_2= 1.717, B_2= 0.163 [1/°C], T = temperature in °C. C_2H_2 concentration= 0.5%.

Similar response patterns were observed for ethylene (C_2H_4). Fig. 2.30(a) shows that InGaN/GaN transducers respond to high concentrations of ethylene already at room temperature. Again, as in the case of H_2 and C_2H_2, the response towards C_2H_4 increases with increasing transducer temperature. Fig. 2.30(b) shows the response to a series of C_2H_4 concentration steps at the maximum transducer temperature of 80°C. This latter experiment shows that the minimum detectable C_2H_4 concentration is in the order of a few ppm at this elevated temperature.

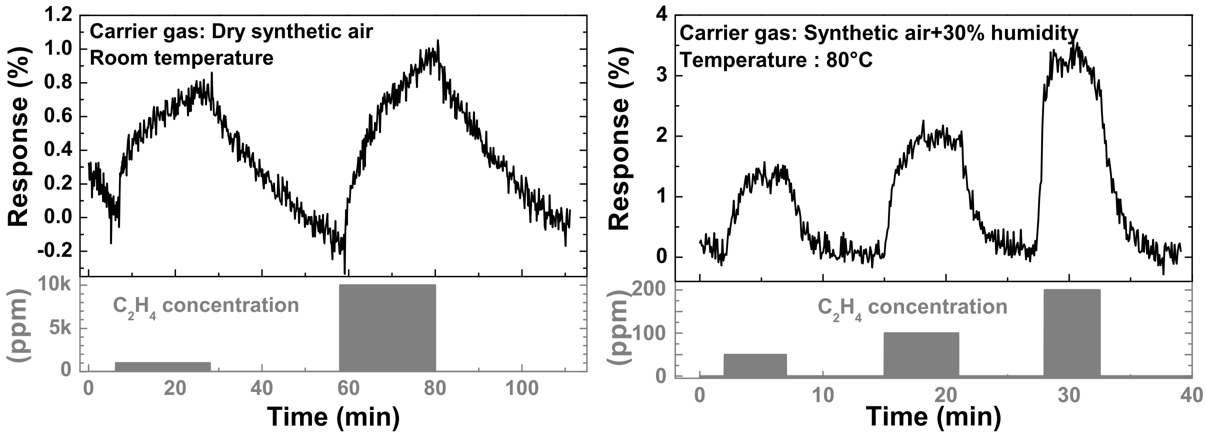

(a) (b)

Figure 2.30: *a) Response to high concentrations of C_2H_4 (10^3 and 10^4 ppm) at room temperature; b) response to low concentrations of C_2H_4 (50, 100 and 200 ppm) at 80°C.*

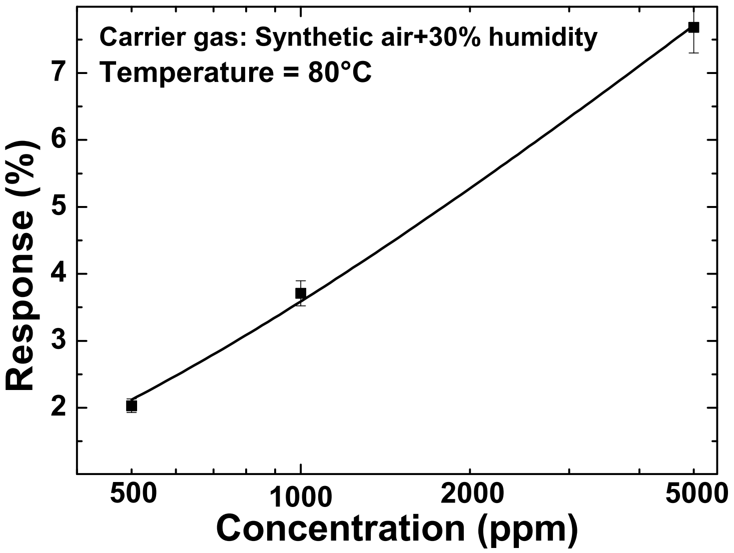

Figure 2.31: *Calibration curve for C_2H_4 at 80°C. The response increases logarithmically with increasing C_2H_4 concentration.*

The calibration graph in Fig. 2.31 the response is plotted as a function of the C_2H_4 concentration. As we have observed in the case of H_2 and C_2H_4 the response increases logarithmically with the C_2H_4 concentration at a given temperature.

The logarithmic dependence of the response to C_2H_4 concentration can be expressed by the following equation:

$$R_{C_2H_4} = a_3 - b_3 * ln(C_{C_2H_4} + c_3) \tag{2.9}$$

$C_{C_2H_4}$: C_2H_4 concentration in ppm, a_3 = -16.91, b_2 = -2.87, c_2 = 250.
Temperature = 80°C.

Saturated hydrocarbons

The extraction of hydrogen atoms from saturated hydrocarbons requires more energy than from unsaturated ones. A small and slow response ($t_r \approx 30$ min) of the GaN/InGaN transducers could nevertheless be observed at room temperature. The example of Fig. 2.32(a) shows that high concentrations (0.5%) of propane (C_3H_8) can be reasonably well detected at 40°C. As the strength of the C-H covalent bond in methane (CH_4) is the strongest among all hydrocarbons [155], it causes the smallest sensor signals among the investigated hydrocarbons. A response towards CH_4 was observed only close to the maximum operating temperature of 80°C (Fig. 2.32(b)). At this temperature 500 ppm of CH_4 caused a 2% increase in the PL whereas only 1 ppm of H_2 was necessary to produce the same PL response (Fig. 2.25).

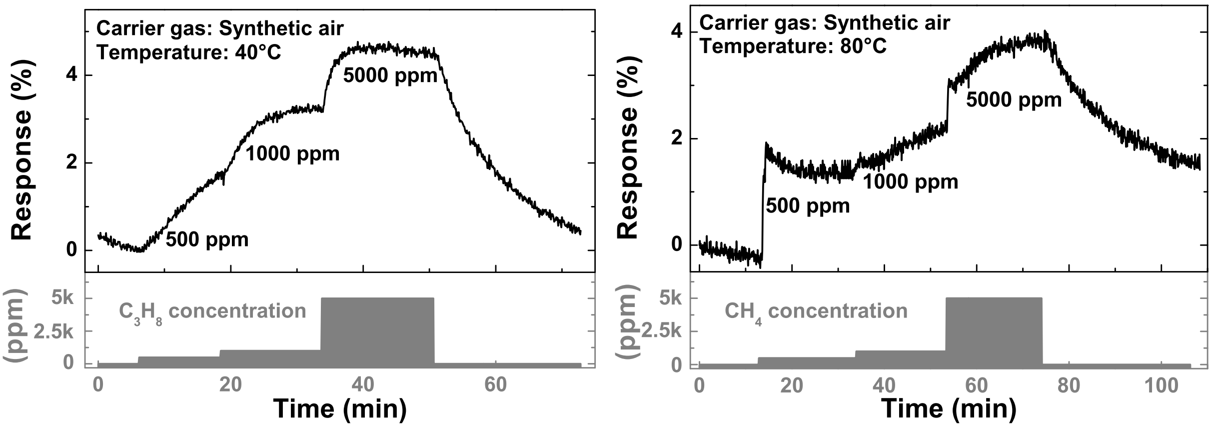

(a) (b)

Figure 2.32: *Response to saturated hydrocarbons: a) response to a series of propane (C_3H_8) concentration steps as applied at 40°C; b) response to methane (CH_4) concentration steps as applied at 80°C.*

2.5.4 Hydrogen and hydrocarbon detection limits

Fig. 2.33 shows the temperature dependence of the H_2 and hydrocarbon gas sensitivities. Whereas an increasing temperature leads to a monotonous decrease in the response and recovery time constants, the situation regarding the absolute value of the gas sensitivity is more complex. H_2, in particular, exhibits a pronounced maximum in the gas response around 80°C. In principle, such a temperature maximum originates from two opposing trends: first, higher temperatures facilitate the dissociation of adsorbed analyte species and the release of atomic hydrogen that can diffuse through the Pt layer and form detectable dipole layers at the Pt/GaN and Pt/InGaN interfaces. The second trend is that, the surface recombination gets more efficient and the relative PL response smaller as the temperature is increased (Fig. 2.12). Qualitatively, the same arguments apply to all analyte species considered so far. The data in Fig. 2.33, however, indicate that the temperature of maximum gas response, in general, lies beyond the maximum operation temperature of the GaN/InGaN transducers.

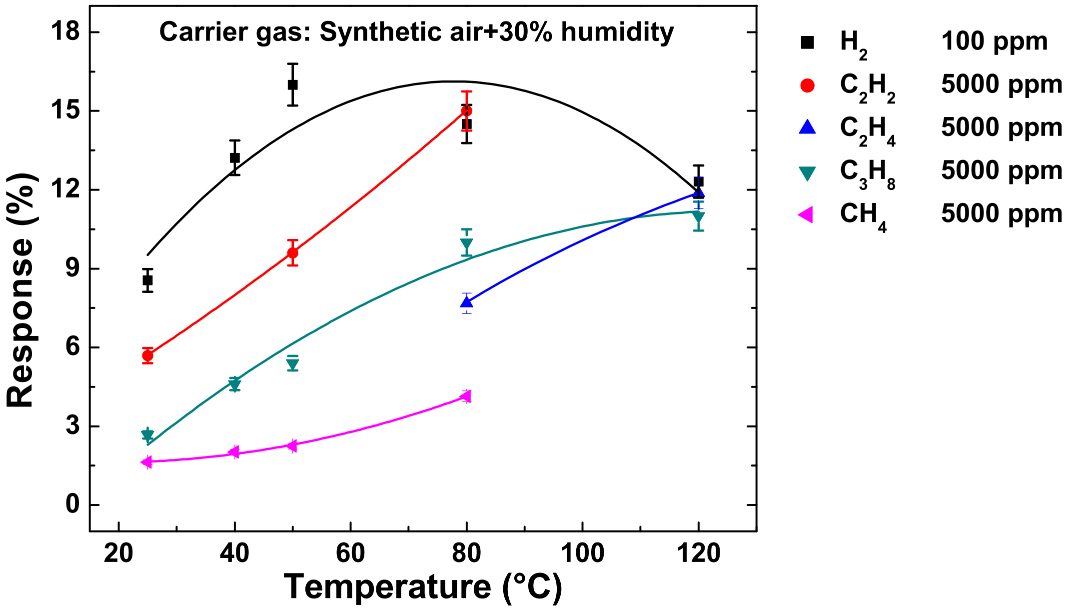

Figure 2.33: *Temperature dependence of the gas response for the analyte gas species discussed above*

Fig. 2.34 presents calibration curves derived from concentration-dependent gas sensing experiments. All data correspond to a transducer temperature of 80°C, which presents an optimum compromise between high gas response and a reasonably short response time. This latter summary shows that H_2 can be detected at much smaller concentrations than all other investigated hydrocarbon species, confirming that the H-H bond is much easier to split than it is to remove atomic or molecular hydrogen from hydrocarbon molecules. The extrapolations of the individual calibration curves towards R=0 confirm this trend and yield estimates for the minimum detectable concentrations of the individual target gases. For clarity these latter data are also reported in Table 2.3.

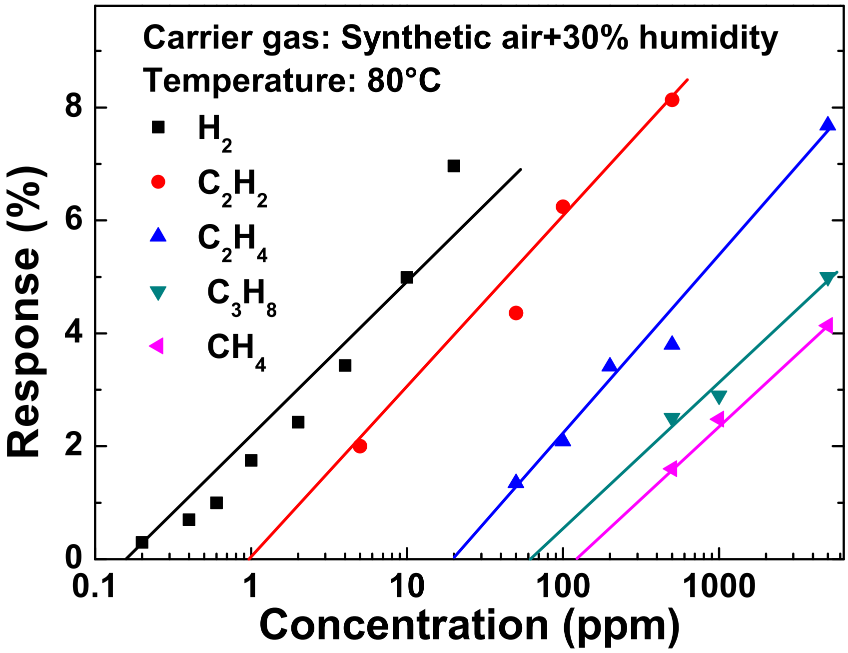

Figure 2.34: *Variation of the gas response towards* H_2 *and different hydrocarbon gases with gas concentration as measured at a transducer temperature of 80°C.*

Gas	**Transducer temperature**	**Minimum detectable concentration**
Hydrogen	RT	10 ppm
Hydrogen	80°C	150 ppb
Acetylene	80°C	1 ppm
Ethylene	80°C	20 ppm
Propane	80°C	80 ppm
Methane	80°C	150 ppm

Table 2.3: *Detector performance for* H_2 *and different hydrocarbon species operated at room temperature and 80°C.*

2.5.5 Synopsis of hydrogen and hydrocarbon sensing

- An all-optical gas sensor system has been demonstrated that is based on Pt-coated, PAMBE-grown GaN/InGaN nanowire optochemical transducers. The transducer principle makes use of chemically-induced changes in the photoluminescence intensity as the nanowires are exposed to H_2 and hydrocarbons.

- Atomic hydrogen from H_2 and HC gases diffuses through the catalytic Pt-coating on the NW transducer and suppresses the surface recombination resulting in an enhancement of PL-intensity.

- Minimum detectable H_2 concentrations are in the order of a few 100 ppb when the transducers are operated at 80°C. In comparison, commercially available field effect gas sensors (Schottky diode or MOSFET) exhibit H_2 detection limits in the range of a few hundred ppm when operated in this same temperature range [50].

- Minimum detectable hydrocarbon concentrations are species-dependent. Unsaturated hydrocarbons can be detected with better response than saturated ones. Minimum detectable acetylene concentrations are in the order of a few ppm at a temperature of 80°C. In comparison, minimum detectable CH_4 concentrations are of the order of 100 to 200 ppm at this same temperature. In all cases the gas response was found to increase logarithmically with the gas concentration.

- Optimum transducer temperatures arise as a compromise between catalytic break up of adsorbed analyte species and a decreasing luminescence yield of the GaN/InGaN transducers. Observed optimum operation temperatures are between 60-100°C. Again, this operation temperature range compares favorably against standard MOS sensors, in particular, when hydrocarbon detection is considered [50].

- The response time at transducer temperature of 80°C varied in the range of 3-4 minutes.

2.6 Oxidizing gases detection

Pt coated nanowire heterostructures described in the previous section showed well pronounced response to hydrogen and hydrocarbon. In the following section the response of uncoated NW transducer to different oxidizing gases will be reported.

2.6.1 Gas sensing test setup

The setup described in section 2.4 was also used for tests with oxidising gases. Synthetic air (80% N_2/20% O_2) was mixed with pure N_2 to produce the desired O_2 concentrations. The other analyte gases investigated (NO_2 and O_3) were diluted in synthetic air to obtain the desired concentration levels. As O_3 is unstable, it could not be supplied from gas cylinders. O_3, rather, was generated by illuminating a flow of synthetic air with an intense Xenon lamp. Controlled concentrations of O_3 were generated by adjusting the UV light intensity. Different relative humidity levels, ranging from 10% to 90%, were generated by vaporizing de-ionized H_2O into the synthetic background air. A total gas flow rate of 1000 standard cubic cm (sccm) was maintained during all measurements.

2.6.2 Experimental results

Response to oxygen

Fig. 2.35 presents the response of one optochemical transducers to increasingly higher O_2 concentrations. This transducer had InGaN NDs with GaN barrier on top of GaN base part, as illustrated in Fig 2.9b. The sequence of gas pulses supplied to this transducer consisted of five pulses of O_2 with concentration increasing from 0.2 - 2.1% O_2/N_2, separated by periods of pure N_2 exposure. This first set of data clearly reveals that increasing O_2 concentrations cause decreasing PL output signal levels, as it has also been reported for AlGaN/GaN NW heterostructures in ref [136]

Fig. 2.36 illustrates how the O_2 response varies as the transducer temperature is raised from room temperature to 120°C. Firstly, it is observed that the background luminescence intensity, as observed at zero O_2 concentration, is deceased as the transducer temperature is raised. Secondly, it is seen that the absolute value of the gas response, i.e. the relative change of the PL output signal upon changing from zero to finite values of O_2/N_2, decreases as well. In addition, a slight drift in the sensor baseline signal can be observed. It was found that this drift is of a purely thermal origin and unrelated to the properties of the optochemical transducers themselves. This drift simply reflects the slow transfer of heat from the ceramic heater substrate through the optochemical transducers towards the macroscopic measurement chamber after a step-function increase of the substrate temperature had been performed.

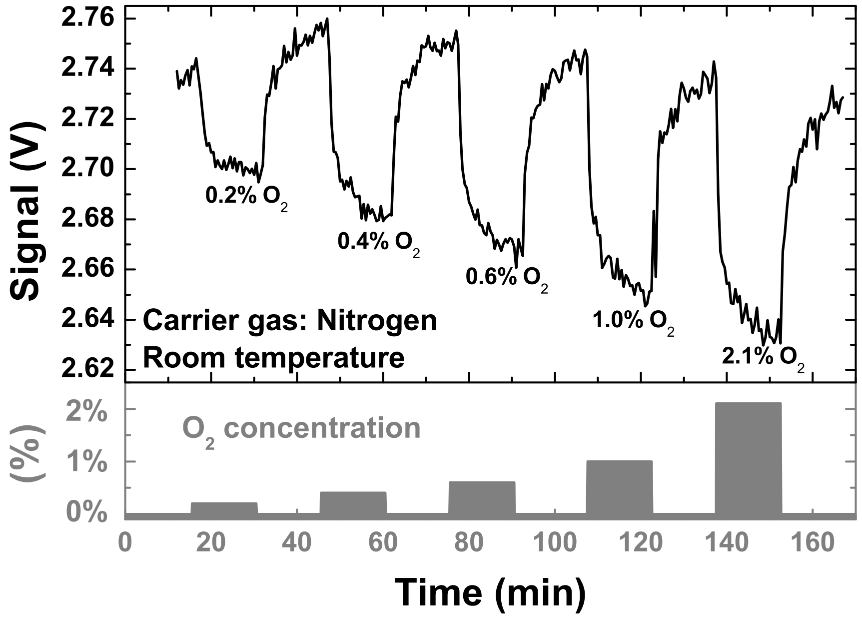

Figure 2.35: *Response of the PL intensity to increasing concentrations of* O_2 *as measured at room temperature. The PL intensity is represented by the photomultiplier output voltage that is plotted on the upper ordinate.*

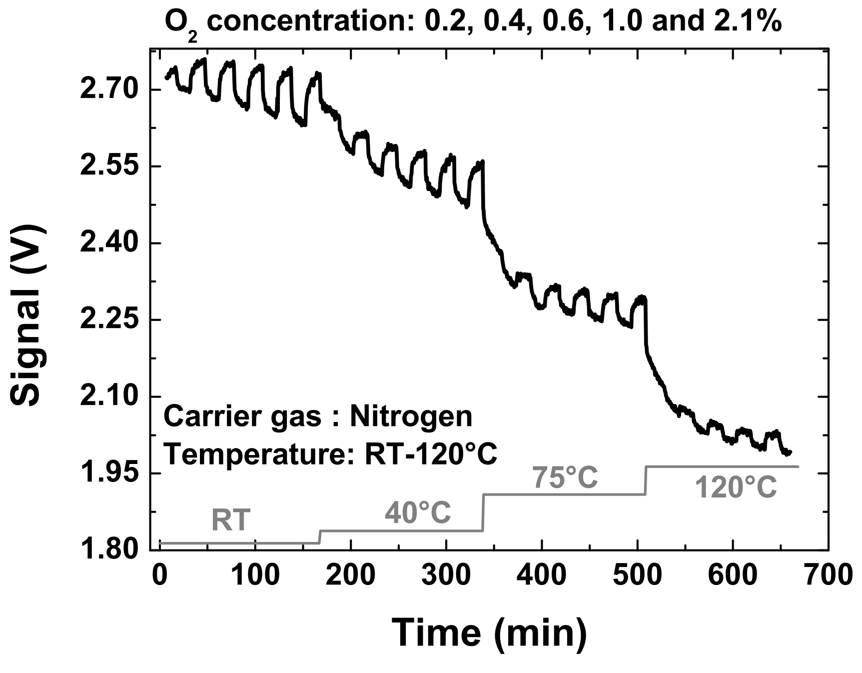

Figure 2.36: *Response to increasing oxygen concentrations as applied at different transducer temperatures (RT-120°C). At each temperature five* O_2 *concentration steps were applied (0.2 to 2.1%* O_2/N_2*).*

Fig. 2.37 presents calibration curves that had been derived from the raw data in Fig. 2.36. This latter graph shows that the gas response

$$R_{O_2}(\%) = |(V_{gas} - V_0) * 100/V_0| \tag{2.10}$$

i.e. the relative change of the sensor output voltage upon gas exposure, is temperature- and concentration-dependent. At a given temperature, the response increases logarithmically with O_2 concentration [156]. In case of H_2 and hydrocarbon gases the PL response also followed a logarithmic dependence to analyte concentration as described in equation 2.6. The dependence of the response to O_2 concentration can be expressed by the following equation:

$$R_{O_2} = a_4 - b_4 * ln(C_{O_2} + c_4) \tag{2.11}$$

C_{O_2}: O_2 concentration in %, a_4 = -3.662, b_4 = 1.001, c_4 = -0.026.
a, b and c are constants derived from data fitting; at room temperature.

The temperature dependence of O_2 response is illustrated in Fig. 2.38. For a given O_2 concentration, R_{O_2} decreases linearly with temperature. Sticking to a fixed O_2 concentration of C_{O_2} = 1%, we find:

$$R_{O_2} = A_4 - B_4 * T \tag{2.12}$$

A_4= 4.13, B_4= 0.0208 [1/°C], T = temperature in °C.

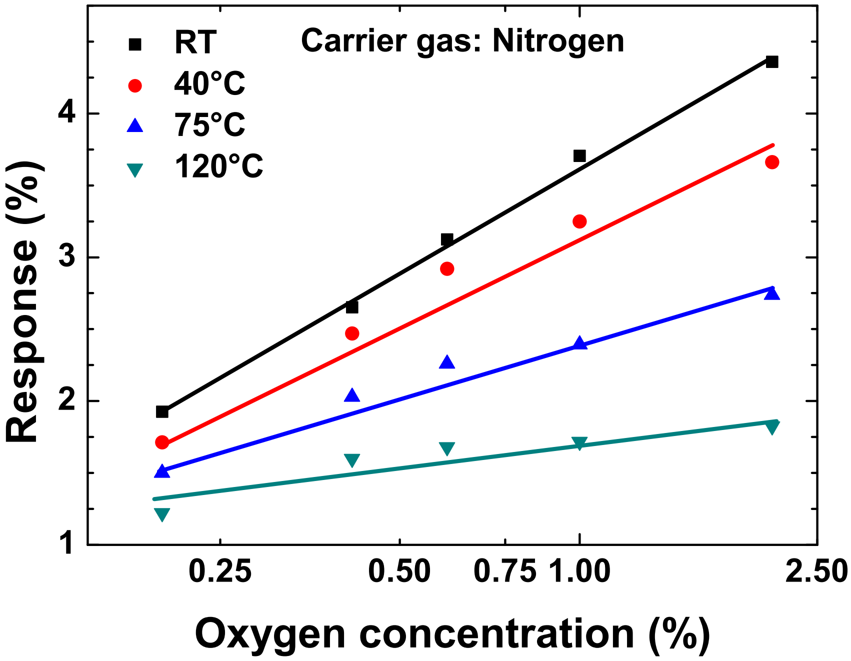

Figure 2.37: *O_2 response observed at different transducer temperatures. The highest sensitivity is observed at room temperature.*

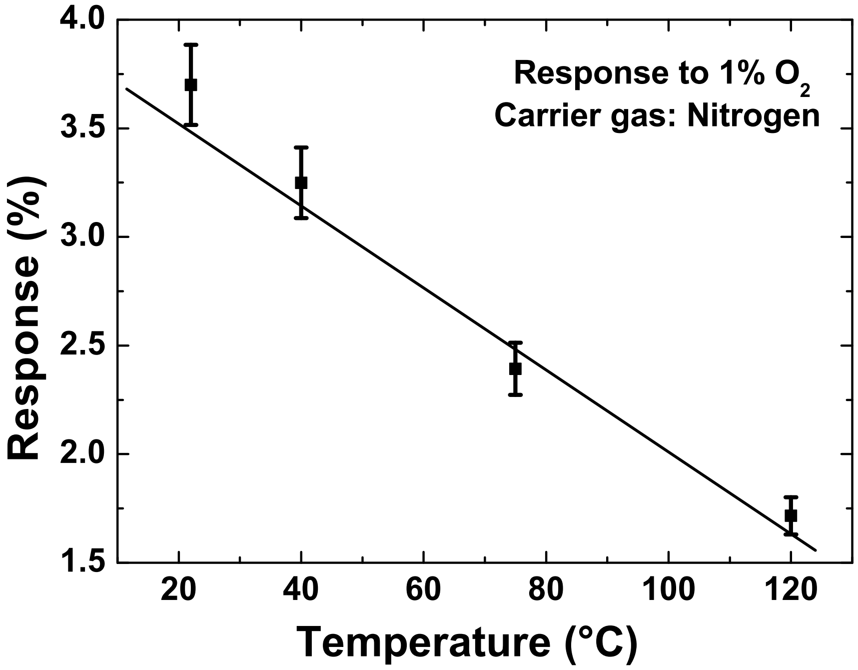

Figure 2.38: *PL response to 1% 0_2 as measured over a range of temperatures.*

Response to nitrogen dioxide and ozone

NO_2 and O_3 gas sensing tests yielded similar results as those presented for O_2 above. However, much lower gas concentrations than O_2 were needed to observe sizeable PL intensity changes. This first fact is illustrated in Fig. 2.39, which shows the room temperature response to NO_2 pulses in humidified synthetic air with NO_2 concentrations ranging between 100 ppb and 1000 ppb.

In a second set of experiments the optochemical transducers were operated at a sequence of increasingly higher transducer temperatures while a sequence of NO_2 gas exposure pulses was applied at each temperature: The obtained result is shown in Fig. 2.40. As in the O_2 case (Fig. 2.36) decreasing PL baseline signals and smaller gas-induced PL changes were observed as the transducer temperature was raised.

Fig. 2.41(a) shows NO_2 response data as derived from the raw data in Fig. 2.40. Again, a logarithmic increase of the relative NO_2 response R_{NO_2} was observed as the NO_2 concentration was raised:

$$R_{NO_2} = a_5 - b_5 * ln(C_{NO_2} + c_5) \tag{2.13}$$

C_{NO_2}: NO_2 concentration in ppb, $a_5 = 14.99$, $b_5 = 3.35$, $c_5 = 41.59$; at room temperature.

Fig. 2.41(b) shows that R_{NO_2} rapidly drops as the transducer temperature is increased. Like in the O_2 case, a linear decrease in R_{NO_2} with temperature is observed. Sticking to a NO_2 concentration of $C_{NO_2} = 250$ ppb, we find:

$$R_{NO_2} = A_5 - B_5 * T \tag{2.14}$$

A_5= 6.8145, B_5= 0.08389 [1/°C], T = temperature in °C.

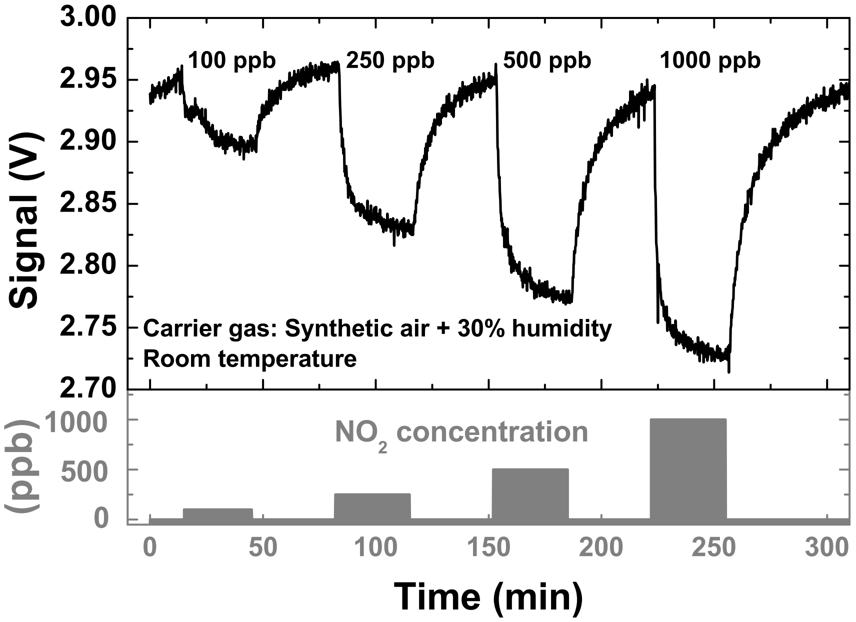

Figure 2.39: *Response of the PL intensity to a sequence of NO_2 concentration steps applied at room temperature. The carrier gas was humidified synthetic air with a relative humidity of 30%.*

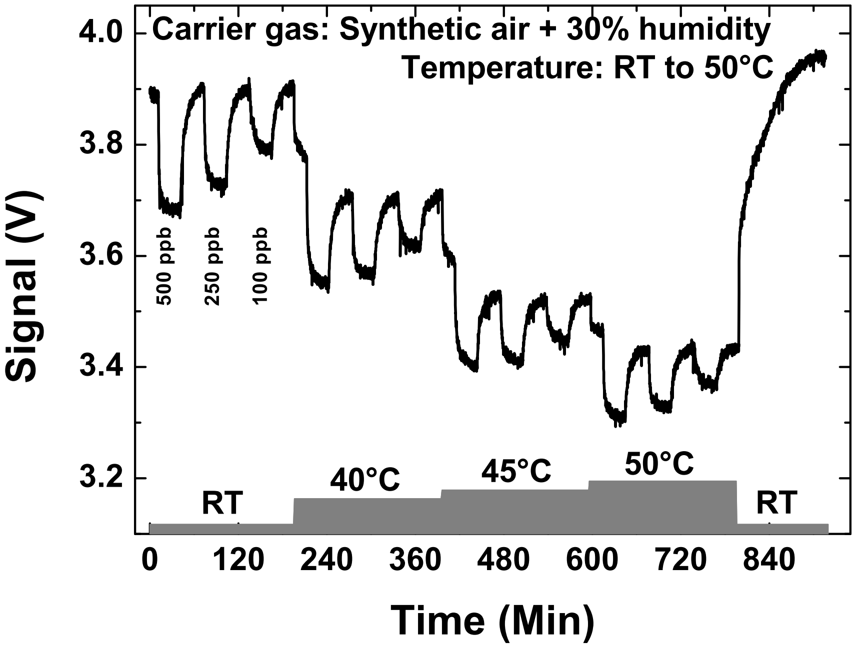

Figure 2.40: *Response of the PL intensity to a sequence of NO_2 concentration steps as applied at increasingly higher temperatures. The carrier gas was humidified synthetic air with a relative humidity of 30%.*

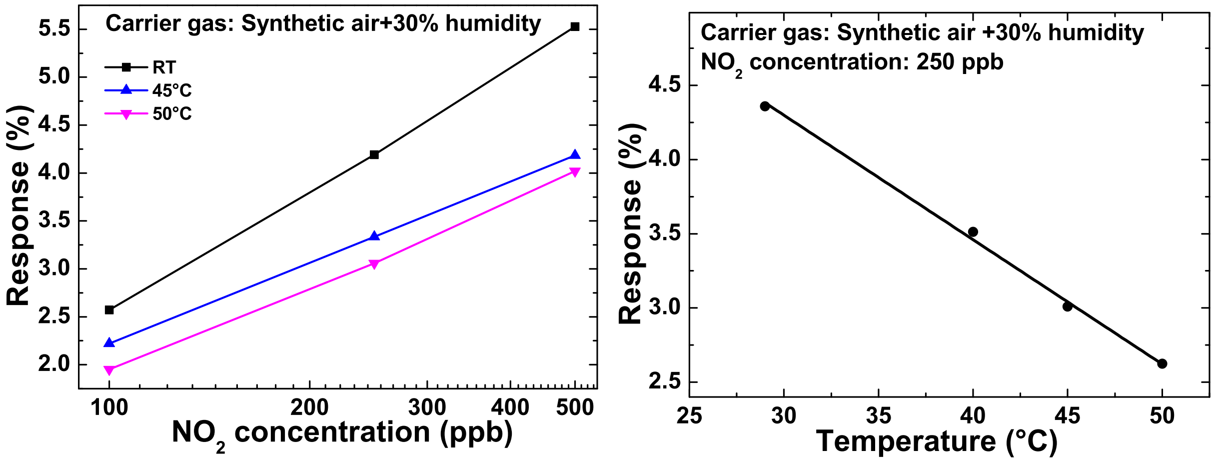

(a) (b)

Figure 2.41: *(a) Variation of the response with increasing NO_2 concentration at three temperatures; (b) temperature dependence of the NO_2 response as measured at a concentration of 250 ppb. The carrier gas in both cases was humidified synthetic air with 30% relative humidity.*

A gas response that has not yet been discussed above is the cross sensitivity to water vapor. As ambient air may unavoidably contain highly variable levels of humidity, this effect needs consideration here. Some key observations with regard to humidity are reported in Figs. 2.42 and 2.43.

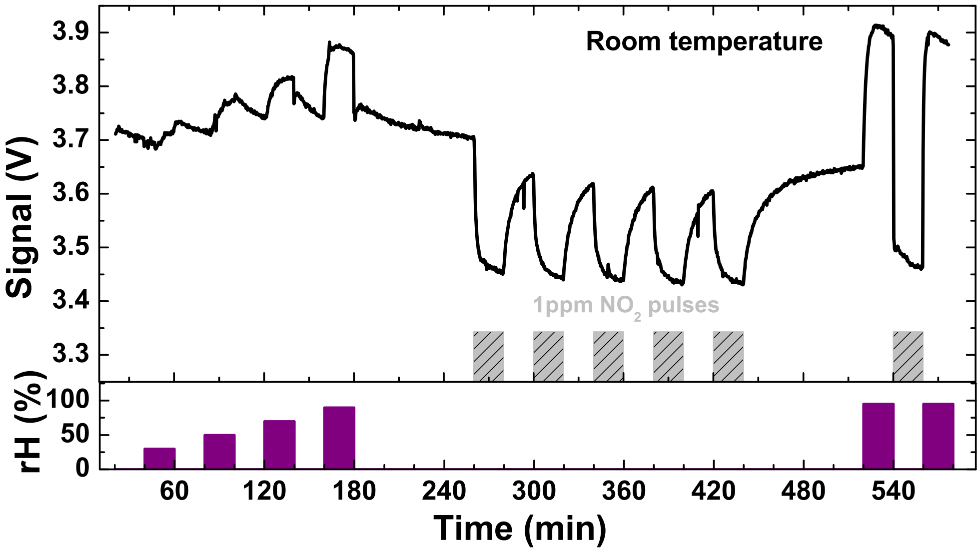

Figure 2.42: *Response to a series of NO_2 gas pulses as applied under dry and humid air conditions.The first four pulses of synthetic air with increasing humidity from 30% to 90% show the trend of enhanced PL intensity with rising humidity.*

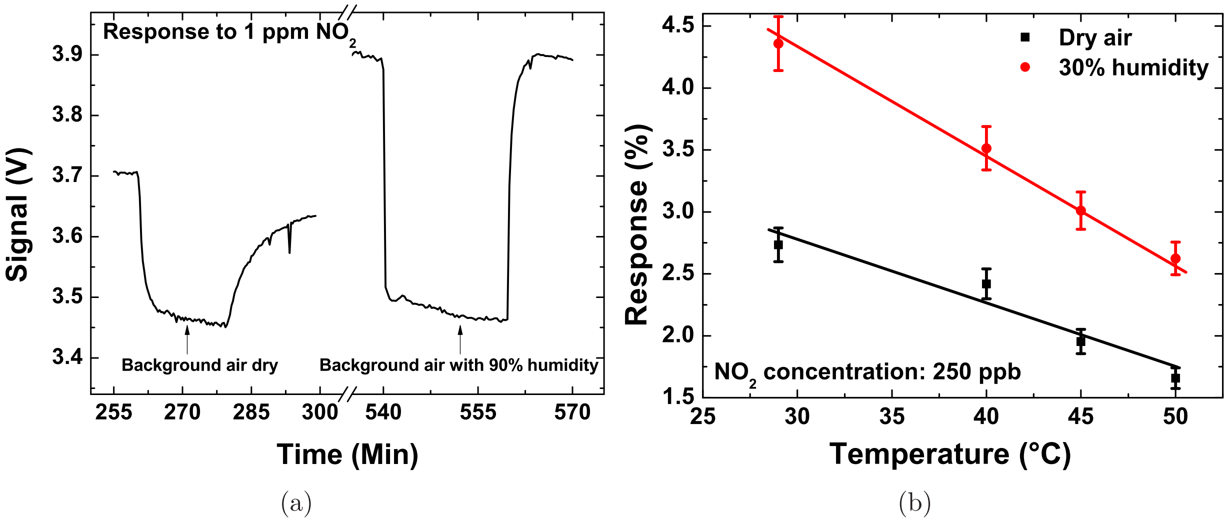

(a) (b)

Figure 2.43: *a)Transient response to 1 ppm NO_2 with dry air and humid air (90% humidity) as carrier gas; b) temperature dependence of the NO_2 response as observed under dry (lower curve) and humid (upper curve) conditions. Presence of humidity enhances the gas response.*

Fig. 2.43(a) illustrates the transient response to 1 ppm NO_2 at room temperature with dry and humid background air. Higher sensitivity and faster response/recovery time can be noticed in presence of humidity. Fig. 2.43(b) shows that irrespective of the transducer temperature, consistently higher gas sensitivities are observed, when the transducers are exposed to NO_2 gases in humid air. Similar enhancement of response was also observed in case of H_2 and HC gases discussed earlier. The formation of hydroxyl (OH) groups on the NW surface in presence of humidity, which influences the surface recombination rate was proposed as a probable reason for this phenomenon in Sec. 2.5.2.

Ozone is a more powerful oxidizing agent compared to NO_2. This results in a higher response of the related PL intensity. A summary of the related experimental results for the O_3 response is given in Figs. 2.44 and 2.45. Fig. 2.44 illustrates the transient response to three different O_3 concentrations in presence of humid background air. Higher O_3 concentration resulted in increased PL quenching similar to O_2 and NO_2 gases described earlier. Fig. 2.45 shows the concentration and temperature dependence of the O_3 response. Similar to the two cases discussed earlier, we observe that the magnitude of the O_3 response R_{O_3} scales logarithmically with the O_3 concentration (Fig. 2.45(a)):

$$R_{O_3} = a_6 - b_6 * ln(C_{O_3} + c_6) \tag{2.15}$$

C_{O3}: O_3 concentration in ppb, a_6 = 12.37, b_6 = 3.03, c_6 = 50.05; at room temperature.

Similar to the cases of O_2 and NO_2, the O_3 response decreases with increasing transducer temperature. This is shown in Fig. 2.45(b). Sticking to a fixed O_3 concentration, R_{O_3} decreases linearly with increasing temperature. At an O_3 concentration of C_{O_3} = 100 ppb, we find:

$$R_{O_3} = A_6 - B_6 * T \tag{2.16}$$

A_6= 7.11656, B_6= 0.07923 [1/°C]; T = temperature in °C.

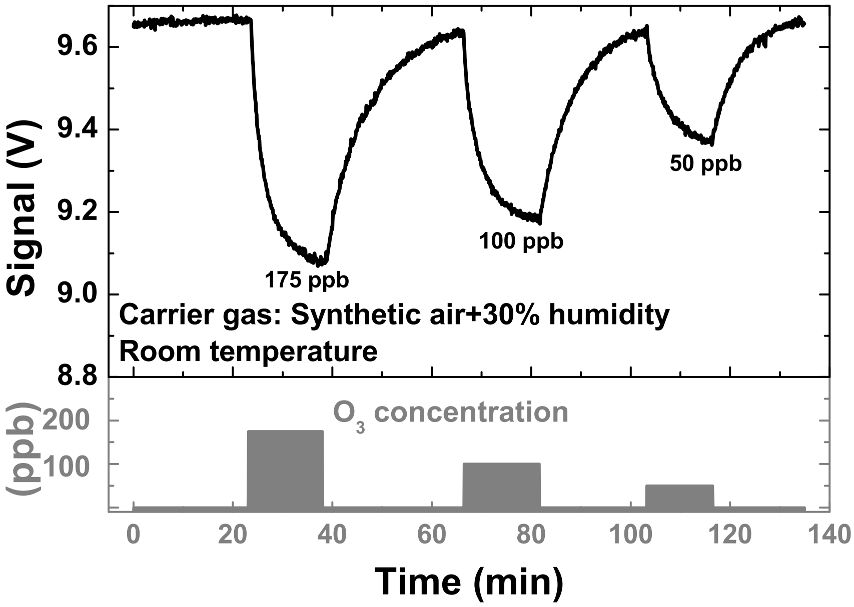

Figure 2.44: *Variation of the PL intensity in response to a sequence of* O_3 *concentration steps as applied at room temperature.*

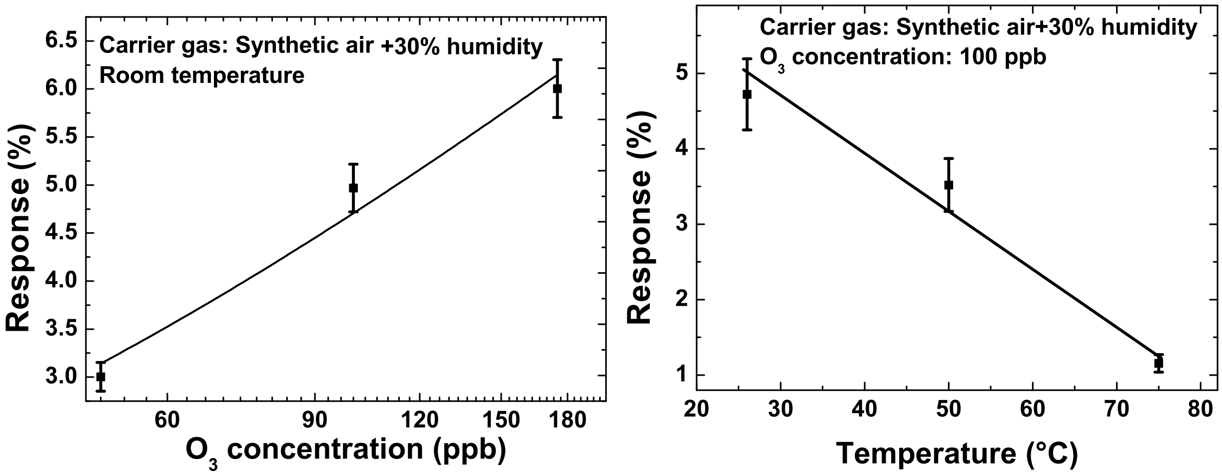

(a) (b)

Figure 2.45: *(a) Variation of the room temperature response with increasing* O_3 *concentration; (b) temperature dependence of the* O_3 *response as measured at a concentration of 100 ppb. The background gas in each case was synthetic air with a relative humidity of 30%.*

2.6.3 Discussion - sensing oxidizing gases

The data summarized above have shown that the gas response towards O_2, NO_2 and O_3 follows fairly similar concentration and temperature dependences. As these species do quench the photoluminescence of the III-nitride nanowires, Teubert et al. proposed that these adsorbates form non-radiative radiation centers on the III-nitride nanowires [136]. Chen et al. suggested that, the adsorbed oxygen could act as a donor-type molecule, which might release electrons and reduce space charges by simply adsorbing onto surface and/or filling the defect sites, resulting in the shortening of surface depletion region width and lowering of surface band bending [157]. In this final section we compare and contrast the observed response patterns with the aim to obtain further clues to the underlying gas response mechanisms.

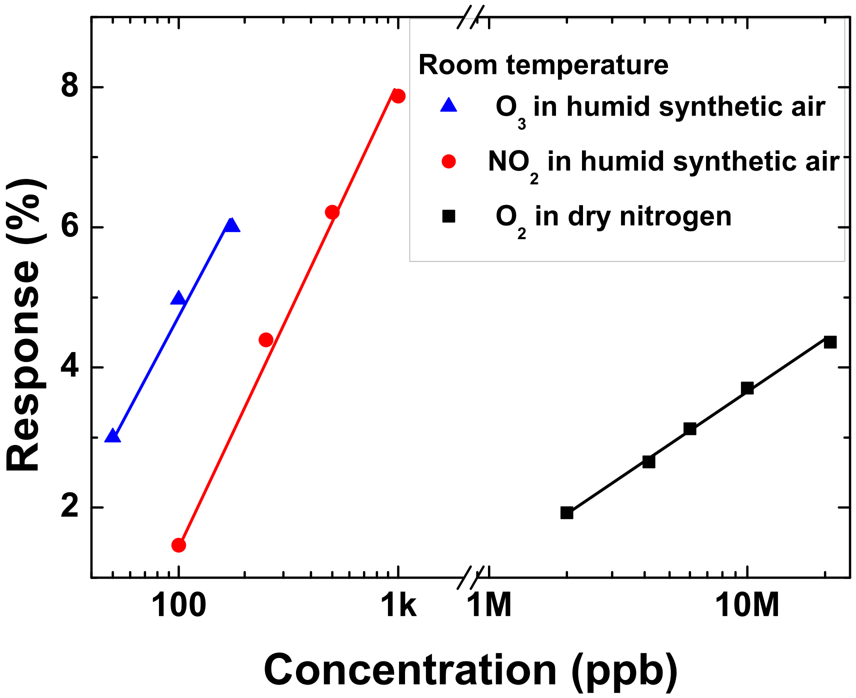

Figure 2.46: *Calibration curves for the three oxidizing gases investigated.*

Considering the absolute values of the gas response, there is a huge difference between O_2, NO_2 and O_3. This difference is visualized in Fig. 2.46 which draws together room temperature calibration curves for all three gases. Whereas NO_2 and O_3 can be detected with ppb sensitivities, O_2 needs to be supplied on the order of 1000 ppm to become detectable.

A possible clue towards explaining these big differences in gas response is considering the vastly different oxidation powers of the three analytes. In order to make this point Table 2.4 compares the electron affinities of the three analytes to their experimentally determined gas response characteristics. The data in the fourth column of Table 2.4 relate to the minimum gas concentration that can be distinguished from the thermal noise of the background PL signal. In order to determine this concentration the usual 3σ criterion with σ being the rms noise voltage was applied. As an alternative measure we have listed in the fifth column the gas concentrations that are needed to attain R_{ox} = 5%.

According to the data of Table 2.4), the electron affinity of O_3 and NO_2 are much higher than that of oxygen. This potentially explains the huge difference in sensitivities between both groups of gases. On the basis of electron affinities alone, NO_2 exhibit higher sensitivity than O_3. Higher NO_2 response was also observed for several kinds of metal oxide thin film sensors (WO_3 [158], In_2O_3, MnO_3 [159]) where both NO_2 and O_3 were investigated with same sensor. In our sensor UV absorption and photolysis of gas molecules also play a role and thus may determine its sensitivity. Bogumil et al., for instance, reported that, NO_2 has much bigger absorption cross section than that of O_3 in UV radiation [160]. Moreover, the photolysis of NO_2 molecules is reported in ref [160]. There, NO_2 photolysis was proposed to proceed according to: $NO_2+h\lambda \rightarrow NO+O$, and a secondary reaction $NO_2+O \rightarrow NO+O_2$. In comparison to NO_2, NO has a very low electron affinity (0.04 eV). Therefore, it can be conceived that a fraction of the NO_2 also disappears through photolysis and thereby shows a lower sensitivity than O_3.

Analyte gas	Electron affinity (eV)	Absorption cross section at 365 nm ($cm^2 molecule^{-1}$)	Minimum detectable concentration	Gas concentration required to obtain R_{ox} = 5%
Oxygen	0.451	n.a.	1000 ppm	3.3%
Nitrogen dioxide	2.273	$5*10^{-19}$	50 ppb	350 ppb
Ozone	2.1028	$1*10^{-23}$	10 ppb	110 ppb

Table 2.4: *Electron affinity, absorption cross section at 365 nm and minimum detectable gas concentrations for the three gases investigated [161].*

One of the most important features for gas sensing is the response time of the transducers. The NWH transducers showed a response time (to reach 90% of the saturation value) of about 3 - 4 min to 1% O_2, 6 - 7 min to 500 ppb NO_2 and 5 - 6 min to 100 ppb O_3.

In addition to the concentration dependence, any model of the NWH gas sensing effect needs to provide an explanation for the temperature dependence of the gas sensitivity. Fig. 2.47 summarizes the temperature dependence already reported above, this time however, in a way that makes apparent that the gas sensitivity reduces to zero at a certain gas-specific temperature. The data of Fig. 2.47 again bring out the huge difference between O_2, on the one hand, and NO_2 and O_3, on the other hand. Whereas in the first case the maximum temperature is likely to occur well beyond the experimentally accessible temperature range, the temperature maxima of the stronger oxidizing gases, NO_2 and O_3, occur only around 90°C.

A common characteristic of all calibration curves for concentration is that, the response varies almost linearly with the logarithm of gas concentration. This fact is illustrated in Fig. 2.34 for H_2 and HC gases and in Fig. 2.46 for oxidizing gases. Such logarithmic dependences emphasize very small gas concentrations and reduce the sensor resolution at larger concentrations. Considering the fact that the form of calibration curves is usually

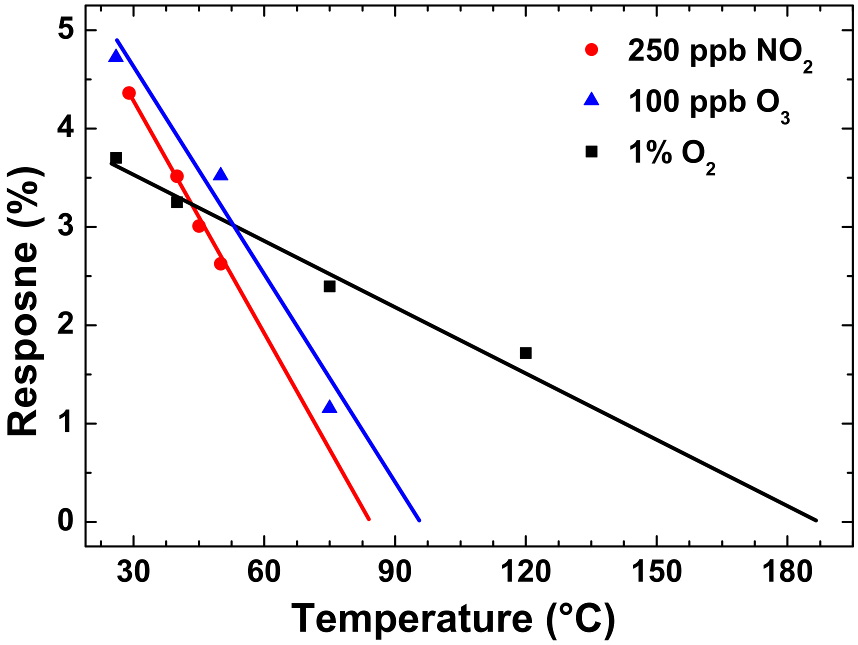

Figure 2.47: *Temperature dependence of the response for three oxidizing gas species investigated*

determined by chemical kinetics, square-root and other fractional power laws are expected [162]. The data of Figs. 2.46 and 2.34 presents the response characteristics in the form of a lin-log plot for the eight investigated gases. This logarithmic relationship is always described with the flowing equation:

$$R_{gas}(\%) = a - b * ln(C_{gas} + c) \tag{2.17}$$

This equation is analogous to "Freundlich adsorption isotherm" which explains the variation of adsorption of a quantity of gas adsorbed by unit mass of solid adsorbent. This linear variation of transducer response to logarithmic analyte concentration is also typical for solid state gas sensors.

ConstantAnalyte gas	Temperature	a	b	c
Hydrogen	80 °C	-7.86	-4.68	5
Acytelene	80 °C	-16.35	-3.73	250
Ethylene	80 °C	-16.91	-2.87	250
Oxygen	RT	-3.662	1.001	-0.026
Nitrogen dioxide	RT	14.99	3.35	41.59
Ozone	RT	12.37	3.03	50.05

Table 2.5: *Comparison of the constants derived from the calibration curves for different anylyte gases.*

The constants a, b and c of equation 2.17 for 6 investigated gases are listed in Table 2.5. Constant b represents the gradient of the calibration curves and therefore, can be related to the physio-chemical properties of the analyte. The other two constant, a and c determine the offset of the curve. The opposite sign of constant b indicates that, the response R_{gas} increases with H_2/HC gases and decreases with oxidizing gases. In the first case, H_2 has the highest value of the gradient followed by C_2H_2 and C_2H_4, which can be explained by the grade of saturation in HC molecules. For oxidizing gases, constant b follows the trend of electron affinity for the three investigated gases, i.e. $NO_2 > O_3 > O_2$, which was presented in Table 2.4).

2.6.4 Synopsis of oxidizing gases sensing

- GaN/InGaN nanowires heterostructures have been investigated as a optical transducer for oxidizing gases;
- The enhancement of surface recombination in NWHs in presence of oxidizing gases is responsible for reduction in PL-intensity;
- At room temperature minimum detectable gas concentrations are 1000 ppm for O_2, 50 ppb for NO_2 and 10 ppb for O_3;
- Above the minimum detectable gas concentrations the gas response increases linearly with the logarithm of the gas concentration;
- The gas response decreases in an approximately linear manner with increasing temperature;
- The response time of the sensors is in the order of few minutes;
- Presence of humidity enhances the sensor sensitivity and response time.

CHAPTER

3

pH monitoring

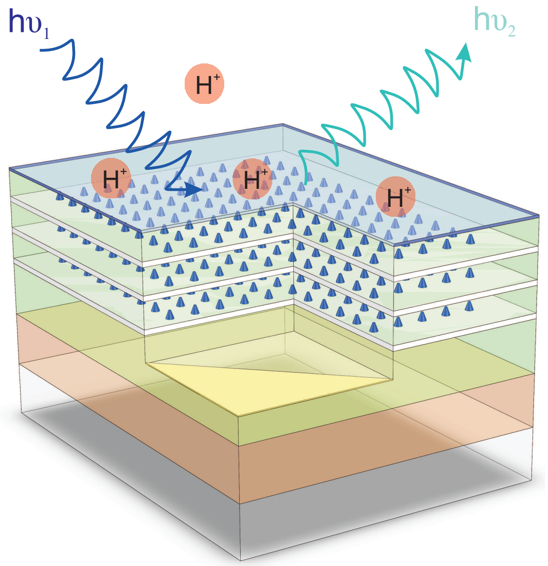

GaN/InGaN quantum dots as optochemical transducer for pH sensing are reported here. The chapter begins with a brief presentation of potential application in an aircraft. The sensing mechanism of the QD transducers is presented briefly, followed by the description of the test setup. The results section illustrates the variation of photoluminescence intensity with applied electrical bias and with different pH medium.

3.1 pH monitoring applications in aircraft

Large quantities of drinking water is carried onboard of commercial aircrafts. The newly developed Airbus A380, for instance, carries an onboard supply of 3 tons of water. In terms of weight such a load is equivalent to about 30 passengers or about 6% of the seating capacity. As this is a non-negligible fraction, workarounds are being thought out that could ameliorate this situation. One of the favorite solutions is carrying liquid H_2 onboard that will be burnt in a fuel cell to generate the electricity required onboard and the required amount of water alongside. In order to comply with authority regulations for the water quality, the pH of the water needs to be adjusted to fall into a relatively narrow pH interval. This request arises from the aircraft-specific requirement that, with the pH staying in the acceptable range, it should be such that deposits inside the piping system are kept to a minimum so that expensive maintenance actions can be avoided. Up to the present time, however, small, rugged and light-weight pH sensors, which maintain their calibration for long time, are not yet available. Considering the fact that bulk GaN-based pH sensors offer excellent chemical stability - not afforded by silicon-based devices - GaN-based QDs sensors could form a very attractive alternative to these present-day pH sensors.

A key advantage of this opto-chemical transducer principle is the strict media separation that is afforded by depositing the QD transducer layers on the top surface of a chemically resistant and optically transparent sapphire substrate while carrying out the optical excitation and the PL readout from the back surface of the sapphire substrate.

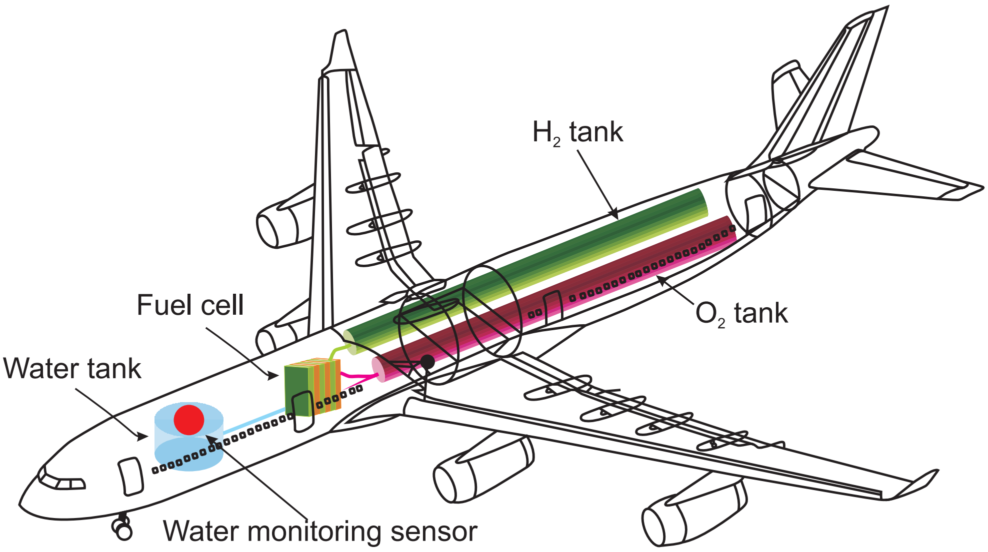

Figure 3.1: *The replacement of conventional auxiliary power units (APU) by fuel cells will allow producing on-board drinking water as a by-product of the power generation and thus increase the payload efficiency of the aircraft. The pH of the fuel cell generated requires continuous monitoring.*

3.2 QD as optical sensing element

Quantum Dots (QD) or semiconductor nanocrystals are almost ubiquitous in the field of nanotechnology. The term quantum dot was first used by E. Brus from Bell Labs in 1980 [163]. A QD is a cluster of a few hundred atoms arranged in binary (e.g. III-V, II-V, SiC and etc.) or ternary compound (e.g. AlGaN, InGaAs, CdZnTe and etc.). The size of QDs typically ranges from 2 to 20 nm. These QDs are small enough to exhibit discrete energy levels. As a consequence, the emission and absorption characteristics of QDs can be tuned to application needs simply by altering their size and their crystal geometry. When the size of the nanocrystals approaches the Bohr exciton radius (2.7 nm for GaN [164]), the wave function of the exciton is confined in all three spatial dimensions with the consequence that quantized energy levels turn up. In particular, the absorption and emission energy increases as the QD size decreases. With this possibility at hand, the PL emission of QDs can be adjusted over a fairly wide range, ranging from the UV to the NIR. As an example, Fig. 3.2 shows ten distinguishable emission colors of ZnS-capped CdSe nanoparticles excited with a near-UV lamp, which were used for gene expression studies [165].

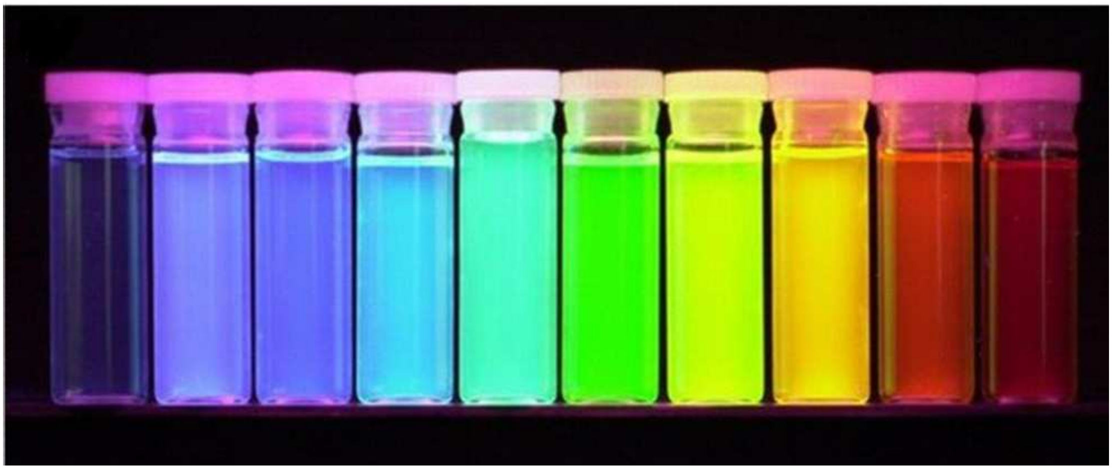

Figure 3.2: *QDs display distinctive colors under UV excitation [165]. CdSe QDs of different sizes are excited with a near-UV lamp. Copyright 2001 Nature Publishing Group.*

Physical sensors
Detecting electromagnetic radiation is an area where QD technology is poised to exert a significant impact. Several works have been reported on QDs for IR detection at low temperature (<200 k) using InGaAs/GaAs material system [166]. QDs are promising materials for making photodetectors because they are strong absorbers of light. Recently, a single layer of PbSe QDs measuring 4 nm in size was demonstrated for sensing in the visible (VIS) wavelength range [167]. Optical temperature sensors using CdSe QDs have been reported by Larrion et al. [168]. A QD based pressure sensor is reported by Kulite Semiconductor, US [169]. The change in the energy band levels of a heterostructures varies as a function of the pressure-induced strain.

Chemical sensors
Examples of chemical species that have been detected with the help of QD detectors include toxic metals, pesticides, explosives, drugs and a range of species of clinical interest [170]. In particular, the photoluminescence of QDs, dispersed in a liquid solution, has been shown to be sensitive to the presence of specific ions. Such possibilities form the basis for several optical ion detection applications [171]. The excellent photo-physical properties of QDs like tunable emission wavelength, broad absorption spectra, narrow and symmetric emission spectra, high emission quantum yield and so on, make them excellent energy donor in various Fluorescence resonance energy transfer (FRET) process [172]. A range of transition metals (Cu, Zn, Ni, Co, etc.) have been investigated with QDs functionalized with different coatings of organic indicator compounds (e.g. Zincon, porphyrin, etc.). Dubach et al. reported ion sensitive QDs (ISQDs) which consists of QDs capped with ion-selective polymer matrix [173]. These ISQDs can detect alkali metal and halogen ions (e.g. Na^+, K^+, Cl^-, etc.). CdTe QDs capped with the amino acid cysteine has been used for sensing TNT. The fluorescence of the QDs is quenched because electrons of the QDs are transfered to the TNT molecules via the formation of what is known as a Meisenheimer complex [174]. Cyanide (CN) modulated quenching behavior of Cu toward the photoluminescence of CdTe QDs has been employed for detecting CN in aqueous solution [175].

A summary that lists few of the QD applications and their sensing approaches is provided in Table 3.1.

Detection Targets	**Sensing Strategy**
Cocaine	Single molecule QD-FRET
TNT	Competitive QD-FRET
Ca^{2+}	QD-FRET with Ca^{2+} sensitive acceptor
Hg^{2+}	CRET with QD
pH	QD-FRET with pH sensitive acceptor
pH	QD quenching through electron transfer
Temperature	QD quenching by temperature
Pressure	QD pressure-induced strain

Table 3.1: *QD sensing strategies and their applications [176].*

3.3 Optochemical pH sensor system based on quantum dots

QDs have been applied for detection and imaging in several areas in life sciences and chemical sensing. Optical pH sensors have found widespread application in environmental analysis, biomedical research, medical diagnosis and industrial process control. Since the first report on an optical fiber-based pH sensor in 1980 [177], numerous kinds of optical pH sensors have been invented and developed for commercial applications. As a common transducer principle such sensors benefit from the pH-dependent fluorescence and absorbance of chemically activated dyes. More recently, pH-sensing QDs based on Cd-chalcogenides have attracted renewed interest in optical pH sensors [170, 178–180]. In the following sections the application of III-nitride QDs for the optical detection of pH changes inside a liquid is presented. This work builds on the observation that oxidised GaN surfaces are pH sensitive and that such III-nitride-based materials feature excellent chemical stability in harsh chemical environments. Excellent optical properties of III-N QDs in term of thermal stability of PL intensity permits the realization of PL-based transducers operating at and above room temperature.

3.4 Sensing principle

A schematic of a typical transducer structure is presented in Fig. 3.3. The transducers consist of several layers (3-5) of InGaN QDs embedded within a GaN matrix. Gas sensing application using similar transducer was reported by Weidemann et al. [181]. Depending on the strength and the direction of external electric fields, the radiative recombination inside such nanostructures can be enhanced or suppressed. Radiative recombination inside InGaN QDs competes with tunneling transport through the thin GaN barriers which separate neighboring QDs. Tunneling photocurrents open non-radiative recombination channels and thus quench the PL. Changes in the internal electric field can also be affected by exposing the QD structures to liquids with different pH values.

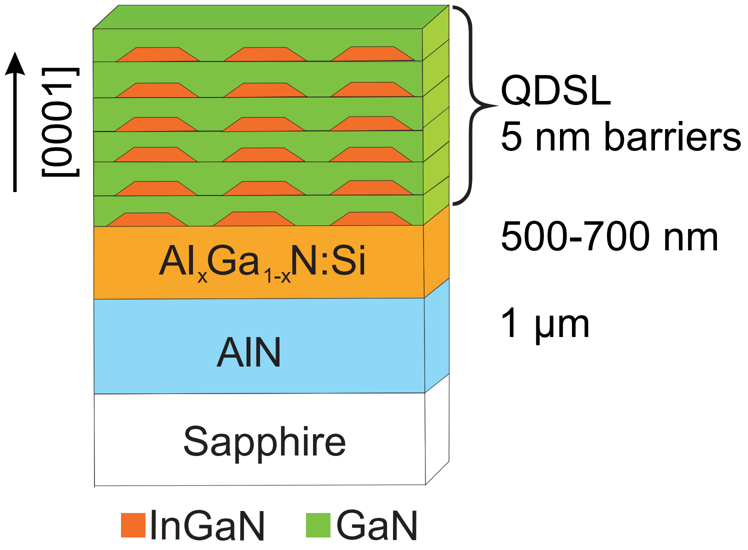

Figure 3.3: *Schematic of the InGaN QD sensor structure (not to scale).*

Steinhoff et al. mentioned that natural oxide such as Ga_xO_y on the GaN surface could be responsible for the pH response of GaN-based pH-sensitive FETs [153]. The pH response of metal oxide surfaces has been explained in terms of the site-binding model by Yates et al. [182]. When exposed to an aqueous solution, amphoteric hydroxyl groups are formed at the oxidic surfaces in contact with aqueous solutions (JOH: J represents Si or metals). These hydroxyl groups may be neutral, protonized or deprotonized depending on the H^+ concentration inside the solution for the relevant reactions, as follows [153, 179, 183–185] :

$$JOH \rightleftharpoons JO^- + H^+ \tag{3.1}$$

$$JOH_2^+ \rightleftharpoons JOH + H^+ \tag{3.2}$$

These dissociation reactions, therefore, lead to a pH dependent net surface charge and a change in surface potential at the solid-liquid interface. Thereby, a change in pH can facilitate or suppress the radiative recombination inside the QD transducers.

3.5 Growth of QD transducers

The optochemical transducers used in this work were grown by the group of Eva Monroy from CEA in Grenoble. 1 μm thick (0001)-oriented AlN-on-sapphire templates were used as substrate for the plasma-assisted molecular beam epitaxy growth. After degreasing and acid cleaning, the substrates were introduced into a growth chamber equipped with standard effusion cells for Ga, In, Al and Si and an HD-25 Oxford Applied Research nitrogen plasma cell. For the growth of the 700 nm thick Si-doped $Al_{0.3}Ga_{0.7}N$ transparent contact layer, the nitrogen-limited growth rate was fixed at 0.3 ML/s (≈ 270 nm/hour), and the substrate temperature, measured by a thermocouple in mechanical contact with the molybdenum sample holder, was set to $T_S = 720°\text{C}$. The Al flux was fixed at 30% of the stoichiometric value (the Al sticking coefficient is known to be unity [186]) and the growth was performed under Ga excess, with a Ga flux close to the Ga accumulation limit.

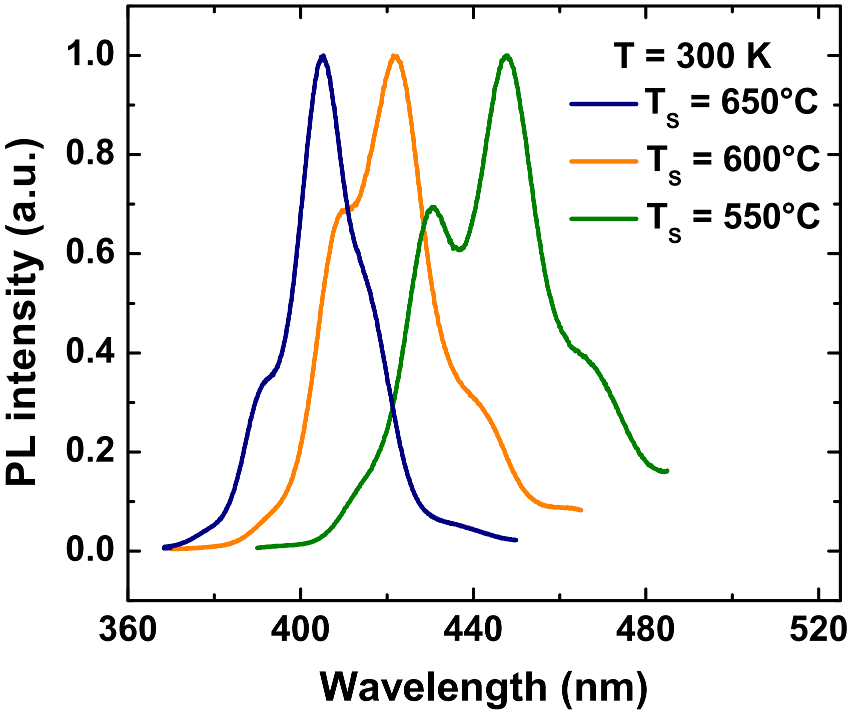

Figure 3.4: *Room temperature (300 K) PL emission from InGaN QD sensor structures where the QDs were deposited at different substrate temperatures. The red shift of the emission wavelength is a result of the enhanced In incorporation in the QDs at lower substrate temperature.*

After the growth of the AlGaN:Si layer and the desorption of the Ga excess, the substrate temperature was decreased to 650-550°C in order to complete the structure with a 5-period InGaN/GaN QD stack. For the generation of InGaN QDs, the Ga flux was fixed at 30% of the stoichiometric value and the In flux was tuned close to the stoichiometry level. Therefore, the Stranski-Krastanov transition is forced by the lattice mismatch, in spite of the slightly metal-rich atmosphere and the well-known surfactant effect of In which promotes two-dimensional growth [187]. For the growth of the 5 nm GaN spacers, the In shutter was closed and a second Ga cell was used, with the Ga flux tuned to the stoichiometric value.

Room-temperature photoluminescence measurements were performed in air by exciting the QDs with a frequency-doubled argon ion laser ($\lambda = 244$ nm). The emission was collected into a Jobin-Yvon HR460 monochromator equipped with an ultraviolet-enhanced charge-coupled device (CCD) camera. The diameter of the excitation spot on the sample was about 100 μm. The excitation power was kept around 100 μW, low enough to avoid screening of the internal electric field. Typical room-temperature PL spectra of transducers grown at various substrate temperatures are presented in Fig. 3.4. The In incorporation rate is very sensitive to the substrate temperature. The PL spectra illustrated here shows the red shift of the emission at decreasing growth temperature, as a result of the enhanced In incorporation in the QWs. The superimposed wavy pattern is due to Fabry-Perot interferences associated with the total nitride thickness.

The evolution of the PL intensity with temperature for a InGaN QD sensor structure is presented in Fig. 3.5. At room temperature the remaining emission intensity amounted to roughly 14% of its 7 K value.

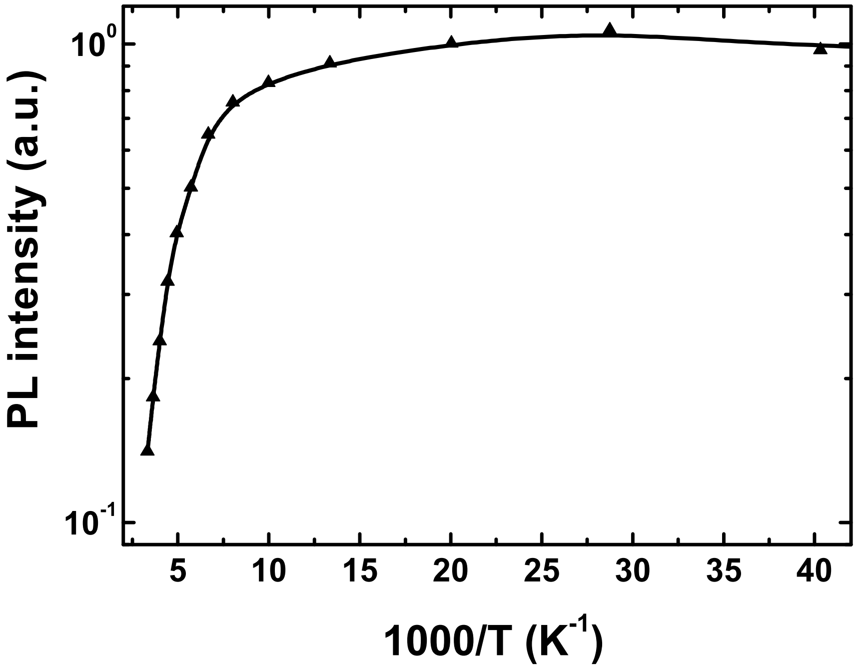

Figure 3.5: *Thermal stability of the PL intensity of the InGaN/GaN QD samples. About 14% of the 7 K PL is detectable at room temperature.*

3.5.1 Preparation of optochemical transducers

The samples were diced into 8 mm x 8 mm plates, and the AlGaN back contact layer was opened at the edges by photolithography and Ar ion-beam etching. Ohmic contacts were realized by deposition of a Ti/Au (25 nm/120 nm) metallization in JLU, Gießen. The as-grown QD samples showed a high density of threading dislocations in the QD multilayers, which resulted in a leakage current across the QD multilayer region [188]. In order to reduce this leakage current, a wet electrochemical oxidation process was carried out. The oxidation was performed using a 3-electrode galvanostat in a pH 11 NaOH solution. During the oxidation process the transducer was reverse-biased (transducer back contact at high and counter electrode at low potential) with a constant current of 20 μA for a total time span of 180 sec. The schematic and a real photograph of the QD transducer sample is presented in Fig. 3.6.

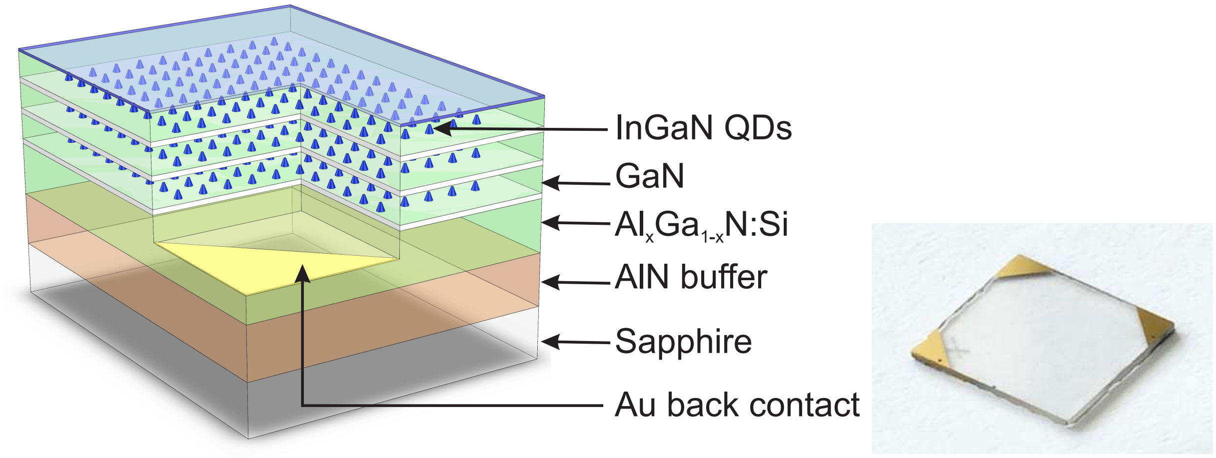

(a)

(b)

Figure 3.6: *a) Schematic of the final transducer structure. With the help of photolithography and ion-beam etching the* $Al_xGa_{1-x}N$*:Si layer was opened. Ohmic contacts were realized by deposition of a Ti/Au on this AlGaN:Si layer. b) photograph of a QD transducer.*

3.6 Sensor system setup

A schematic of the entire experimental setup is presented in Fig. 3.7. The QD transducer elements were mounted inside a small chamber with the transducer layers facing the interior of the cell. This cell had an internal volume of 0.7 cm^3 and contained inlet and outlet ports to enable fluid exchange. Chemically inert black polyoxymethylene (POM) was used for constructing this chamber. A detailed illustration of the measurement chamber is presented in Fig. 3.8. The experimental setup consisted of two primary blocks other than the measurement chamber: the optical system and the fluidic system. The optical system included the optical excitation, the detection and wave-guiding devices. These optoelectronic components are already described in the previous chapter in section 2.4. The QD transducers investigated in this work had a peak emission wavelength at >420 nm. The UV excitation was performed with LED emitting at 365 nm. This large stokes shift eased the system design significantly. The fluidic system consisted of a multi-position valve and a micro pump. The multi-position valve with 10 individually controllable inlets was used to guide different pH solutions to the measurement chamber. A micro pump from HNP Mikrosysteme GmbH was used for directing the different pH solutions to the measurement chamber. Materials for both the valve and the pump system were selected to be chemically inert. A potentiostat from Bank EIC GmbH was used for biasing of the transducers with respect to the electrolyte solution. For enabling this biasing task, an Ag-AgCl reference electrode and a Pt counter electrode were inserted into the measurement chamber.

The complete system is demonstrated in Fig. 3.9. All electronic circuits for driving the optical (LED, photomultiplier) and mechanical components (pump, multi-position valve) were housed inside two separate boxes. All the electronic components were connected to a PC through different BUS systems (RS-232, USB, GPIB). A LabVIEW application was developed for programing a fully automated measurement routine.

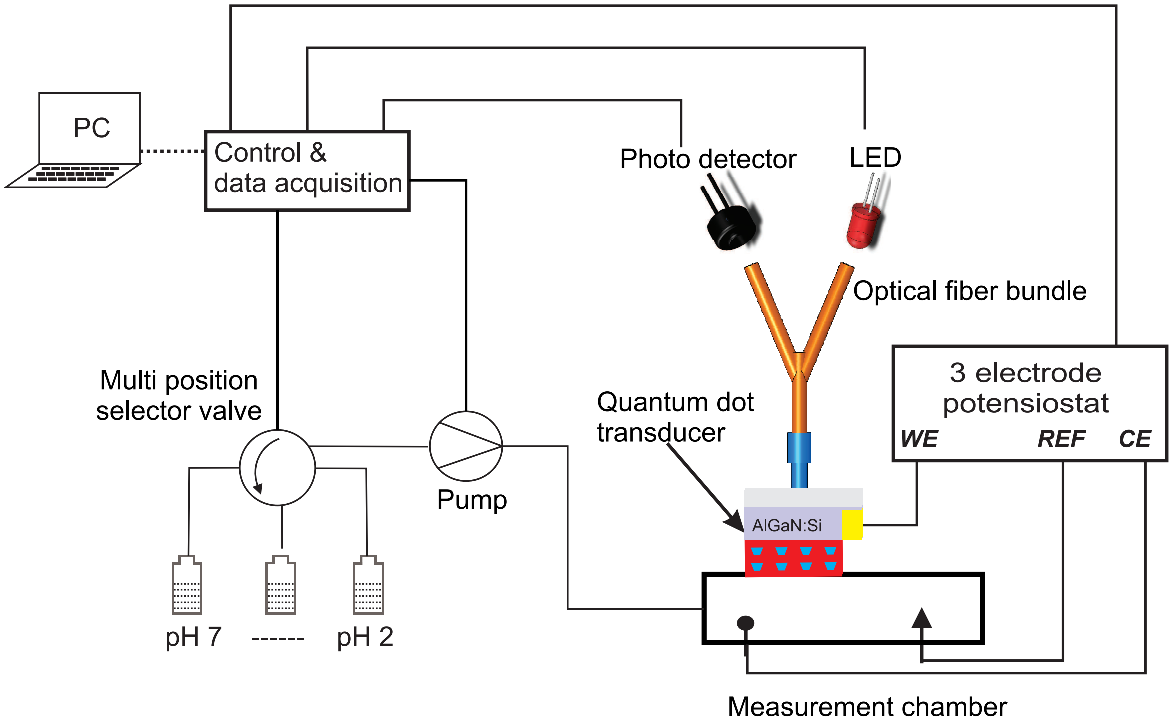

Figure 3.7: *Schematic of the pH measurement setup. The desired fluid is chosen with the help of selector valve. A pump routes the fluid to the measurement chamber. A Y-shaped fiber bundle serves as an optical waveguide. A 3-electrode system is used to apply bias between the QD back contact and the electrolyte.*

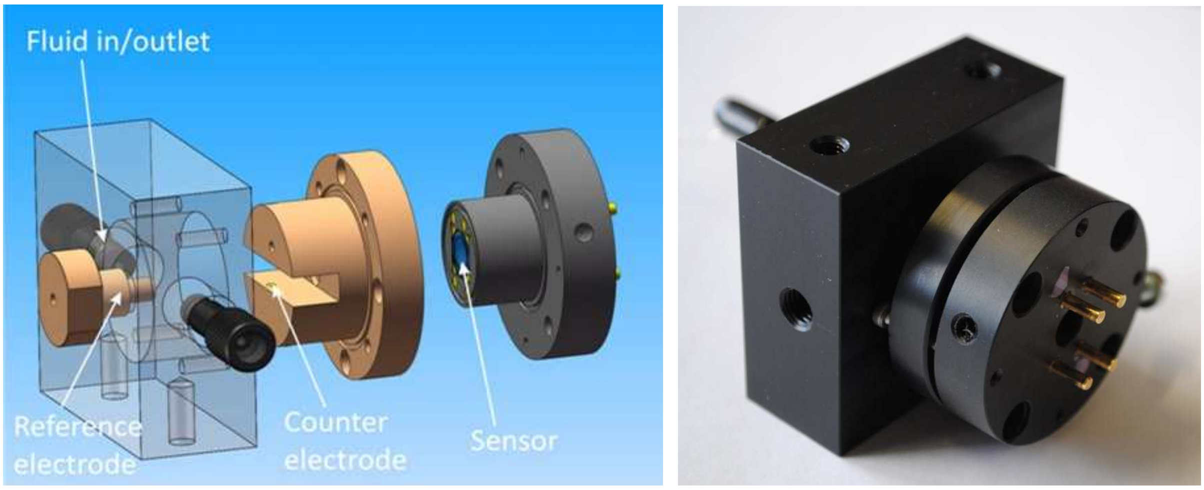

(a) (b)

Figure 3.8: *a)Exploded view of the sensor holder unit. This screw in unit can be fixed to the measurement chamber, b) photograph of the manufactured and assembled measurement chamber*

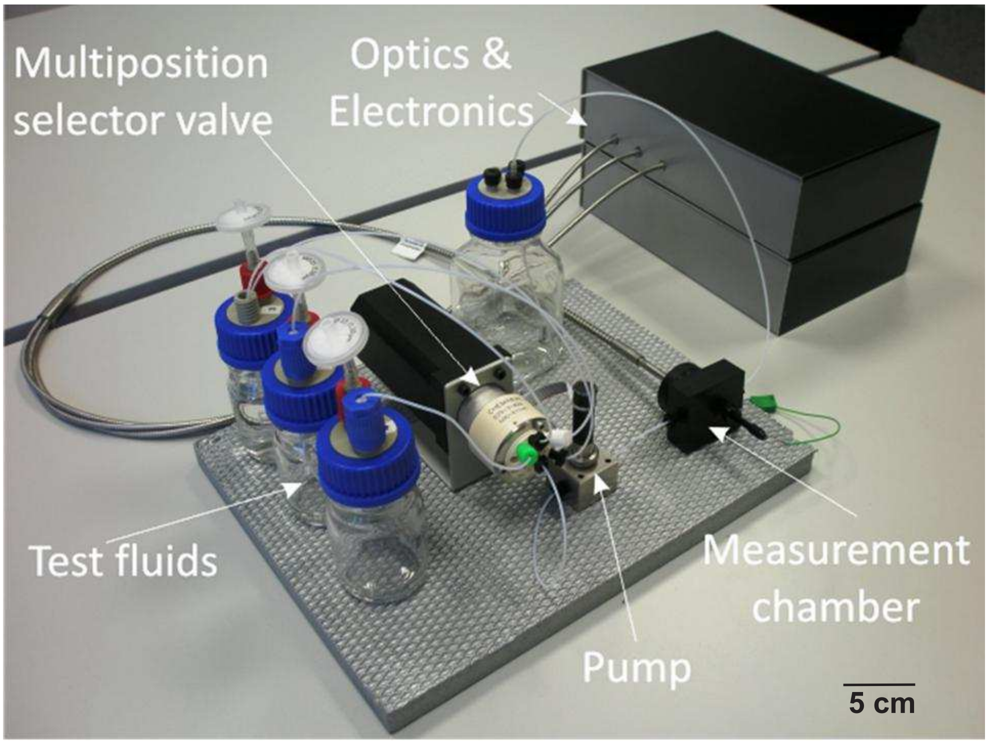

Figure 3.9: *Photograph of the realized sensor system. The system was built with chemically inert fluidic components. The driver electronic boards and the optical components were housed in the two black metallic boxes.*

3.7 Results and discussion

Ready to use pH buffer solutions supplied by Carl Roth GmbH were used as test fluids in all experiments. A constant moderate flow rate was maintained during all tests. All experiments described below were performed at room temperature.

Before performing the tests with the different pH solutions, PL intensity changes were studied that occurred upon application of external electric fields. Polar III-Nitride semiconductors are characterized by polarization-induced internal electric fields which strongly affect the potential profile of nitride-based heterostructures. Therefore, the influence of the applied external electric field in electrolyte for InGaN/GaN QDs will be an interesting aspect to study. In the following we will first show the electric field dependency of the PL intensity at fixed values of pH and then the variation of the PL intensity as the transducers were exposed to different pH solutions at a fixed value of applied electric field.

3.7.1 Electric field dependence

The response of transducer sample C2438 to different bias voltage is illustrated in Fig. 3.10. In this experiment a pH 7 buffer solution was used as an electrolyte and the external bias was raised in 100 mV steps while the PL output of the QD transducers was monitored.

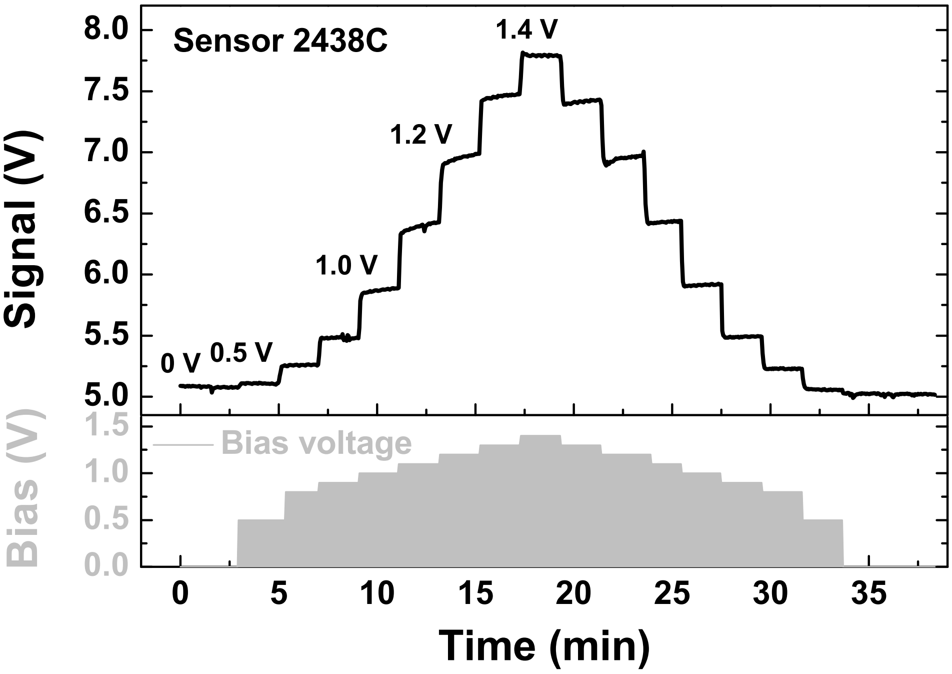

Figure 3.10: *PL intensity response to changes in applied bias.*

In Fig. 3.11, the above set of raw data had been processed to yield a plot of PL signal output versus bias voltage. Fig. 3.11, in addition, contains results obtained on two additional transducers. Obviously, all three transducers reacted in a very similar way to changes in the external bias. Considering these characteristics, the sensor performance with regard to different application requirements can be optimized. Considering sensor 2291C, for instance, and setting the working bias at 1 V, i.e. the lower knee of the PL-bias curve, a fairly wide pH measurement range (pH 2-7) can be obtained. Increasing the bias potential to about 1.2 V, the transducer is biased into the region of highest slope. Under these latter conditions high-resolution measurements within a fairly small range around pH 6-7 can be performed.

According to Steinhoff et al., GaN surfaces in electrolyte solutions showed an almost Nernstian behavior with sensitivities of 57.3 mV/pH for GaN:Si/GaN:Mg FET structures [153]. In order to assess the resolution of our optochemical pH sensor, we have applied a series of 6 mV external potential steps to transducer 2438C while monitoring its PL response. These latter data are reported in Fig. 3.12. The noise in the PL response suggests that this sensor is able to resolve pH steps in the order of 0.1 pH units.

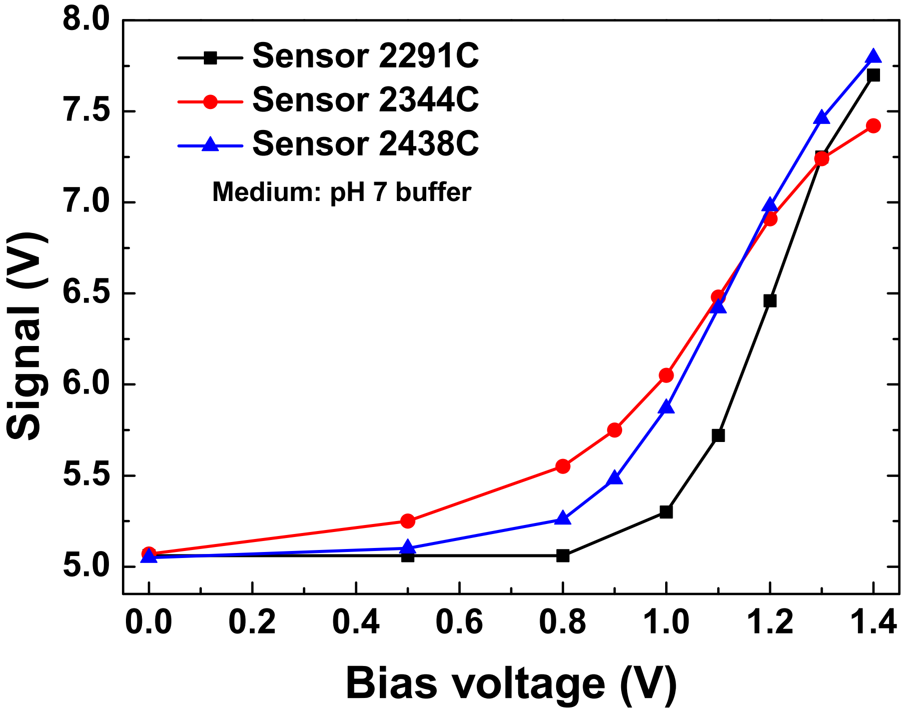

Figure 3.11: *PL intensity as a function of applied cathodic bias for three different transducers.*

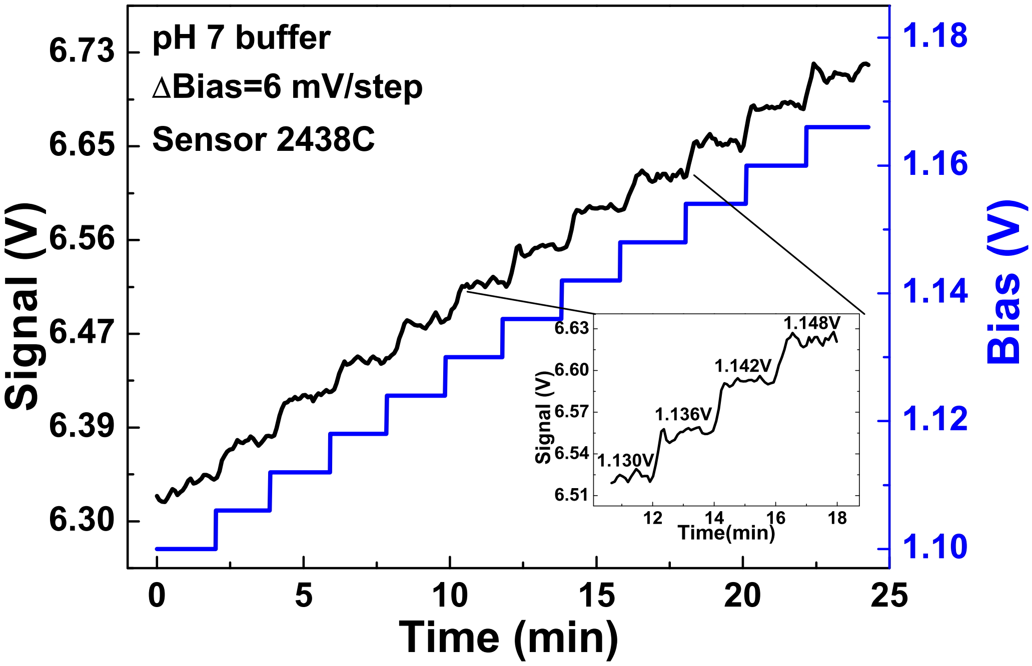

Figure 3.12: *Response of PL signal to 6 mV cathodic bias potential steps. This small variation in bias potential can be clearly resolved from the PL signal.*

3.7.2 Sensing mechanism

The pH sensitivty of GaN/InGaN nanowire PL was reorted by Wallys et al. [189]. Teubert et al. presented InGaN/GaN quantum dots as optical probes for the electric field at the GaN/electrolyte interface [188]. The electronic properties of the QDSL (Quantu Dot Superlattice) structure in contact with electrolyte have been explained in these works vividly. The transducer structures are grown on the c-plane of the wurtzite crystal. Polarization induced internal electric fields strongly affect the band structure of the III-N heterostructures. The band structure shown in Fig. 3.13 reveals that the electrons can escape into the AlGaN buffer region. At the same time, a strong barrier for the holes to the AlGaN layer is formed due to polarization induced charges at the AlGaN/GaN interface. Application of cathodic bias enhances the radiative recombination. In this case, the cathodic bias prevents electrons from escaping into the AlGaN layer and accelerates them towards the surface. This results in an increased electron density close to the surface. Non-radiative surface recombination in the QDs gets saturated and radiative recombination becomes prominent here. The applied cathodic bias also accelerates holes away from the surface resulting in the reduction of surface recombination and suppression of hole transfer to the electrolyte. When all escape mechanisms are fully suppressed, PL intensity reaches its maxima. Application of anodic bias discharges the holes to the electrolyte and electrons to the AlGaN buffer layer. This enhances non-radiative loss mechanisms and thereby reduces the PL intensity. In summary, the applied bias determines the number of photo excited carriers that reach confined QD states.

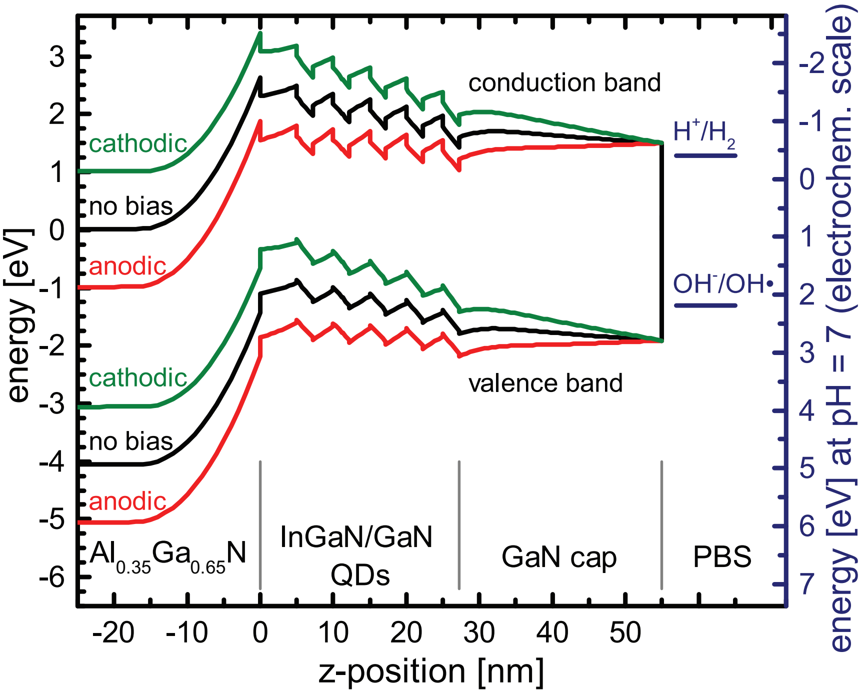

Figure 3.13: *Simulated band diagram of a QD multilayer structure with InGaN/GaN QDs for bias voltage $U = 0$ V (black color), $U = \pm 1000$ mV in cathodic (green color) and anodic polarity (red color) [188]. Application of cathodic (anodic) bias will suppresses (enhance) the non-radiative surface recombination.*

3.7.3 pH experiments

Fig. 3.14 displays the transient response of QD transducer 2291C to different pH solutions. These later results demonstrate very clearly that the PL of this transducer increases as the pH value in the fluid is lowered. The bias voltage was kept fixed at 1.10 V during these measurements. Upon returning to higher pH solutions again, a certain degree of hysteresis is observed. We attribute this effect to the relatively large dead volume of the measurement chamber which slows down the exchange of the fluid.

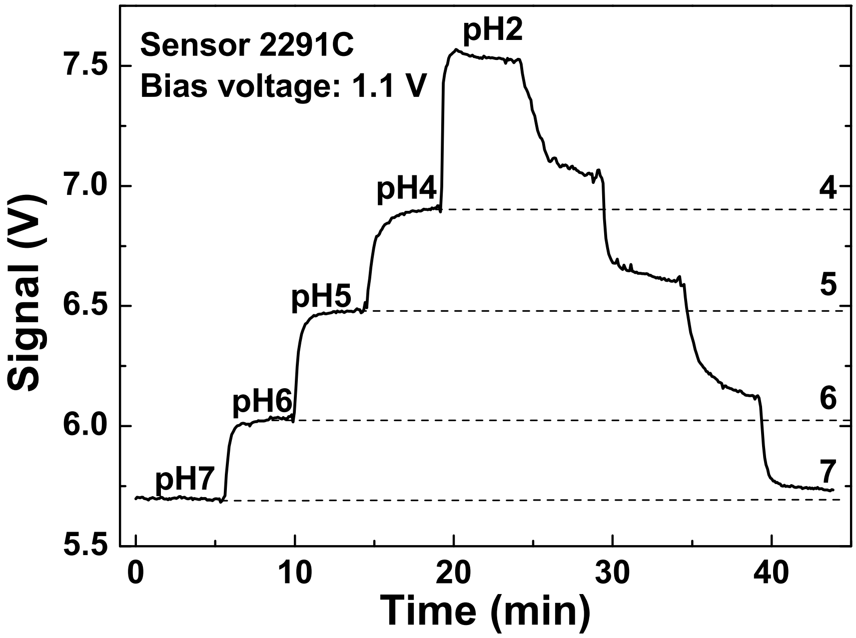

Figure 3.14: *PL response of transducer 2291C to a series of pH steps. Buffer solutions with different pH values were forced through the measurement chamber while maintaining a constant bias voltage of* $V_{bias} = 1.1$ *V. Lower values of pH give rise to a higher PL response.*

Similar experiments like Fig. 3.14 were also performed with the two other transducer structures. The results are summarized in Fig. 3.15. In each case a linear variation of the PL intensity with pH is observed. All three transducers investigated here showed maximum pH sensitivity at bias voltage around 1.0 to 1.1 V. Teubert et al. investigated similar transducers and reported maximum sensitivity occurring at bias potential around 600-700 mV [188]. In this reference, the calibration curve obtained at bias voltage 600 mV also showed almost linear enhancement of PL intensity with decreasing pH value.

3.7.4 Electric field dependent pH measurement

The above results have shown that, at a fixed bias point, the PL intensity of the QD transducers is dependent on the pH value of the test fluid. In the following we will show that, it is also possible to infer the pH value of an aqueous solution from the 1st derivative of the bias potential - PL intensity transfer characteristics curves presented in Fig. 3.11.

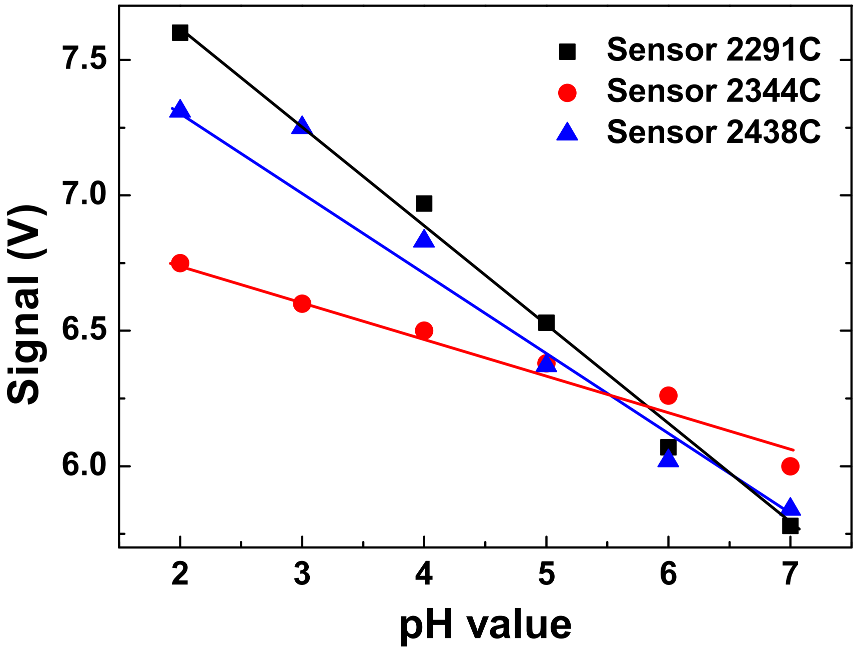

Figure 3.15: *Variation of PL intensity with different pH value for the three investigated transducers. Sensor 2291C was biased at 1.1 V. Sensor 2344C and 2438C were biased at 1.0 V.*

Fig. 3.16 presents transfer characteristics of transducer 2438C as measured over a range of biases extending from 0 to 1.4 V while being immersed in solutions with three different pH values. This same set of measurements, moreover, was repeated at three different LED intensities. Fig. 3.16 shows that under all three illumination conditions, the transfer curves are rigidly shifted towards higher bias levels when the pH is lowered. A second vertical shift towards lower PL intensity is observed when the LED drive current is reduced. The normalized and Gauss fitted first derivative of the curves from Fig. 3.16 are presented in Fig. 3.17. For a definite pH value, the maxima of the first derivative curves i.e. inflection point of the original transfer characteristic with three different light intensities, occur exactly at the same bias voltage. The PL signal – reference bias curve shifts along the voltage axis because of the change of surface potential at the interface of the sensing element and solution with different concentrations of H^+ present in pH buffer solution. Therefore, at constant excitation intensity, the inflection point calculated from the resulting PL intensity is dependent only on the pH value. This observation can be used to determine the pH value of the solution under study without reference to the absolute LED light level. This second method of determining the pH value is insensitive to the actual LED light level and therefore ignores temperature or degradation induced drifts in the LED light output level. An important source of error can thereby be eliminated.

Similar parallel shift in the transfer characteristics with change in pH is reported in several other III-N based pH sensors. Kokawa et al. reported AlGaN/GaN HEMT structures and showed the sensitivity for the potential change around 57 mV/pH [185]. Wallys et al. showed with Ga(In)N nanowire ensembles that, the pH induced shift of PL between 40 and 90 mV/pH [189]. Das et al. used GaN thin film for light addressable potentiometric sensor with pH sensitivity of 52 mV/pH [190]. Teubert et al. showed one order of magnitude

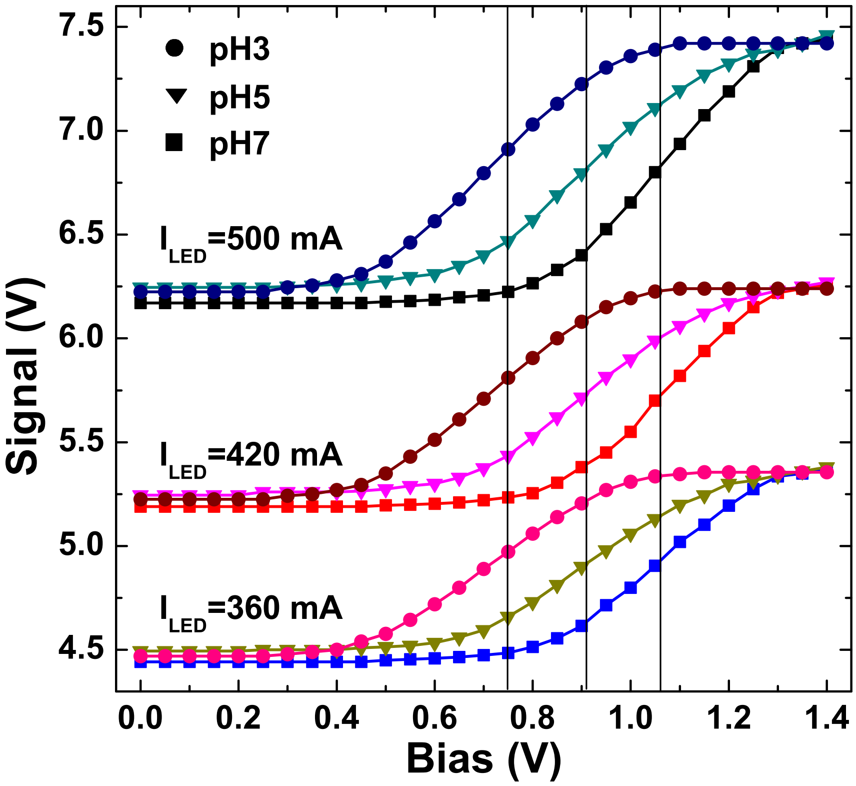

Figure 3.16: *Bias dependence of the PL output signal as measured in different pH solutions and under different LED light intensity levels. The inflection point for each plot is indicated by a vertical line.*

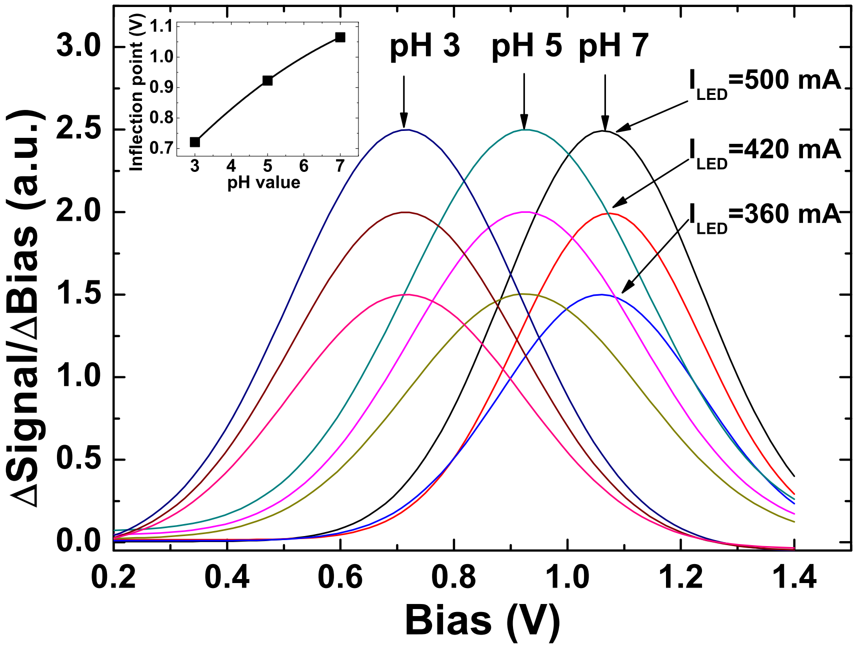

Figure 3.17: *Normalized 1st derivative of the data with of Fig. 3.16 as determined for the three different pH levels; (inset) position of inflection point as a function of pH for a fixed value of bias voltage.*

change in PL intensity obtained with bias voltage change of around 400 mV. Equivalent amount of change in PL intensity was obtained at a fixed bias of 600 mV for change in pH value from 7 to 1. Combining both statements, we can conclude around 400 mV/6pH i.e. the sensitivity of $\approx$ 70 mV/pH. Our investigated InGaN/GaN QD transducer shown in Fig. 3.17 resulted in a sensitivity between 70 to 90 mV/pH, which is in good agreement with the above described works.

3.8 Synopsis of pH detection

- InGaN quantum dots embedded in a GaN matrix layers have been successfully demonstrated as optochemical transducers for pH sensing.
- Three individually prepared sensors have been tested. The optimum working bias of the transducers ranged between 1.0 V and 1.2 V. pH sensitivities varied from 2.5% PL change per pH unit up to 7.5%/pH. Considering the noise levels in the PL output signal, minimum resolvable pH changes in the order of 0.035 to 0.1 pH units have been inferred.
- Commercially available optical pH sensors are mainly based on fluorescent or colorimetric optodes. The major constraint of such optodes is their narrow pH range (2-3 pH units) [191]. Several optodes therefore have usually to be combined to cover a larger pH range. In comparison, the InGaN/GaN QD transducers investigated in this work exhibited a better resolution over the entire range of acidic pH values. In addition, the QD transducers exhibited an almost real-time response. Nevertheless, the stability of these transducers needs to be further investigated.
- To fully cope with commercial pH sensors, the accuracy of the QD sensors needs to be improved. Future work also needs to address the problem of GaN cap layer degradation in basic solutions, i.e. at $pH > 7$.

Conclusion and outlook

Conclusion

The purpose of this study was to explore the real world applications of optochemical sensors especially for safety, security, passenger comfort, smart maintenance and environment friendliness in aircrafts. In this work, three areas of application have been assessed namely hydraulic fluid monitoring, gas monitoring and pH monitoring.

First part of this thesis involves the investigation of non-destructive infrared absorption based sensing principle to determine the health of phosphate-ester aviation hydraulic fluids. FTIR spectra of a wide range of hydraulic fluids with various contaminations were analyzed to determine the contamination dependent absorption lines. Two important chemical contamination parameters, i.e. water and acid formation could be monitored by the changes in the O-H stretching vibration bands in the mid infrared wavenumber range from 3200 cm^{-1} (3.12 μm) to 3800 cm^{-1} (2.63 μm). Both quantities can be assessed by monitoring the strength and the asymmetry of the free water absorption band centered around 3500 cm^{-1}. This sensor principle is independent of the composition of the aryl/alkyl phosphate-ester base fluids, since it senses localized vibrations associated with water and hydrolysis products (alcohols). A sensor system is also realized for online health monitoring of the fluids using commercially available MEMS components. The accessible water detection range (0-1.5%) complies with the range of water contaminations that can appear in the practical aircraft operation. The accessible TAN detection range (0-1 mg KOH/g), however, is somewhat smaller than the maximum desired TAN value of 1.5 mg KOH/g. In the near infrared region, these hydraulic fluids featured water-related absorption lines at around 1.4 μm and 1.9 μm. Making use of these absorption lines, a sensor system with excellent water sensitivity and a much wider optical path was demonstrated. In addition, the correlation between the TAN value and the photoluminescence from hydraulic fluid is reported in this work. The measurement principle is based on the luminescence of phenol molecules, which is one of the degradation products of phosphate-ester hydraulic fluids. For a given hydraulic fluid, changes in the phenol luminescence level found to be a good indicator of degradation.

The investigated sensor concepts in this work can be implemented to monitor relevant contamination parameters online, inside an aircraft or in a ground support car directly on the airfield and thereby, contribute to better maintenance of the hydraulic system and improve the flight safety.

In the second part of the dissertation, an all-optical gas sensor system based on group III-nitride nanowire optochemical transducers is demonstrated. The PAMBE-grown transducer sensing principle is based on the chemically-induced changes in the photoluminescence intensity. For example, exposure of Pt-coated nanowire ensembles to H_2 and HC gases resulted in an increase of the PL intensity which can be attributed to the suppression of surface recombination by local dipole fields of adsorbed atomic hydrogen. On the contrary, uncoated nanowires showed a decrease in PL intensity when exposed to O_2 and other oxidizing gases like NO_2 or O_3, which enhances the non-radiative surface recombination. Minimum detectable H_2 concentration was in the order of few 100 ppb when the transducers were operated at 80°C. In case of HC gases these concentrations were species-dependent, where unsaturated hydrocarbons could be detected with better response than saturated ones. For example, at a temperature of 80°C unsaturated C_2H_2 could be detected in the order of a few ppm whereas, saturated CH_4 could be detected in the order of 100 to 200 ppm. Optimum transducer temperatures arise as a compromise between catalytic break up of adsorbed H_2/HC species and a decreasing luminescence yield of the GaN/InGaN transducers. Optimum operation temperature for H_2/HC was between 60 to 100°C. In contrast, the highest response to oxidizing gases was obtained at room temperature with minimum detectable concentrations as: 1000 ppm for O_2, 50 ppb for NO_2 and 10 ppb for O_3. The response for all investigated gases changed linearly with the logarithm of the concentration. Besides, the response for oxidizing gases decreased in an approximately linear manner with increasing temperature. The response time of the sensors is in the order of few minutes. Furthermore, presence of humidity enhanced the sensor sensitivity and caused faster response and recovery time. This optochemical transducer principle offers the benefit of media separation and thereby has good potential to be implemented in safety critical and harsh environment applications.

In the last part of the thesis, InGaN quantum dots embedded in a GaN matrix layers are successfully demonstrated as optochemical transducers for pH sensing. A model based on the suppression or enhancement of non-radiative recombination processes in semiconductor-electrolyte has been proposed in ref [188]. For a defined electrochemical working point, changing the pH value of the electrolyte results in alteration of both hole transfer to the electrolyte and surface recombination, causing a change in the PL intensity. By using the conductive AlGaN:Si layer as a backside contact, the electrochemical working point could be defined to maximize the transducers sensitivity. The optimum working bias of the investigated transducers ranged between 1.0 V and 1.2 V. PL intensity varied in the range from 2.5% to 7.5%/pH unit. Considering the noise levels in the PL, minimum resolvable pH changes ranged in the order of 0.035 to 0.1 pH units. This InGaN/GaN QD transducers investigated in this work exhibited excellent resolution over the entire range of acidic pH values. In addition, the QD transducers exhibited an almost real-time response. As the entire structure is transparent to both the PL excitation and emission light, media separation can easily be achieved by using the sample as a transparent window separating the test liquid from the excitation source and detector elements.

Outlook

The presented sensor devices bear further room for improvement at various parameters. Moreover, some of the preliminary results obtained in this work require further investigations and verifications. Important aspects to be considered for future work on such sensors are as follows:

Hydraulic fluid monitoring

The sensor system developed in this work using mid infrared absorption lines can be used universally for many other fluids such as, bio fuels, transformer oils, engine oils etc. A detailed investigation for all applicable fluids was beyond the scope of this thesis. The results obtained within this work could not find any conclusive behavior between TAN value and the corresponding near infrared absorption lines and this requires more detailed inspection.

Gas sensor

The preliminary goal of the thesis was to examine the gas detection capability of the nanowire sensor. In spite of the fact that the NW sensor developed in this work is proven to be sensitive to several gases, the selectivity of such sensors has not been studied yet. In future works, the selectivity of these sensors can be addressed using a sensor array with different material composition. In fact, different gases have different UV absorption characteristics. Therefore, wavelength multiplication may also contribute to the enhancement of selectivity. The strong influence of mechanical stress on the NWH confinement potential gives rise to strain-dependent luminescence characteristics. Therefore, the potential of the NWH as pressure sensor can be explored in future work. The optimal performance of the sensor systems could be obtained through the integration of low cost optoelectronic devices, e.g. LEDs and photodiodes as well as enhanced electronics.

pH sensor

The results presented in this dissertation showed the capability of detection in acidic medium, i.e. pH 2-7. The unintentionally doped n-type GaN cap layer of the QD transducer is etched by basic solutions in pH>7. This situation can be improved in future work by p-type doping of the GaN top layer. A larger stokes shift will ease the sensor system design and help to improve the measurement accuracy. A red shift of the PL emission of the sensor will reduce the system cost by utilizing inexpensive blue LEDs and Si photodiodes. The results achieved in this work were obtained with polar QD transducers. Due to the higher PL intensity, semipolar transducers will offer advantages for practical applications. Proper investigation of semipolar transducers could reveal more interesting features.

Bibliography

[1] G. E. Totten, *Handbook of lubrication and tribology.* Florida: CRC Press, 2. ed., 2006.

[2] K. P. C. Vollhardt and N. E. Schore, *Organic chemistry: Structure and function.* New York: W.H. Freeman and Co., 4. ed., 2003.

[3] G. E. Totten and V. Negri, *Handbook of hydraulic fluid technology.* Florida: CRC Press, 2. ed., 2012.

[4] R. L. Shubkin, *Synthetic lubricants and high-performance functional fluids*, vol. 48 of *Chemical industries.* New York: M. Dekker, 1993.

[5] Exxon Mobil Corp., "Stability of Phosphate Ester Aviation Hydraulic Fluids," *Application note*, 2008.

[6] Solutia Inc., "Skydrol-Type IV Fire Resistant Hydraulic Fluids," *Application note*, 2003.

[7] D. Oesterle, "Hydraulic fluid: Pay now or pay later," *Hydraulics & Pneumatics*, vol. 59, p. 46, Aug 2006.

[8] L. Rudnick, *Lubricant additives: Chemistry and applications.* Florida: CRC Press, 2. ed., 2009.

[9] C. Bauer and M. Day, "Water contamination in hydraulic and lube systems," *Practicing Oil Analysis Magazine*, Sep 2009.

[10] D. Wooton, "Oxidation - the lubricant's nemesis," *Practicing Oil Analysis Magazine*, May 2007.

[11] K. Kudlaty, P. Andreas, and A. Koch, "Development of an infrared sensor for on-line analysis of lubricant deterioration," in *Proceedings of the IEEE Sensors*, pp. 903–908, 2003.

[12] M. Adamsa, M. Romeo, and P. Rawson, "FTIR analysis and monitoring of synthetic aviation engine oils," *Talanta*, vol. 73, no. 4, pp. 629–634, 2007.

[13] A. Agoston, C. Oetsch, J. Zhuravleva, and B. Jakoby, "An IR-absorption sensor system for the determination of engine oil deterioration," in *Proceedings of IEEE Sensors*, pp. 463–466, 2004.

[14] J. Kasberger and B. Jakoby, “Design of a Novel Fully Integrated IR - Absorption Sensor System,” in *2007 IEEE Sensors*, p. 515–518, IEEE, 2007.

[15] J. M. Hornback, *Organic chemistry.* Belmont and CA: Thomson, 2. ed., 2005.

[16] P. Kalsi, *Spectroscopy of Organic Compounds.* New Age International (P) Limited, 2004.

[17] A. Lambrecht, S. Hartwig, J. Herbst, and J. Wöllenstein, “Hollow fibers for compact infrared gas sensors,” in *Proceedings of SPIE*, vol. 6901, SPIE, 2008.

[18] B. Wilson, N. Hansen, and T. Peters, “Modular System for Multi-Parameter In-Line Machine Fluid Analysis,” in *Wearcheck Technical Bulletin*, 2000.

[19] N. Robinson, “Monitoring oil degradation with infrared spectroscopy,” *Practicing Oil Analysis Magazine*, Nov 2007.

[20] National Institute of Standards and Technology (NIST), “Infrared spectrum of water,” NIST Chemistry WebBook, 1969.

[21] T. Krist, *Hydraulik Fluidtechnik: Grundlagen der Ölhydraulik und Fluidtechnik.* Würzburg: Vogel, 8. ed., 1997.

[22] R. Behr and V. Baumbach, “Model based aerospace hydraulic fluid lifetime prognostics,” in *Recent Advances in Aerospace Actuation Systems and Components*, 2010.

[23] P. Capper and C. Elliott, *Infrared detectors and emitters: Materials and devices.* Boston: Kluwer Academic, 2001.

[24] A. Rogalski, *Infrared detectors.* Amsterdam: Gordon and Breach, 2000.

[25] M. Henini and M. Razeghi, *Handbook of infrared detection technologies.* New York: Elsevier Advanced Technology, 2002.

[26] K. Laidler, *The world of physical chemistry.* Oxford and and New York: Oxford University Press, 1995.

[27] J. Pippenger and T. Hicks, *Industrial hydraulics.* New York: Gregg Division, McGraw-Hill, 3. ed., 1979.

[28] P. Williams and K. Norris, *Near-infrared technology in the agricultural and food industries.* St. Paul, Minnesota: American Association of Cereal Chemists, 1987.

[29] D. A. Burns and E. W. Ciurczak, *Handbook of near-infrared analysis*, vol. 35 of *Practical spectroscopy.* Florida: CRC Press, 3. ed., 2008.

[30] S. Sasic and Y. Ozaki, *Raman, Infrared, and Near-Infrared Chemical Imaging.* New Jersey: John Wiley and Sons, 1. ed., 2011.

[31] J. Dixon, M. Taniguchi, and J. Lindsey, “Photochemcad 2: A refined program with accompanying spectral databases for photochemical calculations,” *Photochemistry and Photobiology*, vol. 81, no. 1, pp. 212–213, 2005.

[32] SAE Aerospace Standard (AS), “Cleanliness classification for hydraulic fluids,” Feb. 2005.

[33] Airbus:Private communication, “Passenger opinion poll,” 2003.

[34] G. Müller, S. Beer, S. Paul, and A. Helwig, “Novel chemical sensor applications in commercial aircraft,” *Procedia Engineering*, vol. 25, pp. 16–22, 2011.

[35] S. T. P. Webster, S. O’Neill, “A plan to commit unimaginable mass murder,” *The Times (London)*, 2006,11 August.

[36] A. Freiling, “New approaches to aircraft fire protection,” in *International Conference on Automatic Fire Detection*, (Maryland. USA), 2001.

[37] S. Beer, A. Helwig, W. Legner, and G. Müller, “Infrared-based fire gas detection systems,” in *International Conference on Automatic Fire Detection*, (Duisburg, Germany), 2009.

[38] S.-J. Chen, D. C. Hovde, K. A. Peterson, and A. W. Marshall, “Fire detection using smoke and gas sensors,” *Fire Safety Journal*, vol. 42, no. 8, pp. 507–515, 2007.

[39] Po-Chiang Chen, Guozhen Shen, and Chongwu Zhou, “Chemical sensors and electronic noses based on 1-D metal oxide nanostructures,” *IEEE Transactions on Nanotechnology*, vol. 7, no. 6, pp. 668–682, 2008.

[40] A. J. JIN, J. LI, and Y. LU, “The development of chemical nanosensors,” *Sensors & Transducers*, vol. 41, no. 13, pp. 140–146, Oct 2007.

[41] G. S. Korotchenkov, *Handbook of Gas Sensor Materials: Properties, Advantages and Shortcomings for Applications*. Integrated Analytical Systems, Dordrecht: Springer, 2013.

[42] F. Ren and S. Pearton, *Semiconductor Device-Based Sensors for Gas, Chemical, and Biomedical Applications*. Florida: CRC Press, 1. ed., 2011.

[43] W. J. Buttner, M. B. Post, R. Burgess, and C. Rivkin, “An overview of hydrogen safety sensors and requirements,” *International Journal of Hydrogen Energy*, vol. 36, no. 3, pp. 2462–2470, 2011.

[44] E. Jones, “The pellistor catalytic gas detector,” in *Solid State Gas Sensors* (P. Moseley and B. Tofield, eds.), pp. 17–31, Bristol: Adam Hilger, 1987.

[45] J. McAleer, P. Moseley, P. Bourke, J. Norris, and R. Stephan, “Tin dioxide gas sensors: use of the seebeck effect,” *Sensors and Actuators*, vol. 8, no. 3, pp. 251–257, 1985.

[46] V. Casey, J. Cleary, G. D’Arcy, and J. McMonagle, “Calorimetric combustible gas sensor based on a planar thermopile array: fabrication, characterisation, and gas response,” *Sensors and Actuators B: Chemical*, vol. 96, no. 1-2, pp. 114–123, 2003.

[47] J. R. Stetter and J. Li, “Amperometric gas sensors: a review,” *Chemical Reviews*, vol. 108, no. 2, pp. 352–366, 2008.

[48] M. Ando, “Recent advances in optochemical sensors for the detection of H_2, O_2, O_3, CO, CO_2 and H_2O in air,” *TrAC Trends in Analytical Chemistry*, vol. 25, no. 10, pp. 937–948, 2006.

[49] W. P. Jakubik, “Surface acoustic wave-based gas sensors,” *Thin Solid Films*, vol. 520, no. 3, pp. 986–993, 2011.

[50] T. Hübert, L. Boon-Brett, G. Black, and U. Banach, “Hydrogen sensors – a review,” *Sensors and Actuators B: Chemical*, vol. 157, no. 2, pp. 329–352, 2011.

[51] X. Liu, S. Cheng, H. Liu, S. Hu, D. Zhang, and H. Ning, “A survey on gas sensing technology,” *Sensors*, vol. 12, no. 7, pp. 9635–9665, 2012.

[52] P. Tobias, A. Baranzahi, A. Spetz, O. Kordina, E. Janzen, and I. Lundstrom, “Fast chemical sensing with metal-insulator silicon carbide structures,” *IEEE Electron Device Letters*, vol. 18, no. 6, pp. 287–289, 1997.

[53] J. Bodzenta, “Thin palladium film as a sensor of hydrogen gas dissolved in transformer oil,” *Sensors and Actuators B: Chemical*, vol. 87, no. 1, pp. 82–87, 2002.

[54] P. Kreisl, A. Helwig, A. Friedberger, G. Müller, E. Obermeier, and S. Sotier, “Detection of hydrocarbon species using silicon MOS capacitors operated in a non-stationary temperature pulse mode,” *Sensors and Actuators B: Chemical*, vol. 106, no. 2, pp. 489–497, 2005.

[55] P. Kreisl, A. Helwig, G. Müller, E. Obermeier, and S. Sotier, “Detection of hydrocarbon species using silicon MOS field-effect transistors operated in a non-stationary temperature-pulse mode,” *Sensors and Actuators B: Chemical*, vol. 106, no. 1, pp. 442–449, 2005.

[56] D. L.-M. Joel Villatoro and D. Monzón-Hernández, “Optical fiber hydrogen sensor for concentrations below the lower explosive limit,” *Sensors and Actuators B: Chemical*, vol. 110, no. 1, pp. 23–27, 2005.

[57] Y. H. Kim, M. J. Kim, B. S. Rho, M.-S. Park, J.-H. Jang, and B. H. Lee, “Ultra Sensitive Fiber-Optic Hydrogen Sensor Based on High Order Cladding Mode,” *IEEE Sensors Journal*, vol. 11, no. 6, pp. 1423–1426, 2011.

[58] V. I. Gaman, “Basic physics of semiconductor hydrogen sensors,” *Russian Physics Journal*, no. 51, 2008.

[59] T. Seiyama, A. Kato, K. Fujiishi, and M. Nagatani, “A new detector for gaseous components using semiconductive thin films,” *Analytical Chemistry*, vol. 34, no. 11, pp. 1502–1503, 1962.

[60] K. J. Choi and H. W. Jang, “One-dimensional oxide nanostructures as gas-sensing materials: Review and issues,” *Sensors*, vol. 10, no. 4, pp. 4083–4099, 2010.

[61] K. Cammann, B. Ross, A. Katerkamp, J. Reinbold, B. Gründig, and R. Renneberg, “Chemical and biochemical sensors,” in *Ullmann’s Encyclopedia of Industrial Chemistry*, Weinheim: Wiley-VCH, 2000.

[62] A. Qurashi, N. Tabet, M. Faiz, and T. Yamzaki, “Ultra-fast microwave synthesis of ZnO nanowires and their dynamic response toward hydrogen gas,” *Nanoscale Research Letters*, vol. 4, no. 8, pp. 948–954, 2009.

[63] N. Le Hung et al., “Synthesis and hydrogen gas sensing properties of ZnO wirelike thin films,” *Journal of Vacuum Science & Technology A: Vacuum, Surfaces, and Films*, vol. 27, no. 6, p. 1347, 2009.

[64] G. K. Mor, O. K. Varghese, M. Paulose, K. G. Ong, and C. A. Grimes, “Fabrication of hydrogen sensors with transparent titanium oxide nanotube-array thin films as sensing elements,” *Thin Solid Films*, vol. 496, no. 1, pp. 42–48, 2006.

[65] O. K. Varghese, D. Gong, M. Paulose, K. G. Ong, and C. A. Grimes, “Hydrogen sensing using titania nanotubes,” *Sensors and Actuators B: Chemical*, vol. 93, no. 1-3, pp. 338–344, 2003.

[66] Y. Shen, T. Yamazaki, Z. Liu, D. Meng, T. Kikuta, N. Nakatani, M. Saito, and M. Mori, “Microstructure and H_2 gas sensing properties of undoped and Pd-doped SnO_2 nanowires,” *Sensors and Actuators B: Chemical*, vol. 135, no. 2, pp. 524–529, 2009.

[67] B. Wang, L. F. Zhu, Y. H. Yang, N. S. Xu, and G. W. Yang, “Fabrication of a SnO_2 nanowire gas sensor and sensor performance for hydrogen,” *The Journal of Physical Chemistry C*, vol. 112, no. 17, pp. 6643–6647, 2008.

[68] J. M. Baik, M. H. Kim, C. Larson, C. T. Yavuz, G. D. Stucky, A. M. Wodtke, and M. Moskovits, “Pd-sensitized single vanadium oxide nanowires: Highly responsive hydrogen sensing based on the metal insulator transition,” *Nano Letters*, vol. 9, no. 12, pp. 3980–3984, 2009.

[69] J. Choi and J. Kim, “Highly sensitive hydrogen sensor based on suspended, functionalized single tungsten nanowire bridge,” *Sensors and Actuators B: Chemical*, vol. 136, no. 1, pp. 92–98, 2009.

[70] X.-J. Huang and Y.-K. Choi, “Chemical sensors based on nanostructured materials,” *Sensors and Actuators B: Chemical*, vol. 122, no. 2, pp. 659–671, 2007.

[71] W. Lim, J. S. Wright, B. P. Gila, J. L. Johnson, A. Ural, T. Anderson, F. Ren, and S. J. Pearton, “Room temperature hydrogen detection using Pd-coated GaN nanowires,” *Applied Physics Letters*, vol. 93, no. 7, p. 072109, 2008.

[72] A. Sadek, A. Trinchi, W. Wlodarski, K. Kalantar-zadeh, K. Galatsis, C. Baker, and R. Kaner, “A room temperature polyaniline nanofiber hydrogen gas sensor,” in *IEEE Sensors, 2005*, pp. 207–210, IEEE, 2005.

[73] Q. Cao and J. A. Rogers, “Ultrathin films of single-walled carbon nanotubes for electronics and sensors: A review of fundamental and applied aspects,” *Advanced Materials*, vol. 21, no. 1, pp. 29–53, 2009.

[74] Y. Sun and H. Wang, "High-performance, flexible hydrogen sensors that use carbon nanotubes decorated with palladium nanoparticles," *Advanced Materials*, vol. 19, no. 19, pp. 2818–2823, 2007.

[75] A. Kolmakov, Y. Zhang, G. Cheng, and M. Moskovits, "Detection of CO and O_2 using tin oxide nanowire sensors," *Advanced Materials*, vol. 15, no. 12, pp. 997–1000, 2003.

[76] H. T. Chen, S. J. Xiong, X. L. Wu, J. Zhu, J. C. Shen, and P. K. Chu, "Tin oxide nanoribbons with vacancy structures in luminescence-sensitive oxygen sensing," *Nano Letters*, vol. 9, no. 5, pp. 1926–1931, 2009.

[77] N. Murayama, N. Izu, W. Shin, and I. Matsubara, "Application of nano-sized CeO_2 powder for fast response oxygen sensors," *Key Engineering Materials*, vol. 421-422, pp. 323–327, 2009.

[78] G. Neri, A. Bonavita, G. Micali, G. Rizzo, N. Pinna, and M. Niederberger, "In_2O_3 and Pt-In_2O_3 nanopowders for low temperature oxygen sensors," *Sensors and Actuators B: Chemical*, vol. 127, no. 2, pp. 455–462, 2007.

[79] J. H. He, C. H. Ho, and C. Y. Chen, "Polymer functionalized ZnO nanobelts as oxygen sensors with a significant response enhancement," *Nanotechnology*, vol. 20, no. 6, p. 065503, 2009.

[80] Y.-J. Choi, I.-S. Hwang, J.-G. Park, K. J. Choi, J.-H. Park, and J.-H. Lee, "Novel fabrication of an SnO_2 nanowire gas sensor with high sensitivity," *Nanotechnology*, vol. 19, no. 9, p. 095508, 2008.

[81] J. Huang and Q. Wan, "Gas sensors based on semiconducting metal oxide one-dimensional nanostructures," *Sensors*, vol. 9, no. 12, pp. 9903–9924, 2009.

[82] N. Barsan, D. Koziej, and U. Weimar, "Metal oxide-based gas sensor research: How to?," *Sensors and Actuators B: Chemical*, vol. 121, no. 1, pp. 18–35, 2007.

[83] C. Wang, L. Yin, L. Zhang, D. Xiang, and R. Gao, "Metal oxide gas sensors: Sensitivity and influencing factors," *Sensors*, vol. 10, no. 3, pp. 2088–2106, 2010.

[84] B. S. Kang, H.-T. Wang, L.-C. Tien, F. Ren, B. P. Gila, D. P. Norton, C. R. Abernathy, J. Lin, and S. J. Pearton, "Wide bandgap semiconductor nanorod and thin film gas sensors," *Sensors*, vol. 6, no. 6, pp. 643–666, 2006.

[85] M.-W. Ahn et al., "Gas sensing properties of defect-controlled ZnO-nanowire gas sensor," *Applied Physics Letters*, vol. 93, no. 26, p. 263103, 2008.

[86] I.-D. Kim et al., "Ultrasensitive chemiresistors based on electrospun TiO_2 nanofibers," *Nano Letters*, vol. 6, no. 9, pp. 2009–2013, 2006.

[87] S.-H. Wang, T.-C. Chou, and C.-C. Liu, "Nano-crystalline tungsten oxide NO_2 sensor," *Sensors and Actuators B: Chemical*, vol. 94, no. 3, pp. 343–351, 2003.

[88] M. Law, H. Kind, B. Messer, F. Kim, and P. Yang, "Photochemical sensing of NO_2 with SnO_2 nanoribbon nanosensors at room temperature," *Angewandte Chemie International Edition*, vol. 41, no. 13, p. 2405, 2002.

[89] L. Valentini, I. Armentano, J. M. Kenny, C. Cantalini, L. Lozzi, and S. Santucci, "Sensors for sub-ppm NO_2 gas detection based on carbon nanotube thin films," *Applied Physics Letters*, vol. 82, no. 6, p. 961, 2003.

[90] J. Li, Y. Lu, Q. Ye, M. Cinke, J. Han, and M. Meyyappan, "Carbon nanotube sensors for gas and organic vapor detection," *Nano Letters*, vol. 3, no. 7, pp. 929–933, 2003.

[91] G. Faglia, A. Baratto, G. Sberveglieri, M. Zha, and A. Zappettini, "Adsorption effects of NO_2 at ppm level on visible photoluminescence response of SnO_2 nanobelts," *Applied Physics Letters*, vol. 86, no. 1, p. 011923, 2005.

[92] E. Comini, C. Baratto, G. aglia, M. Ferroni, and S. G., "Single crystal ZnO nanowires as optical and conductometric chemical sensor," *Journal of Physics D: Applied Physics*, vol. 40, no. 23, p. 7255, 2007.

[93] A. Setaro, A. Bismuto, S. Lettieri, P. Maddalena, E. Comini, S. Bianchi, and G. Baratto, C.and Sberveglieri, "Optical sensing of NO_2 in tin oxide nanowires at sub-ppm level," *Sensors and Actuators B: Chemical*, vol. 130, no. 1, pp. 391 – 395, 2008.

[94] S. J. Pearton et al., "GaN, ZnO and InN nanowires and devices," *Journal of Nanoscience and Nanotechnology*, vol. 8, no. 1, pp. 99–110, 2008.

[95] B. Kang, Y. Heo, L. Tien, D. Norton, F. Ren, B. Gila, and S. Pearton, "Hydrogen and ozone gas sensing using multiple ZnO nanorods," *Applied Physics A*, vol. 80, no. 5, pp. 1029–1032, 2005.

[96] G. Kenanakis, D. Vernardou, E. Koudoumas, G. Kiriakidis, and N. Katsarakis, "Ozone sensing properties of ZnO nanostructures grown by the aqueous chemical growth technique," *Sensors and Actuators B: Chemical*, vol. 124, no. 1, pp. 187–191, 2007.

[97] M. Epifani et al., "Chemical synthesis of In_2O_3 nanocrystals and their application in highly performing ozone-sensing devices," *Sensors and Actuators B: Chemical*, vol. 130, no. 1, pp. 483 – 487, 2008.

[98] S.-S. C. Forest, W. Chang-Ren, C. Yu-Lin, L. Hsiao-Lan, C. Min-Hung, and W. Ren-Jang, "Fast-response ozone sensor with ZnO nanorods grown by chemical vapor deposition," *Sensors and Actuators B: Chemical*, vol. 144, no. 1, pp. 120 – 125, 2010.

[99] M. Degner, N. Damaschke, H. Ewald, S. O'Keeffe, and E. Lewis, "UV LED-based fiber coupled optical sensor for detection of ozone in the ppm and ppb range," in *2009 IEEE Sensors*, pp. 95–99, IEEE, 2009.

[100] P. Youngmin, D. Ki-Young, L. Jinwoo, C. Jinnil, B. Gwi-Nam, and J. Byeong-Kwon, "Development of an ozone gas sensor using single-walled carbon nanotubes," *Sensors and Actuators B: Chemical*, vol. 140, no. 2, pp. 407 – 411, 2009.

[101] F. Hernandez-Ramirez, A. Tarancon, O. Casals, J. Arbiol, A. Romano-Rodriguez, and J. Morante, “High response and stability in CO and humidity measures using a single SnO_2 nanowire,” *Sensors and Actuators B: Chemical*, vol. 121, no. 1, pp. 3–17, 2007.

[102] D. Zhang, C. Li, X. Liu, S. Han, T. Tang, and C. Zhou, “Doping dependent NH_3 sensing of indium oxide nanowires,” *Applied Physics Letters*, vol. 83, no. 9, p. 1845, 2003.

[103] Q. Wan, J. Huang, Z. Xie, T. Wang, E. N. Dattoli, and W. Lu, “Branched SnO_2 nanowires on metallic nanowire backbones for ethanol sensors application,” *Applied Physics Letters*, vol. 92, no. 10, p. 102101, 2008.

[104] Y. Wang, I. Ramos, and J. J. Santiago-Aviles, “Detection of moisture and methanol gas using a single electrospun tin oxide Nanofiber,” *IEEE Sensors Journal*, vol. 7, no. 9, pp. 1347–1348, 2007.

[105] J. Chen, K. Wang, L. Hartman, and W. Zhou, “H_2S detection by vertically aligned CuO nanowire array sensors,” *The Journal of Physical Chemistry C*, vol. 112, no. 41, pp. 16017–16021, 2008.

[106] H. Y. Yu, B. H. Kang, U. H. Pi, C. W. Park, S.-Y. Choi, and G. T. Kim, “V_2O_5 nanowire-based nanoelectronic devices for helium detection,” *Applied Physics Letters*, vol. 86, no. 25, p. 253102, 2005.

[107] J. G. Lu, P. Chang, and Z. Fan, “Quasi-one-dimensional metal oxide materials—Synthesis, properties and applications,” *Materials Science and Engineering: R: Reports*, vol. 52, no. 1-3, pp. 49–91, 2006.

[108] H. Morkoç, *Materials Properties, Physics and Growth.* Handbook of Nitride Semiconductors and Devices, Weinheim: Wiley-VCH, 2009.

[109] H. Morkoç, *Electronic and Optical Processes in Nitrides.* Handbook of Nitride Semiconductors and Devices, Weinheim: Wiley-VCH, 2008.

[110] T. Seong, J. Han, H. Amano, and H. Morkoç, *Three-nitride Based Light Emitting Diodes and Applications.* Topics in applied physics, Springer, 2013.

[111] Z. Feng, *III-Nitride Devices and Nanoengineering.* Imperial College Press, 2008.

[112] B. Gil, *III-Nitride Semiconductors and Their Modern Devices.* Series on Semiconductor Science and Technology, OUP Oxford, 2013.

[113] F. Ren, B. Chu, K. Chen, C. Chang, V. Chen, and S. Pearton, “GaN-based sensors,” in *GaN and ZnO-based Materials and Devices* (S. Pearton, ed.), vol. 156 of *Springer Series in Materials Science*, pp. 165–207, Heidelberg: Springer, 2012.

[114] J. Schalwig, G. Müller, M. Eickhoff, O. Ambacher, and M. Stutzmann, “Gas sensitive GaN/AlGaN-heterostructures,” *Sensors and Actuators B: Chemical*, vol. 87, no. 3, pp. 425–430, 2002.

[115] M. Eickhoff, J. Schalwig, O. Weidemann, L. Gorgens, G. Müller, and M. Stutzmann, "Group III-nitride devices for field effect based gas detection," in *12th International Conference on Semiconducting and Insulating Materials, 2002. SIMC-XII-2002*, p. 64–69, IEEE, 2002.

[116] G. Müller, J. Schalwig, P. Kreisl, A. Helwig, E. Obermeier, O. Weidemann, M. Stutzmann, and M. Eickhoff, "High-temperature operated field-effect gas sensors," in *Encyclopedia of Sensors*, pp. 1–28, 2002.

[117] T. Kuykendall, P. Ulrich, S. Aloni, and P. Yang, "Complete composition tunability of InGaN nanowires using a combinatorial approach," *Nature Materials*, vol. 6, no. 12, pp. 951–956, 2007.

[118] J. Wu, "When group-III nitrides go infrared: New properties and perspectives," *Journal of Applied Physics*, vol. 106, no. 1, p. 011101, 2009.

[119] P. Ruterana, M. Albrecht, and J. Neugebauer, *Nitride semiconductors: Handbook on materials and devices*. Weinheim: Wiley-VCH, 1. ed., 2003.

[120] M. O. Manasreh, *III-nitride semiconductors: Electrical, structural, and defects properties*. Amsterdam and New York: Elsevier, 2000.

[121] X. B. Zhang, T. Taliercio, S. Kolliakos, and P. Lefebvre, "Influence of electron-phonon interaction on the optical properties of III nitride semiconductors," *Journal of Physics: Condensed Matter*, vol. 13, no. 32, pp. 7053–7074, 2001.

[122] W. Götz, N. M. Johnson, C. Chen, H. Liu, C. Kuo, and W. Imler, "Activation energies of Si donors in GaN," *Applied Physics Letters*, vol. 68, no. 22, p. 3144, 1996.

[123] J. A. Garrido, E. Monroy, I. Izpura, and E. Muñoz, "Photoconductive gain modelling of GaN photodetectors," *Semiconductor Science and Technology*, vol. 13, no. 6, pp. 563–568, 1998.

[124] R. Calarco, M. Marso, T. Richter, A. I. Aykanat, R. Meijers, A. v.d. Hart., T. S., and H. Lüth, "Size-dependent photoconductivity in MBE-grown GaN−nanowires," *Nano Letters*, vol. 5, no. 5, pp. 981–984, 2005.

[125] F. Furtmayr, J. Teubert, P. Becker, S. Conesa-Boj, J. R. Morante, A. Chernikov, S. Schäfer, S. Chatterjee, J. Arbiol, and M. Eickhoff, "Carrier confinement in GaN/Al$_x$Ga$_{1-x}$N nanowire heterostructures (0 <x$\leq$ 1)," *Physical Review B*, vol. 84, no. 20, 2011.

[126] J. Johansson and K. A. Dick, "Recent advances in semiconductor nanowire heterostructures," *CrystEngComm*, vol. 13, no. 24, p. 7175, 2011.

[127] L. Rigutti et al., "Optical properties of GaN and GaN/AlN nanowires: the effect of doping and structural defects," *physica status solidi (c)*, vol. 7, no. 7-8, pp. 2233–2235, 2010.

[128] R. Songmuang, G. Katsaros, E. Monroy, P. Spathis, C. Bougerol, M. Mongillo, and S. d. Franceschi, "Quantum transport in GaN/AlN double-barrier heterostructure nanowires," *Nano Letters*, vol. 10, no. 9, pp. 3545–3550, 2010.

[129] I. Krestnikov et al., “Quantum dot origin of luminescence in InGaN-GaN structures,” *Physical Review B*, vol. 66, no. 15, 2002.

[130] J. Lähnemann et al., “Coexistence of quantum-confined stark effect and localized states in an (In,Ga)N/GaN nanowire heterostructure,” *Physical Review B*, vol. 84, no. 15, 2011.

[131] L. J. Lauhon, M. S. Gudiksen, and C. M. Lieber, “Semiconductor nanowire heterostructures,” *Philosophical Transactions of the Royal Society A: Mathematical, Physical and Engineering Sciences*, vol. 362, no. 1819, pp. 1247–1260, 2004.

[132] H. Morkoç, *GaN-based Optical and Electronic Devices.* Handbook of Nitride Semiconductors and Devices, Weinheim: Wiley-VCH, 2009.

[133] R. Yan, D. Gargas, and P. Yang, “Nanowire photonics,” *Nature Photonics*, vol. 3, no. 10, pp. 569–576, 2009.

[134] Y. Li, F. Qian, J. Xiang, and C. M. Lieber, “Nanowire electronic and optoelectronic devices,” *Materials Today*, vol. 9, no. 10, pp. 18–27, 2006.

[135] F. Limbach et al, “Current path in light emitting diodes based on nanowire ensembles,” *Nanotechnology*, vol. 23, no. 46, p. 465301, 2012.

[136] J. Teubert, P. Becker, F. Furtmayr, and M. Eickhoff, “GaN nanodiscs embedded in nanowires as optochemical transducers,” *Nanotechnology*, vol. 22, no. 27, p. 275505, 2011.

[137] T. Kehagias et al., “Nanostructure and strain in InGaN/GaN superlattices grown in GaN nanowires,” *Nanotechnology*, vol. 24, no. 43, p. 435702, 2013.

[138] P. G. Moses and C. Walle, “Band bowing and band alignment in InGaN alloys,” *Applied Physics Letters*, vol. 96, no. 2, p. 021908, 2010.

[139] F. Furtmayr, M. Vielemeyer, M. Stutzmann, A. Laufer, B. K. Meyer, and M. Eickhoff, “Optical properties of Si- and Mg-doped gallium nitride nanowires grown by plasma-assisted molecular beam epitaxy,” *Journal of Applied Physics*, vol. 104, no. 7, p. 074309, 2008.

[140] F. Furtmayr et at., “Nucleation and growth of GaN nanorods on Si (111) surfaces by plasma-assisted molecular beam epitaxy - the influence of Si- and Mg-doping,” *Journal of Applied Physics*, vol. 104, no. 3, p. 034309, 2008.

[141] T. Yao and S.-K. Hong, *Oxide and nitride semiconductors: Processing, properties, and applications.* Berlin: Springer, 2009.

[142] G. Yi, *Semiconductor Nanostructures for Optoelectronic Devices: Processing, Characterization and Applications.* Nano Science and Technology, Berlin: Springer, 2012.

[143] S. Paul, A. Helwig, G. Müller, F. Furtmayr, J. Teubert, and M. Eickhoff, “Optochemical sensor system for the detection of H_2 and hydrocarbons based on InGaN/GaN nanowires,” *Sensors and Actuators B: Chemical*, vol. 173, pp. 120–126, 2012.

[144] V. E. Antonov, I. T. Belash, and V. Y. Malyshev, “The solubility of hydrogen in the platinum metals under high pressure,” *Platinum Metals Rev*, vol. 28, no. 4, pp. 158–163, 1984.

[145] W. Eberhardt, F. Greuter, and E. Plummer, “Bonding of H to Ni, Pd, and Pt surfaces,” *Physical Review Letters*, vol. 46, no. 16, pp. 1085–1088, 1981.

[146] A. Helwig, G. Müller, G. Sberveglieri, and G. Faglia, “Gas response times of nano-scale SnO_2 gas sensors as determined by the moving gas outlet technique,” *Sensors and Actuators B: Chemical*, vol. 126, no. 1, pp. 174–180, 2007.

[147] E. Calleja, M. Sánchez-García, F. Sánchez, F. Calle, F. Naranjo, E. Muñoz, U. Jahn, and K. Ploog, “Luminescence properties and defects in GaN nanocolumns grown by molecular beam epitaxy,” *Physical Review B*, vol. 62, no. 24, pp. 16826–16834, 2000.

[148] O. Weidemann, M. Hermann, G. Steinhoff, H. Wingbrant, A. Lloyd Spetz, M. Stutzmann, and M. Eickhoff, “Influence of surface oxides on hydrogen-sensitive Pd:GaN schottky diodes,” *Applied Physics Letters*, vol. 83, no. 4, p. 773, 2003.

[149] C. Pfüller, O. Brandt, F. Grosse, T. Flissikowski, C. Chèze, V. Consonni, L. Geelhaar, H. Grahn, and H. Riechert, “Unpinning the fermi level of GaN nanowires by ultraviolet radiation,” *Physical Review B*, vol. 82, no. 4, 2010.

[150] L.-H. Peng, C.-W. Shih, C.-M. Lai, C.-C. Chuo, and J.-I. Chyi, “Surface band-bending effects on the optical properties of indium gallium nitride multiple quantum wells,” *Applied Physics Letters*, vol. 82, no. 24, p. 4268, 2003.

[151] D.E. Williams, “Conduction and gas response of semiconductor gas sensors,” *Solid State Gas Sensors*, pp. 71–123, 1987.

[152] J. Watson, “The stannic oxide gas sensor,” *Sensor Review*, vol. 14, no. 1, pp. 20–23, 1994.

[153] G. Steinhoff, M. Hermann, W. J. Schaff, L. F. Eastman, M. Stutzmann, and M. Eickhoff, “pH response of GaN surfaces and its application for pH-sensitive field-effect transistors,” *Applied Physics Letters*, vol. 83, no. 1, pp. 177–179, 2003.

[154] A. Helwig, G. Müller, J. Garrido, and M. Eickhoff, “Gas sensing properties of hydrogen-terminated diamond,” *Sensors and Actuators B: Chemical*, vol. 133, no. 1, pp. 156–165, 2008.

[155] A. E. Shilov and G. B. Shulpin, *Activation and catalytic reactions of saturated hydrocarbons in the presence of metal complexes.* New York: Kluwer Academic Publishers, 2000.

[156] Y. Hu, O. K. Tan, W. Cao, and W. Zhu, “Fabrication and characterization of nano-sized $SrTiO_3$-based oxygen sensor for near room-temperature operation,” *IEEE Sensors Journal*, vol. 5, no. 5, pp. 825–832, 2005.

[157] R.-S. Chen, A. Ganguly, L.-C. Chen, and K.-H. Chen, "Recent advances in gan nanowires: Surface-controlled conduction and sensing applications," in *GaN and ZnO-based Materials and Devices* (S. Pearton, ed.), vol. 156 of *Springer Series in Materials Science*, pp. 295–315, Heidelberg: Springer, 2012.

[158] S. Vallejos, V. Khatko, J. Calderer, I. Gracia, C. Cané, E. Llobet, and X. Correig, "Micro-machined WO_3-based sensors selective to oxidizing gases," *Sensors and Actuators B: Chemical*, vol. 132, no. 1, pp. 209–215, 2008.

[159] A. Gurlo, N. Barsan, M. Ivanovskaya, U. Weimar, and W. Gopel, "In_2O_3 and MoO_3 and In_2O_3 thin film semiconductor sensors: interaction with NO_2 and O_3," *Sensors and Actuators B: Chemical*, vol. 47, no. 13, pp. 92–99, 1998.

[160] K. Bogumil, J. Orphal, J. Burrows, *et al.*, "Temperature dependent absorption cross sections of O_3, NO_2, and other atmospheric trace gases measured with the SCIAMACHY spectrometer," in *Proceedings of the ERS-Envisat-Symposium, Goteborg, Sweden*, 2000.

[161] C. A. Grimes, E. C. Dickey, and M. V. Pishko, *Encyclopedia of sensors.* Stevenson Ranch and Calif: American Scientific Publishers, 2006.

[162] N. Barsan and U. Weimar, "Conduction model of metal oxide gas sensors," *Journal of Electroceramics*, vol. 7, pp. 143–167, 2001.

[163] U. Resch-Genger, M. Grabolle, S. Cavaliere-Jaricot, R. Nitschke, and T. Nann, "Quantum dots versus organic dyes as fluorescent labels," *Nature Methods*, vol. 5, no. 9, pp. 763–775, 2008.

[164] G. Steude, B. K. Meyer, A. Goldner, A. Hoffmann, F. Bertram, J. Christen, H. Amano, and I. Akasaki, "Optical investigations of AlGaN on GaN epitaxial films," *Applied Physics Letters*, vol. 74, no. 17, p. 2456, 1999.

[165] M. Han, X. Gao, J. Z. Su, and S. Nie, "Quantum-dot-tagged microbeads for multiplexed optical coding of biomolecules," *Nature Biotechnology*, vol. 19, no. 7, pp. 631–635, 2001.

[166] R. Bogue, "Quantum dots: a bright future for photonic nanosensors," *Sensor Review*, vol. 30, no. 4, pp. 279–284, 2010.

[167] F. Prins et al., "Fast and efficient photodetection in nanoscale quantum-dot junctions," *Nano Letters*, vol. 12, no. 11, pp. 5740–5743, 2012.

[168] B. Larrión et al., "Photonic crystal fiber temperature sensor based on quantum dot nanocoatings," *Journal of Sensors*, vol. 2009, no. 19, pp. 1–6, 2009.

[169] Kulite Semiconductor, "Quantum dot based pressure switch," in *US patent*, no. US 7,358,581 B2, 2008.

[170] M. F. Frasco and N. Chaniotakis, "Semiconductor quantum dots in chemical sensors and biosensors," *Sensors*, vol. 9, no. 9, pp. 7266–7286, 2009.

[171] F. Arregui, *Sensors Based on Nanostructured Materials*. Heidelberg: Springer, 2009.

[172] S. Huang, H. Qiu, Q. Xiao, C. Huang, W. Su, and B. Hu, “A simple QD–FRET bioprobe for sensitive and specific detection of hepatitis B virus DNA,” *Journal of Fluorescence*, vol. 23, no. 5, pp. 1089–1098, 2013.

[173] J. M. Dubach, D. I. Harjes, and H. A. Clark, “Ion-selective nano-optodes incorporating quantum dots,” *Journal of the American Chemical Society*, vol. 129, no. 27, pp. 8418–8419, 2007.

[174] Y. Chen, Z. Chen, Y. He, H. Lin, P. Sheng, C. Liu, S. Luo, and Q. Cai, “L-cysteine-capped CdTe QD-based sensor for simple and selective detection of trinitrotoluene,” *Nanotechnology*, vol. 21, no. 12, p. 125502, 2010.

[175] L. Shang, L. Zhang, and S. Dong, “Turn-on fluorescent cyanide sensor based on copper ion-modified CdTe quantum dots,” *The Analyst*, vol. 134, no. 1, p. 107, 2008.

[176] Y. Zhang and T.-H. Wang, “Quantum dot enabled molecular sensing and diagnostics,” *Theranostics*, vol. 2, no. 7, pp. 631–654, 2012.

[177] J. I. Peterson, S. R. Goldstein, R. V. Fitzgerald, and D. K. Buckhold, “Fiber optic pH probe for physiological use,” *Analytical Chemistry*, vol. 52, no. 6, pp. 864–869, 1980.

[178] Q. Ma and X. Su, “Recent advances and applications in QDs-based sensors,” *The Analyst*, vol. 136, no. 23, p. 4883, 2011.

[179] M. Tomasulo, I. Yildiz, and F. M. Raymo, “pH-Sensitive Quantum Dots,” *The Journal of Physical Chemistry B*, vol. 110, no. 9, pp. 3853–3855, 2006.

[180] T. Jin, A. Sasaki, M. Kinjo, and J. Miyazaki, “A quantum dot-based ratiometric pH sensor,” *Chemical Communications*, vol. 46, no. 14, p. 2408, 2010.

[181] O. Weidemann, P. K. Kandaswamy, E. Monroy, G. Jegert, M. Stutzmann, and M. Eickhoff, “GaN quantum dots as optical transducers for chemical sensors,” *Applied Physics Letters*, vol. 94, no. 11, p. 113108, 2009.

[182] D. E. Yates, S. Levine, and T. W. Healy, “Site-binding model of the electrical double layer at the oxide/water interface,” *Journal of the Chemical Society, Faraday Transactions 1*, vol. 70, p. 1807, 1974.

[183] B. S. Kang et al., “pH sensor using AlGaN/GaN high electron mobility transistors with Sc_2O_3 in the gate region,” *Applied Physics Letters*, vol. 91, no. 1, p. 012110, 2007.

[184] L. Bousse, N. d. Rooij, and P. Bergveld, “Operation of chemically sensitive field-effect sensors as a function of the insulator-electrolyte interface,” *IEEE Transactions on Electron Devices*, vol. 30, no. 10, pp. 1263–1270, 1983.

[185] T. Kokawa, T. Sato, H. Hasegawa, and T. Hashizume, “Liquid-phase sensors using open-gate AlGaN/GaN high electron mobility transistor structure,” *Journal of Vacuum Science & Technology B: Microelectronics and Nanometer Structures*, vol. 24, no. 4, p. 1972, 2006.

[186] E. Monroy et al., “Surfactant effect of in for AlGaN growth by plasma-assisted molecular beam epitaxy,” *Journal of Applied Physics*, vol. 93, no. 3, p. 1550, 2003.

[187] J. Neugebauer, T. Zywietz, M. Scheffler, J. Northrup, H. Chen, and R. Feenstra, “Adatom kinetics on and below the surface: The existence of a new diffusion channel,” *Physical Review Letters*, vol. 90, no. 5, 2003.

[188] J. Teubert, S. Koslowski, S. Lippert, M. Schafer, J. Wallys, G. Dimitrakopulos, T. Kehagias, P. Komninou, A. Das, E. Monroy, and M. Eickhoff, “InGaN/GaN quantum dots as optical probes for the electric field at the GaN/electrolyte interface,” *Journal of Applied Physics*, vol. 114, no. 7, p. 074313, 2013.

[189] J. Wallys, J. Teubert, F. Furtmayr, D. M. Hofmann, and M. Eickhoff, “Bias-enhanced optical pH response of group III Nitride nanowires,” *Nano Letters*, vol. 12, no. 12, pp. 6180–6186, 2012.

[190] A. Das, A. Das, L. B. Chang, C. S. Lai, R. M. Lin, F. C. Chu, Y. H. Lin, L. Chow, and M. J. Jeng, “GaN thin film based light addressable potentiometric sensor for pH sensing application,” *Applied Physics Express*, vol. 6, no. 3, p. 036601, 2013.

[191] A. Richter, G. Paschew, S. Klatt, J. Lienig, K.-F. Arndt, and H.-J. P. Adler, “Review on Hydrogel-based pH sensors and microsensors,” *Sensors*, vol. 8, no. 1, pp. 561–581, 2008.

List of symbols and abbreviations

Symbols

λ_{ex}	Excitation wavelength
λ_{em}	Emission wavelength
λ_c	Center wavelength of a bandpass filter
λ_p	Peak emission wavelength
α	Absorption coefficient
R	Response
Tr	Transmission
δ	Relative deviation of signal

Abbreviations

ADC	Analog to Digital Converter
APU	Auxiliary Power Unit
a.u.	Arbitrary unit
CB	Conduction Band
CW	Continuous Wave
DAP	Donor Acceptor Pair
DAQ	Data Acquisition
D^0X	Donor-bound exciton
ECS	Environmental Control Systems
FET	Field Effect Transistor
FTIR	Fourier Transform Infrared
FWHM	Full Width at Half Maximum
GPIB	General Purpose Interface Bus
GSE	Ground Support Equipment
HC	Hydrocarbon
HEMT	High Electron Mobility Transistors
HVPE	Hydride Vapor Phase Epitaxy
IR	Infrared
LED	Light Emitting Diode
MIR	Mid Infrared
MEMS	Micro Electro Mechanical System
MOS	Metal Oxide Semiconductor
MOX	Metal Oxide

ND	Nanodisc
NDIR	Non Dispersive Infrared
NIR	Near Infrared
NW	Nanwire
NWH	Nanowire Heterostructure
n.i.d.	Not intentionally doped
OP	Operational amplifier
PAMBE	Plasma Assisted Molecular Beam Epitaxy
PEEK	Polyaryl-Ether-Ether-Ketone
POM	Polyoxymethylene
PCB	Printed Circuit Board
PCCN	Particle Contamination Count Number
PL	Photoluminescence
PMT	Photomultiplier Tube
QD	Quantum Dot
RT	Room Temperature
SA	Synthetic Air
SBB	Surface Band Bending
SCCM	Standard cubic centimeter
SEM	Scanning Electron Microscope
TAN	Total Acid Number
TEM	Transmission Electron Microscopy
TTL	Transistor Transistor Logic
USB	Universal Serial Bus
UV	Ultraviolet
VB	Valance Band
z.a.	Zone Axis

Acknowledgments

I would like to express the sincere gratitude to my adviser **Prof. Martin Eickhoff** for accepting me as a student in Justus Liebeig Univetsity. Throughout this work, I got the invaluable support, perfect guidance, useful suggestions, magnificent cooperation and effective advice from him. I especially thank to my supervisor in EADS **Dr. Gerhard Müller**, whose contribution in this work was unforgettable. I am very grateful to him for his kind and affectionate support during the thesis period. I would like to thank **Dr. Andreas Helwig**, whose helping and friendly guidance made this work possible. I am very thankful to him for making me familiarized with all the technological steps required for this work. I would like to convey my thanks to **Wolfgang Legner** for his sincere cooperation, effective suggestions regarding the implementation of technical thoughts. Many thanks to **Dr. Alois Friedberger** for providing invaluable support during the thesis period.

The collaboration partners from the Airbus - Hamburg, WSI - Munich, CEA - Grenoble, deserves a huge acknowledgment for their helping hands and exchange of ideas during this project. **Dr. Jörg Teubert** from JLU helped me with advices and analytical explanations for understanding the sensor physics. Thanks also to **Dr. Eva Monroy** from CEA and **Dr. Florian Furtmayr** from WSI for invaluable support with transducer samples. Special thanks to **Dr. Volker Baumbach** from Airbus for supporting the hydraulic sensor works.

I would like to convey my heartfelt thanks to my colleagues **Martin Kluge**, **Sebastian Beer**, **Michael Frazech**, **Angelika Hackner**, **Thomas Ziemann** for their valuable contributions towards this work.

List of publications

Journal contributions

- **S. Paul**, A. Helwig, G. Müller, F. Furtmayr, J. Teubert and M. Eickhoff, “Detection of Oxidising Gases using an Optochemical Sensor System Based on InGaN/GaN Nanowires” *Submitted to Sensors and Actuators B: Chemical*
- **S. Paul**, A. Helwig, G. Müller, F. Furtmayr, J. Teubert and M. Eickhoff, “Optochemical sensor system for the detection of H_2 and hydrocarbons based on InGaN/GaN nanowires ” *Sensors and Actuators B: Chemical*, Vol 173, pp. 120-126, 2012, doi.org/10.1016/j.snb.2012.06.022
- **S. Paul**, W. Legner, A. Hackner, G. Müller and V. Baumbach “Multi-Parameter Monitoring System für Hydraulische Flüssigkeiten” *Technisches Messen* Vol 78, No. 5, pp. 260-267, doi:10.1524/teme.2011.0117
- **S. Paul**, W. Legner, A. Krenkow, G. Müller, T. Lemettais, F. Pradat, and D. Hertens, “Chemical Contamination Sensor for Phosphate Ester Hydraulic Fluids” *International Journal of Aerospace Engineering*, vol. 2010, doi:10.1155/2010/156281

Conference Contributions

- **S. Paul**, A. Helwig, G. Müller, P. Becker, F. Furtmayr, J. Teubert and M. Eickhoff “Optical sensor system detecting ppm concentrations of hydrogen and hydrocarbon gases at low temperature using GaN/InGaN nanowires" *IEEE Sensors*, Limerick, Ireland October, 2011.
- **S. Paul**, A. Helwig and G. Müller, “A MEMS miniaturized monitoring system for aviation hydraulic fluids" *1st Annual World Congress of Nano-S & T*, Dalian, China, Oct. 2011. (Invited talk)
- G. Müller, S. Beer **S. Paul**, A. Helwig “Chemical sensor applications in commercial aircraft", *Eurosensors XXV*, Athens, Greece, Sep. 2011. (Invited paper)
- **S. Paul**, W. Legner, A. Hackner, G. Müller, V. Baumbach, “Multi-parameter monitoring system for aviation hydraulic fluids" *Smart Systems Integration*, Como, Italy, Mar. 2010.
- **S. Paul**, A. Helwig, G. Müller, F. Furtmayr, J. Teubert and M. Eickhoff, “InGaN/GaN nanowire based opto-chemical sensor for detecting hydrogen and hydrocarbons at low temperature" *14th International Meeting on Chemical Sensors - IMCS*, Nuremberg, Germany, May. 2012.

- **S. Paul**, A. Helwig, G. Müller, F. Furtmayr, J. Teubert and M. Eickhoff, “Opto-chemical sensor system based on InGaN/GaN nanowires for detection of oxidizing gases" *14th International Meeting on Chemical Sensors - IMCS*, Nuremberg, Germany, May. 2012.
- **S. Paul**, A. Helwig, a. Das, J. Teubert, E. Monroy, G. Müller and M. Eickhoff, “Opto-chemical sensor system based on InGaN/GaN quantum dots for pH detection" *14th International Meeting on Chemical Sensors - IMCS*, Nuremberg, Germany, May. 2012.
- **S. Paul**, A. Helwig, G. Müller, P. Becker, F. Furtmayr, J. Teubert and M. Eickhoff, “Optical sensor for room temperature hydrogen and hydrocarbon detection using GaN/InGaN nanowires" *SPIE Microtechnologies, Optics + Optoelectronics*, Prague, Czech Republic, Apr. 2011.
- **S. Paul**, V. Baumbach, A. Helwig and G. Müller, “Infrared absorption based sensor for aviation hydraulic fluids" *5th International Conference on Recent Advances in Aerospace Actuation Systems and Components (R3ASC'12)*, Toulouse France, Jun. 2012.

Patent application

- **S. Paul**, A. Helwig and G. Müller, "Vorrichtung und Verfahren zum Erfassen von Kontaminationen in einem Hydrauliksystem"
  German patent *No. DE/ 15.04.10/DEA102010015083*, 2011.
- G. Müller, **S. Paul** and A. Helwig, "Sensor und Verfahren zur Online-Überwachung der Särezahl eines Hydraulikfluids in einem Hydrauliksystem in einem Luftfahrtzeug"
  German patent *Filed application No. 10 2012 100 794.2*, 2012.
- M. Eickhoff, A. Helwig, G. Müller, J. Teubert, **S. Paul** and J. Wallys, "Optischer pH-Wert-Sensor"
  German patent *Filed application No. 10 2012 021*, 2012.
- M. Eickhoff, A. Helwig, G. Müller, J. Teubert, **S. Paul** and P. Becker, "Optischer Gassensor zur simultanen Detektion mehrerer (oxidierender und reduzierender) Gase"
  German patent *Application filed*, 2013.